EPFL

On the Capability of Wall-Modeled Large Eddy Simulations to Predict Particle Dispersion in Complex Turbulent Flows

Mohamed Aly Hashem Mohamed SAYED

École
polytechnique
fédérale
de Lausanne

2022

To my parents...

Science is what we understand well
enough to explain to a computer. Art is
everything else we do.

— *Donald Knuth*

Acknowledgements

Affidavit of Honour

I, undersigned, **Mohamed Aly Sayed**, hereby declare that the work presented in this manuscript is my own work, carried out under the scientific direction of **Dr. Abdel Dehbi**, **Dr. Konstantin Mikityuk** in accordance with the principles of honesty, integrity and responsibility inherent to the research mission. The research work and the writing of this manuscript have been conducted in compliance with both the Paul Scherrer Institute charter for Ethics in Research and the Swiss Federal Institute of Technology Lausanne (EPFL) charter on the fight against plagiarism. This research project is sponsored by Swiss National Science Foundation (SNSF) under grant number [200021-175532] in membership with the Federal pension fund PUBLICA according to the regulation of ETH domain (VR-ETH 1). This thesis has not been submitted previously either in Switzerland or in another country in the same or in a similar version to any other examination body.

Cairo, 7 August 2022   M.A. S.
Born in November 1994   Egypt

Abstract

Predicting particle transport in turbulent flows has a plethora of applications, some of which are: the transport of atmospheric aerosols, the deposition of blood cells in the arteries of human bodies and the atomization of fuel droplets in combustion chambers of propulsion systems. Today this is mostly done using Computational Fluid Dynamics (CFD) methods. To this end, the main impetus for the present research is the assessment of computational methodologies to simulate the transport and deposition of droplets and fission particles simulants in various components of nuclear reactors, which is considered an issue of high safety relevance. In order to accurately describe particle dispersion in a medium, one has to first properly compute the carrier fluid field, which is a rather challenging task, especially in complex 3D wall-bounded turbulent flows. While Reynolds-Averaged Navier-Stokes (RANS) approaches are generally unsatisfactory and Direct Numerical Simulations (DNS) are computationally prohibitive, the Large Eddy Simulation (LES) stands as the most adequate tool to address complex flows at reasonably high turbulence levels. Particulate flows require that the wall boundary layer be accurately resolved, since it is near the wall that particle physics is the most complex due to turbulence anisotropy and inhomogeneity. However, wall-bounded LES which resolves the boundary layer has stringent spatial resolution requirements in all directions. This translates into large CPU needs, which scales with the power of Reynolds number (i.e. $Re^{\frac{9}{4}}$). To address this bottleneck, recent research has proposed the so-called Wall Modeled LES (WMLES), which is a promising alternative to dramatically reduce the dependency of conventional LES on Reynolds number. The novel WMLES methodology has been applied with success in a limited number of complex wall-bounded fluid flows. Our investigation aims to take the WMLES methodology one step further by modeling the dispersion of inertial particles in an Euler/Lagrange framework and under simplified conditions. As a first step in this project, a Lagrangian Particle Tracking (LPT) algorithm was implemented in T-Flows code to simulate the dispersed phase. A point-particle approach was adopted whereby the fluid velocity is interpolated to the particle center-of-mass. We assume that particulate loading is dilute enough to justify a one-way coupling treatment. The LPT algorithm was tested and results were compared against the commercial code ANSYS Fluent through canonical turbulent flows in a verification step. Then, the algorithm was validated against the reference experimental data in 90-degree bend flow. To qualify a suitable WMLES model for later solving complex configurations, two recent WMLES methods were investigated; the Algebraic

WMLES (AWMLES) model by Shur et al., 2008, and the Elliptic Relaxation Hybrid RANS/LES (ER-HRL) model (Hadziabdic and Hanjalic, 2020). The first one employs the RANS mode in the very thin near-wall layer using the Prandtl mixing length damping, and switches to the traditional LES Smagorinsky mode all the way to the bulk region. The second approach employs a three-equation linear eddy viscosity (LEV) model while in RANS mode, and switches to the Smagorinsky dynamic model in the outer flow region. Both models were assessed with scrutiny in a turbulent channel flow where mean flow and Root Mean Square (RMS) values obtained by each model were compared to DNS data. To account for the effect of the unresolved scales on particle dispersion, two promising particle Sub-Grid Scale (SGS) approaches which have been proposed recently were investigated. The rationale behind those models is to redefine the fluid velocity seen by the particle - taking the modeled (unresolved) part of turbulent kinetic energy into account. The first model is the Fukagata model (Fukagata et al., 2004) which is based on the inclusion of artificial stochasticity via the Brownian diffusion force, and the second one is the $\zeta - SGS$ model, which was proposed during the course of this project (Sayed et al., 2021-b). The $\zeta - SGS$ model is coupled with particle motion through the wall-normal velocity transport equation (i.e. ζ). This model was shown to be very cost-effective when using relatively coarse meshes. The predictions of both models have been validated against DNS data in periodic channel flow at two Reynolds numbers $Re_\tau = 150, 590$. To check model performance in complex flows, three benchmark configurations have been carefully assessed, namely: Differentially Heated Cavity (DHC), Gas Cyclone Separator (GCS) and the swirl vane (droplet separator). As will be shown later, the flow topology in each of those configurations revealed the potential of using SGS models versus ignoring them. The thesis is organized as follows: the second Chapter discusses the most relevant turbulence models and the ones used in this thesis. The third Chapter i.e. LPT reports the main framework of the particle tracking algorithm in T-Flows and the associated particle SGS models within the implemented algorithm. In Chapter 4, the LPT algorithm alongside the implemented WMLES models are validated in turbulent channel flow against DNS data. Further validation and assessment of WMLES are conducted in complex flows in Chapters 5-7 where the Differentially Heated Cavity (DHC), Gas Cyclone Separator (GCS), and the swirl vane are investigated respectively. In the last Chapter, an extensive summary is given for the work done throughout the thesis. In addition, future recommendations are reported as perspectives for future developments in this direction.

Key words

Particle-laden Flows - Hybrid LES/RANS - Wall-Modeled LES - Particle Dispersion - Multiphase Flow Modeling - Heat Transfer - Turbophoresis - Lagrangian Particle Tracking - Particle Subgrid scale modeling - Complex Turbulent Flows.

Zusammenfassung

Für die Vorhersage des Partikeltransports in turbulenten Strömungen gibt es eine Vielzahl von Anwendungen, darunter der Transport von atmosphärischen Aerosolen, die Ablagerung von Blutzellen in den Arterien des menschlichen Körpers und die Zerstäubung von Kraftstofftröpfchen in den Brennkammern von Antriebssystemen. Dies geschieht heute meist mit Methoden der numerischen Strömungsmechanik (CFD). Zu diesem Zweck ist der Hauptimpuls für die vorliegende Forschung die Bewertung von Berechnungsmethoden zur Simulation des Transports und der Ablagerung von Tröpfchen und Spaltpartikel-Simulanzien in verschiedenen Komponenten von Kernreaktoren, was als ein Thema von hoher Sicherheitsrelevanz angesehen wird. Um die Partikeldispersion in einem Medium genau zu beschreiben, muss man zunächst das Feld des Trägerfluids richtig berechnen, was insbesondere bei komplexen wandbegrenzten turbulenten 3D-Strömungen eine recht anspruchsvolle Aufgabe ist. Während RANS-Ansätze (Reynolds-Averaged Navier-Stokes) im Allgemeinen unbefriedigend und DNS-Simulationen (Direct Numerical Simulations) rechnerisch unerschwinglich sind, stellt die Large-Eddy-Simulation (LES) das am besten geeignete Werkzeug dar, um komplexe Strömungen bei angemessen hohen Turbulenzgraden zu untersuchen. Partikelströmungen erfordern eine genaue Auflösung der Wandgrenzschicht, da die Partikelphysik in der Nähe der Wand aufgrund der Turbulenzanisotropie und Inhomogenität am komplexesten ist. Die wandgebundene LES, die die Grenzschicht auflöst, hat jedoch strenge Anforderungen an die räumliche Auflösung in allen Richtungen. Dies führt zu einem hohen CPU-Bedarf, der mit der Potenz der Reynoldszahl skaliert (d. h. $Re^{\frac{9}{4}}$). Um dieses Problem anzugehen, wurde in der jüngsten Forschung die so genannte Wall Modeled LES (WMLES) vorgeschlagen, die eine vielversprechende Alternative darstellt, um die Abhängigkeit der herkömmlichen LES von der Reynoldszahl drastisch zu verringern. Die neuartige WMLES-Methode wurde bereits in einer begrenzten Anzahl komplexer wandbegrenzter Strömungen mit Erfolg angewendet. Unsere Untersuchung zielt darauf ab, die WMLES-Methodik einen Schritt weiter zu bringen, indem wir die Dispersion von Trägheitspartikeln in einem Euler/Lagrange-Rahmen und unter vereinfachten Bedingungen modellieren. Als erster Schritt in diesem Projekt wurde ein Lagrangescher Partikelverfolgungsalgorithmus (LPT) in den T-Flows-Code implementiert, um die dispergierte Phase zu simulieren. Es wurde ein Punkt-Partikel-Ansatz gewählt, bei dem die Fluidgeschwindigkeit auf den Partikelschwerpunkt interpoliert wird. Wir gehen davon aus, dass die Partikelbelastung ausreichend verdünnt ist, um eine einseitige Kopplung zu

rechtfertigen. Der LPT-Algorithmus wurde getestet und die Ergebnisse wurden in einem Verifikationsschritt mit dem kommerziellen Programm ANSYS Fluent für kanonische turbulente Strömungen verglichen. Anschließend wurde der Algorithmus anhand der experimentellen Referenzdaten für eine 90-Grad-Krümmung validiert. Um ein geeignetes WMLES-Modell für die spätere Lösung komplexer Konfigurationen zu qualifizieren, wurden zwei neuere WMLES-Methoden untersucht: das algebraische WMLES-Modell (AWMLES) von Shur et al., 2008 und das Elliptische Relaxations-Hybrid-RANS/LES-Modell (ER-HRL) (Hadziabdic und Hanjalic, 2020). Das erste Modell verwendet die RANS-Methode in der sehr dünnen wandnahen Schicht unter Verwendung der Prandtl-Mischlängendämpfung nd wechselt dann zur traditionellen Smagorinsky-Methode der LES, die bis in den Bulk-Bereich reicht. Der zweite Ansatz verwendet ein Drei-Gleichungen-Modell der linearen Wirbelviskosität im RANS-Modus und wechselt im äußeren Strömungsbereich zum dynamischen Smagorinsky-Modell. Beide Modelle wurden in einer turbulenten Kanalströmung untersucht, wobei die von jedem Modell erzielten mittleren Durchflusswerte und der quadratische Mittelwert (englisch: root mean square RMS) mit DNS-Werten verglichen wurden. Um die Auswirkungen der unaufgelösten Skalen auf die Partikeldispersion zu berücksichtigen, wurden zwei vielversprechende Partikel-Sub-Grid-Scale (SGS)-Ansätze untersucht, die kürzlich vorgeschlagen wurden. Der Grundgedanke hinter diesen Modellen ist die Neudefinition der vom Partikel wahrgenommenen Flüssigkeitsgeschwindigkeit, unter Berücksichtigung des modellierten (unaufgelösten) Teils der turbulenten kinetischen Energie. Das erste Modell ist das Fukagata-Modell (Fukagata et al., 2004), das auf der Einbeziehung künstlicher Stochastizität über die Brownsche Diffusionskraft beruht, und das zweite ist das $\zeta - SGS$-Modell, das im Rahmen dieses Projekts vorgeschlagen wurde (Sayed et al., 2021-b). Das $\zeta - SGS$-Modell ist mit der Partikelbewegung über die Transportgleichung für die Wandnormalgeschwindigkeit (d. h. ζ) gekoppelt. Dieses Modell hat sich als sehr kosteneffizient erwiesen, wenn relativ grobe Netze verwendet werden. Die Vorhersagen beider Modelle wurden mit DNS-Daten in periodischer Kanalströmung bei zwei Reynoldszahlen, Re_τ = 150 und 590, validiert. Um die Leistung des Modells in komplexen Strömungen zu überprüfen, wurden drei Benchmark-Konfigurationen sorgfältig bewertet, nämlich: Differentially Heated Cavity (DHC), Gas Cyclone Separator (GCS) und der Tropfenabscheider. Wie später demonstriert wird, zeigt die Strömungstopologie in jeder dieser Konfigurationen das Potenzial der Verwendung von SGS-Modellen im Vergleich zu deren Nichtberücksichtigung. Die Arbeit ist wie folgt aufgebaut: Im zweiten Kapitel werden die wichtigsten Turbulenzmodelle und die in dieser Arbeit verwendeten Modelle vorgestellt. Das dritte Kapitel, LPT, beschreibt das Grundgerüst des Partikelverfolgungsalgorithmus in T-Flows und die zugehörigen Partikel-SGS-Modelle innerhalb des implementierten Algorithmus. In vierten Kapitel wird der LPT-Algorithmus zusammen mit den implementierten WMLES-Modellen in einer turbulenten Kanalströmung anhand von DNS-Daten validiert. Eine weitere Validierung und Bewertung von WMLES in komplexen Strömungen erfolgt in den Kapiteln 5-7, in denen der Differentially Heated Cavity (DHC), der Gas Cyclone Separator (GCS) bzw. die Drallschaufel untersucht werden. Im letzten Kapitel wird eine ausführliche Zusammenfassung der in dieser Arbeit geleisteten Arbeit gegeben. Darüber hinaus werden Empfehlungen für zukünftige Entwicklungen in dieser Richtung gegeben.

Schlüsselwörter

Partikelbeladene Strömungen - Hybride LES/RANS - Wandmodellierte LES - Partikeldispersion - Modellierung von Mehrphasenströmungen - Wärmeübertragung - Turbophorese - Lagrangesche Partikelverfolgung - Modellierung von Partikeluntergittern - Komplexe turbulente Strömungen.

Résumé

Prévoir le transport de particules dans des écoulements turbulents a une pléthore d'applications, dont certaines sont : le transport d'aérosols atmosphériques, le dépôt de cellules sanguines dans les artères du corps humain et l'atomisation de gouttelettes de combustible dans les chambres de combustion des systèmes de propulsion. Aujourd'hui, cela se fait principalement en utilisant des méthodes de dynamique des fluides computationnelles (CFD). À cette fin, le moteur principal de la présente recherche est l'évaluation de méthodes de calcul pour simuler le transport et le dépôt des gouttelettes et des particules de fission simulantes dans divers composants des réacteurs nucléaires, qui est considéré comme une question de grande pertinence pour la sécurité. Afin de décrire avec précision la dispersion des particules dans un milieu, il faut d'abord calculer correctement le champ de fluide porteur, ce qui est une tâche assez difficile, en particulier dans les écoulements turbulents complexes délimités par des parois en 3D. Bien que les approches Reynolds-Average Navier-Stokes (RANS) soient généralement insatisfaisantes et que les simulations numériques directes (DNS) soient prohibitives sur le plan informatique, les simulations des grands échelles (LES) est l'outil le plus adéquat pour traiter les écoulements complexes aux niveaux de turbulence raisonnablement élevés. Les écoulements de particules exigent que la couche limite de la paroi soit résolue avec précision, car c'est près de la paroi que la physique des particules est la plus complexe en raison de l'anisotropie de turbulence et de l'inhomogénéité. Toutefois, les ERP encadrés qui résolvent la couche limite ont des exigences strictes de résolution spatiale dans toutes les directions. Cela se traduit par des besoins importants en CPU, qui s'échelonnent avec la puissance du nombre de Reynolds (c'est-à-dire $Re^{\frac{9}{4}}$). Pour remédier à ce goulot d'étranglement, des recherches récentes ont proposé le modèle mural LES (WMLES), qui est une alternative prometteuse pour réduire considérablement la dépendance des ERP conventionnels à l'égard du nombre de Reynolds. La nouvelle méthodologie WMLES a été appliquée avec succès dans un nombre limité d'écoulements complexes de fluides confinés à la paroi. Notre étude vise à pousser la méthodologie WMLES plus loin en modélisant la dispersion des particules inertielles dans un cadre Euler/Lagrange et dans des conditions simplifiées. Dans un premier temps, un algorithme LPT (Lagrangian Particle Tracking) a été implémenté dans le code T-Flows pour simuler la phase dispersée. Une approche par particules ponctuelles a été adoptée selon laquelle la vitesse du fluide est interpolée au centre de masse des particules. Nous supposons que la

charge particulaire est suffisamment diluée pour justifier un traitement de couplage unidirectionnel. L'algorithme LPT a été testé et les résultats ont été comparés au code commercial ANSYS Fluent à travers des écoulements turbulents canoniques dans une étape de vérification. Ensuite, l'algorithme a été validé par rapport aux données expérimentales de référence dans un écoulements de courbure de 90 degrés. Pour qualifier un modèle WMLES approprié pour la résolution ultérieure de configurations complexes, deux méthodes WMLES récentes ont été étudiées : le modèle Algébrique WMLES (AWMLES) par SHUR et al., 2008, et le modèle Elliptique de Relaxation Hybride RANS/LES (ER-HRL) (HADZIABDIC et HANJALIC, 2020). La première utilise le mode RANS dans la couche très mince près de la paroi en utilisant l'amortissement de longueur de mélange Prandtl, et passe au mode traditionnel Smagorinsky de LES jusqu'à la région bulk. La deuxième approche utilise un modèle de viscosité de Foucault linéaire (LEV) à trois équations en mode RANS, et passe au modèle dynamique Smagorinsky dans la région d'écoulement externe. Les deux modèles ont été évalués avec attention dans un canal turbulent où les valeurs moyennes d'écoulement et de quadrature moyenne (RMS) obtenues par chaque modèle ont été comparées aux données DNS. Pour tenir compte de l'effet des échelles non résolues sur la dispersion des particules, deux approches prometteuses de l'échelle de sous-maille des particules (SGS) qui ont été proposées récemment ont été étudiées. La raison d'être de ces modèles est de redéfinir la vitesse du fluide vue par la particule - en tenant compte de la partie modélisée (non résolue) de l'énergie cinétique turbulente. Le premier modèle est le modèle de Fukagata (FUKAGATA et al., 2004) qui est basé sur l'inclusion de la stochasticité artificielle via la force de diffusion brownienne, et le second est le modèle ($\zeta - SGS$) qui a été proposé au cours de ce projet. (SAYED et al., 2021-b). Le modèle ($\zeta - SGS$) est couplé avec le mouvement des particules à travers l'équation de la vitesse normale de la paroi (c.-à-d. ζ). Il a été démontré que ce modèle est très rentable lorsqu'on utilise des maillages relativement grossières. Les prédictions des deux modèles ont été validées contre les données DNS en écoulement de canal périodique à deux nombres de Reynolds (Re_τ = 150, 590). Pour vérifier les performances du modèle dans des écoulements complexes, trois configurations de référence ont été soigneusement évaluées, à savoir : la cavité différentiellement chauffée (DHC), le séparateur cyclone à gaz (GCS) et la girouette (séparateur de gouttelettes). Comme nous le verrons plus loin, la topologie des écoulement dans chacune de ces configurations a révélé le potentiel d'utiliser les modèles SGS plutôt que de les ignorer. La thèse est organisée comme suit : le deuxième chapitre examine les modèles de turbulence les plus pertinents et ceux utilisés dans cette thèse. Le troisième chapitre c.-à-d. LPT rend compte du cadre principal de l'algorithme de suivi des particules dans T-Flows et les modèles SGS de particules associés dans l'algorithme mis en œuvre. Dans le chapitre 4, l'algorithme LPT aux côtés des modèles WMLES mis en œuvre est validé dans le écoulement de canaux turbulents par rapport aux données DNS. Une validation et une évaluation plus poussées du WMLES sont effectuées dans des écolements complexes dans les chapitres 5 à 7 où la cavité différentielle chauffée (DHC), le séparateur de cyclones gazeux (GCS) et la girouette sont étudiés respectivement. Dans le dernier chapitre, un résumé détaillé est donné pour le travail effectué tout au long de la thèse. En outre, les recommandations futures sont présentées sous forme de perspectives pour les développements futurs dans cette direction.

En outre, des recommandations futures sont présentées comme des perspectives pour les développements futurs dans cette direction.

Mots clés

écoulement chargés de particules - hybrides LES/RANS - modèles muraux LES - dispersion des particules - dodélisation d'écoulement multiphase - transfert de chaleur - turbophorèse - suivi des particules lagrangiennes - modélisation à l'échelle du sous-maille de particules - écoulement turbulents complexes.

Contents

List of Figures

List of Tables

Acronyms

- AMMD : Aerodynamic Mass Median Diameter

- ARTIST: AeRosol Trapping In a STeam generator

- ATS : Automatic Tracking Scheme

- AWMLES : Algebraic WMLES

- BCD : Bounded Central Difference

- BCs : Boundary Conditions

- BL : Boundary Layer

- CAD : Computer-Aided Design

- CFD : Computational Fluid Dynamics

- CFL : Courant–Friedrichs–Lewy number

- CLES : Coarse LES

- COR : Coefficient Of Restitution

- CRW : Continuous Random Walk

- DHC : Differentially Heated Cavity

- DIANA : DIfferentially heated cavity with Aerosol in turbulent NAtural convection

- DNS : Direct Numerical Simulation

- DRW : Discrete Random Walk

- ER-HRL: Elliptic Relaxation Hybrid RANS/LES

- GCS : Gas Cyclone Separator

- IRC : Intermediate Realistic conditions

- LES : Large Eddy Simulation

- LEVM : Linear Eddy Viscosity Model

- LPT : Lagrangian Particle Tracking

- MUSCL : Monotonic Upstream-centered Scheme for Conservation Laws

- PSI : Paul Scherrer Institut

- QUICK : Quadratic Upstream Interpolation for Convective Kinematics

- RANS : Reynolds-Averaged Navier Stokes

- RMS : Root Mean Square

- SEIM : Stochastic Eddy Interaction Model

- SGDH : Simple Gradient Diffusion Hypothesis

- SGS : Sub-Grid Scale

- SIMPLE: Semi-Implicit Method for Pressure Linked Equations

- SMART : Sharp and Monotonic Algorithm for Realistic Transport

- SSMA : Subgrid Stochastic Acceleration Model

- SVS : Swirl Vane Separator

- TKE : Turbulent Kinetic Energy

- WMLES : Wall-Modeled LES

- WRLES : Wall-Resolved LES

Nomenclature

L Representative physical length scale [m]

L_c Cavity side length [m]

ΔT Temperature difference [K]

α Thermal diffusivity ($\frac{k_f}{\rho c_p}$) [m^2/s]

β_D Particle decay constant [1/s]

λ Mean free path [m]

y^+ Non-dimensional wall distance $\left(\frac{y u_\tau}{\nu}\right)$ [m]

α_s Grid stretching factor [-]

β Thermal expansion coefficient [1/K]

ΔX_i Cell base size [m]

δ Periodic channel height [m]

δ_v Viscous time scale [s]

ϵ Turbulent dissipation (TKE) [m^2/s^3]

η Particle retention/ deposition efficiency [-]

κ' Von Kármán constant [-]

μ Dynamic molecular viscosity of carrier fluid [$kg/(m.s)$]

ν Kinematic molecular viscosity (momentum diffusivity i.e. $\frac{\mu}{\rho}$) [m^2/s]

ν_t Turbulent eddy viscosity (turbulent diffusivity) [m^2/s]

ρ_f Fluid mass density [kg/m^3]

ρ_p Particle mass density [kg/m3]

ρ_{ref} Reference density [kg/m^3]

τ_c Fluid circulation timescale (L/V_r) [s]

τ_f Kolmogorov timescale (fluid timescale) [s]

$\tau_{ij} = u_i u_j$ Reynolds stress tensor $[m^2/s^2]$

τ_p Particle relaxation time [s]

τ_p Particle timescale (also: particle relaxation time) [s]

τ_w Wall shear stress $[kg/(m.s^2)]$

ζ Variance of wall-normal fluctuations normalized by TKE [-]

b Bin's ordinal number [-]

C_0 Initial particle concentration [-]

C_c Cunningham slip-correction factor [-]

C_{dyn} Dynamic Smagorinsky coefficient [-]

C_d Drag coefficient [-]

c_p Heat capacity $[J/K]$

C_t Local particle concentration in time [-]

d_{AMMD} Particle aerodynamic diameter $\left(\sqrt{\frac{\rho_p}{\rho_{H_2O}}d_p^2}\right)$ [m]

D_p Pipe diameter [m]

d_p Particle diameter [m]

F The elliptic-relaxation transport function $[1/s]$

f Stokes drag correction factor $\left(\frac{Re_p}{24}C_d\right)$ [-]

g_i Gravity vector $[m/s^2]$

k Turbulent kinetic energy (TKE) $[m^2/s^2]$

k_f Fluid thermal conductivity $[W/(mK)]$

k_p Particle thermal conductivity $[W/(m.K)]$

k_{SGS} Subgrid scale turbulent kinetic energy (SGS-TKE) $[m^2/s^2]$

Kn Knudsen number $(\frac{\lambda}{L})$ [-]

L_K Kolmogorov length scale [m]

m_p Particle mass $[kg]$

N_b Number of bins across the channel [-]

P_k Production of turbulent kinetic energy $(2\nu_t S_{ij} S_{ij})$ $[m^2/s^3]$

Pr Prandtl number $(\frac{\alpha}{\nu})$ [-]

Pr_t Turbulent Prandtl number $(\frac{\alpha_t}{\nu_t})$ [-]

Ra Rayleigh number $\left(\frac{g\beta\Delta T L_C^3}{\nu\alpha}\right)$ [-]

Re Bulk Reynolds number [-]

Re_τ Shear (friction) Reynolds number [-]

S_{ij} Strain rate tensor [1/s]

$St = \tau_p^+$ Particle Stokes number (τ_p/τ_f) [-]

T Temperature $[K]$

t^+ Dimensionless time [-]

T_{ref} Reference temperature $[K]$

u_τ Friction velocity $\left(\frac{\tau_w}{\rho}\right)$ $[m/s]$

$u_i\theta$ Turbulent heat flux $[m.K/s]$

U_i Dimensional fluid velocity vector [m/s]

U_i Fluid velocity vector [m/s]

$U_{p,i}$ Dimensional particle velocity vector [m/s]

$V_{p,i}$ Particle velocity vector [m/s]

V_r Fluid circulation speed due to thermal stratification $\left(\frac{\alpha\sqrt{Ra}}{L_C}\right)$ $[m/s]$

V_{TS} Particle terminal speed $(\tau_p g_i)$ $[m/s]$

$X_{p,i}$ Particle local Cartesian coordinates [m]

y^+ Non-dimensional wall distance [-]

1 Introduction

1.1 Background

Predicting particle transport in turbulent flows is today mostly done using Computational Fluid Dynamics (CFD) methods. While being involved in most of the engineering applications, the Reynolds-Averaged Navier-Stokes (RANS) approach suffers from inaccuracies and lacks important details about the unsteady flow information. In addition, standard RANS methods fail in complex 3D flows which exhibit high levels of anisotropy and secondary motions. Such deficiencies render RANS unsatisfactory in CFD-based design. A good overview of RANS modeling and its limitations is archived through the works of Bush et al., 2019; P. A. Durbin and Pettersson Reif, 2010; Hanjalic and Launder, 2011; Wilcox, 1993

On the other side of the spectrum, the Direct Numerical Simulations (DNS), although being the most accurate with the absence of modeling errors, it is considered computationally prohibitive in complex and high Reynolds number flows. As a common ground, the Large Eddy Simulation (LES) stands as the most adequate tool to address complex flows at reasonably high turbulence. However, it must be recalled that particulate flows require that the wall boundary layer be fully resolved since it is near the wall that particle physics is the most complex (i.e. particle-wall interactions such as particle bouncing and deposition). As a matter of fact, wall-bounded LES which resolves the boundary layer (also known as Wall-Resolved LES or WRLES) has stringent spatial resolution requirements in all directions. This is due to the ever-decreasing turbulent length scale relative to the boundary layer thickness (which itself decreases with higher Re numbers). As a result, performing LES translates into very large CPU needs which grow exponentially with the Reynolds (Re) number. A clear picture of LES modeling and its resource requirements can be found in Geurts, 2004; Sagaut, 2006.

To circumvent the problem of the boundary layer resolution, a divide-and-conquer tactic must be employed. This means that the turbulence cannot be addressed throughout the whole domain at once. Instead, the domain is compartmentalized into zones, where turbulence is resolved in some parts and modeled in others. Such a strategy is referred to as Scale-Resolving Simulation (SRS).

To this end, the so-called hybrid models are increasingly applied, whereby inertial and energy-containing eddies are resolved away from walls while the wall boundary layers are covered by a RANS model. A plethora of such models have been proposed over the last two decades, some of which are detached eddy simulation (DES) (Spalart, 2000; Strelets, 2001; Travin et al., 2004), scale-adaptive simulation (SAS) (Egorov et al., 2010; Menter and Egorov, 2010), and Partially Averaged Navier–Stokes (PANS) models (Girimaji and Abdol-Hamid, 2005). More advanced versions of DES include delayed DES (DDES), shear-layer-adapted (SLA) DDES (DDESSLA), and improved DDES (IDDES) (Gritskevich et al., 2012; Shur et al., 2008, 2015; Spalart et al., 2006. More recent developments have been done in this area like the shielded detached eddy simulation (SDES) and the stress-blended eddy simulation (SBES) models (Menter, 2018).

A further step is to apply a RANS model only in the innermost part of the wall boundary layer (the thin viscous sub-layer) and then to switch to an LES model for the main part of the boundary layer to the bulk flow. Such models are termed wall-modeled LES (WMLES) models. In this light, two WMLES are employed in this work: an algebraic WMLES (termed as AWMLES throughout this thesis) and the Elliptic Relaxation Hybrid RANS/LES (ER-HRL). The algebraic model is a promising approach that has been proposed by Shur et al., 2008 as an alternative to dramatically reduce the LES dependency on the Reynolds number. The AWMLES endeavors to avoid resolving small near-wall scales through a hybrid treatment in which an implicit RANS model is applied in the very thin near-wall layer (through Prandtl mixing length formulation), whereas the LES approach is applied further away as the grid size is large enough to resolve the local scales. The AWMLES methodology has been applied with success in a limited number of complex wall-bounded fluid flow simulations (Menter, 2013). However, it was shown in Sayed et al., 2020 that the model still suffers from bridging problems at the RANS/LES interface. This usually results in the common log-layer mismatch (LLM) conundrum, which needs extra empiricism to be remedied. The second model discussed in this project is the ER-HRL approach, which is based on an explicit three-equation RANS formulation in the near-wall region switching to the dynamic Smagorinsky model in the LES region. This ER model has proved to be very robust and highly efficient in several canonical and complex industrial flows Hadziabdic et al., 2021; Hadziabdic and Hanjalic, 2020; H. Hadžiabdić et al., 2022; Sayed et al., 2021-b; Sayed et al., 2021-a.

For particulate flows, however, WMLES has not yet been tested, to the best of our knowledge. This Ph.D. project hereafter aims at modeling the dispersion of inertial particles using WMLES in an Euler/Lagrange approach under simplified conditions. The study will concern applications where particles (order of a few microns) are much smaller than the Kolmogorov scale, and therefore flow around particles need not be resolved. Rather, a point-particle approach will be adopted in the Lagrangian simulation. In addition, we consider very dilute particle-laden flow where the one-way coupling is adequate and particle-particle interactions are negligible. Lastly, walls on which particles impact are considered smooth, and particle deposits are negligible enough not to alter the smoothness of the wall.

As will be discussed below, the first step in this project is the implementation of a Lagrangian particle tracking algorithm in the T-Flows code (Ničeno, 2001) which has been used as a framework code in this thesis. As a second step, we validate WMLES predictions of fluid flow statistics in the canonical periodic channel flow configurations, for which DNS data are available at a wide range of Reynolds numbers Sayed et al., 2020. In a third step, two promising models for the effects of the subgrid scales (SGS) on particle transport will be implemented and tested. Lagrangian simulations using WMLES were conducted and validated against DNS data in channel flows at low-to-mid shear Reynolds numbers Sayed et al., 2021-b. Finally, WMLES particulate flow simulations performed were compared to WRLES and experimental data in a number of complex flows, namely in a differentially heated cavity, a cyclone, and swirl wane of steam generator (ARTIST project).

The project results offer a thorough assessment of the capability of two common WMLES approaches to compute particulate flows in complex geometries at a reduced CPU cost relative to the classical LES. The gathered information is first of a kind and was disseminated through a number of journal publications. These will give researchers in many disciplines a large validation database of the WMLES approach for particulate flows.

1.2   The state of research in particulate flow modeling

There are two main families of methods to treat particle dispersion in fluid flows: the Eulerian (Euler-Euler method) and Lagrangian (or Euler-Lagrange) methods. In the Euler-Euler (E-E) or "two-fluid" approach, the main challenge resides in accurately defining the inter-phase exchange rates and closure laws that arise from the averaging procedures (Drew, 1983). In addition, the strong coupling between the phases renders the E-E approach quite delicate to handle, especially at boundaries where the solid phase may be removed or reflected. The Lagrangian approach (E-L) treats particles as a discrete phase that is dispersed in the continuous phase (Maxey, 1987). In the E-L framework, the controlling phenomena for particle dispersion in the field are assessed using a rigorous treatment of the forces acting on the particle. The predictive capability of Lagrangian particle dispersion in turbulence flows is determined to a large extent by the accuracy of the underlying carrier fluid flow field. More details for each method with its pros and cons are laid out in Chapter 3. As will be shown later, we use the E-L approach throughout this project for all the investigated cases. In the following, the most recent developments in particle SGS modeling will be discussed as well as the novelty brought by this present work in this context. Such developments are assessed through both types of flows: forced convection and naturally convected flows.

1.2.1   Forced particulate flows

As DNS and traditional LES methodologies are very time-consuming, especially when coupled to Lagrangian particle tracking (LPT), a long-lasting effort has been made at Paul Scherrer Institute (PSI) to couple the mean-field of RANS-type models with stochastic models to

supply physically credible velocity fluctuations and hence allow relatively accurate predictions of particulate flows in simple, topologically one-dimensional flows. In Dehbi, 2008a, the Lagrangian particle dispersion in the ANSYS Fluent code, based on the Discrete Random Walk (DRW), was modified to include a better treatment of particle–turbulence interactions close to walls where anisotropic effects are most significant. The fluid RMS velocities in the boundary layer are no longer assumed isotropic, but rather computed using fits of DNS data obtained in channel flow. Confrontation of the new model predictions against experimental data (pipe, 90-degree bend, and human mouth throat geometry (MTG)) showed significantly improved accuracy compared to the code's default isotropic model, yet there is always an over-prediction of deposition for particles which have very low inertia. This is principally due to the discrete nature of the DRW model, which imposes non-physically large (infinite) fluid accelerations at the end of each discrete eddy lifetime.

A better model for RANS-type simulations was proposed by Dehbi, 2008b, and makes use of the normalized stochastic Drift Correction Langevin model (DCM) to describe fluid fluctuations seen by inertial particles in a continuous rather than a discrete way. Validations of the model were performed against particle deposition data in turbulent pipe flows, 90-degree bends, as well as more complex 3D flows inside an idealized human mouth-throat geometry, showing better agreement with the data compared to the DRW of Dehbi, 2008a. The RANS-Langevin model was further validated (Dehbi, 2009) against experiments where thermal gradients induce a strong thermophoretic force on the particles in the direction of the wall, and the agreement with the data was found to be good.

As a follow-up Dehbi, 2011 considered particulate flows with more complex yet topologically one-dimensional flows, i.e. the idealized MTG, and made a detailed comparison against the experimental flow field and particle deposition data. Both RANS-Langevin and LES simulations were performed. With extensive validation against flow field and particle deposition data, it was demonstrated that RANS-Langevin yields accuracy which compares favorably with the more computationally intensive LES approach. Finally, for simplified configurations, the model was successfully validated against DNS channel flow data (Dehbi, 2010).

Later on, a flow with a more challenging geometry was considered, i.e. the T-junction Dehbi and De Crécy, 2011. In that work, a turbulent fluid-particle mixing was simulated downstream of a T-junction using the E-L approach whereby tracer particle trajectories are computed and mixing of the streams deduced from the relative concentration of particles originating from the two inlet branches of the Tee. In a first simulation, RANS Reynolds Stress Model (RSM) is used to obtain the mean flow field, whereas the fluid fluctuations are specified from the Langevin model. Simulation results are compared to experimental data on the mixing of two isothermal streams consisting of tap and deionized water, respectively. It was found that RSM-Langevin yields strong under-prediction of the mixing. A closer look at the results showed that the Reynolds stresses, which are required inputs to the DCM model are poorly predicted with the RANS model. Detached Eddy Simulations (DES) was subsequently performed to provide the mean flow field, and the DES Langevin model predictions for mixing improved significantly

when compared to the experimental data. The reason of using a DES mean flow field rather than the instantaneous field was to reduce the particle Lagrangian computational time which considerably exceeded the fluid time.

A similar approach was used by Mukin and Dehbi, 2016. The time-averaged DES field was coupled to the stochastic Langevin model of Dehbi, 2008b to compute particle deposition in a complex tube bundle geometry in which the flow emerges from a broken tube. The flow field and particle deposition predictions compared reasonably well with the measured data but it is believed that better agreement could be achieved if time-averaging of the DES field is not done, as information is invariably lost in such procedures.

From this wide-ranging set of validations, we conclude that for topologically one-dimensional forced particulate flows, the RANS-Langevin approach can provide reasonable agreement with the data. On the other hand, when the flow departs significantly from a one-dimensional topology, only LES-and-DES types of approaches are able to predict more accurately turbulent particulate flows. This brings us to the main impetus of using hybrid RANS/LES models in this project.

1.2.2 Naturally-convected particulate flows

In the context of naturally driven turbulent flows, small particles with diameters in the micron size have been observed to deposit at rates significantly higher than predicted by a simple theoretical model in closed containments. To elucidate this phenomenon, spectral DNS (Puragliesi, 2010) and spectral-element LES (Bosshard et al., 2013) of particulate flow inside a differentially heated cavity (DHC) at Rayleigh number (Ra) 10^9 have been performed in the framework of PhD theses within our group. This allowed a deep understanding of the complex interactions between turbulent structures and particles in a closed environment simulating a nuclear power plant containment to be obtained.

Most recently, a counterpart experimental Ph.D. investigation inside a cubical DHC with a side 0.7 m has been performed at PSI (Kalilainen et al., 2016) and was able to supply both detailed flow field measurements using Particle Image Velocimetry (PIV) as well as particle concentration data as a function of space and time. Simulations of these tests were most recently investigated (Dehbi et al., 2017) using an Euler-Lagrange approach with classical LES for the continuous phase. Predictions of the flow field, as well as particle depletion rates, showed excellent agreement with the experimental data of Kalilainen et al., 2016. It is worth noting that these classical LES simulations took many months of CPU time on a 128-core HPC machine. These experimental and numerical databases provide excellent validation information for the WMLES simulations proposed in this project. As will be discussed in detail, Chapter 5 sheds the light on particulate flow prediction in DHC using coarse LES (CLES) - in an attempt to alleviate the CPU cost of investigating such long-residence-time dispersed flows.

1.3 Project novelty: Hybrid RANS/LES in complex dispersed flows

While CPU-modest RANS approaches are disqualified because they lose turbulent details through a-priori temporal averaging, DNS approaches, while very rigorous because they contain no modeling errors, are extremely CPU-intensive, and hence not feasible for high turbulence flows or complicated geometries.

Classical LES, which is a compromise between RANS and DNS, is in some cases, the preferred choice in CFD computations. Despite its increasing popularity, LES CPU requirements are still very high, especially for wall-bounded flows, and increase exponentially with turbulence (Re or Ra numbers). As mentioned above, hybrid models have been proposed in an attempt to decrease the computational expense of LES simulations. Grossly speaking, this is achieved by involving both RANS and LES formulations at different parts of the computational domain.

In such hybrid approaches, LES is used in the region far from the wall where large eddies are prevalent, whereas the near-wall region characterized by small eddies is covered by a RANS model. Out of the all proposed hybrid models over the last two decades, the WMLES approach seems to be the most promising method - blending between the accurate representation of the turbulent physics and the significant CPU cost reduction. According to Menter, 2013, the WMLES requires about 40 cells in the boundary layer to cover the wall-normal direction, 10 cells in the streamwise direction, and 20 in the span. Thus one needs about 6000 to 8000 cells to encompass a volume δ^3, δ being the boundary layer thickness. When the Reynolds number is low, the WMLES and classical LES have the same resolution requirements. For high Re numbers, the lower cell count and correspondingly larger time steps translate into WMLES CPU requirements that are orders of magnitude smaller than classical LES.

In this thesis, two WMLES models are investigated. The first model is the algebraic WMLES (WMLES) by Shur et al., 2008 which employs a modified Smagorinsky model in the away from the wall, while it activated a zero-equation RANS mode based on the Prandtl mixing length in the near-wall region. The second model which is novel to use in this area of research, is the Elliptic Relaxation Hybrid RANS/LES (ER-HRL) model. This second model is based on an explicit three-equation RANS formulation in the near-wall region that switches to the dynamic Smagorinsky model in the LES region. As will be discussed next in Section 1.4, each of these models were supplemented with an appropriate particle SGS model to incorporate the effects of unresolved scales on particle motion. This was extensively analysed in Chapter 4 where both WMLES models were assessed in a turbulent channel flow investigating the potential of each to endeavor more complex geometries.

To study particle dispersion, this investigation proposes an E-L framework aimed at applications where particles (order of a few microns) are much smaller than the Kolmogorov scale, and therefore flow around particles will not be resolved. Rather, a point-particle approach will be adopted in the Lagrangian simulation. In addition, we consider very dilute particle-laden flow, and one-way coupling is employed, whereby particles do not affect the carrier flow, and particle wake interference and particle-particle collisions are negligible. Lastly, walls on which

particles impact are considered smooth, and particle deposits are negligible enough so as not to alter the smoothness of the wall. Once particles hit the wall, their fates (elastic/inelastic bounce, sticking) depend on the problem tackled, and justification for each case will be given in the next chapters of this thesis.

Since we deal in this work with heavy particles that are larger than a few hundred nanometers, only the drag and gravity forces are considered to be significant. To predict in Lagrangian fashion the dispersion of spherical particles in turbulent flow under the one-way coupling assumption, one solves the vectorial particle equation of motion (Eq. 1.1). This will be explained in detail in Chapter 3 (Lagrangian Particle Tracking).

$$\frac{dV_p}{dt} = f\frac{(U - V_p)}{\tau_p} + g + \sum_{i=1}^{n} F_i \tag{1.1}$$

where the subscript p relate to particle quantities; V_p being the particle velocity, τ_p is the particle relaxation time. U is the fluid velocity at particle location, g is the gravity acceleration vector, f is an empirical drag coefficient depending on the particle Reynolds number, and F_i is the additional forces per unit mass. The equation of motion is solved assuming that the gas flow field remains constant during each time interval of the WMLES simulation since the trajectory integration time-step is much smaller than the smallest time scale (Kolmogorov scale) for the considered small particles.

1.3.1 Particle subgrid scale modeling

In the context of LES/WMLES, the definition of the fluid velocity (U) seen by the particle must be given. In earlier times, one would simply equate that velocity with the LES spatially filtered velocity, ignoring the effect of the filtered subgrid scales (SGS). Recent studies however have shown that the unresolved scales of the fluid velocity can have significant effects on particles with relaxation times smaller than the Kolmogorov time scale (Bini and Jonesa, 2007; Cernick et al., 2015). For these particles, an SGS model is required in the particle equations of motion. Among all models, two promising approaches which have been proposed recently to define the fluid velocity seen by the particle will be investigated: the Fukagata model and the $\zeta - SGS$ model.

The Fukagata SGS model attempts to capture SGS influence through the inclusion of a stochastic "SGS Brownian force" in the particle equation of motion (Fukagata et al., 2004). This model recovers enough of the SGS kinetic energy, but shows limitations in predicting preferential particle clustering. This is due to the assumption of homogeneous isotropic SGS turbulence which is least accurate close to the walls. The second approach (i.e. $\zeta - SGS$ model) proposed by Sayed et al., 2021-b is based on the concept of feeding particles with wall anisotropy through the variance of wall-normal transport (ζ). Such deconvolution retrieves the modeled part of

the most important velocity component for particle deposition i.e. wall-normal component. As will be shown later, both models are investigated with scrutiny in a turbulent channel flow (Chapter 4) to assess their potential to proceed with accuracy with more complex flows.

1.4   Main project milestones

1.4.1   Implementation of Lagrangian Particle Tracking algorithm (LPT)

The first step in the present project was to build the main framework for particulate flow simulations. A Lagrangian Particle Tracking (LPT) algorithm was implemented in the research code T-Flows. The code is a general-purpose finite-volume second-order accurate CFD solver based on unstructured mesh. The code was first created by Bojan Niceno during his Ph.D. work (Ničeno, 2001).

1.4.2   Flow field validation against DNS data of periodic channel flow

After the LPT and WMLES implementation in T-Flows, several tests were done on the periodic channel flow where the computed flow field by WMLES was compared to DNS data at several shear Reynolds numbers. Since some reasonable amount of work has been done before in this area by other authors, there was enough LES data to compare the obtained results against.

1.4.3   Implementation of particle SGS models

To compute the one-way coupling Lagrangian trajectories of particles from the WMLES solution, one requires additional modeling to capture the effect of the filtered-out kinetic energy. For this, the promising Fukagata et al., 2004 SGS model that has been proposed in recent literature was used. In addition, the novel $\zeta - SGS$ model has been proposed through this project Sayed et al., 2021-b. As mentioned above, both models will be tested through different applications and flow topologies.

1.4.4   WMLES particulate flow validation in canonical channel flow

As will be shown in Chapter 4, LPT was validated in a periodic channel flow at two Reynolds numbers (i.e. $Re_\tau = 150, 590$). The simulations using two WMLES models supplemented with the above-mentioned particle SGS models for the unresolved scales were conducted, and results were compared against the databases for the various measures of particle dispersion, namely: relative concentration, RMS and mean velocity profiles.

1.4.5   WMLES particulate flow validation in complex turbulent flows

Having validated the implemented models and LPT algorithm in canonical flow, we endeavor to test the WMLES approach in complex particulate wall-bounded flows that have a wide range of applications. The considered types of flows chosen in this work have high-quality fluid field and particle deposition data in the literature. In the following set of flow cases, we show the investigated simulations through the present work, each represented by a separate chapter as will be shown later.

1. Particle deposition rates in a differentially heated cavity (DHC): As mentioned in Section 1.2.2, a recent experimental Ph.D. investigation (Kalilainen et al., 2016) has collected high-quality data on the flow field and monodisperse particle depletion rates inside a differentially heated cubical cavity at turbulent Rayleigh number 10^9. Despite a simple geometry, the turbulent flow inside the DHC is rather complex with recirculation-and-laminarization zones and boundary layer detachment. The particle-laden flow was also computed using well-resolved classical LES (Dehbi et al., 2017). In a preliminary investigation done by the author (Sayed et al., 2021-c), it was found that URANS and hybrid RANS-LES models fail to produce modeled turbulent kinetic energy (TKE) due to the laminarization phenomenon. As an alternative LES was applied on the coarse mesh. Such an idea resulted in very interesting findings which will be discussed in Chapter 5.

2. Particle separation in a reverse-flow gas cyclone: As will be shown in Chapter 6, the flow inside a Stairmand high-efficiency gas cyclone with a dust bin collector was investigated. Well resolved LES and high-quality experimental data from the literature were used to validate the obtained results Derksen, 2003; Hoekstra, 2000; José de Souza et al., 2012. The Eulerian statistics were assessed through mean and RMS values of both axial and tangential velocity components at a high Reynolds number of Re= 280,000. separation efficiency inside cyclone was computed through a systematic analysis of a wide range of particle Stokes numbers, where results were compared to porous and well-resolved LES as well as experimental data (Derksen, 2003; José de Souza et al., 2012; Xiang et al., 2001).

3. Droplet deposition in a swirl vane of a steam generator: In the ARTIST project (Güntay et al., 2008) conducted at the Paul Scherrer Institut, experiments have been performed using a droplet-laden flow directed at a 1:1 swirl vane of a nuclear power steam generator. High-quality Laser Doppler Anemometry (LDA) data were generated on fluid velocity and second-order statistics upstream and downstream of the vane. Droplet retention efficiency data was also obtained as a function of droplet size and gas flow rate. Since all walls are hydrophilic and velocities are relatively small (less than 1 m/s), droplets were assumed to be removed from the stream upon impact. Therefore, the sticking impact probability was assumed to be 1. Due to the high level of complexity, the commercial package ANSYS Fluent was used as a more robust CFD code to solve this case.

1.5   Relevance and impact

As computer power and resources are ever-increasing, Large Eddy Simulation-based approaches are gradually replacing traditional RANS as the favored computational tools to address complex flows for which not only mean-field but also accurate turbulence statistics are required. Despite this trend, classical LES remains very time-consuming, which translates into long waiting times and large computer energy consumption. This gets worse as the simulated turbulence level increases since LES CPU requirements grow exponentially with the Re number.

The WMLES is a novel modeling approach that depends only mildly on the Reynolds number in wall-bounded flows, which means much higher turbulence levels are more easily addressed compared to well-resolved LES. Thus, savings in computer time of one order of magnitude or more are possible within the framework of WMLES. We, therefore, investigate in this project whether these substantial computing savings can be reached without significantly compromising accuracy. To this end, two promising particle SGS models that have been recently proposed have been implemented in the research open-source code T-Flows. The models have been validated for both forced and naturally convected flows in canonical and complex wall-bounded configurations. The main findings of this project were published in quality journals as open access (OA), and made available to the large community which uses classical LES in wide-ranging applications.

2 Turbulence Modeling
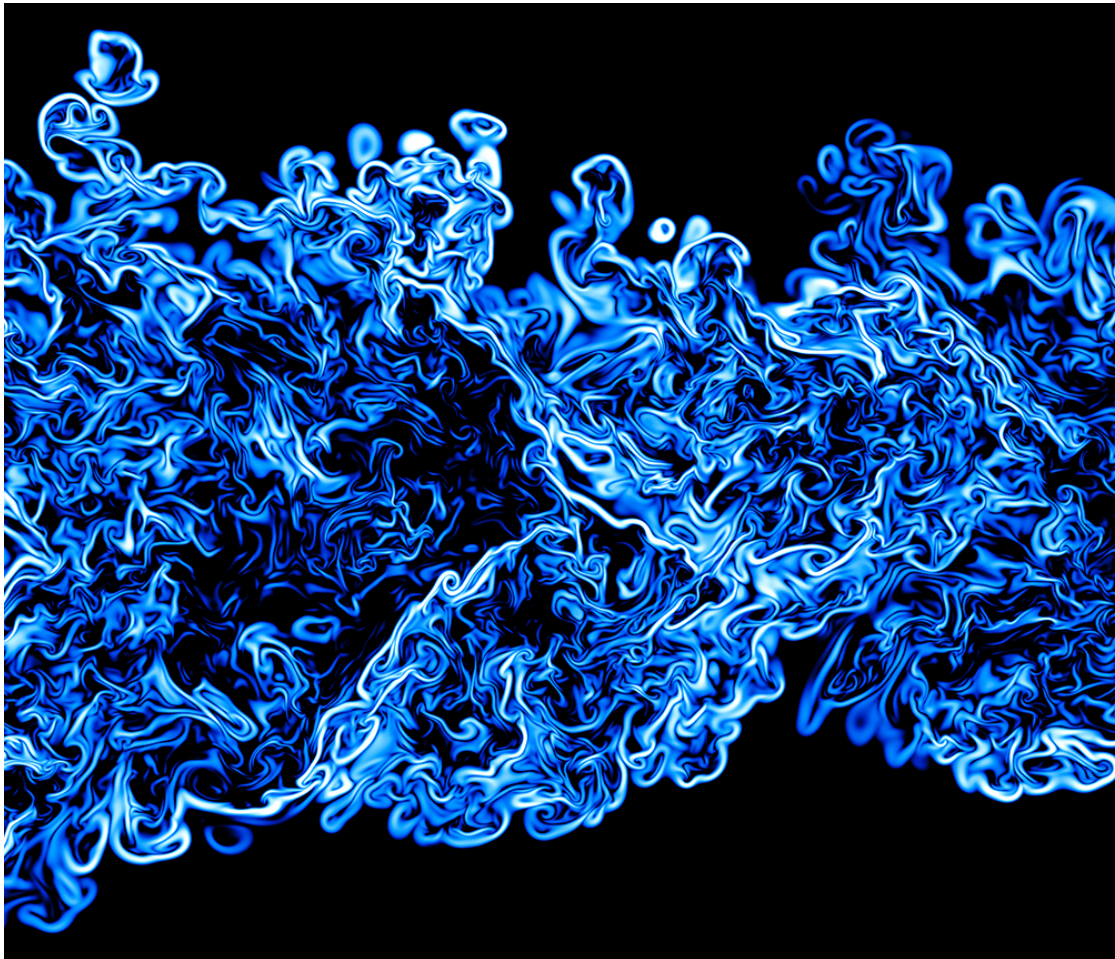
Figure 2.1 – DNS of turbulent shear flow: a slice through the field of the scalar dissipation reveals the small-scale structure of turbulence. *C*opyright: CNRS UMR 6614 CORIA and JSC.

2.1   Theoretical background and main concepts

Turbulence has always been one of the most challenging problems in physics. This is mainly due to its unpredictable, three dimensional, erratic, irreversible, self-sustaining and chaotic features (Bernard and Wallace, 2002; Frisch, 1995; Mathieu and Scott, 2000; Pope, 2000; Tennekes and Lumley, 1972). As a matter of fact, turbulent flows are ubiquitous in nature and are observed in our daily life; e.g. in the atmosphere (Wyngaard, 2010), in the ocean (Thorpe, 2005), in geosciences (Schmitt and Huang, 2016) and in climate models (Beniston, 2012). The word "turbulence" was first introduced in fluid mechanics literature in 1887 by William Thompson (Kelvin), 1887). Before that time, scientists noticed and recognized turbulence in different flows in nature but referred to the phenomena in other different lexicon. For example Joseph Boussinesq used "tumultuous movements", "eddy agitations", "liquid eddy theory" (Boussinesq, 1868, 1877, 1897), and Osborne Reynolds used "sinuous paths", "sinuous motion", "irregular eddies" (Reynolds, 1883, 1895).

Ever since, tens of thousands of research papers have been published to investigate the dynamics of turbulence through different flow phenomena (Schmitt, 2017). An important feature of turbulence is the superior ability of fluid transport and mixing compared to laminar flow. This was proved through the dye-experiment of Osborne Reynolds (Reynolds, 1883). A decade later, the concept of Reynolds number was established (Reynolds, 1894), which is a non-dimensional number defined as $Re = \frac{UD}{\nu}$, where U and D are the characteristic velocity and length scales of the flow, and ν is the fluid viscosity. With such definition, the flow is characterized by the ratio of inertial forces (governed by the flow geometry) to viscous forces (controlled by dissipation rate). Turbulence occurs at high Reynolds numbers by excessive kinetic energy in some parts of a fluid flow, which overcomes the damping effect of the fluid viscosity. However, it remains very difficult to draw the line between an "orderly" laminar flow and a turbulent flow, which makes turbulent flow extremely challenging to predict.

As inferred by the above discussion, an essential feature of turbulent flows is that the fluid field varies significantly and chaotically in both position and time. In 1822, the governing equations of the fluid motion were first derived by the French mathematician Claude Louis Navier (along with George Stokes) from Newton's second law of motion. The summary of their work laid the foundation of fluid dynamical research (known as Navier-Stokes Equations or NSEs), which is a set of equations representing the conservation of flow momentum and mass. As will be introduced in Section 2.2, a flow where the velocity field is denoted by $U(x, t)$ i.e. x being the position and t is time) has been represented in engineering applications by averaging Navier-Stokes equations either over time or space or both.

One of the biggest challenges that comes with turbulent flows is the vast range of motion scales. It is usually the case that turbulent eddies emerge at the largest length scales and die out at very tiny scales that dissipate into heat at solid boundaries. Quoting Lewis Fry Richardson *"Big whirls have little whirls that feed on their velocity, and little whirls have lesser whirls and so on to viscosity"*.

One of the earliest visualizations of this feature of turbulence was presented before any scientific explanation through the works of Leonardo Da Vinci (Fig. 2.2). It is reported that the word "turbulenza" appeared for the first time in the Codex Atlanticus [I] through da Vinci's work of studies of water to conceptualize turbulence. After 500 years and in honor of da Vinci's pioneering artwork, researchers have reproduced the physics behind one of his most famous drawings *RCIN 912660* (Fig 2.2) using the Smoothed Particle Hydrodynamics (SPH) (Colagrossi et al., 2021).
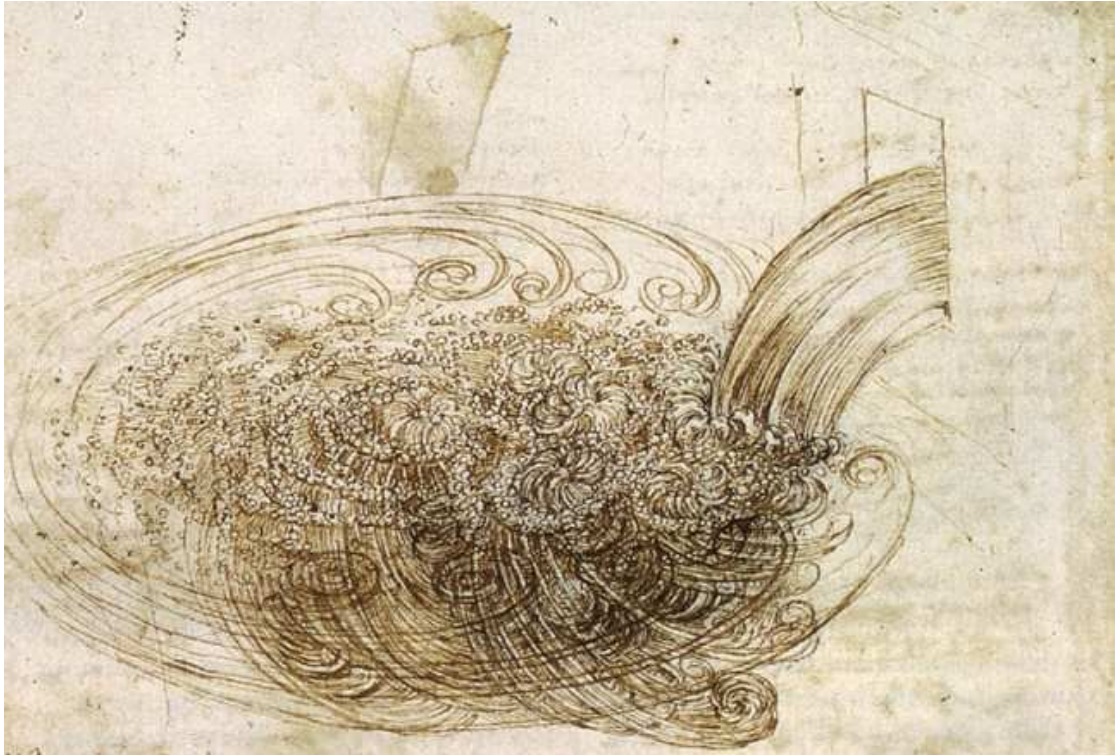
Figure 2.2 – Leonardo da Vinci's Studies of water (c.1510-12). The fall of a stream of water from a sluice into a pool. Bottom part of the sheet RCIN 912660. Royal Collection Trust Copyright Her Majesty Queen Elizabeth II 2021.

As seen from Fig. 2.2, the turbulent structures are noticeable eddies of different length scales. The separation between these scales is more pronounced as Reynolds number increases as mentioned by (Pope, 2000). The largest energy-containing eddies are determined by flow geometry (i.e. boundary conditions) and the smallest dissipative ones are dominated by viscosity where energy is dissipated into heat. In order to accurately represent these scales of motion, the flow field has to be properly resolved (or modeled) using one of the three main mathematical approaches to achieve that namely: Direct Numerical Simulation (DNS), Large Eddy Simulation (LES) and Reynolds Averaged Navier-Stokes (RANS). A DNS solution of the flow field represents the most accurate picture of turbulence since it resolves the whole range

---

[I]The Codex Atlanticus is a 12-volume, bound set of drawings and writings by Leonardo da Vinci, the largest single set. Its name indicates the large paper used to preserve original Leonardo notebook pages, which was used for atlases.

of motion scales (Fig. 2.3). With such a vast spectrum of turbulent scales, the cost of DNS increases drastically with Reynolds number (roughly goes with Re^3), requiring staggering number of CPU hours to converge one simulation. For this reason, DNS is only used as a research tool to help validate newly developed turbulence models and investigate new flow phenomena of interest.

On the other hand, while being the cheapest method, RANS has its own drawbacks, especially in complex industrial flows with secondary motions and swirling effects where it does not give an accurate prediction of the flow. LES however is considered relatively a good compromise between RANS and DNS, since it has the potential to provide a time-dependent solution with accurate prediction of the turbulent quantities. In the following, the concept and formulation of both LES and RANS methods are presented. In Section 2.4, the state-of-the-art of hybrid RANS/LES models used in this thesis are reported from a wall-modeling view point.
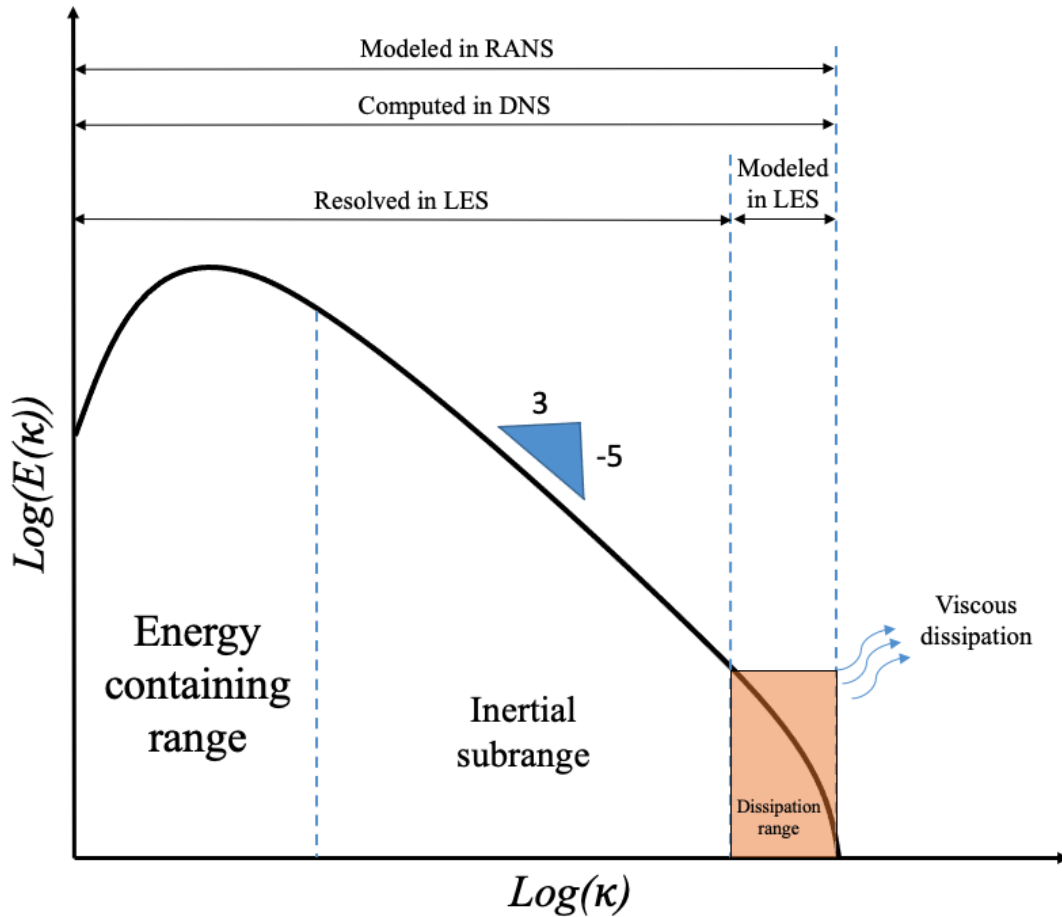
Figure 2.3 – Schematic showing the enegry spectrum of isotropic trubulence (solid black line) as a function of the wave number, $\kappa = 2\pi/l$ where l is the eddy length scale.

2.2 Large Eddy Simulation (LES)

While RANS is usually disqualified because it smears the turbulent details through *a-priori* temporal averaging of the governing equations, and DNS - albeit very accurate since all the scales are resolved (no modeling errors) - is impractical for the industry as a result of its prohibitive cost, classical Large-Eddy Simulations (LES) stands as a trade-off between RANS and DNS. In the following, both the advantages and disadvantages of using LES will be discussed, as well as the area of application in hybrid RANS/LES models.

2.2.1 Flow governing equations and filtering concept

The fluid motion is described by the Navier-Stokes (conservation of momentum equation) complemented by the conservation of mass and energy. In the present work, we consider an incompresssible Newtonian fluid with constant viscosity for which the system of equations (in Einstein's notation for repeated indices, i, j = 1, 2, 3) read:

$$\frac{\partial U_i}{\partial x_i} = 0 \tag{2.1}$$

$$\frac{\partial U_i}{\partial t} + \underbrace{U_j \frac{\partial U_i}{\partial x_j}}_{\text{non-linearity}} = -\frac{1}{\rho}\frac{\partial p}{\partial x_i} + \nu\left(\frac{\partial^2 U_i}{\partial x_i \partial x_j}\right) \tag{2.2}$$

$$\frac{\partial T_i}{\partial t} + U_j \frac{\partial T_i}{\partial x_j} = \alpha \frac{\partial^2 T_i}{\partial x_j^2} \tag{2.3}$$

where U_i is the instantaneous velocity vector, T is the instantaneous temperature field and α is the thermal diffusivity. It is important to mention that a perfect fluid is assumed here i.e. enthalpy depends only on the temperature.

Unlike DNS, LES is based on resolving only the large three-dimensional unsteady motions, whereas the effects of smaller scales are modeled. Motivated by the inaccuracy of RANS and high-cost limitation DNS, LES has been reported as a reliable CFD tool, especially in flows where large-scale unsteady fluctuations are significant (e.g. flow over bluff bodies which includes unsteady vortex shedding and unsteady separation). As shown in Fig. 2.3, the turbulent energy spectrum is characterized by three main ranges: a) the energy containing range, b) the inertial sub-range, and c) the dissipation range. The first two ranges are not universal since they depend on the flow configuration, and therefore they are resolved explicitly in LES. The dissipation range however contains tiny scales that are dominated by viscosity (i.e. where

turbulent kinetic energy is dissipated into heat). As mentioned by (Pope, 2000), most of the CPU cost expended by DNS goes to resolving these dissipative motion scales. For this reason, the dissipation range is modeled when performing LES to avoid the extremely high cost of DNS. In order to perform an LES simulation, three main conceptual steps have to be done:

1. A filtering operation is performed over the conservation equations to separate small scales from large ones of interest. Both the instantaneous velocity and temperature fields are decomposed into a filtered component and a residual one:

$$U(x,t) = \underbrace{\overline{U}(x,t)}_{\text{spatially-filtered}} + \underbrace{u(x,t)}_{\text{residual field}} \tag{2.4}$$

$$T(x,t) = \overline{T}(x,t) + t(x,t) \tag{2.5}$$

   As will be explained in Section 2.2.2, the effects of the residual (unresolved) velocity u(x,t) and temperature t(x,t) fields are normally accounted for using an appropriate Subgrid-scale (SGS) model.

2. Using Eq. 2.4, the filtered form of Navier-Stokes equations yields the residual (SGS) stress tensor, τ_{ij^R}. This tensor arises from filtering the nonlinear advection term in the momentum equation.

3. The system of equations is then closed by modeling the SGS stress tensor using an eddy viscosity model through Boussinesq's approximation (Boussinesq, 1877).

In order to adequately resolve the filtered field on a relatively coarse grid, (Leonard, 1974) defines a filtered velocity field by the following convolution integration:

$$\overline{U}(x,t) = \int_{-\infty}^{\infty} G(r,x)U(x-r,t)\,dr \tag{2.6}$$

where G(r,x) is a low-pass filter function that satisfies the normalization condition:

$$\int_{-\infty}^{\infty} G(r,x)\,dr = 1 \tag{2.7}$$

The most commonly used filters in LES through the literature are:

- The sharp Fourier filter (Leonard, 1974) is defined in wave space as:

$$G(\kappa) = \begin{cases} 1, & \text{if } \kappa < \pi/2. \\ 0, & \text{otherwise.} \end{cases} \tag{2.8}$$

- The Gaussian filter is:

$$G(r) = \sqrt{\frac{6}{\pi \Delta^2}} exp\left(\frac{-6r^2}{\Delta^2}\right) \tag{2.9}$$

- The sharp Fourier filter (Leonard, 1974) defined in wave space:

$$G(r) = \begin{cases} 1/\Delta, & \text{if } |r| < \Delta/2. \\ 0, & \text{otherwise.} \end{cases} \tag{2.10}$$

In all the above Δ is the grid cut-off length (also known as filter width) which is defined as the cubic root of cell volume (i.e. $\Delta = (h_x h_y h_z)^{1/3}$).

Since T-Flows is a finite-volume unstructured code, the box filter is employed. With such a filter, LES is conducted in an implicit manner where the filter clips any scales that lie below the grid cut-off length. When applying the filtering decomposition (Equations 2.5, 2.6), the governing equations yield:

$$\frac{\partial \overline{U_i}}{\partial x_i} = 0 \tag{2.11}$$

$$\frac{\partial \overline{U_i}}{\partial t} + \overline{U_j}\frac{\partial \overline{U_i}}{\partial x_j} = -\frac{1}{\rho}\frac{\partial p}{\partial x_i} + \nu\left(\frac{\partial^2 \overline{U_i}}{\partial x_i \partial x_j}\right) - \frac{\partial \overline{u'_i u'_j}}{\partial x_j} \tag{2.12}$$

$$\frac{\partial \overline{T}}{\partial t} + \overline{U_j}\frac{\partial \overline{T}}{\partial x_j} = \frac{\partial}{\partial x_j}\left(\alpha \frac{\partial \overline{T}}{\partial x_j} - \overline{u'_j T'}\right) \tag{2.13}$$

where the term $\overline{u_i u'_j}$ in Eq. 2.13 is the residual stress tensor (τ^R_{ij}), which represents the effect of unresolved scales of motion on the filtered velocity field (Eq. 2.15). In case of homogeneous turbulence, this tensor is reduced to 6-element symmetric tensor since $\overline{u'_i u'_j} = \overline{u'_j u'_i}$).

$$\tau^R_{ij} = -\overline{u'_i u'_j} = \overline{U_i U_j} - \overline{U_i}\ \overline{U_j} \tag{2.14}$$

Since this tensor introduces 6 new unknowns, it must be modeled to close the system of equations. As will be explained in Section 2.2.2 below, this closure is achieved by linking the residual SGS fluctuations to the mean velocity gradients through the eddy viscosity analogous to any stress-strain relationship. In a similar fashion, the turbulent heat flux $\overline{u_j t}$ is modeled

17

where the residual turbulent heat flux is related to the mean temperature gradients through thermal eddy diffusivity (as in Eq. 2.16). This heat flux model is referred to as the Simple Gradient Diffusion Hypothesis (SGDH).

$$\overline{u_j \theta} = -\alpha_t \frac{\partial \overline{T}}{\partial x_j} \tag{2.15}$$

The thermal diffusivity is calculated from the definition of the turbulent Prandtl number, Pr_t which usually takes the value 0.9.

$$Pr_t = \frac{\nu_t}{\alpha_t} \tag{2.16}$$

2.2.2 Subgrid-Scale Modeling in LES

As a result of spatial filtering, small scales that fall below the mesh cut-off have to be recovered using an appropriate SGS model. In principle, as motion scales get smaller, they become more universal as they lose orientation. Conversely, relatively larger scales of motion are much more challenging to recover. By "larger" here we mean eddies that are proportional to the mesh cut-off length and are energetically anisotropic and inhomogeneous. In that case orientation becomes more important, and therefore, modeling larger scales become much more challenging.

Smagorinsky Subgrid-Scale Model

The concept of sub-grid scale (SGS) modeling was first initiated by (Smagorinsky, 1963). It is based on the Boussinesq eddy viscosity approximation which links the traceless part of the residual stress tensor τ_{ij}^R to the strain rate $\overline{S_{ij}}$:

$$\tau_{ij}^R = 2\nu_t \overline{S_{ij}} - \frac{2}{3} K \delta_{ij} \tag{2.17}$$

where k is the Turbulent Kinetic Energy (TKE) computed from (Eq. 2.19), and δ_{ij} is the Kronecker delta.

$$k = \frac{1}{2} \overline{u_i u_i} \tag{2.18}$$

In Eq. 2.18, the turbulent eddy viscosity v_t is obtained from the dimensional analysis:

$$v_t \propto l_s u_{sgs} \tag{2.19}$$

where both the length scale l_s and velocity scale u_{sgs} of the residual stress tensor are defined as in Eq. 2.20-2.21. Computing the eddy viscosity as a scalar quantity is not "strictly" correct. However, In most cases, the eddy viscosity is computed algebraically (as an isotropic scalar quantity) to avoid the need of solving additional transport equations that would increase the computational expense which is high by default when performing LES. Therefore, the term "approximation" properly holds for this approach.

$$l_s = \Delta = (\nabla \mathcal{V})^{\frac{1}{3}} \tag{2.20}$$

$$u_{sgs} = l_s \overline{|S|} \tag{2.21}$$

Above, $\nabla \mathcal{V}$ is the computational cell volume, and $\overline{|S|} = \sqrt{2\overline{S_{ij}S_{ij}}}$ is the magnitude of the strain-rate tensor $\overline{S_{ij}}$ which is defined as

$$\overline{S_{ij}} = 0.5\left(\frac{\partial \overline{U_i}}{\partial x_j} + \frac{\partial \overline{U_j}}{\partial x_i}\right) \tag{2.22}$$

Finally the eddy viscosity reads:

$$v_t = (C_s \Delta)^2 \overline{|S|} \tag{2.23}$$

where C_s is the proportional factor referred to as Smagorinsky constant. One major draw back about this SGS model is that for different flow configurations, the optimal value for this constant is different (usually varies between 0.065 and 0.2). In the near-wall region, C_s must have a lower value to account for wall anisotropy. This is normally achieved through damping functions which work as a smooth exponential decay of C_s value. As will be shown in Section 2.4.1, the most commonly used damping functions are Van Driest and Piomelli functions. In Smagorinsky SGS model, Van Driest function is used as follows:

$$C_s = C_{so}\left(1 - e^{-\frac{y^+}{25}}\right)^2 \tag{2.24}$$

where C_{so} is the value of Smagorinsky constant away from any solid boundary, and y^+ is the distance to the nearest wall normalized by wall units (i.e. $y^+ = \frac{yu_\tau}{v}$). The friction velocity U_τ is

defined from the wall shear stresses τ_w as:

$$U_\tau = \sqrt{\frac{\tau_w}{\rho}}$$ (2.25)

Despite being straightforward and easy to implement, the Smagorinsky SGS model is too dissi-
pative and suffers from inaccuracies in predicting the energy transfer from small scales near
the wall to larger ones (i.e. back scatter). Such limitations make this model only appropriate
for use when employing sufficiently fine meshes and in flows where transition processes are
not very dominant.

Dynamic Subgrid-Scale Model

In contrast to Smagorinsky SGS model, the dynamic model by (Germano et al., 1991) computes
Smagorinsky constant as a parameter that varies in space and time. The main idea of the model
is to account for part of the inertial subrange through modeling the residual modeled scales
of motion. This additional layer of modeling is encapsulated in the Smagorinsky parameter
across the grid. In other words, the SGS model in this case does not only see the smallest
length scale of the employed grid (as in Smagorinsky SGS model) but also a coarser grid scale
($\widehat{\Delta}$) which is taken to be double the cutoff length of the constructed grid i.e. ($\widehat{\Delta} = 2\Delta$). In
the following, the symbol (ˆ) will denote the quantities filtered by the test filter. With such
definition, it can be shown both the subgrid τ_{ij} and test filter T_{ij} stress tensors read:

$$\tau_{ij} = \overline{U_i U_j} - \overline{U_i}\ \overline{U_j} \approx \tau_{ij}^{mod}(C, \Delta, \overline{U})$$ (2.26)

$$T_{ij} = \widehat{\overline{U_i U_j}} - \widehat{\overline{U_i}}\ \widehat{\overline{U_j}} \approx T_{ij}^{mod}(C, \widehat{\Delta}, \widehat{\overline{U}})$$ (2.27)

It must be noted that the test filter is applied to the governing equations that are already
filtered (Eq. 2.12-2.14). In that light, the total stresses (Eq. 2.28) can be substituted by the
subgrid-scale filtered ones from Eq. 2.27. The resulting expression is known as Germano
identity (Eq. 2.29), where L_{ij} represents the all the resolved scales lying between the grid
filter and test filter wave numbers (see Fig. 2.4). In a similar fashion to Eq. 2.7, the filtered
velocity field by the test filter ($\widehat{\overline{U_i}}$) can be computed from the resolved velocities $\overline{U_i}$ through an
appropriate filtering function ($\widehat{G}$).

$$T_{ij} = \underbrace{\widehat{\overline{U_i}\ \overline{U_j}} - \widehat{\overline{U_i}}\ \widehat{\overline{U_j}}}_{L_{ij}} + \widehat{\tau_{ij}}$$ (2.28)

Following Boussinesq approximation, L_{ij} in Eq. 2.29 can be expressed in terms of modeled stresses:

$$L_{ij} = \underbrace{-2C\widehat{\Delta}^2\widehat{|S|}\ \widehat{\overline{S}_{ij}}}_{T_{ij}^{mod}} + \underbrace{-2C\widehat{\Delta^2|S|\ \overline{S}_{ij}}}_{-\tau_{ij}^{mod}} \qquad (2.29)$$

In ideal cases, L_{ij} should be equal to L_{ij}^{mod}. This condition is fulfilled using the least squared minimization (LSM) by (Lilly, 1992). By arranging Eq. 2.30, it reads

$$L_{ij} = \underbrace{-2C(\widehat{\Delta}^2\widehat{|S|}\ \widehat{\overline{S}_{ij}} - \widehat{\Delta^2|S|\ \overline{S}_{ij}})}_{M_{ij}} \qquad (2.30)$$

Finally the Smagorinksy parameter can be obtained by multiplying both sides of Eq. 2.31 by M_{ij}:

$$C_{dyn} = -\frac{1}{2}\frac{L_{ij}M_{ij}}{M_{ij}M_{ij}} \qquad (2.31)$$

As shown above, the apparent advantage of the dynamic model over the Smagorinsky SGS model is that the Smagorinsky constant doesn't have to be predefined by the user and tuned according to the flow configuration. Instead, it is computed in a transient manner by the model itself during the simulation. Another advantage of the dynamic model is that it predicts a more accurate behavior of the flow near the wall, dropping the need to employ a damping function. In addition, the model allows negative values for the C_{dyn} and hence it can better predict back-scatter. To achieve this higher accuracy, one has to pay the price of greater simulation cost to use the model.

Although LES has proved to be accurate in predicting wall-bounded turbulent flows dominated by large-scale coherent structures, the high demand on grid resolution (especially in the near-wall region) still limits LES to low-to-moderate Reynolds and Rayleigh numbers with simple flow configurations. This is due to the existence of very small eddy structures near the wall which drive the dynamics of the boundary layer. These small structures grow linearly with more distance from the wall and vice versa - with a strong dependence on the operating Reynolds number - leaving very tiny eddies to be resolved in the wall proximity. While the total number of cells required by LES away from walls is proportional to $Re^{0.4}$ (as reported in (Chapman, 1979)) which makes LES affordable in the off-wall region, it scales with $Re^{1.8}$ in near the wall. It must be stressed that a proper treatment in the near-wall region is of a crucial
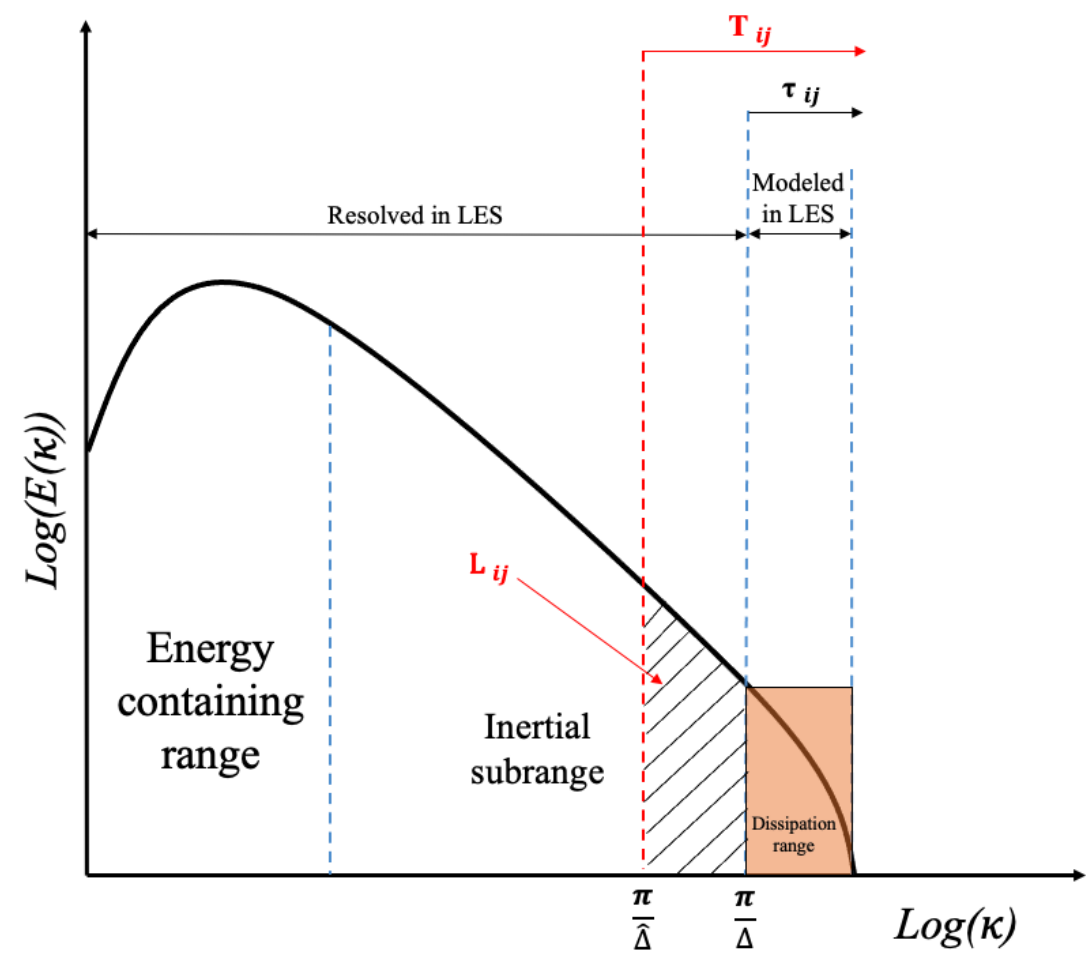
Figure 2.4 – Illustration showing the region of interest for both the sub-grid and test filters.

importance to accurately predict the boundary layer. This is very challenging since the cut-off length of the mesh has to be proportional to the size of the boundary layer eddies. Besides, with increasing the upstream velocity, smaller eddies appear at the same distance from the wall, making LES too expensive to use at high Reynolds number wall-bounded flows.

2.3   Reynolds-Averaged Navier-Stokes (RANS) Models

Despite the fact that RANS also requires a special grid clustering the wall-perpendicular direction, it can - in contrast to LES - tolerate much coarser grids in both the streamwise and spanwise directions. Being able to use such low resolution grids makes RANS the best option when investigating simple industrial flows. As indicated in Fig. 2.3, RANS methods are based on modeling all scales of motion where the whole energy spectrum is ensemble-averaged, giving a global representation of the turbulent flow fields.

Notwithstanding the continuous advances in RANS turbulence modeling through the last couple of decades (e.g. nonlinear differential and algebraic second moment closures, non-linear eddy viscosity models and multi-scale concepts), RANS models still suffer from some deficiencies especially when dealing with complex flows (e.g. transitional flows, flows with separation or circulation zones, flows with 3D effect and secondary motions, etc.). Although many existing RANS models have been tuned to tackle these deficiencies, they still fail to predict high moment turbulent statistics in a universal manner.

The long-established RANS models based on the linear eddy viscosity (LEV) assumption by (Boussinesq, 1877) are too simple to accurately predict the wall shear stress. The main reason for that is the crude approximation that the deviatoric part of the Reynolds stress tensor is aligned with the mean rate-of-strain tensor. In addition, models based on LEV concept treat the near wall area as an isotropic region when in fact the boundary layer is highly anisotropic. It's recalled that more sophisticated RANS models based on nonlinear eddy viscosity closures were adapted to predict complex 3D flows. However such models still do not meet the required level of accuracy, especially in case of flows dominated by large turbulent structures (M. Hadžiabdić, 2006).

In this section, two RANS models are considered, both of which are tailored for the near-wall treatment in the framework of hybrid RANS/LES models used through this work. That said, the focus here is on the capability of each model to predict the near-wall region with a high performance and not the flow prediction of the whole domain. In general, there are several modeling approaches in RANS. The most common two are the Eddy Viscosity (EV) and the Second Moment Closure (SMC) models. The eddy viscosity models are famous for their simplicity and straightforwardness, where the Reynolds stresses are directly related to the mean-flow rate of strain. The proportionality constant is computed from the length scale velocity scales of the grid-resolved motion.

In a more sophisticated manner, the second moment closure models (also known as Reynolds Stress Models (RSM)) represent the physics of the near-wall region in a better way by accounting for wall-anisotropy. This is done by solving a transport equation for each component of the Reynolds stress tensor. However, in some cases the enhancement of the flow prediction is unmatched by the expensive simulation cost, which stems from solving six additional equations to NSE each time step. However, it was shown in the literature that RSM also fails in complex industrial flows with swirling effects and secondary motion.

2.3.1 Reynolds equations

The pioneering work done by Oswald Reynolds in the 19th century laid a solid basis for RANS turbulence modeling. In (Reynolds, 1894), he proposed the idea that the instantaneous flow field is composed of a mean part and a fluctuating one. This has been known after as "Reynolds decomposition". by such decomposition, the instantaneous velocity field in all directions can be written as in Eq. 2.33. For the sake of simplicity, all ensemble-averaged quantities will take the same symbol as the spatially-filtered ones (i.e. averaged velocity is $\overline{U}(x,t)$).

$$U(x,t) = \underbrace{\overline{U}(x,t)}_{\text{ensemble-averaged}} + \underbrace{u'(x,t)}_{\text{fluctuating part}} \tag{2.32}$$

The ensemble-averaged (mean) part of the velocity is defined as follows:

$$\overline{U}^{(n)}(x,t) = \frac{1}{n}\sum_{i=1}^{n} U^{(i)}(x,t) \tag{2.33}$$

where n is the number of realizations

Applying such averaging, the following rules can be derived:

$$\overline{U(x,t) + V(x,t)} = \overline{U}(x,t) + \overline{V}(x,t) \tag{2.34}$$

$$\overline{C.U(x,t)} = C\overline{U}(x,t), C = constant \tag{2.35}$$

$$\overline{\frac{\partial U(x,t)}{\partial x}} = \frac{\partial \overline{U}(x,t)}{\partial x} \tag{2.36}$$

$$\overline{\overline{U}(x,t)} = \overline{U}(x,t) \tag{2.37}$$

Analogous to spatial filtering in LES and applying the above rules, the ensemble-averaged Navier Stokes equations (i.e. Reynolds-Averaged Navier-Stokes) read:

$$\frac{\partial \overline{U_i}}{\partial x_i} = 0 \tag{2.38}$$

$$\frac{\partial \overline{U_i}}{\partial t} + \overline{U_j} \frac{\partial \overline{U_i}}{\partial x_j} = -\frac{1}{\rho} \frac{\partial p}{\partial x_i} + \nu \left(\frac{\partial^2 \overline{U_i}}{\partial x_i \partial x_i} \right) - \frac{\partial \overline{u_i' u_j'}}{\partial x_j} \tag{2.39}$$

$$\frac{\partial \overline{T}}{\partial t} + \overline{U_j} \frac{\partial \overline{T}}{\partial x_j} = \frac{\partial}{\partial x_j} \left(\alpha \frac{\partial \overline{T}}{\partial x_j} - \overline{u_j' t} \right) \tag{2.40}$$

The Reynolds stress tensor term $(\overline{u_i' u_j'})$ here is similar to the residual stress tensor in LES (Eq. 2.15), except that it represents the effect of turbulent fluctuations on the momentum transport. Applying Boussinesq's eddy viscosity approximation, this stress tensor reads:

$$\tau_{ij} = \nu_t \underbrace{\left(\frac{\partial \overline{U_i}}{\partial x_j} + \frac{\partial \overline{U_j}}{\partial x_i} \right)}_{\text{time-averaged strain rate}} - \frac{2}{3} k \delta_{ij} \tag{2.41}$$

The turbulent heat flux is modeled through simple gradient diffusion hypothesis (also known as the isotropic gradient model):

$$\overline{u_j' \theta'} = -\alpha_t \frac{\partial \overline{T}}{\partial x_j} \tag{2.42}$$

Despite having a simplified picture of modeling the turbulence mechanism especially in the near-wall region, the EV approach is used in most CFD applications for practical reasons. However, for relatively complex 3D flows, such an approach fails completely, which limits its use to canonical flow benchmarks. In the following, some details are provided about each of the $k - \epsilon$ and the $\zeta - F$ RANS models. Each of these models is adopted in a hybrid mode with LES as will be shown in Section 2.4.

2.3.2 The $k - \epsilon$ model

The $k - \epsilon$ model is one of the most commonly used turbulence models in CFD. In addition to NSEs, it solves two additional partial differential transport equations for both the turbulent

kinetic energy k and its dissipation ϵ. As most of the standard RANS models, $k - \epsilon$ is based on isotropic turbulence assumption i.e. the ratio of each of the Reynolds stress components to the counterpart mean rate of deformation is the same in all directions. By a simple dimensional analysis of k and ϵ, the characteristic length scale L_c and characteristic time scale τ_c can be defined as:

$$L_c = k^{\frac{2}{3}}/\epsilon \qquad (2.43)$$

$$\tau_c = k/\epsilon \qquad (2.44)$$

Accordingly the turbulent eddy viscosity reads:

$$\nu_t = C_\mu f_\mu k^2/\epsilon \qquad (2.45)$$

where f_μ is a damping function to diminish the eddy viscosity value in close to the wall, and C_μ is of the five model constants (defined in Table 2.1). There are several versions of $k - \epsilon$ model in literature. In this work, the model of (Abe et al., 1994) was used. The model constitutive equations read:

$$\frac{Dk}{Dt} = P_k - \epsilon + \nabla.\left(\left(\nu + \frac{\nu_t}{\sigma_k}\right)\nabla k\right) \qquad (2.46)$$

$$\frac{D\epsilon}{Dt} = C_{\epsilon 1}\frac{\epsilon}{k}P_k - C_{\epsilon 2}f_2\frac{\epsilon^2}{k} + \nabla.\left(\left(\nu + \frac{\nu_t}{\sigma_\epsilon}\right)\nabla\epsilon\right) \qquad (2.47)$$

where $P_k = 2\nu_t\overline{S_{ij}}\ \overline{S_{ij}}$ is the production of turbulent kinetic energy, and f_2 is another damping function defined as:

$$f_2 = \left[1 - exp\left(-\frac{y^*}{3.1}\right)\right]\left[1 - 0.3exp\left\{-\left(\frac{Re_t}{6.5}\right)^2\right\}\right] \qquad (2.48)$$

The eddy viscosity damping function is formulated as:

$$f_\mu = \left[1 - exp\left(-\frac{y^*}{14}\right)\right]\left[1 + \frac{5}{Re_t^{3/4}}exp\left\{-\left(\frac{Re_t}{200}\right)^2\right\}\right] \qquad (2.49)$$

Table 2.1 – $k - \epsilon$ model parameters

C_μ	$C_{\epsilon 1}$	$C_{\epsilon 2}$	σ_k	σ_ϵ
0.22	1.5	1.9	1.4	1.4

above, $Re_t = \frac{k^2}{\epsilon \nu}$ is the turbulent Reynolds number and $y^* = \frac{(\epsilon \nu)^{1/4} y}{\nu}$ is the non-dimensional distance to the nearest wall in terms of the model quantities.

2.3.3   The $\zeta - F$ model

One of the most rigorous RANS models developed in the last three decades is the $\overline{v^2} - F$ model by (P. Durbin, 1991). The model was initially proposed to treat the wall-blocking effects by solving two additional equations to the standard $k - \epsilon$ model. One equation for a the velocity scale $\overline{v^2}$ representing the wall-normal fluctuation variance, and an elliptic-relaxation function to provide wall anisotropic effects through the pressure-velocity correlation. Although the $\overline{v^2} - F$ model performance is superior to the $k - \epsilon$ model, it still suffered some numerical instabilities with non-stiff boundary conditions. Motivated by the drawbacks of the $\overline{v^2} - F$ model, the $\zeta - F$ is a four-equation model that was developed by (Hanjalić et al., 2004), based on normalizing the $\overline{v^2}$ equation by turbulent kinetic energy (i.e. $\zeta = \overline{v^2}/k$). Solving a transport equation for ζ instead of the wall-normal fluctuation variance proved to make the model more robust, especially at early stages of the simulation where the predicted flow field is way far from the final fully-developed behaviour. In addition, the model have much less uncertainty in reproducing turbulent kinetic energy production P_k which appears as a source term in the ζ transport equation. Aside from k, ϵ and ζ equations, the elliptic relaxation function F constitutes the fourth transport equation in this model. This function is based on the enhanced pressure strain model by (Speziale et al., 1991). The quasi-linear pressure strain SGS model was found to enhance the prediction capability of the wall stress anisotropy (M. Hadžiabdić, 2006). The model equations read:

$$\frac{Dk}{Dt} = P_k - \alpha \epsilon + \nabla.((\nu + \nu_t)\nabla k) \tag{2.50}$$

$$\frac{D\epsilon}{Dt} = \frac{(C_{\epsilon 1}P_k - C_{\epsilon 2}\epsilon)}{\tau} + \nabla((\nu + \nu_t)\nabla \epsilon) \tag{2.51}$$

$$\frac{D\zeta}{Dt} = F - \frac{\zeta}{k}P_k + \nabla((\nu + \nu_t)\nabla \zeta) \tag{2.52}$$

Table 2.2 – $\zeta - F$ model parameters

C_μ	$C_{\epsilon 1}$	$C_{\epsilon 2}$	$c1$	C'_2	C_τ	C_L	a	C_η	C_α
0.22	1.4(1+0.012/ζ)	1.9	0.4	0.65	6.0	0.36	0.6	85	0.8

The elliptic-relaxation function is then introduced to account for the inviscid wall-blocking effects

$$L^2 \nabla^2 F - F = \frac{1}{\tau}\left(c1 + C'_2 \frac{P_k}{\epsilon}\right)\left(\zeta - \frac{2}{3}\right) \tag{2.53}$$

Above, τ and L_K are Kolmogorov time and length scales (Eq. 2.54-2.55). All model parameters are defined in Table 2.2.

$$\tau = max\left[min\left(\frac{k}{\epsilon}, \frac{a}{\sqrt{6}C_\mu \mid S \mid \zeta}\right), C_\tau \left(\frac{\nu}{\epsilon}\right)^{\frac{1}{2}}\right] \tag{2.54}$$

$$L = C_L\left(max\left[min\left(\frac{k^{\frac{2}{3}}}{\epsilon}, \frac{k^{\frac{1}{2}}}{\sqrt{6}C_\mu \mid S \mid \zeta}\right), C_\eta \left(\frac{\nu^3}{\epsilon}\right)^{\frac{1}{4}}\right]\right) \tag{2.55}$$

In the following Section, the manifestation of the above mentioned RANS models into hybrid RANS/LES is described.

2.4   Hybrid RANS/LES Models

Although LES is commonly used in the academic research, its application to industrial problems is very limited because of the excessive grid resolution requirements near the wall. The reason is that the largest scales in turbulent spectra are structurally (spatially) still small relative to the grid employed. This is even more pronounced at high Reynolds number flows. Moreover, the lifetime of each of those scales is "instantaneous", which requires very small time step sizes not to damp significant eddy fluctuations. As Reynolds numbers goes up, the boundary layer thickness decreases, requiring higher grid resolution to solve the smaller scales created at the wall vicinity. This implies heavy restrictions on the computational domain in order to properly resolve all important scales. That said, and since LES resolution cannot be much larger that the boundary layer thickness, solving realistically high Reynolds numbers using LES is very costly, which limits LES to low-to-moderate Reynolds numbers only. For this reason, there is always a pressing need to find an alternative approach by which the computer cost is reasonably reduced without significantly compromising accuracy.

A promising approach called Wall-Modeled Large Eddy Simulation (WMLES) aims at overcoming Reynolds number scaling limitations through employing a grid resolution comparable to the one used by off-wall LES or RANS and still give an accurate time-dependent solution.

This ambitious goal of predicting an ever increasing Reynolds number and still being able to capture the peak of Turbulent Kinetic Energy (TKE) to a good level of accuracy is a challenging task. The main idea behind this approach is to activate RANS mode in the inner part of the logarithmic layer - scaling in a moderate way with $Re^{0.5}$ (instead of $Re^{\frac{9}{4}}$ for LES) - and switch to LES in the outer part. This is known as hybrid RANS/LES models.

In general, there are two classes of hybrid methods: the zonal and non-zonal (seamless) methods. The zonal approach is characterized by predefined LES and RANS zones. In both zones, Navier-Stokes equations are solved in a transient mode using a single mesh. The biggest challenge in this approach is that the spatially-filtered equations from LES region meet the ensemble-averaged ones from RANS at the interface. This implies that a compatibility condition at the interface has to be fulfilled to guarantee a smooth transition between the two regions. Intuitively, the lack of thereof can cause a mismatch in the outer sublayer of the boundary layer (known as the log-layer mismatch (LLM)). Since the predicted modeled (eddy) viscosity in RANS region is usually much higher than in LES region, a damping function must be used to diminish the viscosity near the interface. In that sense, employing an appropriate damping function can help avoid interface-mismatch and guarantee a fast transition from RANS to LES.

As an alternative, the seamless approach employs one single turbulence model for both zones. Here, the employed eddy viscosity model works as RANS in the near-wall region and as a SGS model away from the wall. This way, a smoother but also faster transition can be achieved from RANS to LES through eddy viscosity. Usually this bridge is established using two length scale definitions: one for RANS in the near-wall region and one for LES away from wall. Once passed the interface, the original definition of RANS length scale is replaced by a parameter for the grid cut-off. Although length scales vary from one model to another, the rationale of RANS/LES blending functions is usually the same. One of the earliest and best models reported in that regard is the Detached-Eddy-Simulation (DES) proposed by (Spalart et al., 1997). This model has been so far one of the most tested hybrid RANS/LES models due to its simplicity. It incorporates only one transport equation turbulence model by (Spalart and Allmaras, 1992) (SA). In the near-wall region, the model uses the wall distance as a length scale, while it switches to the classical grid cut-off in LES mode. Due to its consistency and reliability, the DES model is very popular for solving wall-bounded turbulent flows efficiently. Although such seamless approaches are straightforward and easy to implement in CFD codes, matching the interface conditions is still a challenging task. This is more obvious in complex flows where the location of transition between RANS and LES is very difficult to predict.

Since the end-goal of this project is to assess hybrid RANS/LES model prediction of particle dispersion in 3D flows with relatively lower CPU cost, an accurate prediction of the primary (carrier) fluid flow is a must for a sound particle tracking procedure. In this light, the question to be answered first is: Could hybrid RANS/LES models predict the majority of TKE to a sufficient level on relatively coarser (RANS-type) grids? To answer that question, some of the efforts to combine RANS and LES are presented. Two of the most efficient hybrid RANS/LES

models; are the Algebraic Wall-Modeled LES (AWMLES) and the Elliptic-Relaxation Hybrid RANS/LES (ER-HRL) models. These were assessed in different configurations from simple canonical flows to complex 3D industrial ones (Chapters 4-9). While the AWMLES model uses one blending function to switch between RANS and LES zones, the ER-HRL model offers two switching criteria as will be explained later. Another difference between the two models is that in AWMLES the RANS mode is activated implicitly near the wall by incorporating a mixing length model with a damping function, while in ER-HRL, a four-equation RANS model is explicitly activated to model the wall region. This is going to be explained in more detail in Sections 2.4.1, 2.4.2 below.

2.4.1 The Algebric Wall-Modeled LES (AWMLES)

In 2008, (Shur et al., 2008) proposed a WMLES model in which most of the turbulent structures are resolved except in the near wall-region. The key parameter in this model is the modified sub-grid length scale, whose dependence on the grid size was extended to include the wall-distance as well. In addition, the model was shown to resolve the known log-layer mismatch problem (also known as the grey-zone problem) which is common in most WMLES models. This is done through two different formulations for computing the turbulent eddy viscosity v_t, between which the solver switches according to the computational cell size and wall normal distance. From wall-modeling view point, the model covers the inner part of the boundary layer in RANS mode using Prandtl Van-Driest mixing length (Eq. 2.56). Since the model's eddy viscosity is calculated algebraically, it will be referred to hereinafter as the Algebraic Wall-Modeled LES (AWMLES).

$$v_t \propto (\kappa y)^2 \, | \, S \, | \tag{2.56}$$

where $| \, S \, |$ is the strain rate magnitude. The model switches to a modified version of LES Smagorinsky model at the outer part of the logarithmic region of the BL up to the bulk region. In this range the model uses the SGS eddy viscosity:

$$v_t \propto (C_s \Delta^*)^2 \, | \, S \, | \tag{2.57}$$

where C_s is Smagorinsky constant and Δ^* is the modified length scale (Eq. 2.58)

As inferred from the energy budget concept, the near wall turbulence increase linearly with the wall distance. This in turn results in smaller and smaller eddies as the vicinity of the wall is approached. This phenomena stems from the effect of molecular viscosity which damps the eddies inside the viscous sublayer (VS) of the boundary layer, and therefore, this puts some limitation on dealing with high Reynolds numbers (for which the VS becomes thinner). In AWMLES approach, RANS layer extends outside the viscous super layer to model a bigger part of the boundary layer as seen in (Fig. 2.5) decreasing considerably the stringent dependency of the mesh resolution requirements on Reynolds number.
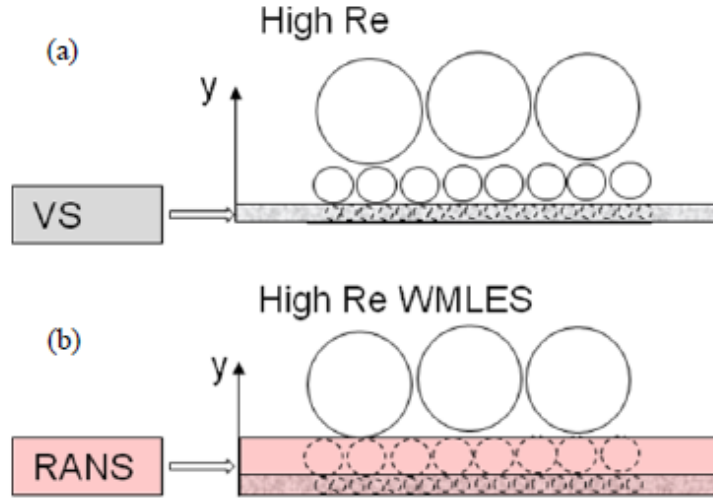
Figure 2.5 – Concept of WMLES for high Reynolds number flows (a) Wall-resolved LES. (b) WMLES (Schematic is taken from Menter, 2015).

By using Wall-Modeling approach, the wall-parallel spacings can be larger than the wall distance, which violates the normal LES standard that the sub-grid eddies are all results of the energy cascade. In order to avoid that, (Shur et al., 2008) introduced a new element in the sub-grid length scale equation; which is the distance to the wall (d_w in Eq. 2.58). This definition replaces the traditional Smagorinsky's SGS length (cubic root of the computational cell volume). With such modification, the sub-grid length-scale includes an explicit wall-distance dependence which finally leverages the model to have alleviated dependency of Reynolds number on the employed grid.

In the very close vicinity of the wall, the local sub-grid length scale should not completely follow the drastic decrease in wall normal step typical of this region (specially at high Re numbers when boundary layer thickness gets thinner) and, therefore, should depend only on the wall parallel steps (Δ_x, Δ_z). A definition for the sub-grid length scale that satisfies these requirements yields the form:

$$\Delta_{WM} = min\{max\{C_w d_w, C_w h_{max}, h_{wn}\}, h_{max}\}, \tag{2.58}$$

where h_{wn} is the grid step in the wall-normal direction and C_w is an empirical constant, which is not SGS model dependent, its value being set to 0.15 based on the wall-resolved LES of channel flow with the Standard Smagorinsky SGS model. The parameter h_{max} is used as an upper-limit when wall distance goes to infinity i.e. it is set to the maximum value of the local grid spacings in the 3 directions. This is an important factor since there is no point to have a

spacing below that limit away from the wall in any direction.

$$h_{max} = f(h_x, h_y, h_z), \tag{2.59}$$

where h_x, h_y, and h_z are the local grid steps in streamwise, wall-normal, and spanwise directions respectively. The modified length scale Δ_{WM} is then inserted in the eddy viscosity equation instead of the old volume-cubic root approach.

The equation of SGS eddy viscosity to be solved (accounting for the unresolved sub-grid scales) reads:

$$\nu_t = min\{(\kappa' y)^2, (C_{smag}\Delta)^2\}\{f_d\} \, |S| \tag{2.60}$$

where the Piomelli damping function reads

$$f_d = 1 - exp[-(y^+/25)^3] \tag{2.61}$$

Above $|S|$ is the magnitude of strain rate tensor and κ' is Von karman constant (set to 0.41), y is the wall distance and f_d is the wall-damping function of (Piomelli et al., 1988) by which the SGS eddy viscosity is smoothly damped at the wall vicinity (see Fig. 2.6). This performance suits WMLES better than the classical Van-Driest damping function which is commonly used with the old Smagorinsky model . The AWMLES uses a DES-like method which couples the Prandtl mixing length model that gives a RANS solution near the wall and Smagorinsky SGS models in which the length scales automatically switches to LES mode.

It's also obvious from Figure 2.6 that, unlike the Van Driest damping, the Piomelli damping function becomes almost idle at approximately y^+=50 and below that it damps the SGS eddy viscosity starting at the logarithmic layer down to the wall where it goes to zero and only the effect of molecular viscosity takes place.

Although the AWMLES is considered a promising model in implicit wall-modeled LES, it was shown by (Shur et al., 2008) that for moderate Reynolds numbers, the eddy viscosity formulation (Eq. 2.60) needs some extra empiricism to enhance the prediction of mean flow. As will be reported in Chapter 4, the model was implemented and tested on the periodic channel flow benchmark, where results were compared to the ER-HRL model against both DNS and LES databases.

2.4.2 The Elliptic-Relaxation Hybrid RANS/LES (ER-HRL)

Impelled by the drawbacks of the $k - \epsilon$ model, the $\zeta - F$ model was blended with LES in one hybrid scheme by (M. Hadžiabdić, 2006). A special feature of the $\zeta - F$ model emanates from the elliptic relaxation treatment of the wall blocking non-viscous effects instead of using
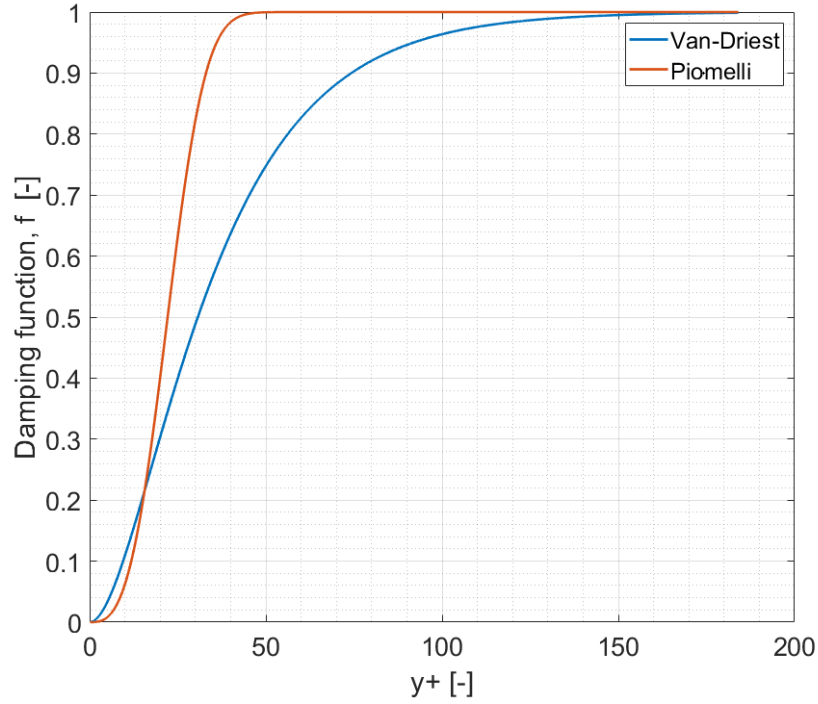
Figure 2.6 – Comparison between Piomelli and Van-Driest damping functions' behavior near the wall.

damping functions. As will be discussed below, this is achieved through the elliptic relaxation transport equation F. Unlike other seamless methods, the ER-HRL model does not use a single turbulence model for RANS in wall proximity and LES SGS model in LES zone. However, it uses $\zeta - F$ as RANS mode near the wall, whereas away from wall it switches to the dynamic SGS model. In a recent study, the ER-HRL was shown to have a high level of robustness in complex industrial flows (Hadziabdic and Hanjalic, 2020). For a smooth transition between RANS and LES zones, the model offers two efficient switching criteria. The subgrid scale (SGS) eddy viscosity, ν_t, is computed as a blending function of both RANS and LES eddy viscosity values (as in Eq. 2.63). This serves as the first switching criterion between LES and RANS modes.

$$\nu_t = max(\nu_{t,RANS}, \nu_{t,LES}) \tag{2.62}$$

where $\nu_{t,RANS}$ (with $C_\mu = 0.22$ as in (P. Durbin, 1991) is defined as

$$\nu_{tRANS} = C_\mu \zeta k \tau \tag{2.63}$$

$$\nu_{tLES} = (\varDelta)^2 C_{dyn} \,|\, S \,| \tag{2.64}$$

C_{dyn} is the dynamic Smagorinsky parameter, and $|S| = \sqrt{2S_{ij}S_{ij}}$ is the magnitude of the

strain rate S_{ij}. The four-equation RANS model was first proposed by (Hanjalić et al., 2004) to mitigate the scaling of computational cost with Reynolds number in turbulent wall-bounded flows. The model was recently tested in complex industrial configurations, capturing with high accuracy the Eulerian (flow) statistics at high turbulence levels using relatively coarse meshes (Hadziabdic and Hanjalic, 2020). As mentioned above, the model offers a second switching criterion which ensures a fast LES/RANS passage. This is accomplished through the blending function α (Eq. 13), which is incorporated in the TKE transport equation k (Eq. 7) to re-scale the dissipation rate ϵ. In the near-wall region, the model acts in unsteady RANS (URANS) mode (where $\alpha = 1$), while away from the wall, α becomes larger than 1 since the characteristic length from the RANS energy-containing range becomes more prominent (Eq. 14). This results in damping of the TKE (Eq. 7), and hence diminishing ν_{tRANS} (Eq. 5), which in turn activates the LES mode through Eq. 4. The RANS mode in this model is a four-equation model that transports the quantities $k - \epsilon - \zeta - F$ (Equations 7-10). This RANS model was shown to have a high level of robustness in a number of benchmarks (Hanjalić et al., 2004). For the LES mode, the Smagorinsky dynamic model is activated, which predicts the correct eddy viscosity needed to damp fluctuations in the near-wall region (M. Hadžiabdić, 2006). It was also noted by (Hadziabdic and Hanjalic, 2020) that the backscatter of the dynamic LES subgrid scale model ensures a smooth transition across the RANS-LES interface, which substantially mitigates the log-layer mismatch anomaly.

$$\frac{Dk}{Dt} = P_k - \alpha\epsilon + \nabla.((\nu + \nu_t)\nabla k) \tag{2.65}$$

where $P_k = 2\nu_t S_{ij} S_{ij}$ is the production of TKE. The dissipation rate transport equation reads

$$\frac{D\epsilon}{Dt} = \frac{(C_{\epsilon 1} P_k - C_{\epsilon 2}\epsilon)}{\tau} + \nabla((\nu + \nu_t)\nabla\epsilon) \tag{2.66}$$

Derived from ν^2 and k equations in (P. Durbin, 1991), the transport equation of the normalized wall-normal stress reads

$$\frac{D\zeta}{Dt} = F - \frac{\zeta}{k} P_k + \nabla((\nu + \nu_t)\nabla\zeta) \tag{2.67}$$

The elliptic-relaxation equation is then introduced to account for the inviscid wall-blocking effects with time and length scale limiters as shown below

$$L^2\nabla^2 F - F = \frac{1}{\tau}\left(c1 + C'_2 \frac{P_k}{\epsilon}\right)\left(\zeta - \frac{2}{3}\right) \tag{2.68}$$

$$\tau = max\left[min\left(\frac{k}{\epsilon}, \frac{a}{\sqrt{6}C_\mu |S|\zeta}\right), C_\tau\left(\frac{\nu}{\epsilon}\right)^{\frac{1}{2}}\right] \tag{2.69}$$

Table 2.3 – Model parameters

C_μ	$C_{\epsilon1}$	$C_{\epsilon2}$	$c1$	C'_2	C_τ	C_L	a	C_η	C_α
0.22	1.4(1+0.012/ζ)	1.9	0.4	0.65	6.0	0.36	0.6	85	0.8

$$L_K = C_L\left(max\left[min\left(\frac{k^{\frac{2}{3}}}{\epsilon}, \frac{k^{\frac{1}{2}}}{\sqrt{6}C_\mu\,|\,S\,|\,\zeta}\right), C_\eta\left(\frac{\nu^3}{\epsilon}\right)^{\frac{1}{4}}\right]\right) \tag{2.70}$$

Above, τ and L_K are Kolmogorov time and length scales, respectively, and are defined as follows

$$\alpha = max(1, \frac{L_{RANS}}{L_{LES}}) \tag{2.71}$$

$$L_{RANS} = \frac{k^{1.5}}{\epsilon} \tag{2.72}$$

$$L_{LES} = C_\alpha(\Delta X.\Delta Y.\Delta Z)^{\frac{1}{3}} \tag{2.73}$$

Model parameters were fixed in all simulations, and the values used are shown in Table 1 for reproducibility.

3 Lagrangian Particle Tracking
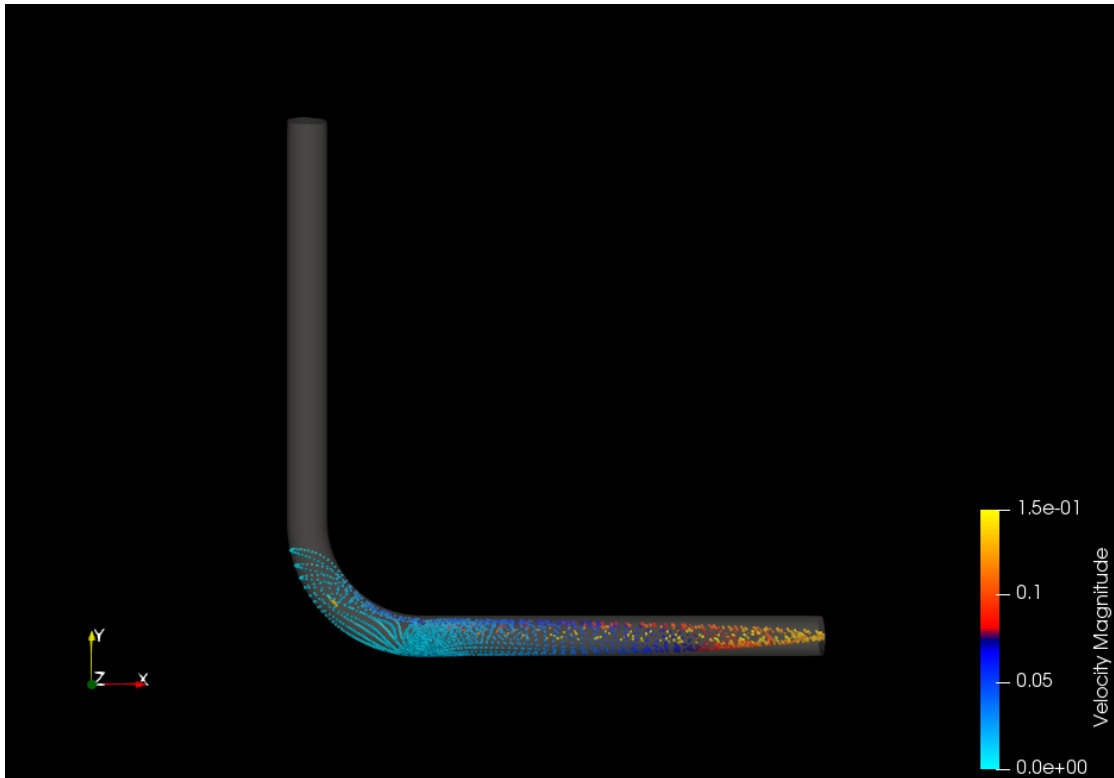
Figure 3.1 – A visualization showing a snapshot of 2500 mono-dispersed particles in a 90-degree-bend flow using T-Flows. Color map shows particle velocity magnitude.

3.1   Introduction

Discrete particle transport in turbulent flows has a plethora of medical and engineering applications, some of which are: growth of rain drops and cloud formation Devenish et al., 2012; Warhaft, 2008, air pollution, sand and dust storms Luo et al., 2016; Rahman et al., 2016; Sajjadi et al., 2016, transport and deposition of particulate flows in respiratory airways Cheng, 2003; Longest et al., 2008; Matida et al., 2004; Tavakol et al., 2017; L. Tian and Ahmadi, 2013; Zamankhan et al., 2006, deposition of blood cells in the arteries of human bodies Dueñas-Pamplona et al., 2021, mixing and evaporation of fuel droplets in combustion mechanisms Gong et al., 2021; Ra and Reitz, 2009; Saufi et al., 2019, spout-fluid bed techniques Yang et al., 2016, and deposition of fission particles in various components of nuclear reactors following a severe accident Dehbi et al., 2016. In order to accurately describe particle dispersion in such complex particulate flows, one has to first properly compute the carrier fluid field.

In the past few decades, two different approaches have been proposed to model particle motion in fluid flow: the Lagrangian-Eulerian (E-L) and the Eulerian-Eulerian (E-E) approaches. In the Lagrangian approach, particles are introduced in the domain through a Lagrangian Particle Tracking (LPT) algorithm (also referred to as Discrete Particle Simulation (DPS)), where the motion of an individual particle is modelled within an Eulerian (continuum-like) phase e.g. droplets, bubbles, or sand particles. The main advantage of this approach is that it can provide information on particle behavior (i.e. particle residence time and particle local velocity and position) for a relatively wide range of particle sizes. However, for high particle loading (i.e. high concentration dispersive flows), the advantage of using the E–L approach might be jeopardized by a prohibitive CPU cost needed for the simulation Gharaibah et al., 2015.

While in E-L only one set of conservation equations is solved - considering a point-source approximation, the E-E approach is based on treating the different phases mathematically as inter-penetrating continua i.e. the phases share the same volume and penetrate each other in space and exchange mass, momentum and energy. That said, it is obvious that E-E models as many sets as there are of phases coupled by phase interaction terms Pouraria et al., 2016. Since E-E imposes no restrictions on the volume or the number of fractions of dispersed phases, this makes it a more effective method, especially in large dispersions Zhang et al., 2019. However, this approach becomes computationally expensive when dealing with multiple particle classes/sizes. In such a frame, E-E regards each particle as a continuum where its average spacing is described by a particle density function, which makes it a very costly approach to deploying. For this reason, the E-E approach can be costly in some applications incorporating a wide range of particle sizes Gharaibah et al., 2015. In such applications, it is clear that the E-L approach is the best option of choice. Over the last few decades, both approaches have been used in a number of implemented particle codes (Balashazy, 1994; Chen and Pereira, 1997; Chorda et al., 2002; Kipfer et al., 2003; Lohner and Ambrosiano, 1990; Morency et al., 2003; Naterer, 2002; Norment, 1985; Oliviera et al., 1997; Patankar and Joseph, 2001; Seldner and Westermann, 1988; Zhou and Leschziner, 1999). As will be explained in

detail later, we use the E-L approach throughout this project.

In this chapter, we first show the structure of LPT algorithm implementation in T-Flows i.e. governing equations, main forces acting on a particle and the assumptions made throughout this work. Since the aim of the present work is to assess particle dispersion in wall-modeled LES on relatively coarse grids, the effect of unresolved turbulent scales on particle motion can be crucial. In this light, two particle SGS models were used in this project. The first one is the commonly used Fukagata SGS model (Fukagata et al., 2004) based on the Brownian diffusion force to induce turbulent-like stochasticity to particle motion. The second model is a novel particle subgrid scale approach based on the transport equations from the $k - \epsilon - \zeta - F$ RANS mode (i.e. ζ-SGS model). In a recent study, the ζ-SGS model showed a high level of robustness in hybrid RANS/LES framework, where low-to-moderate shear Reynolds numbers were investigated in a periodic channel flow (Sayed et al., 2021-b).

For LPT code verification and validation (V & V), we use two flow configurations i.e. T-junction and 90-degree bends - to test the implemented algorithm. Firstly, the code is verified in a laminar T-junction flow where results were compared against the commercial package ANSYS Fluent. The main idea of the verification step is to make sure the implemented equations are properly solved. In a second step, both laminar and turbulent flows were investigated in 90-degree bends where results were validated against experimental data for a wide range of particle sizes. The validation step predicates that the algorithm is using the right equations to accurately present the physical phenomena under study.

3.2   Algorithm outline and main assumptions

As mentioned in Chapter 2, in order to accurately simulate particle dispersion, fluid velocity at particle location must be correctly computed. To achieve this, a two-step procedure is performed; a search step and an interpolation step. In the search step, the whole computational domain is scanned to detect the closest cell center to the particle location. Then, from the cell index, the closest node to this particle can be identified. This is a necessary operation at the first time step where particles are introduced into the domain. Once done, the algorithm locates the neighbouring cells encapsulating the particle's closest node. In an optimized fashion, those very surrounding cells are to be scanned for the next time step after advancing the particle (i.e. instead of scanning the whole domain).

Upon advancing the particle, the algorithm starts to determine the closest new cell center and then the closest node to particle and so on. This procedure is the most efficient when keeping the particle advancement bounded. By this we mean that the user must make sure that particle time step size satisfies the Nyquist stability criterion (i.e. $\delta t_p \leq \tau_p/2$). As will be further explained in Section 3.3.1, Such criterion helps prevent particles from getting lost. Following the search step and knowing the fluid velocity at the particle's closest cell center, this velocity is interpolated to the particle position. In this work, we use 3D linear interpolation between cell center and particle location. As will be shown later, despite being very efficient

at interpolation, this scheme can lead to some numerical artifacts in statistically developing simulations that are relatively lengthy. This is because some tiny numerical errors might accumulate over large time intervals causing un-physical behavior of particles.

A number of particle tracking codes have been designed using these two components (Darmofal and Haimes, 1996; Li and Modest, 2001; Lohner and Ambrosiano, 1990; Pokrajac and Lazic, 2002). In this study, an LPT algorithm is implemented in the general-purpose code T-Flows. T-Flows is a computational fluid dynamics (CFD) program for simulation of turbulent, single and multiphase flows. The code was initially developed during the PhD work of Ničeno, 2001, focusing on conjugate heat transfer flows using Large Eddy Simulation (LES). The numerical method is based on collocated finite volume approach on unstructured arbitrary grids, and turbulence models include a range of Reynolds-averaged Navier-Stokes (RANS) models, large eddy simulations (LES), as well as hybrid RANS-LES. For parallel computations, the code mainly uses message passing interface (MPI) for sub-domain inter-communication. By the time of writing this thesis, the multiphase models include an algebraic volume of fluid (VOF) method and Lagrangian particle tracking model. Three-phase flows situations (two fluid phases with VOF and one solid phase as particles) are also supported. With the advent of modern parallelized Navier-Stokes unstructured flow solvers - like T-Flows as many other open-source codes, the mesh sizes of have grown to such an extent that the calculation of particle trajectories can be performed in a very efficient manner (with a careful implementation of the above-mentioned two operations). The present work describes the implementation and validation of an efficient particle trajectory code using the data-structure and libraries of the unstructured flow solver T-Flows. The development of the LPT algorithm was performed along the following assumptions:

- All particles are spherical in shape.

- Particle-particle collision is neglected.

- Particle collision with wall does not alter its smoothness.

- In default mode, particles are only subject to aerodynamic drag and gravity forces.

- Particles do not change shape or size during the simulation.

- LPT adopts one-way coupling approach: flow momentum is not affected by particle motion.

- The response of particle collision on the wall depends on the wall setup: either perfectly elastic (i.e. particle retrieves its full momentum after bouncing), or absorbing/ sticky walls (i.e. particles deposit once touched the wall).

- Point-particle approach is adopted i.e. fluid velocity is interpolated to the particle position prevailing in the absence of the particle.

3.3   Governing equations

In this project, we consider mono-dispersed particles. The main physical forces acting on particles are aerodynamic drag and gravity, whereas other forces like Saffman lift force and Basset history force were neglected. Aside from the physical forces, some other fictitious forces are sometimes added to account for SGS (or unresolved scales') effect on particle motion. As will be shown later, these SGS effects are modeled in a subtle manner as additional forces acting on the particle. In Section 3.2.2 we discuss the details of the used particle SGS models in this work in order to help particles retrieve some of the information lost by mesh coarseness.

Since only dilute flows (i.e. flows with low particle concentration) are considered in the present work, the effect of particle movement on the surrounding fluid is neglected (one-way coupling treatment). It must be stressed that such assumption does not mean that particle has no feedback on the carrier fluid, but rather that the inclusion of this feedback is not significant in such flow configurations (i.e. very dilute particle-laden flow). In this light, the computation of particle trajectory is partially decoupled from the fluid flow solution, and therefore can be performed as a post-processing step. In this framework, particle motion is described by Newton's second law; which is a second order ordinary differential equation (ODE) in time. The intergration of that ODE can be performed using one of the commonly used schemes, e.g. Adams-Bashforth predictor/corrector, the explicit Runge-Kutta scheme or Shampine, 1975. As will be shown below, we use in this work the Runge-Kutta forth order scheme (RK4).

3.3.1   Lagrangian equation of motion

The motion of the particles is tracked by solving the Lagrangian equation of motion, which is derived from first principles (i.e. Newton's second law ($F = m\vec{a}$)). The particle equation of motion reads:

$$m_p \frac{dV_{p,i}}{dt} = C_D \rho_f (U_i - V_{p,i}) \mid U_i - V_{p,i} \mid \frac{A_p}{2} + m_p g + \sum_{l=1}^{n} F_i m_p \tag{3.1}$$

where U_i is the fluid velocity (interpolated to the particle position), $V_{p,i}$ is particle velocity in the corresponding three orthogonal directions, C_D is the drag coefficient, A_p is particle surface area, m_p is particle mass, g is the gravity vector, and F_i is the additional forces per unit mass. As mentioned above, in addition to drag and gravity forces, the modeling of other phenomena is included in the equation of motion as additional forces. This is represented in Eq. 3.1 in the term ($\sum_{i=1}^{n} F_i$). As will be explained below, some of those forces represent the effect of the sub-grid scales on particle advancement (Section 1.4).

It should be mentioned that a fully explicit scheme was used for LPT in this work; meaning that particle velocity and particle location are decoupled (i.e. solved one after another and not

simultaneously). In that sense, once particle velocity is obtained, local particle location can be obtained integrating the following equation

$$\frac{dx_{pi}}{dt} = V_{p,i} \tag{3.2}$$

Along side with particle inertia, a very important parameter representing particle relative velocity is particle Reynolds number Re_p. This parameter depends on both flow and particle features as in Eq. 3.3 below

$$Re_{p,i} = \rho_f \frac{|U_i - V_{p,i}| \, d_p}{\mu_f} \tag{3.3}$$

Since the drag force depends on the flow velocity experienced by particle, the drag coefficient for a particle depends on the Reynolds number. In the present work, we use the empirical relation by Schiller and Naumann, 1935, which reads

$$C_D = \frac{24}{Re_p}(1 + 0.15Re_p^{0.687}) = \frac{24}{Re_p}f \tag{3.4}$$

Rearranging Eq. 3.1 and dividing by particle mass, the Lagrangian equation of motion yields:

$$\frac{dV_{p,i}}{dt} = f\frac{(U_i - V_{p,i})}{\tau_p} + g + \sum_{i=1}^{n} F_i \tag{3.5}$$

where n is number of considered forces acting on the particle and f is a correction factor for the Stokes drag (defined as $f = \frac{Re_p}{24}C_d$). A key parameter to judge particle inertia is the particle Stokes number St, which is defined as particle relaxation time (or timescale) divided by fluid timescale. The particle relaxation time, τ_p is defined as follows:

$$\tau_p = \frac{\rho_p d^2}{18\mu_f} \tag{3.6}$$

For fluid time scale, it must be mentioned that the definition depends on the nature of the flow i.e. laminar or turbulent. In case of laminar flow, the timescale is based on the bulk velocity as

follows

$$\tau_{f(laminar)} = \frac{L}{U_b} \tag{3.7}$$

where L is the characteristic length for a given case. On the other hand, for a wall-bounded turbulent flow configuration, the timescale is based on the friction velocity (u_τ) which represents wall shear stress. In such way the flow time scale reads

$$\tau_{f(turbulent)} = \frac{u_\tau^2}{\nu} \tag{3.8}$$

From Eq. 3.5, it can be seen that the drag force is dependent on the slip velocity between the particle and the carrier flow. For this reason, the fluid velocity must be known ahead of LPT computations. As expressed below, the particle velocity is computed by time-integration of particle acceleration using Runge-Kutta forth order (RK4) scheme (also known as the classical Runge Kutta method):

$$V_{p,i+1} = V_{p,i} + \frac{1}{6}[k_1 + 2(k_2 + k_3) + k_4]\delta t \tag{3.9}$$

where δ is particle time step. It should be pointed out that the accuracy of this scheme is essentially embedded in its formulation which incorporates four integration sub-steps in this case (i.e. truncation error O(h^5)). As can be seen from (Eq. 3.10-3.13), each of these sub-steps is represented by one time split, k_i .

$$k_1 = f_n(t_n, y_n) = f\frac{(U_i - V_{p,i})}{\tau_p} + \sum_{i=1}^{i=n} F_i \tag{3.10}$$

$$k_2 = f_n(t_n + \frac{h}{2}, y_n + \frac{k_1}{2}) = f\frac{\left[U - [V_{p,i} + \frac{k_1\delta t}{2}]\right]}{\tau_p} \tag{3.11}$$

$$k_3 = f_n(t_n + \frac{h}{2}, y_n + \frac{k_2}{2}) = f\frac{\left[U - [V_{p,i} + \frac{k_2\delta t}{2}]\right]}{\tau_p} \tag{3.12}$$

$$k_4 = f_n(t_n + h, y_n + k_3) = f \frac{\left[U - [V_{p,i} + k_3 \delta t] \right]}{\tau_p} \tag{3.13}$$

Finally updating particle's position through Euler forward time advancement

$$x_{p,i+1} = x_{p_i} + V_{p,i} \delta t \tag{3.14}$$

It should be mentioned that the particle time step in all of our simulations is determined as a fraction of the global (flow) time step. In this context the global time step is divided by a specific integer for each particle size to obtain the particle time step δt. This number is mainly bounded by the Nyquist stability criterion (Marks, 1991), which dictates that for a unique signal to be accurately reconstructed, the sampling rate ($\frac{1}{\delta t}$) should be greater than or equal to twice the highest frequency in the domain ($\frac{1}{\tau_p}$). In the context of Lagrangian tracking, the particle time step used in the numerical integration should be half of particle relaxation time τ_p fulfilling the condition:

$$\delta t \le \frac{\tau_p}{2} \tag{3.15}$$

3.4   Particle subgrid scale (SGS) modeling

The inclusion of the SGS effect for turbulent flows has been shown to ameliorate the predictions of particle statistics, especially when the particle timescale is small and the grid employed is relatively coarse Armenio et al., 1999; Cernick et al., 2015; Marchioli, Salvetti, et al., 2008. As will be shown below, two particle SGS models were implemented to analyse the effect of unresolved motions on particle dispersion. Each model formulation will be explained including some numerical details for the reproducibility of results in the future.

3.4.1   The Fukagata et al., 2004 model

The stochastic SGS model of Fukagata et al., 2004 imitates the Brownian motion by adding an additional force to the Lagrangian equation of motion. This force is called the *Brownian diffusion force*. The rationale behind this approach is the incorporation of stochasticity to account for part of the instantaneous under-resolved motions and their influence on particle

dispersion. In order to achieve that, an additional term is included in Eq. 3.5 so that it reads:

$$\frac{dV_{p,i}}{dt} = f\frac{(U_i - V_{p,i})}{\tau_p} + \frac{F_{SGS,i}}{m_p}, \quad \frac{F_{SGS,i}}{m_p} = \frac{\sigma_s}{\Delta t}\zeta_i \tag{3.16}$$

where σ_s is the increment in RMS velocity due to the SGS velocity fluctuations during the fluid time step, Δt, and ζ is a Gaussian random number with zero mean and unit standard deviation computed using Box-Muller algorithm Box and Muller, 1958. The drag force (and any other standard force, if any) is computed only from the resolved fluid velocities, while σ_s is modelled using the kinetic theory of particle motion in homogeneous isotropic turbulence M. W. Reeks, 1991:

$$\sigma_s = \sqrt{\frac{2}{3}k_{SGS}\lambda}, \tag{3.17}$$

where the parameter λ is defined as:

$$\lambda = \beta_1\left[1 - exp(-\alpha(1+\theta))\right] - \beta_2 e^{-2\alpha}\left[1 - e^{\alpha(1-\theta)}\right] \tag{3.18}$$

where the variables α, θ, β_1 and β_2 are defined as follows

$$\alpha = \frac{\Delta t}{\tau_p}, \theta = \frac{\tau_p}{T^*_{L,SGS}}, \beta_1 = \left(\frac{1}{1+\theta}\right), \beta_2 = \left(\frac{1}{1-\theta}\right) \tag{3.19}$$

Above, Δt is the fluid global time step, while $T^*_{L,SGS}$ is the SGS fluid integral timescale along the inertial particle's path. The SGS fluid integral timescale for a fluid particle is calculated by following correlation from Gicquel et al., 2002 and Heinz, 2003:

$$T_{L,SGS} = \left(\frac{1}{2} + \frac{3}{4}C_0\right)^{-1}\frac{k_{SGS}}{\epsilon_{SGS}}. \tag{3.20}$$

According to Cernick et al., 2015, the fluid integral timescale can be calculated from Eq. 3.20 - since the model assumes $T^*_{L,SGS} = T_{L,SGS}$. For modelling k_{SGS}, the dynamic Smagorinsky model Lilly, 1992 is used:

$$k_{SGS} = C_I \Delta^2 |S|^2 \tag{3.21}$$

where $|S|$ is the magnitude of strain rate tensor, C_I is the Smagorinsky dynamic constant which is calculated based on the smallest (resolved) scales from Moin et al., 1991, and Δ is the length scale of the dynamic model (i.e. cubic root of the cell volume). The subgrid scale dissipation is then computed from the following relationship by Gicquel et al., 2002:

$$\epsilon_{SGS} = C_\epsilon \frac{(k_{SGS})^{\frac{3}{2}}}{\Delta} \tag{3.22}$$

where C_0 and C_ϵ are the Langevin model constant and LES dissipation constant, respectively. The standard values for those constants are $C_0 = 2.1$ $C_\epsilon = 1.0$, and have been fixed throughout all our investigations during this study.

3.4.2 $\zeta - SGS$ **model**

In a way analogous to Continuous Random Walk (CRW) models, the $\zeta - SGS$ model is proposed as robust and cost-effective method to retrieve SGS seen by particle. This model is simply based on recovering the modeled part of the wall-normal velocity component (computed in RANS mode) $V_{p,2})_{mod}$ which is the scalar surrogate for the wall-normal turbulent stress component proposed by P. Durbin, 1991. This modeled fluid velocity is then added to the resolved part, and the resultant is seen by particle (as in Eq. 3.23). This very component is most influential for particle deposition rates on the wall.

$$V_{p,2} = V_{p,2})_{res} + V_{p,2})_{mod} \tag{3.23}$$

$$V_{p,2})_{mod} = \sqrt{\zeta k} \tag{3.24}$$

where ζ represents the variance of wall-normal velocity fluctuation normalised by turbulent kinetic energy, and $V_{p,2}$ is the total wall-normal fluid velocity interpolated at the particle position. It is worth mentioning that the value of $V_{p,2})_{mod}$ at each cell center is always clipped at zero as a lower bound. For this, a correction is needed to account for the orientation of the modeled component of the wall normal velocity. This is achieved by multiplying the modeled component ($V_{p,2})_{mod}$) by a unit vector pointing in the direction of the resolved one, $V_{p,2})_{res}$ before computing the total wall normal velocity. As shown above, the numerical implementation of this model is rather simple but the physics behind it is far from trivial. In a recent study published by the author, it was shown that this particular $\zeta - SGS$ model has a high level of robustness on coarse meshes in periodic channel flow (Sayed et al., 2021-b). The study focused on a wide range of particle sizes at low-to-moderate shear Reynolds numbers. This is going to be shown in detail later in Chapter 4.

3.5 Thermophoresis

Thermophoresis is a force exerted on small particles when suspended in a gas in which there exists a temperature gradient. Such phenomenon is of practical importance in many industrial applications, such as in thermal precipitators, which are very effective in removing sub-micron-sized particles from gas streams. The fundamental dynamics responsible for thermophoresis were first investigated by Maxwell (Kennard, 1938) while attempting to explain the radiometer effect[I]. A common example of thermophoresis is the blackening of the glass globe of a kerosene lantern. The temperature gradient established between the flame and the globe drives the carbon particles produced in the combustion process towards the colder globe, where they deposit.

In a pioneering work, Talbot et al., 1980 proposed an expression for the thermophoretic force that matches within 20% the experimental data available to that date. Such form accounts for temperature gradient on particle motion spanning the entire range of Knudsen numbers ($0 \leq \lambda/L \leq \infty$). The thermophoretic force per unit mass in the three orthogonal directions $F_{th,i}$ can be defined as:

$$F_{th,i} = -D_{T,p} \frac{1}{m_p T} \frac{dT}{dx_i}$$

(3.25)

Above T is the local temperature at particle location and $D_{T,p}$ is the thermophoretic coefficient which reads:

$$D_{T,p} = \frac{6\pi d_p \mu^2 C_s \left(k_f/k_p + C_t k_n \right)}{\rho_f (1 + 3 C_m k_n) \left(1 + 2 k_f/k_p + 2 C_t k_n \right)}$$

(3.26)

C_s, C_t, C_m are the dimensionless constants of the Talbot model having the values of 1.17, 2.18 and 1.14, and k_f and k_p are the fluid and particle thermal conductivities taking the values $2.434 x 10^{-5}$ and 0.02723 $W.m^{-1}.k^{-1}$ respectively. The Knudsen number k_n, which is defined as the ratio of the medium mean free path to the characteristic length of the considered fluid reads

$$k_n = \frac{2\lambda}{d_p}$$

(3.27)

Where λ is the fluid mean free path (i.e. the average distance atoms or molecules travel

---

[I]The radiometer is a light bulb-shaped device containing an object that looks like a weather vane (wings arranged in a circle like spokes of a wheel). It was developed to measure the intensity of radiant energy, or heat to help understand the principles of energy conversion. When light rays hit the vanes of a radiometer, the black sides of the vanes absorb the rays better than the white sides. This causes the black side to become hotter than the white side (thermal energy).

between successive collisions) having the value 0.066 μm for air at pressure 101 kPa and temperature 293 K.

3.6   Turbophoresis

In similar fashion to thermophoresis, it is found that particles tend to migrate in the opposite direction of turbulence intensity gradient. This effect was coined by Caporaloni et al., 1975 as Turbophoresis. Such effect has been observed to segregate particles entrained in high velocity gases axially toward the wall region. Since the vertical gradient of turbulence near a depositing surface is large, turbophoresis is expected to enhance rate of particle deposition onto the surface in the direction of decreasing turbulence intensity.

It was also predicted independently by M. Reeks, 1983 who derived it rigorously from the particle kinetic equation. In that study, M. Reeks, 1983 showed that turbophoresis arose from a force balance between the net drag force and the gradient of the particle kinetic stresses acting on the particles due to the turbulence. He predicted that this would lead to a build-up of concentration near the wall, a feature which has been observed both experimentally (Dasgupta et al., 1997) and in Direct Numerical Simulation (DNS) (Soldati and Marchioli, 2009).

Due to the imposed no-slip condition at the wall, turbulence intensity has sharp gradients in the wall vicinity. As a result, particles with longer residence times accumulate in low-speed streaks (where turbulence intensity is low). It was shown in the study by Soldati and Marchioli, 2009 that turbophoresis is maximum when particle relaxation time is of the order of the characteristic time of the near-wall coherent structures (buffer layer). This translates to about 20 viscous time scales, $\delta_v = v/u_\tau$ (i.e. the friction velocity being $u_\tau = \sqrt{\tau_w/\rho_f}$ where τ_w is the wall shear stress).

3.7   Particle statistics

Lagrangian statistics were obtained by the ensemble averaging procedure. In such averaging, the mean of a quantity β that is a function of a microstate is computed as follows:

$$\overline{\beta} = \frac{1}{n_p n_{ts} n_{ss} n_b} \sum_{i=1}^{n_p} \sum_{j=1}^{n_{ts}} \sum_{k=1}^{n_{ss}} \sum_{l=1}^{n_b} \beta(x, y, z, t) \tag{3.28}$$

where n_{ss} is the total number of sub-time-steps (defining particle time step size), n_p is the number of particles passing through each cell, n_b is the number of cells per bin thickness, and n_{ts} is the number of global time steps to fill the averaging time interval by a specific number of sub-steps (with a lower bound that fulfills the Nyquist criterion Marks, 1991). As demonstrated by Fig. 3.2, the particle is detected within the same cell at several time instances. In such case,

each sub-time step is considered as a new *state*, then averaging is performed over the total number of states. It has to be mentioned that the number of realizations must be large enough to eliminate the effect of unsteady turbulent fluctuations.
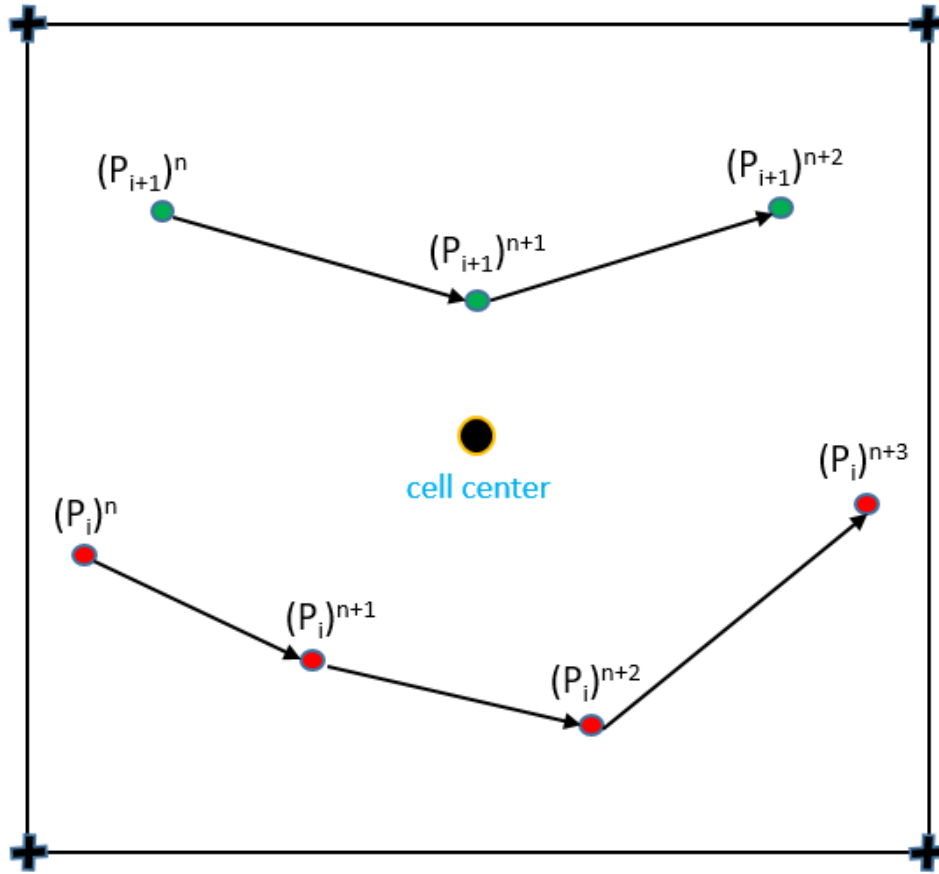
Figure 3.2 – A schematic showing different locations of a particle represented as different states during particle statistics procedure

3.8   LPT algorithm verification & validation

In the following, the implementation of LPT algorithm in the open-source code T-Flows will be tested. As known, testing new developments in CFD codes is usually followed by two steps; a verification step and a validation step (V & V). Since the present project is based on a cumulative framework, this V & V step is crucial to the code reliability. In this light, two flow configurations, namely: T-junction and 90-degree bends were used in the V & V process. As will be shown below, T-Flows predictions of T-junction flow were compared to the ones obtained by ANSYS Fluent as a reference for code verification. In a second step, the algorithm was validated against experimental data in the 90-degree bend configuration.

3.8.1   T-Junction flow

As a simple case for testing the algorithm, a laminar flow in a rectangular T-junction (as in Fig. 3.3) was used to check the implementation of the Lagrangian equation of motion (Eq. 3.5). At first, some sanity checks were made to test the main two operations of the LPT algorithm i.e. scanning and interpolation procedures. Secondly, particle trajectory obtained by T-Flows LPT is compared to the one by Fluent - given the same mesh and same particle injection point.
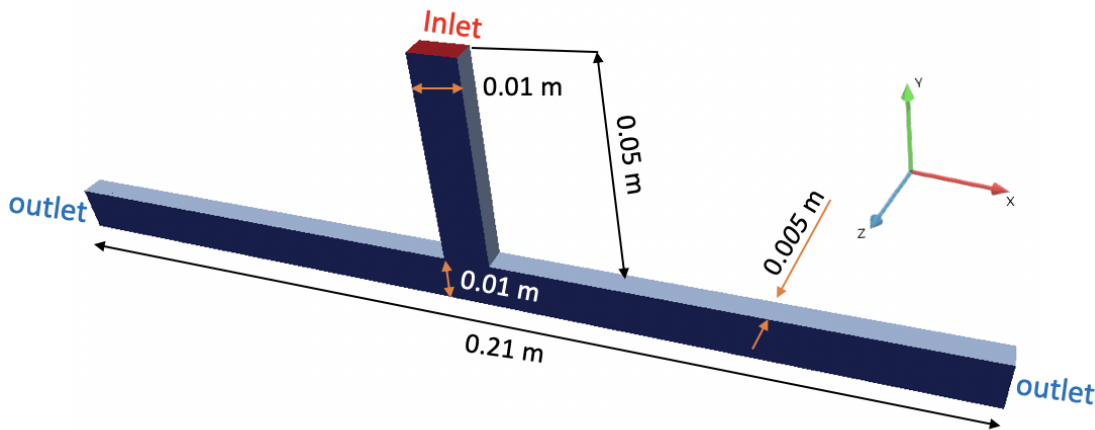
Figure 3.3 – Geometry of a rectangular T -junction

To accurately predict particle trajectory, the fluid velocity at particle location must be correct. This is achieved through a proper interpolation of flow velocity from the cell center to particle location. Therefore, it is a must to make sure that fluid velocity is computed correctly before the interpolation step. To check this, we consider a laminar T-junction flow with two inlets as a preliminary step (as in Fig. 3.4). After reaching steady state condition, mean velocity profiles are reported at different sections of the T-junction right branch (i.e. x=0, x=0.5D_p, x=1D_p, and x=3D_p), where the origin is located on the center-line at the heart of the T-junction and D_p is the T-junction pipe diameter. T-Flows prediction of x-velocity profiles are compared to the ones obtained by Fluent at each location. As can be seen from Fig. 3.5, profiles are

matching for both codes. A grid with total number of 106,496 cells was used to solve the primary (background flow) with a resolution of 64x64 cells at the heart of the T-junction.
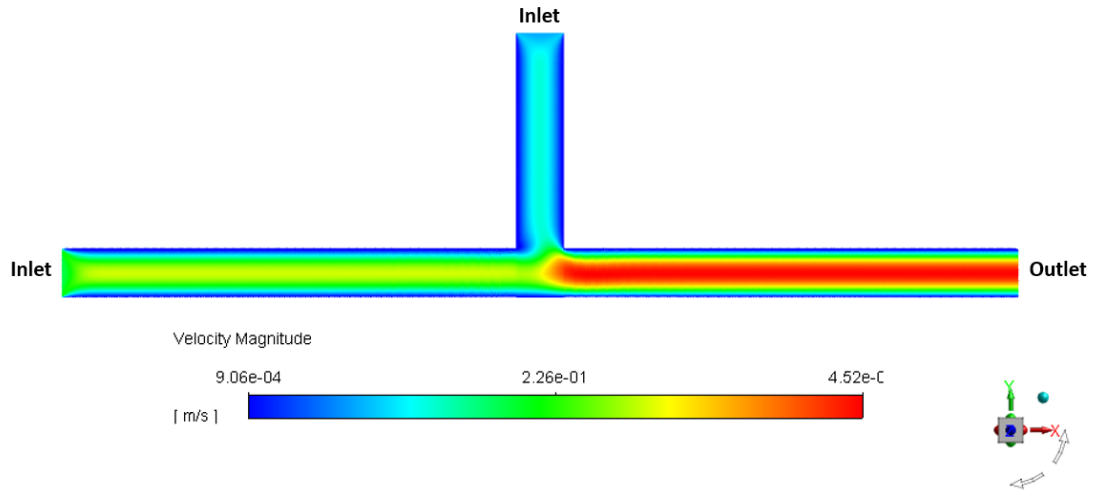
Figure 3.4 – Contours of mean velocity magnitude at the T-junction with two inlet boundary conditions. Inlet velocities are 0.1m/s and 0.2m/s on top and left sections respectively.

The next step in the verification process is to verify the particle trajectory predicted by the implemented algorithm. For this, we consider a T-junction with only one inlet section. Such configuration is more optimal for testing particle paths, especially if any deviation from symmetry was spotted. As in Fig. 3.6, we use a parabolic velocity inlet at the top with 1.5 m/s at the bulk, whereas pressure outlet was defined for the right and left ends of the T. As mentioned above, a preamble check on the scanning operation is required to make sure the algorithm is implemented properly. To achieve that, the search algorithm was checked through injecting a single particle at the inlet section and tracing it down to the outlet. To examine how the scanning for particle works, the location of both of closest cell center and node to the particle were plotted on top of the particle path. As seen from Fig. 3.7, the test reveals that the scanning process is performed consistently and accurately. Such simple test on a laminar flow can reveal any possible bugs in the implementation of scanning process. Another qualitative check done to see the behavior of a group of injected particles, was to introduce 16 particles in an equi-distant fashion from the center line at the inlet section. As shown below (Fig. 3.8), particles' trajectories show a perfectly symmetric shape around y-axis as expected.
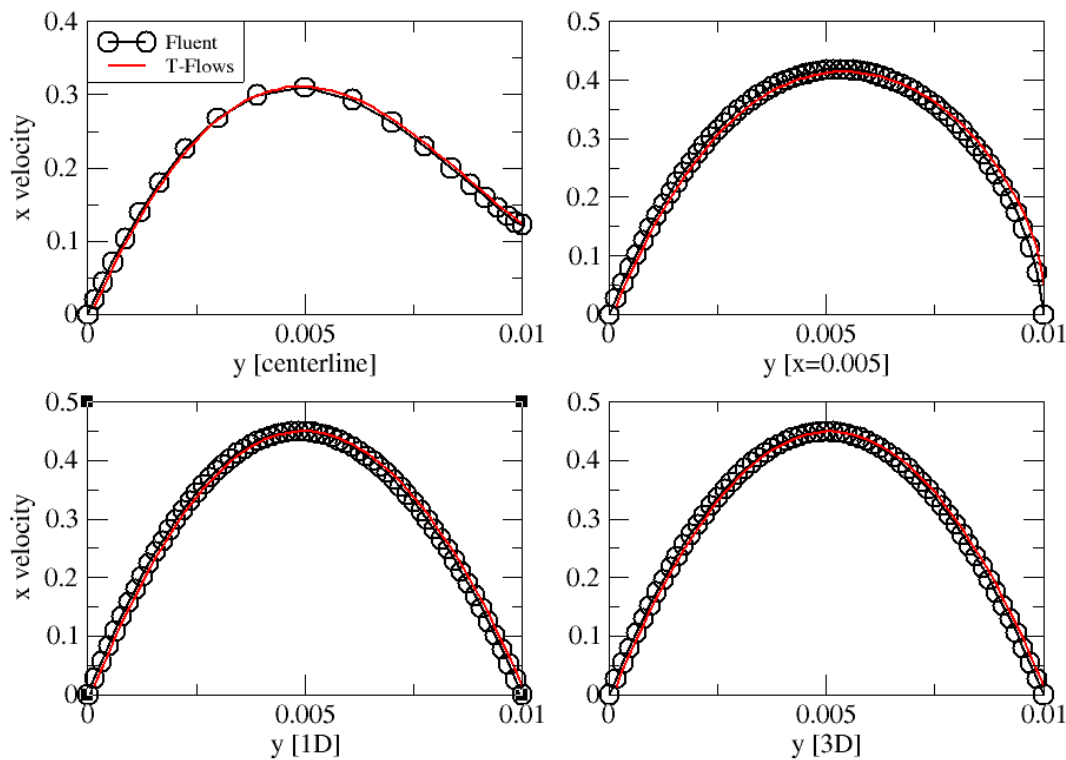
Figure 3.5 – Comparison for y-velocity profiles at different cross sections at the right half of the T-junction between T-Flow and Fluent
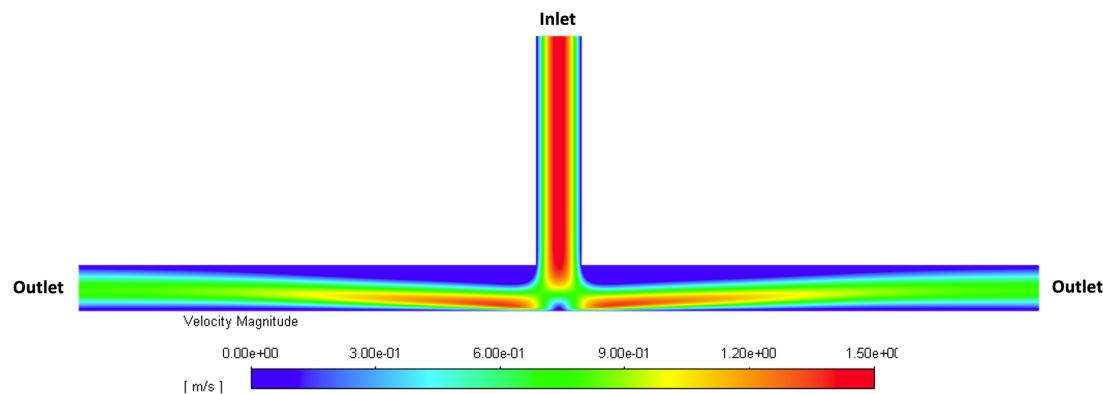
Figure 3.6 – Contours of mean velocity magnitude at the T-junction with one inlet boundary condition. Inlet velocity is a parabolic profile with 1.5 m/s at the bulk.
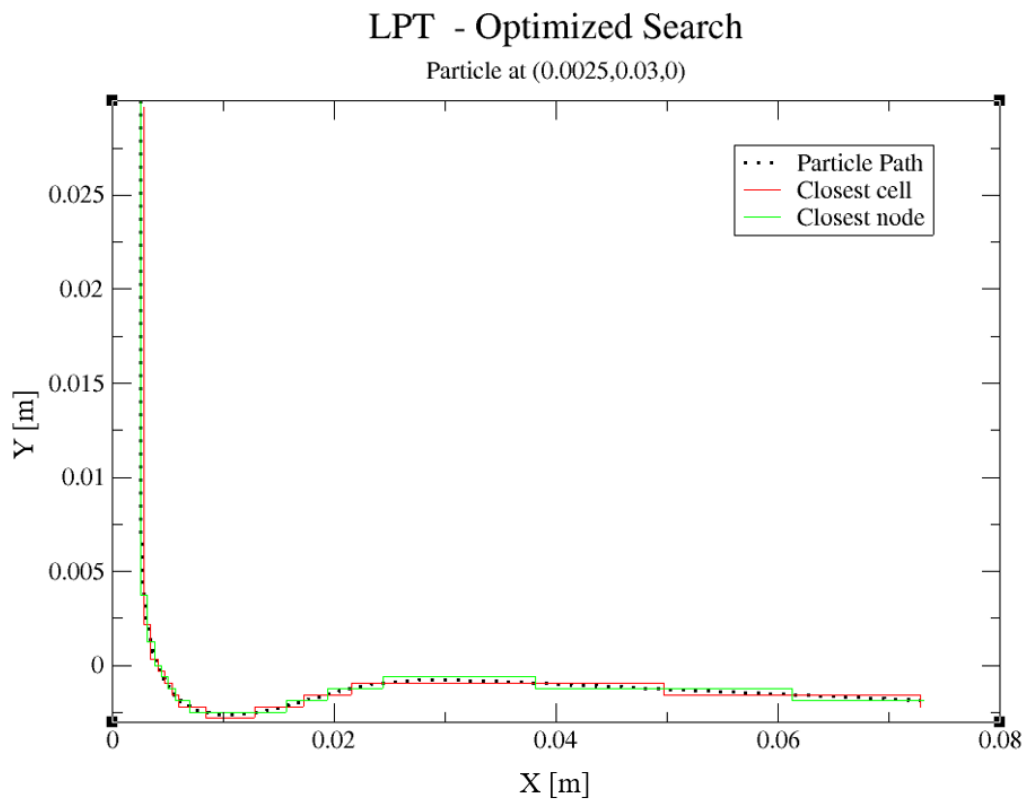
Figure 3.7 – Single particle trajectory is plotted alongside the closest cell and node positions to the particle in time and space
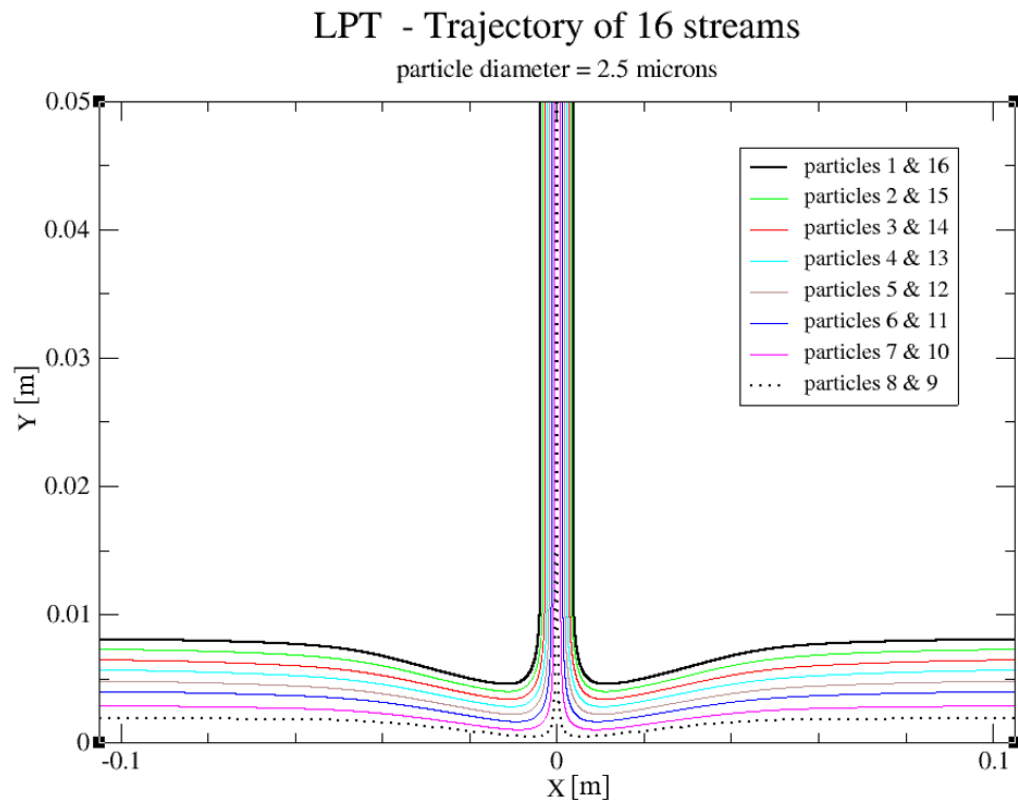
Figure 3.8 – The trajectory of 16 particles injected in an equi-distant space across the inlet.

To verify that algorithm implementation is accurately representing the conceptual description of LPT, we compare the trajectory of a single particle to the corresponding prediction from ANSYS Fluent. The same domain dimensions and problem setup were used for both codes. As shown in Fig. 3.9, particle paths are in an excellent match between the two codes with error margin ($L_{\infty norm}$= 0.0112), where $L_{\infty norm}$ is computed as follows:

$$L_{\infty norm} = \frac{| r_{calculated} - r_{Reference} |}{r_{Reference}}$$

(3.29)

where r is distance to particle location measured from the origin.
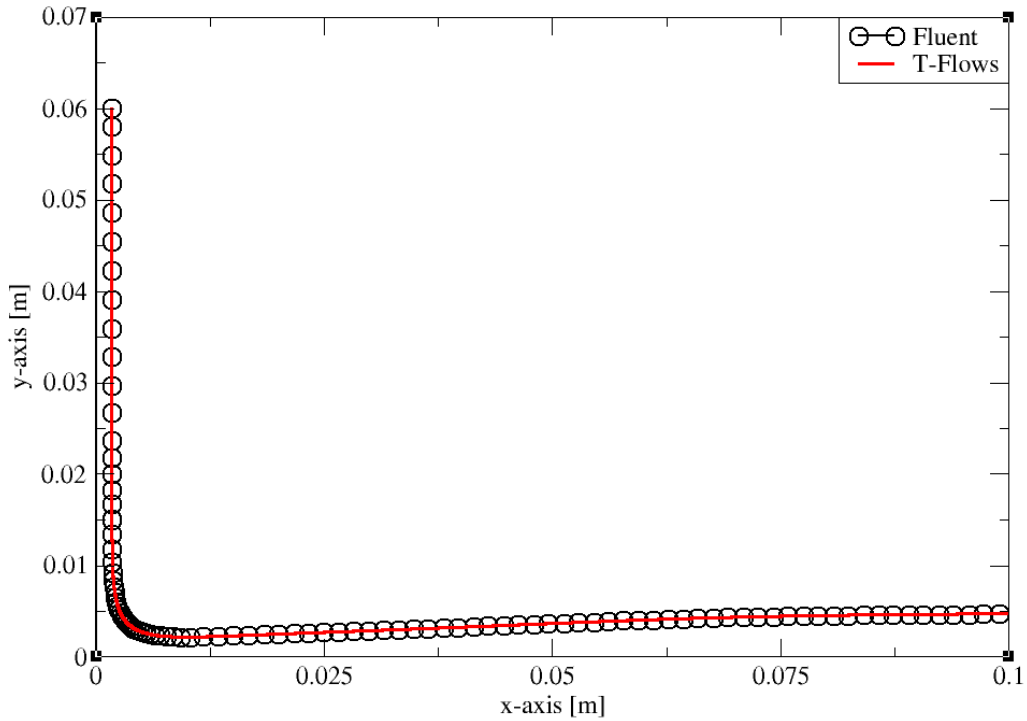
Figure 3.9 – Particle trajectory from T-Flows and Fluent in T-junction at Re = 1360

3.8.2 Flow in 90-degree bends

As a second phase, we choose the 90-degree bend configuration to validate the algorithm. The objective of this section is to test the algorithm implementation in both laminar and turbulent flows. Analogous to the T-junction analysis, we compare the primary flow statistics obtained by T-Flows to the ones obtained by ANSYS Fluent. Once done, we compare particle deposition efficiencies obtained by T-Flows against the reference data. As shown in Fig. 3.10, a fully structured mesh was generated with an octagonal core-block to align with the flow

configuration. No-slip boundary condition is assumed for the wall with the sticky choice for the dispersed phase (particle is assumed deposited once it touches the wall).

As will be shown later, two Reynolds numbers were investigated to assess the prediction of particle deposition efficiency. The fluid mass density and the dynamic viscosity used were 1.2 kg/m^3 and $1.8x10^{-5} kg/m.s$ respectively. To represent both laminar and turbulent flow regimes, two flat velocity inlets of 1m/s and 3m/s were assigned to the inlet section rendering Reynolds numbers Re = 1360, 4080. For a second-stage verification of LPT, we use the laminar case i.e. Re= 1360 for more tractability. To make sure the solution is not grid-dependent, three grids (M0, M1 and M2) were used having total cell counts of 266400, 729120 and 1065600 respectively. It can be seen from Fig. 3.11-3.12 that for both x and y-velocity profiles, meshes M1 and M2 exhibit more or less the same results with no significant deviation. Therefore, the medium mesh i.e. M1 was used for the rest of this analysis since it can be deemed sufficient to capture the main flow features. The advection scheme used in this part was QUICK scheme for both codes. It must be stressed that the first order upwind scheme, despite being very stable, can be very diffusive and lead to over-damped flow. This can be the case even with laminar flow that the first order upwind results into inaccurate solution (see Appendix B).

In a code-to-code verification, velocity profiles obtained by T-Flows were compared to the ones computed by Fluent. Both x and y-velocity profiles are plotted on both horizontal and vertical lines at the exit of bend (x=0.139m). It can be seen from Fig. 3.13-3.14 that the primary flow representation by both codes shows a perfect agreement. Following that, we examine particle deposition efficiency which is defined as the number of deposited particles divided by total number of injected particles. In this analysis, twelve swarms of different particle sizes i.e. $d_p = 3 - 70\mu m$ were introduced at rest. The mass density of the particles has been set to 1000 kg/m^3. For each simulation, a swarm of 2500 particles were distributed uniformly in equi-radial-and-azimuthal distances over the entrance of the bend section (see Fig. 3.15). After 40 flow through times, all particles were observed to either have deposited or escaped from the outlet section. Deposition efficiency as a function of particle diameter obtained by T-Flows was compared to the prediction by Fluent. From Fig.3.16, it can be seen that - apart from small deviations in deposition below particle size $d_p = 30 \mu m$ - both codes give similar results.
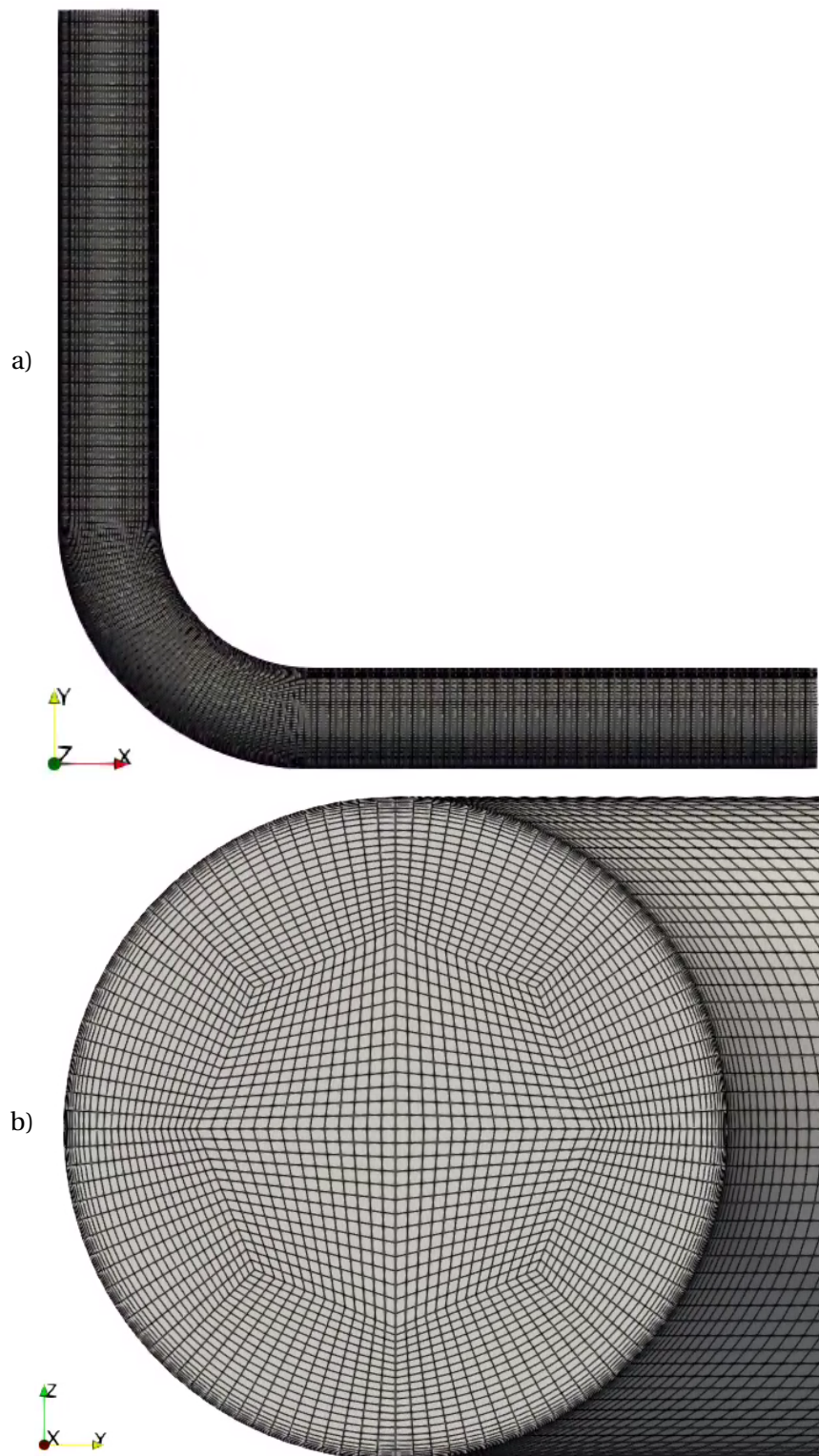
Figure 3.10 – Fully structured octagonal-core grid used for 90-degree bend configuration; a) side view; b) inlet section.
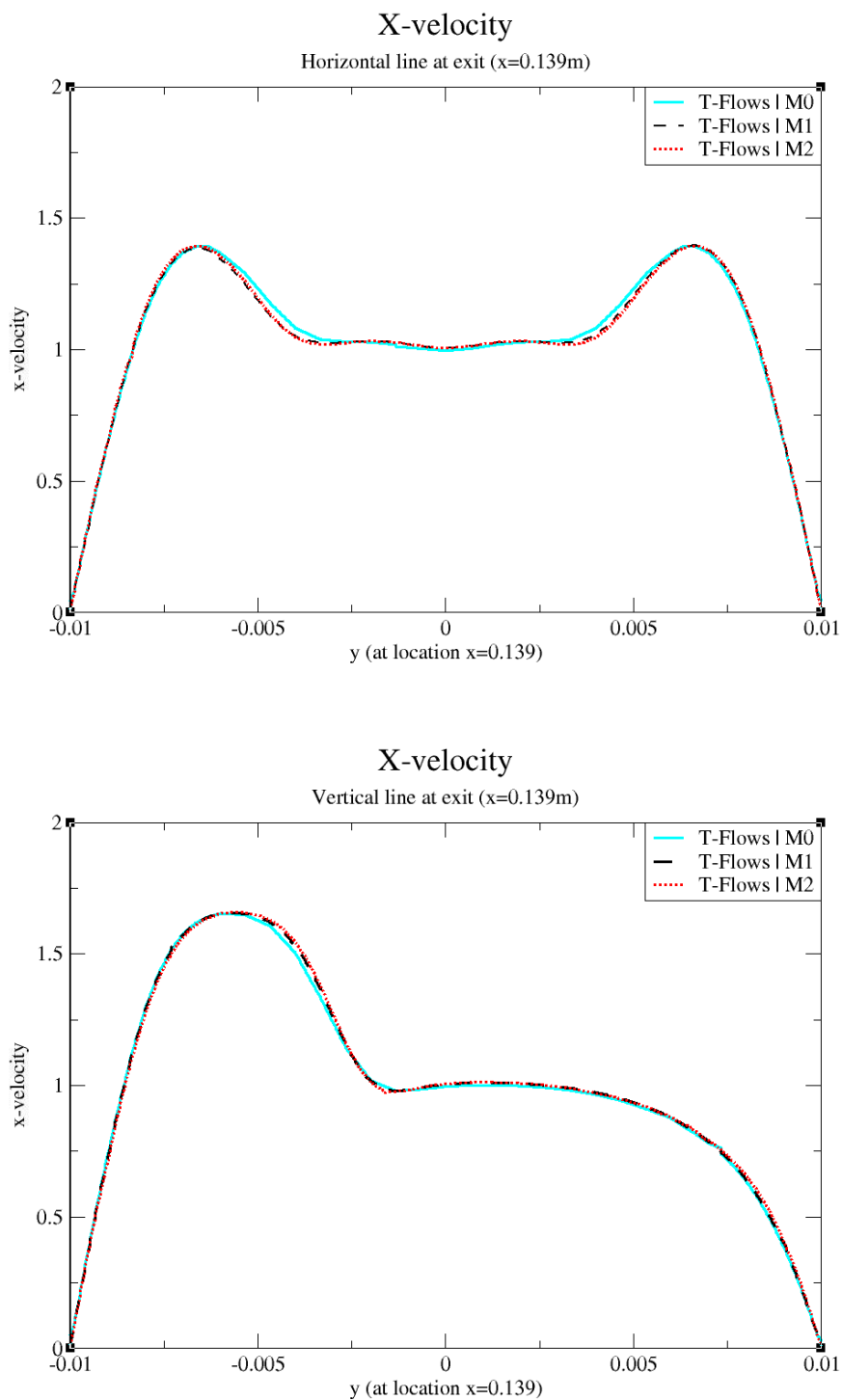
Figure 3.11 – Mesh dependency test using three meshes. M0 represents the coarsest mesh and M2 is the finest. X-velocity profiles are plotted on both horizontal and vertical lines at the exit of bend (x=0.139m).
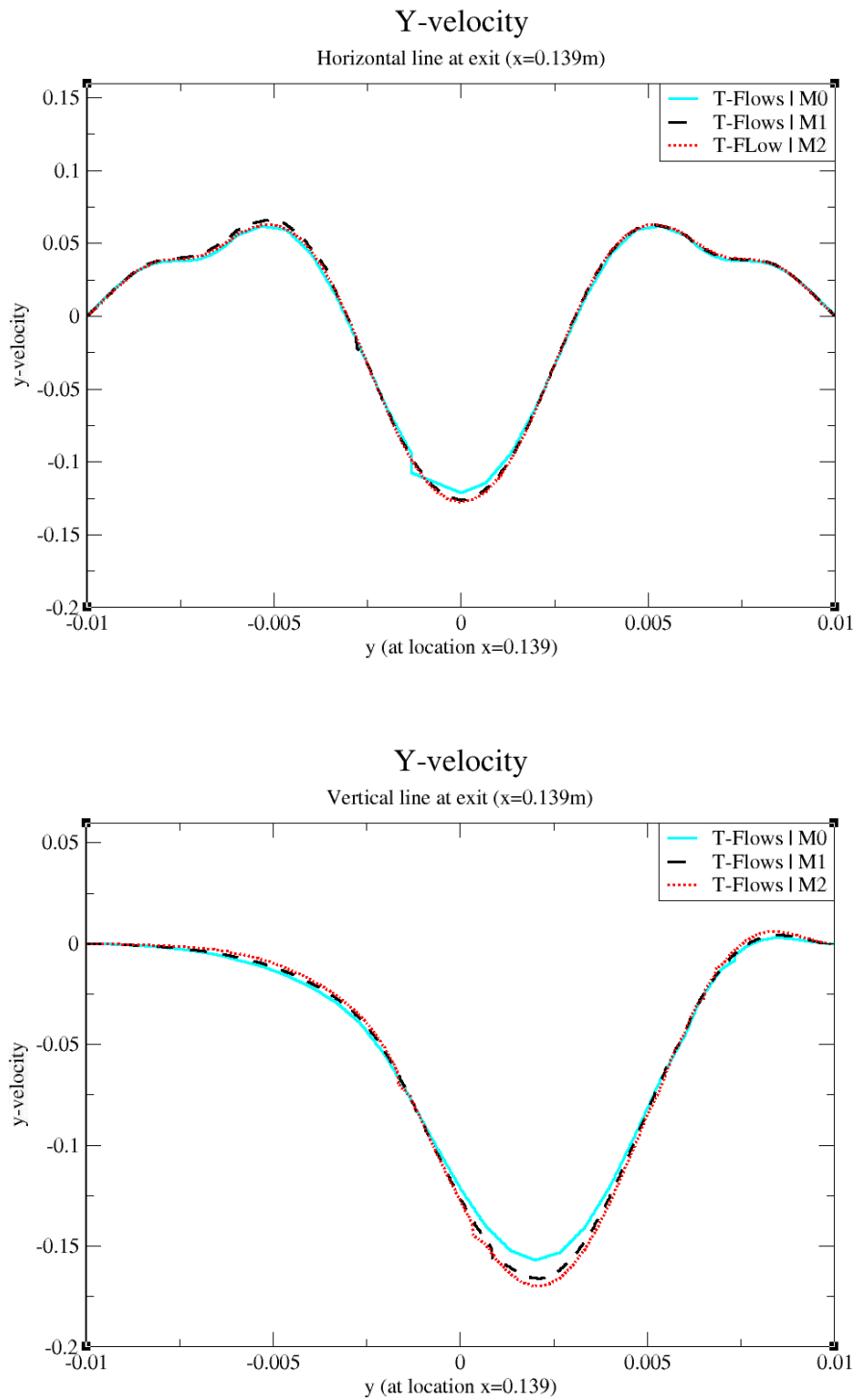
Figure 3.12 – Mesh dependency test using three meshes. M0 represents the coarsest mesh and M2 is the finest. Y-velocity profiles are plotted on both horizontal and vertical lines at the exit of bend (x=0.139m).
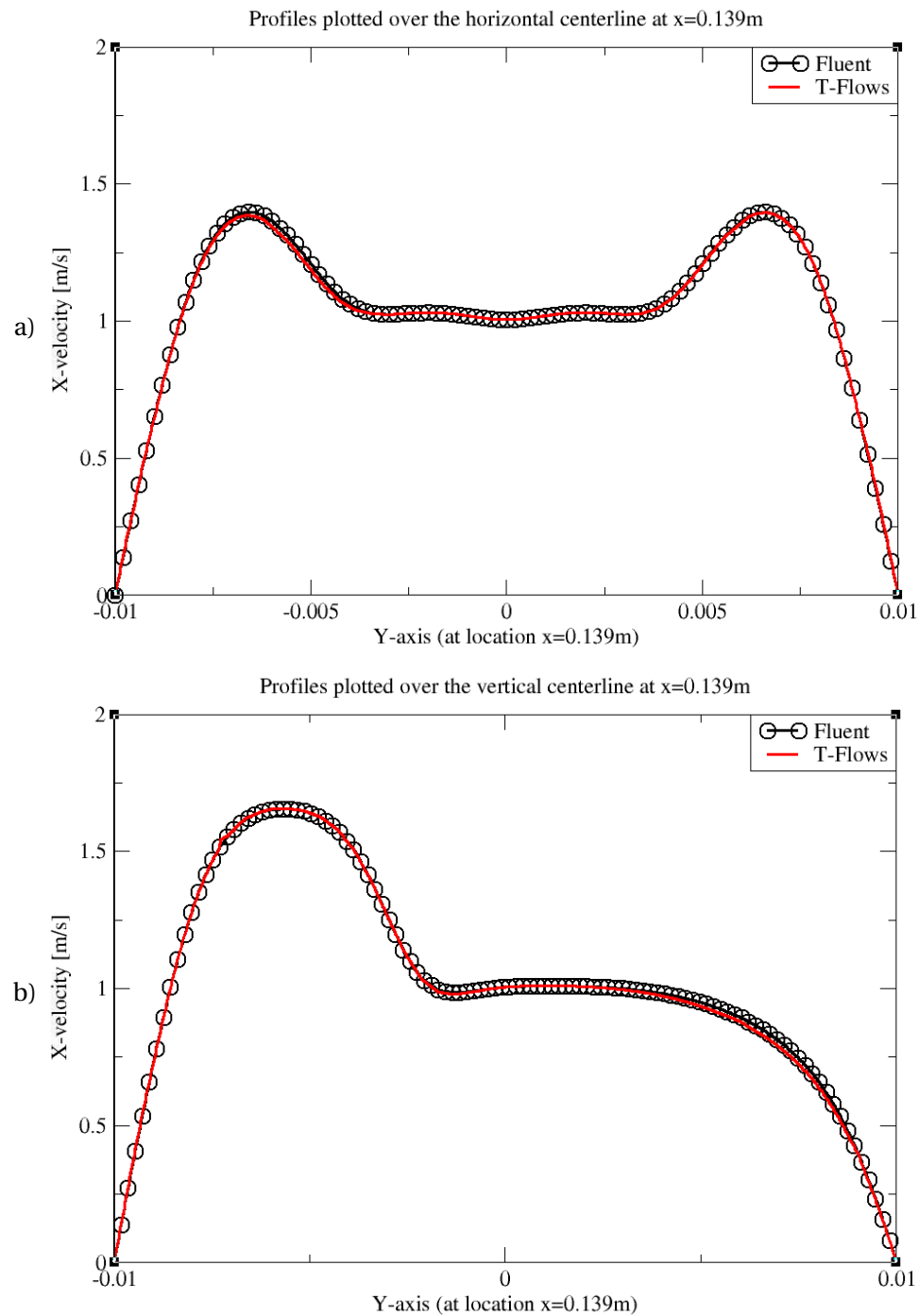
Figure 3.13 – Mean X-velocity profiles at the outlet section (x=0.139m) from both T-Flows and Fluent. Profiles are reported at the two orthogonal axes: a) horizontal line, b) vertical line
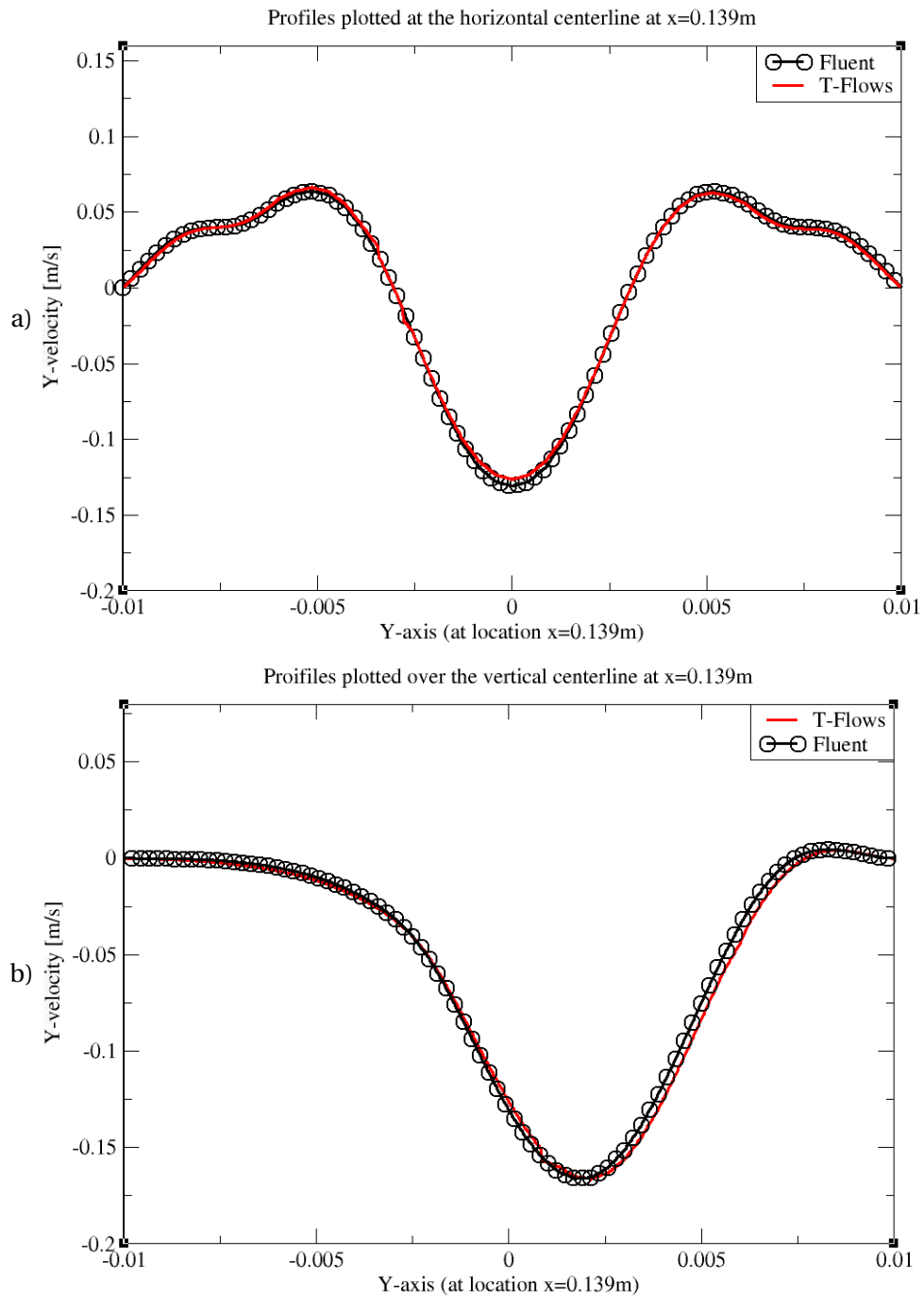
Figure 3.14 – Mean Y-velocity profiles at the outlet section (x=0.139m) from both T-Flows and Fluent. Profiles are reported at the two orthogonal axes: a) horizontal line, b) vertical line
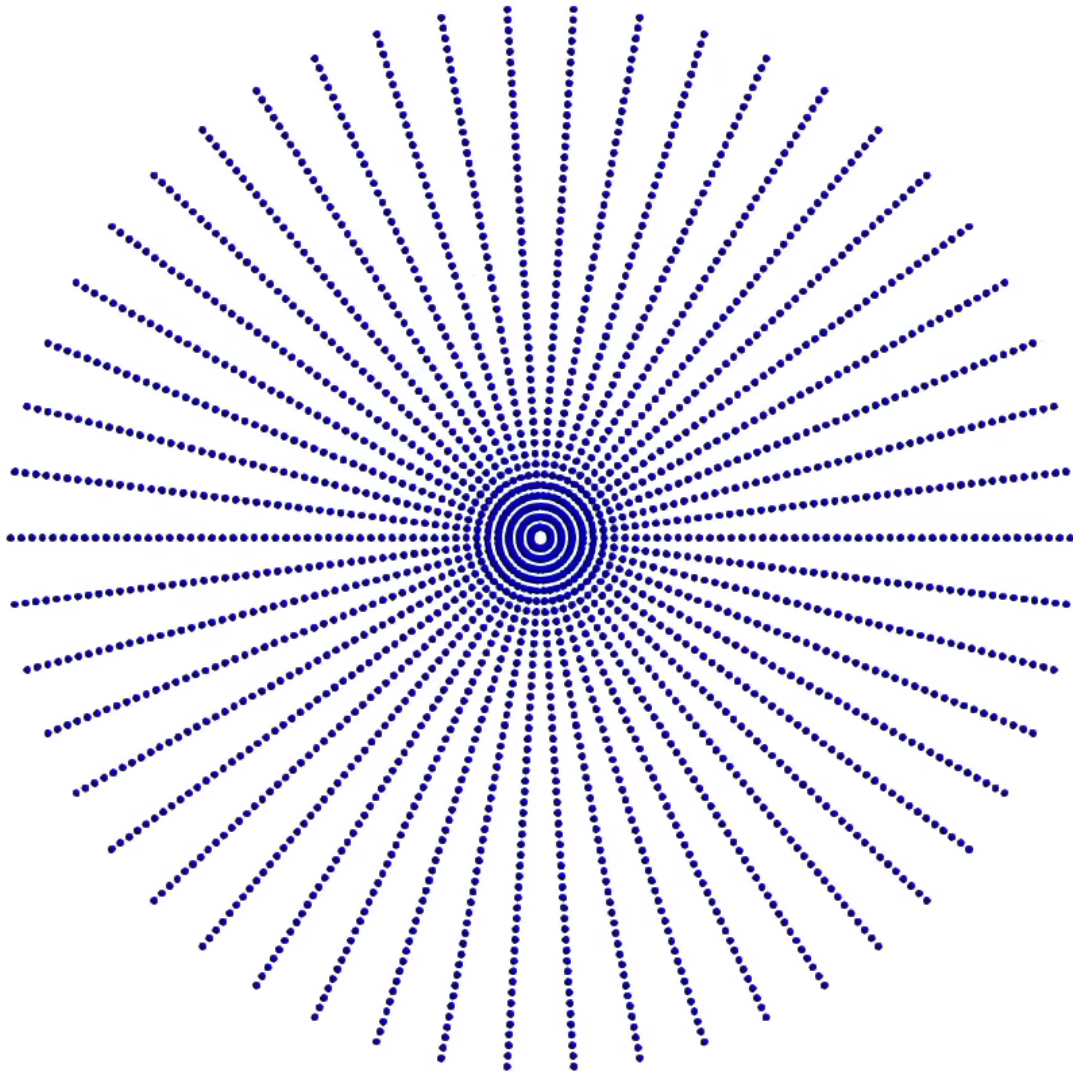
Figure 3.15 – Uniform distribution of 10,000 particles at the entrance of the bend section.

As a final step, a validation case is conducted with turbulent flow regime at Re = 4080. It can be seen in Fig. 3.17 that turbulence is created after the bend section and sustained downstream to the outlet section. In such flow configuration, the experimental data from Pui et al., 1987 were used to assess particle deposition efficiency. Nine sets of particle swarms i.e. d_p = 3 - 50 μm were injected at the same position mentioned above (bend entrance) from test, where the Lagrangian tracking was performed in a transient mode with the carrier flow. It is worth mentioning that the inclusion of the gravity effect on particles is negligible in this assessment. Since the dispersed flow here is wall-impaction driven, the injection location across the height of the inlet section does not matter, neither the injection surface.

As seen from Fig. 3.18 the predicted deposition efficiency by T-Flows was compared to both Fluent and the experimental data. The $k - \epsilon$ model was used in both codes in the standard form. As can be seen from the Figure, the deposition efficiency plots from both codes are very similar except from particle size 20μm where Fluent shows some overprediction of the deposited particles. This deviation can be attributed to the different time integration scheme used in Fluent which depends on adapting particle time-step to a prescribed tolerance. To check the potential of adding the LES dynamic model to the picture, the Elliptic-Relaxation Hybrid RANS/LES (ER-HRL) model was used in T-Flows. Despite a very slight enhancement for particle deposition for low-inertia particles, the effect of including the dynamic model is negligible on the global trend. This is no surprise since the ER-HRL is more suited for much higher Reynolds numbers - and the modification on the RANS formulation in this context does not add much to particle transport. Adding to this point, the RMS of velocity fluctuations are not significant for particle motion in this problem, since deposition is more governed by impaction. In comparison with the experimental results, predictions by T-Flows lie within approximately 20% margin as a maximum deviation.
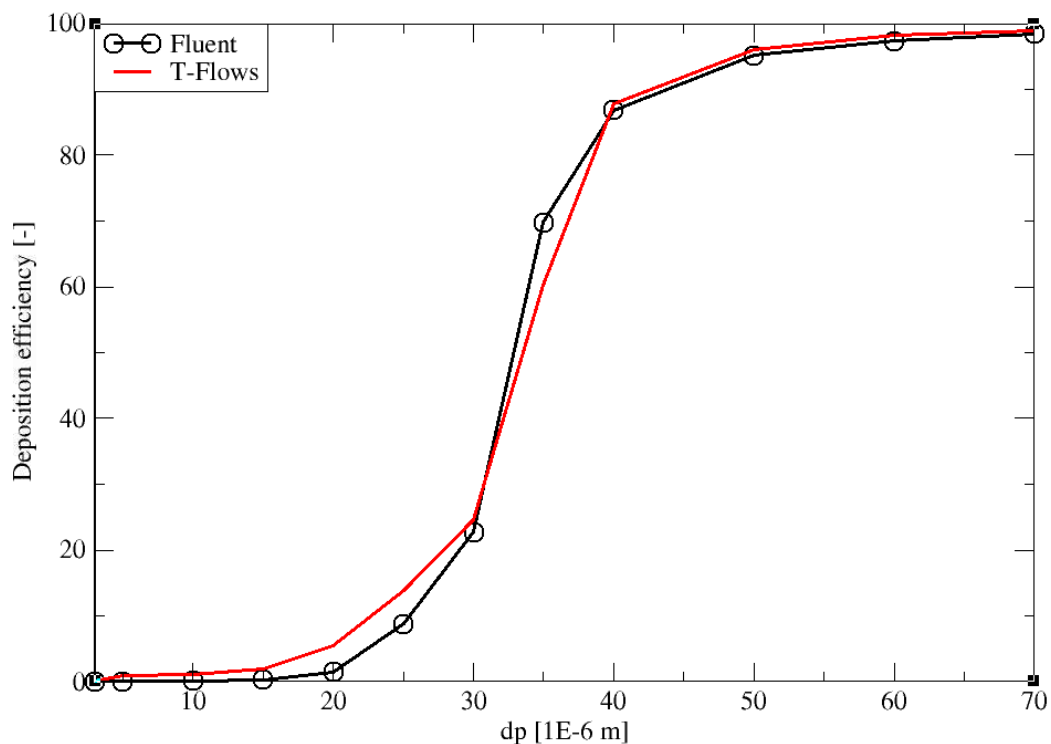
Figure 3.16 – Particle deposition efficiency depicted by both Fluent and T-Flows codes - inter-code comparison for verification
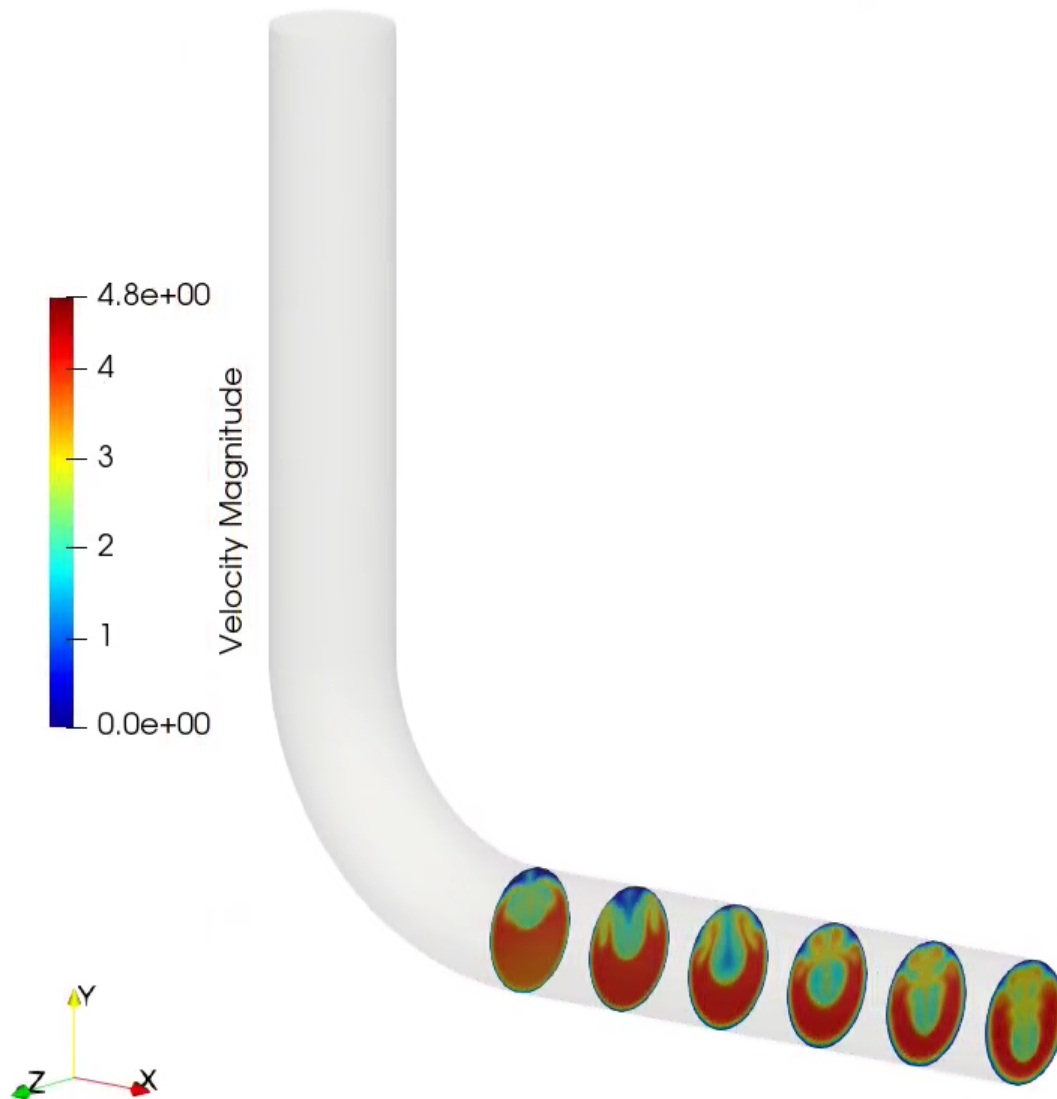
Figure 3.17 – Instantaneous velocity fields at different cross-sections representing the main turbulent structures emerging downstream the bend section. Profiles are reported at six equi-distant x-positions from the bend section end to the outlet section (i.e. x = 0.04 - 1.4 m).
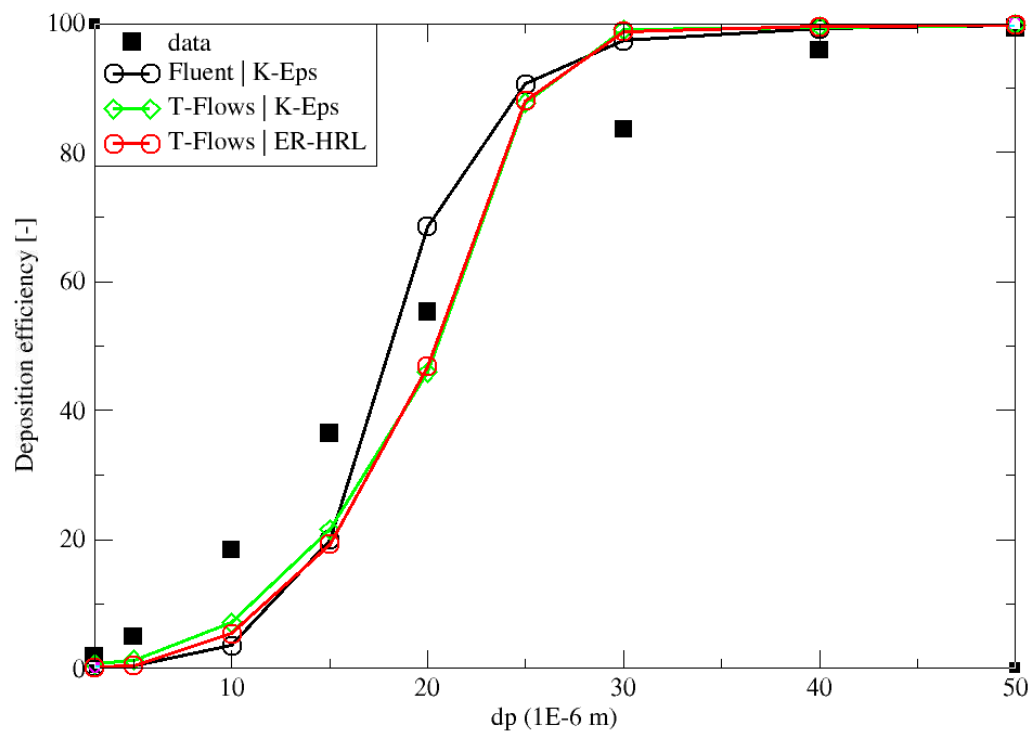
Figure 3.18 – Particle deposition efficiency depicted by both Fluent and T-Flows codes - inter-code comparison for verification

3.9   Conclusions

In this chapter, the implementation of Lagrangian particle tracking algorithm (LPT) in T-Flows code was documented. The algorithm consists of two main operations: a scanning step, and an interpolation one. In the scanning step and upon injecting the particle, we browse through all cells to locate the particle position. Once done, an optimized search process is employed, where the particle is searched only through the encapsulating cells to the particle nearest node. The second step of the algorithm is fluid velocity interpolation to the particle location. All particles are advanced through a post-processing step in a point-particle approach. This implies that the fluid velocity at the particle location is incorporated in the Lagrangian equation of motion as if the particle was not there. In addition, since we only consider low-concentration dispersed flows (also known as dilute flows), the particle has no feedback on the carrier (primary) fluid flow.

To verify the algorithm, two flow configurations were considered namely; T-junction flow, and 90-degree-bend. In the first case, a rectangular T-junction was used to verify the LPT algorithm using a laminar flow. To ensure a sound analysis, fluid velocity profiles obtained by T-Flows were compared to the ones calculated by Fluent. Profiles are reported at different locations across the T-outlet branch. In a qualitative way, particle tracks were reported in a symmetric flow configuration as a sanity check to make sure the Lagrangian equation of motion is properly computed. Followed by this, a single-particle trajectory was compared between both codes. The rationale of this step is to check any possible discrepancy in the deterministic behavior of the laminar flow. Results from T-Flows show an excellent agreement with ANSYS Fluent.

To validate the algorithm, the flow in 90-degree-bends was used. At first, the flow statistics were investigated where both spanwise and wall-normal velocity profiles are reported. Similarly, predictions from T-Flows are compared to ANSYS Fluent to verify the case. The experimental data from Pui et al., 1987 was used to assess our results. As the key factor in the analysis, particle deposition efficiency was compared against the reference data in both laminar and turbulent flow regimes i.e. Re = 1360, 4080. For the laminar case, T-Flows predictions match Fluent very well except for the particle size at the cut-off i.e. $d_p = 20\ \mu$m. This deviation is most probably linked to the different time-integration scheme used in Fluent. For the turbulent flow case i.e. Re = 4080, results from T-Flows show a global good agreement with the experimental data within a range of 20% of maximum deviation. Results are deemed very satisfactory to move further to test the code in more challenging forced and buoyancy-driven flows. As will be seen later, a few remarks are given on LPT in 90-Degree-Bends for the sake of documentation (Chapter). Those remarks can also serve as a brief guide for future researchers in this direction.

4 Periodic Channel Flow
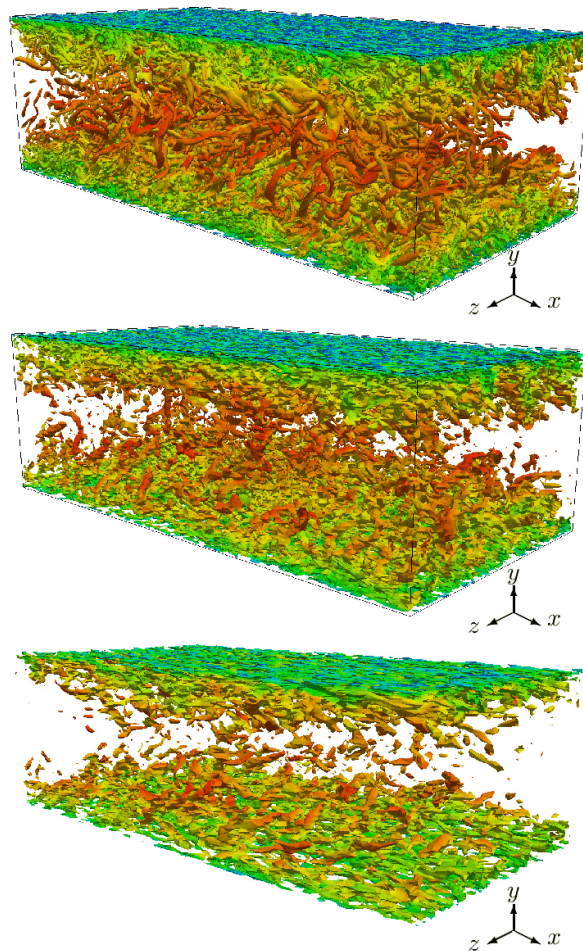
Figure 4.1 – Turbulent vortical structures in a periodic channel flow. The image is taken from the PhD thesis: Anisotropy-resolving subgrid-scale modelling using explicit algebraic closures for large-eddy simulation - Amin Rasam 2014.

4.1   Overview

In the previous two chapters, the implemented turbulence models needed for computing the fluid flow, and the Lagrangian particle tracking (LPT) algorithm for particle simulation have been shown. In the following, we test the implemented hybrid RANS/LES models against reference LES and DNS data. As one of the main canonical benchmarks in CFD, the particulate channel flow is chosen to validate the LPT algorithm. Succeeding the analysis of the channel flow, the qualified model will then be used in more complex flow configurations to reveal the model robustness within an Euler/Lagrange framework. As will be shown in the following chapters, more complex flows namely: Differentially Heated Cavity (DHC), swirl vanes will be addressed in Chapters 5-7.

In this chapter, we focus on the dispersion of inertial particles using Wall Modeled Large Eddy Simulations (WMLES) in Euler/Lagrange framework. We focus on particle-laden flow in a periodic rectangular plane channel. This is done through a systematic analysis of the dispersion of six sets of particles having Stokes numbers St= 0.2, 1, 5, 15, 25, 125 at shear Reynolds numbers of Re_τ =150, 590. The fluid flow is solved using two hybrid RANS/LES models. The first one is the Algebraic WMLES by Shur et al., 2008, which implicitly employs RANS mode in the very thin near-wall layer using the Prandtl mixing length damping, and switches to the traditional LES Smagorinsky mode all the way to the bulk region. The second model is the ER-HRL model (Hadziabdic and Hanjalic, 2020), which employs a four-equation linear eddy viscosity (LEV) model while in RANS mode in the wall-adjacent region, and switches to the Smagorinsky dynamic mode in the outer (bulk) flow region. For the discrete phase, a point-particle approach is adopted whereby the fluid velocity is interpolated to the particle center-of-mass. We assume in addition that the particle loading is dilute enough to justify a one-way coupling treatment. Moreover, the particle collision with the wall is assumed to be perfectly elastic. For each hybrid model, a particle subgrid-scale (SGS) model has been coupled to account for the effect of the smallest (unresolved) scales on particle dispersion.

To account for subgrid-scale (SGS) effects on particle motion, we use two different models. The first one is the model of Fukagata et al., 2004 for AWMLES, which adds some stochasticity to the particle advancement in a way similar to the Discrete Random Walk (DRW) approach. For the ER-HRL model we propose a novel approach where the transport equations of the turbulent quantities are employed to retrieve the SGS motions seen by a particle i.e. the $\zeta - SGS$ model (see Section 3.4.2). A quantitative validation against DNS data is accomplished by comparing the various measures of particle dispersion, namely: particle concentration profiles, mean velocities, and RMS of velocities. As will be detailed in this chapter, results show a good global agreement between both AWMLES and ER-HRL predictions and DNS data at a low Reynolds number of Re_τ=150, whereas the ER-HRL shows much better predictability than AWMELS for higher shear Reynolds number i.e. Re_τ = 590. In addition, the ER-HRL model outperforms the LES subgrid stochastic acceleration (LES-SSAM) approach at Re_τ = 590 with a much coarser grid.

4.2   Introduction

Predicting particle transport in turbulent flows has a plethora of applications, some of which are: transport of atmospheric aerosols, deposition of blood cells in the arteries of human bodies, mixing of fuel droplets in combustion chambers of propulsion systems, and deposition of fission particles in various components of nuclear reactors following a severe accident. In particular, particle dispersion in periodic channel flow has been a topic of interest for many researchers as one of the main benchmarks to validate particle tracking algorithms. In the last few decades, several studies have investigated particulate channel flow at a wide range of shear Reynolds numbers (i.e. Re_τ = 150 - 5200). In this chapter we focus on low-to-moderate Reynolds number where we investigate Re_τ = 150, 590.

While Reynolds-Averaged-Navier-Stokes (RANS) models are generally unsatisfactory and Direct Numerical Simulations (DNS) are computationally prohibitive, the Large Eddy Simulation (LES) stands as the most adequate tool to address complex flows at reasonably high turbulence levels. Particulate flows require that the wall boundary layer (BL) be accurately resolved since it is near the wall that particle physics is the most complex due to turbulence anisotropy and inhomogeneity. However, wall-bounded LES which resolves the BL has stringent spatial resolution requirements in all directions. This translates into large CPU needs, which grow exponentially with the Reynolds number i.e. proportional to $Re^{\frac{9}{4}}$ near the wall (M. Hadžiabdić, 2006).

To address this bottleneck, recent research has proposed the so-called Wall Modeled LES (WMLES), which is a promising alternative to dramatically reduce the LES dependency on the Reynolds number. The rationale behind WMLES models is to activate RANS mode at the near-wall region where both spatial and temporal scales are very small to be resolved, and switch to LES when the mesh size is sufficient to resolve the local large scales up to the free stream. With such a methodology, WMLES can tolerate much coarser grids in both streamwise and spanwise directions without significantly compromising the accuracy (Menter, 2013). The novel WMLES methodology has been applied with success in a limited number of complex wall-bounded fluid flows (Bose and Park, 2018).

Through this chapter, we investigate two WMLES models. The first one is based on a wall-modeled LES with algebraic wall damping function by Shur et al., 2008, hereinafter as "AWM-LES". As explained in Chapter 2, the algebraic formulation employs LES in the whole computational domain with an implicit RANS mode activated in the near-wall region through the Prandtl mixing length and Smagorinsky filter width. The second approach is the ER-HRL model in which the RANS mode is explicitly activated near the wall up to the logarithmic layer [I], then the LES dynamic model is applied in the bulk region to resolve the energy-containing scales of motion.

[I]The region of the boundary layer known as the inertial sublayer or logarithmic region. The term 'logarithmic' derives from the classical description (see Coles and Hirst, 1969), where the mean velocity, U, follows a logarithmic profile with distance from the wall

To the best of our knowledge, most the work done in the area of predicting particle dispersion in wall-bounded turbulent flows was achieved with pure DNS or LES simulations Dritselis and Vlachos, 2008; Geurts and Kuerten, 2012; Horne and Mahesh, 2019; Mallouppas and Wachem, 2013; Marchioli et al., 2007; Marchioli and Soldati, 2002; Marchioli, Soldati, et al., 2008; Picciotto et al., 2005; Pozorski and Apte, 2009; Rouson and Eaton, 2001; Vinkovic et al., 2011; Zamansky et al., 2011. With such methods, the study of dispersed flows is restricted to low Reynolds numbers and simple geometries due to the extortionate cost of both methods – on different levels – compared to RANS. On the other hand, stochastic models have been gaining increased popularity in the last few decades on account of their ease of implementation in CFD codes and vast area of application. Two of the most common stochastic models reported in the literature are Discrete Random Walk (DRW) and Continuous Random Walk (CRW) models (Bocksell and Loth, 2001, 2006; Dehbi, 2008b, 2010; Gosman and Ioannides, 1981; Horn and Schmid, 2008; Iliopoulos and Hanratty, 1999; Iliopoulos et al., 2003; Kallio and Reeks, 1989; MacInnes and Bracco, 1992; M. Mito and Hanratty, 2002; Y. Mito and Hanratty, 2004).

Unlike DRW models, CRW proved to be a more accurate approach as it better represents particle physics. It was shown in the works of Bocksell and Loth, 2006 that particle statistics are better predicted when accounting for Stokes number effect. This was achieved by including the finite-inertia correction term to the Markov chain, which was further investigated later by Mofakham and Ahmadi, 2019, 2020, who studied the performance of the CRW model using both the conventional non-normalized and normalized Langevin equations with and without the drift correction term (initially suggested by Legg and Raupach, 1982). It was also shown by the authors that the inclusion of BL-Correction factor in the Normalized-CRW model leads to a more accurate prediction of particle concentration profiles in inhomogeneous turbulent flows compared to the DRW model.

Although CRW models can give reliable results in wall-bounded flows, they rely on Eulerian statistical moments given by DNS databases as an approximation. As a result, RANS-CRW modeling is inadequate in 3D turbulent flows where DNS data are not available, especially for complex industrial flows. An alternative way to investigate particle dispersion is the probability density function (PDF) kinetic approach, which proves to be accurate in predicting particle statistics (Marchioli, Soldati, et al., 2008; Moin et al., 1991). PDF methods however require prior knowledge of mean and turbulent statistics of the carrier fluid, and hence, have limited applicability. Our investigation aims therefore to take the WMLES methodology one step further by modeling the dispersion of inertial particles in an Euler/Lagrange framework and under simplified conditions. We use the available DNS and LES data in the literature to validate the aforementioned hybrid model for plane channel flow. The objective is to construct a credible methodology by which the employed grid has a reduced scaling on the Reynolds number. In such a way, more complex 3D flows can be addressed later on at a reasonable cost.

In the light of WMLES models, it is reported by Sayed et al., 2020; Sayed et al., 2021-a that the algebraic formulation of WMLES by Shur et al., 2008 is only efficient in predicting flow statistics for channel flow at low-to-moderate shear Reynolds numbers. This is due to the

weak shielding by the implicit RANS mode in the viscous super-layer, which produces an inaccurate prediction of flow behavior, especially at higher Reynolds numbers. This might be attributed to the inability of the eddy viscosity blending criteria (Eq. 2.60) to properly correct values for balancing the momentum equation. To remedy this deficit, some extra empiricism might be needed in the switching criteria between RANS and LES modes, which makes it an open point of research. On the other hand, it was shown by Hadziabdic and Hanjalic, 2020 that the ER-HRL model is capable of predicting the turbulent flow statistics at high Reynolds numbers on relatively coarse grids. For this study, we focus on the periodic channel flow as a benchmark problem to validate the ER-HRL model for particulate flows against LES and DNS data. We investigate the model behavior through two different shear Reynolds numbers i.e. Re_τ =150, 590.

To account for the effect of subgrid motion scales on particle dispersion, a new particle SGS model (i.e. $\zeta - f$) was proposed in Sayed et al., 2021-b based on wall-normal velocity variance and turbulent kinetic energy. The rationale of the model is to retrieve the unresolved wall-normal velocity component and feed it to the particle Lagrangian equation of motion in a transient manner. This very component is most important for particle deposition prediction in the near-wall region. As will be shown later, the model shows a high level of robustness on coarse meshes relative to the AWMLES complemented with the Fukagata SGS model (Fukagata et al., 2004). The results of both approaches will be reported for each of the studied Reynolds numbers.

The rest of this chapter is organized as follows: in section 4.3, we explain the numerical tools used for simulating both the primary flow and the discrete phase. In Section 4.4, we show the results for flow statistics, and in Section 4.5 we report qualitative and quantitative particle analyses. In the final section, we summarize the results of the work done and give recommendations for future research in this area.

4.3   Numerical set-up

In this section, the set-up for solving the continuous phase (primary flow) and the dispersed phase (Lagrangian particles) is presented. Two models are used to solve the continuous phase: AWMLES and ER-HRL. The dispersed phase is investigated in a second step by solving an additional momentum equation for each particle, i.e. the Lagrangian equation of motion. To account for dissipation motion scales, we use two particle SGS models (one for each hybrid model): The model of Fukagata et al., 2004 for AWMLES, and our $\zeta - SGS$ model for ER-HRL.

We consider air as incompressible Newtonian fluid for which we solve Navier-Stokes equations (NSE). The air density used is $1\ kg/m^3$ and the dynamic viscosity is set to $3.0x10^{-5}kg/(m.s)$. To guarantee fully developed conditions for the primary flow, 10 flow through (transient) times were computed for each case. As in Table 4.1, t' is the flow transient time, Δt is the flow time step interval, u_τ (defined as $\sqrt{\frac{\tau_w}{\rho_f}}$) is the frictional velocity, ρ_f and ρ_p are fluid and particle

densities (they have been set to 1 kg/m^3 and 1000 kg/m^3 respectively), and u_b is the flow bulk velocity. The kinematic viscosity v has been set to $3x10^{-5}$ m^2/s for all simulations. Time step size was prescribed to achieve time-accurate solution with Courant number (CFL) ≤ 1 throughout all simulations.

Table 4.1 – Primary flow and dispersed phase main parameters

Re_τ	$u_\tau[m/s]$	$u_b[m/s]$	t'	Δt
150	0.004255	0.064672	100	0.5
590	0.01643	0.226	27.8	0.05

We treat particles as point-mass, rigid spheres with perfectly elastic wall collisions. We track each particle separately and independently in a Lagrangian/Eulerian frame of reference through the particle equation of motion (Eq. 3.1). We only consider the non-linear Stokes drag. Both lift and gravity forces are not accounted for in our simulations since their effects are negligible in the given conditions according to Marchioli & Soldati Marchioli et al., 2007. Particle advancement is done in a post-processing step after computing the primary flow at each global (primary flow) time step.

For time integration scheme, we use forth order Runge-Kutta, while spatial interpolation of fluid velocity at particle location is done by three-dimensional linear interpolation as in Rouson and Eaton, 2001. Particles are initially distributed in random positions covering the whole domain. Since we are aiming at the collective behavior of particle dispersion, we track particles under simplified conditions in which particle size and concentration are small enough to assume very dilute flow. This implies that particle-particle collision is neglected, and that particles have no feedback on the carrier fluid (one-way coupling). We trace six swarms of particles, 10^5 particles each to have one-to-one comparison with the DNS study conducted by Marchioli et al., 2007, characterized by the dimensionless particle-to-fluid timescale ratio (Stokes number) as in Table 4.2. This range of particle inertia was reported for both hybrid models studied i.e. AWMLES and ER-HRL and for both Reynolds numbers $Re_\tau = 150, 590$. We define Stokes number as

$$St = \tau_p{}^+ = \frac{\tau_p}{\tau_f} \tag{4.1}$$

where $\tau_p = \frac{\rho_p d_p^2}{18\mu}$ is the particle relaxation time , and $\tau_f = \frac{v}{u_\tau{}^2}$ is fluid time scale.

A particle is considered to have impacted the wall when its center is one radius or less away from the wall. Also, we assume that particle collisions with the wall do not alter its smoothness. The coefficient of restitution (COR[II]) is set to 1.0 in all the cases reported here to emulate perfectly elastic collisions.

[II]COR is defined here as the ratio of the final to initial speed after the particle collides with the wall

Table 4.2 – Particle diameters, relaxation times and particle maximum Reynolds number for each studied case

Re_τ	$St = \tau_p^+$	$\tau_p(s)$	$d_p(\mu m)$	d_p^+	$(Re_{p_{max}})_{ER-HRL}$	$(Re_{p_{max}})_{AWMLES}$	n_{ss}
150	0.2	0.3314	423.0	0.0599	0.0845	0.29	4
	1	1.657	945.93	0.1342	0.3369	1.145	2
	5	8.285	2115.16	0.3	1.318	1.764	2
	15	24.85	3663.56	0.5196	4.668	4.335	2
	25	34.18	4729.64	0.6708	7.218	6.91	2
	125	207.1	10575.8	1.5	19.58	30.57	2
590	0.2	0.0208	106.0	0.0569	0.0691	0.4332	5
	1	0.1032	236.12	0.1342	0.2368	1.401	2
	5	0.5162	527.98	0.3	0.6189	3.766	2
	15	1.549	914.49	0.5196	3.17	8.782	2
	25	2.581	1180.06	0.6708	5.515	10.87	2
	125	12.91	2639.92	1.5	22.23	28.11	10

To have a quantitative evolution of particle concentration near the wall, we adopt the same analysis employed in Marchioli et al., 2007. We report the instantaneous particle distribution at different times of the simulation where the background flow is frozen and a snapshot of the status of the particle is taken. To report relative concentration, the channel height was divided into $N_b = 64$ bins (Fig. 4.2) using Chebyshev polynomials (Eq. 4.2) and counting the number of particles confined between each two successive bins at each snapshot.

$$\Delta Z_{bin}^+ = \frac{Re_\tau}{2}\left[1 - cos\left(\pi\frac{b-1}{N_b-1}\right)\right]$$

(4.2)

Above b is the bin's ordinal number and the cumulative wall-normal thickness of the bins at b = 64 is equal to the achieved shear Reynolds number (at half of the channel height). As will be shown below, we analyze particle number density profiles and particle statistics for the span of three orders of magnitude of particle inertia at each of $Re_\tau = 150, 590$. We compare the obtained results against DNS data for each particle set in the following sections. It is worth mentioning that particle transport behavior is studied in a statistically developing manner. The reason behind this is that it would take much longer for the dispersed phase to have a statistically stationary state compared to the carrier fluid, according to Marchioli, Soldati, et al., 2008. Lagrangian statistics were obtained by the ensemble averaging procedure. So for each quantity β, the average is computed as follows

$$\overline{\beta} = \frac{1}{n_p n_{ts} n_{ss} n_c}\sum_{i=1}^{n_p}\sum_{j=1}^{n_{ts}}\sum_{k=1}^{n_{ss}}\sum_{l=1}^{n_b}\beta(x,y,z,t)$$

(4.3)

Above, n_{ss} is the total number of sub-time-steps (defining particle time step size), n_p is the
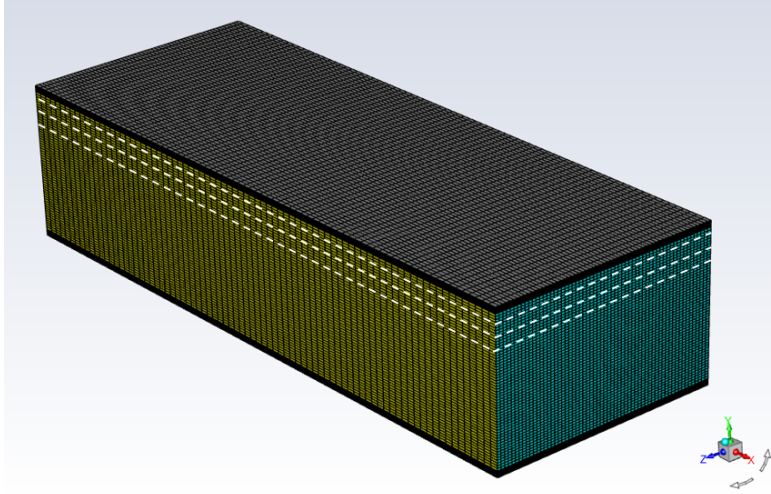
Figure 4.2 – A schematic showing the orientation of slicing used across the channel to measure concentration

number of particles passing through each cell, n_c is the number of cells per bin thickness, and n_{ts} is the number of global time steps to fill the averaging time interval by a specific number of sub-steps (with a lower bound that fulfills the Nyquist criterion Marks, 1991 as in Table 4.2).

It is clear that each sub-time step the particle is detected within the same cell is accounted for as a new *state*, then we average over the total number of states. The number of bins is chosen to coincide with the number of nodes across the channel height. In such an arrangement, the realizations of both the particles and the carrier flow are locally gathered at the same position. In addition, slab thickness distribution was analyzed for both the Chebyshev (Eq. 4.2) by Moin and Kim, 1982 and hyperbolic tangent (Eq. 4.4) distributions, and we found that the latter distribution provides a larger number of thin slabs not only in the bulk region but also near the wall. For this sake, particle central statistics reported here are gathered using the hyperbolic tangent clustering as follows

$$y_i = \frac{1}{2} tanh[\zeta_j tanh^{-1}(\alpha_s)] \tag{4.4}$$

$$\zeta_j = -1 + 2(j-1)(N_y - 1) \tag{4.5}$$

Above, N_y is the number of grid elements in wall normal direction and α_s is the cell-size stretching factor which was set (as in Table 4.3) so we have the first cell y^+ value less than 1.0 in each case.

4.4 Results

4.4.1 Flow Statistics

To assess the capability of the aforementioned hybrid models in predicting particle transport, we compare their predictions in a consistent investigation for two Reynolds numbers i.e. $Re_\tau = 150, 590$. Flow central moment statistics i.e. mean velocity profiles, TKE, and wall-normal RMS velocity were gathered after reaching statistically stationary flow. The parameters denoted by "+" refer to normalized cell size in streamwise, spanwise and wall-normal directions respectively by the viscous length scale, $\delta_v = \nu/u_\tau$. Wall-normal mesh refining is introduced by the hyperbolic tangent function (as in Eq. 4.4) for clustering the cells near the wall and hence obtaining the desired first wall-normal distance, y_1^+. Results of flow statistics at $Re_\tau = 150$ are compared against DNS data from Moser et al., 1999, and for high Reynolds number $Re_\tau = 590$ case we compare results against DNS from Lee and Moser, 2015. Out of the three RMS velocity values, we focus on the vertical (wall-normal) RMS velocity since it is the one responsible for particle impaction against the wall.

Like LES, hybrid models work in a transient mode whose solution also depends on the grid employed. This is due to the unresolved motion scales (SGS effects), and a perfectly grid-independent LES is a DNS which is not the objective of our study. For this reason, one should only seek grid sensitivity in terms of turbulent statistics predictions. As mentioned by Pope, 2000, a mesh that captures 80% of the total TKE can be deemed sufficient for a good LES. As shown in Figures 4.3, 4.4, flow is computed using three different grids to check mesh dependency for each model at $Re_\tau = 150$. As in Figures 4.5, both hybrid models capture the Eulerian statistics very well at $Re_\tau = 150$. The grid used for particle statistics is the same for both AWMLES and ER-HRL models (M1 and M11 respectively as in Table 4.3).

Table 4.3 – Grid resolutions for mesh dependency test at $Re_\tau = 150$

Model	*Grid*	N_x	N_y	N_z	α_s	D_x^+	D_y^+	D_z^+	$N_{tot}(10^5)$	y_1^+
AWMLES	M0	34	64	53	0.927	26.45	7.03	1.68 - 11.59	1.15	0.82
	M1	34	64	64	0.87	26.45	7.03	1.73 - 6.85	1.39	0.86
	M2	68	128	128	0.87	13.23	3.5	0.85 - 3.43	1.11	0.5
ER-HRL	M00	34	64	44	0.927	26.265	6.977	1.721 - 11.391	1.39	0.861
	M11	34	64	64	0.87	26.265	6.977	1.717 - 6.81	1.39	0.869
	M22	44	64	64	0.86	13.20.296	6.977	1.802 - 6.68	2.21	0.915

As the Reynolds number increases, it is noticed that the ER-HRL model becomes more sensitive to grid resolution - especially for the wall-normal direction. For this sake, we focus in particular on the mesh sensitivity of the ER-HRL for the higher Reynolds number case i.e. $Re_\tau = 590$. In this light, three meshes were used to study the model sensitivity to the mesh resolution (Fig. 4.6). The details of each of these meshes are reported in Table 4.4. It was noticed that the model works in hybrid RANS/LES mode only when using the coarse mesh which captures the peak of both the TKE and the wall-normal RMS velocity fairly well. For this reason, we use the coarse mesh to further assess the ER-HRL model in hybrid mode throughout this study.

75
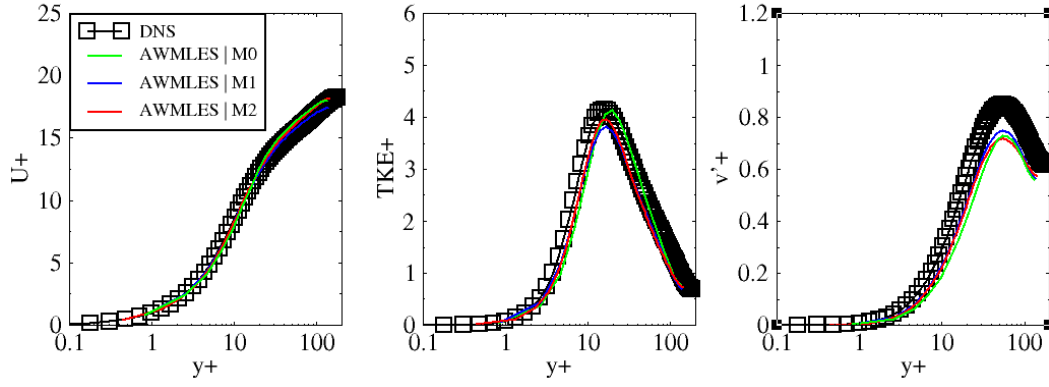
Figure 4.3 – Mesh dependency analysis for AWMLES model using three grids. Statistics at $Re_\tau = 150$ are compared against DNS data from Moser et al., 1999
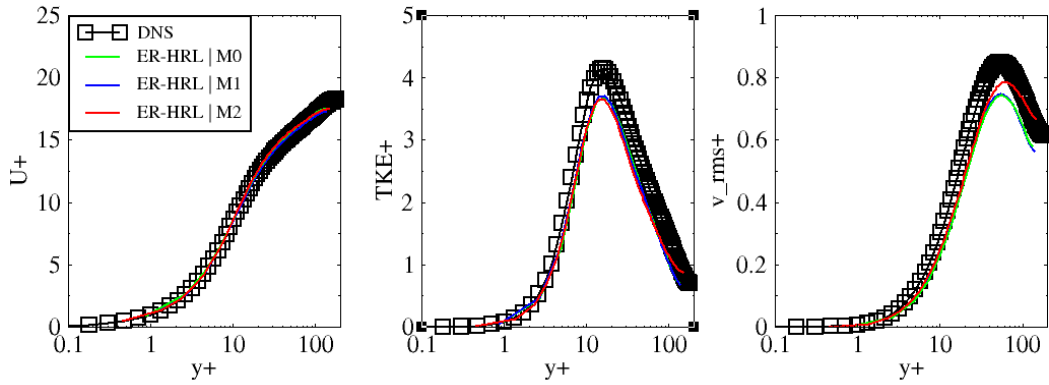
Figure 4.4 – Mesh dependency analysis for ER-HRL model using three grids. Statistics at $Re_\tau = 150$ are compared against DNS data from Moser et al., 1999.
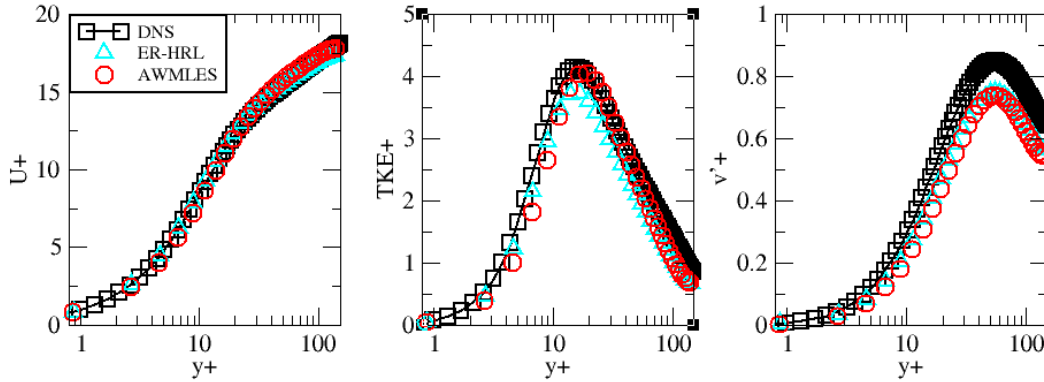
Figure 4.5 – Comparison of mean velocity profile (left), turbulent kinetic energy (middle), and wall normal rms velocity (right) for each of AWMLES and ER-HRL models against DNS data at Re_τ = 180. Square symbol represents DNS from Moser et al., 1999, while Cyan up-triangles and red circles are own data for ER-HRL model and AWMLES respectively. Mesh used for both of AWMLES and ER-HRL models is the same, aforementioned as M1/M11 in Table 3.

Once the mesh is refined, the modeled part of TKE diminishes, and hence the prediction of the majority of total TKE is tasked to the LES mode. In other words, the ER-HRL model behaves in LES mode with a dynamic subgrid-scale stress/flux model for unresolved motion scales. It was shown by M. Hadžiabdić and Hanjalić, 2008 that this model exhibits a large sensitivity to the mesh resolution, especially in the wall vicinity. It should also be noted that the RANS model contribution to the hybrid model is quite insignificant at a low Reynolds number (i.e. Re_τ = 150). In contrast, wall modeling is more prominent at a higher Reynolds number (i.e. Re_τ = 590) where the peak value of TKE is located in the wall vicinity. This can be observed by the visualization below for the modeled part of TKE (Fig. 4.7).

Table 4.4 – Mesh resolutions for grid sensitivity analysis at Re_τ = 590

Mesh	N_x	N_y	N_z	D_x^+	D_y^+	D_z^+	$N_t x 10^4$
Coarse	16	32	32	215	53.7	0.898 - 94.3	1.6
Medium	32	64	64	21.3	3.1	0.877 - 4.5	13.1
Fine	64	128	128	6.13	1.53	0.882 - 1.72	104.9

To explore hybrid model efficacy in predicting the wall-normal RMS velocity we compare its predictions for the two Reynolds numbers against its self-inherent RANS model (i.e. $k-\epsilon-\zeta-F$). In Figures 4.9, 4.10, we show the flow statistics predicted by both the ER-HRL and the pure RANS $k-\epsilon-\zeta-F$ models using the same meshes (i.e. M11 in Table 4.3 and coarse mesh in Table 4.5. As can be seen from Figure 3, both the mean flow and the TKE is better predicted by the ER-HRL model with a maximum deviation of 10% at the peak of the TKE. The same holds as well for the RMS of wall-normal velocity. On the other hand, pure RANS is missing approximately 20% of the wall-normal velocity fluctuation.
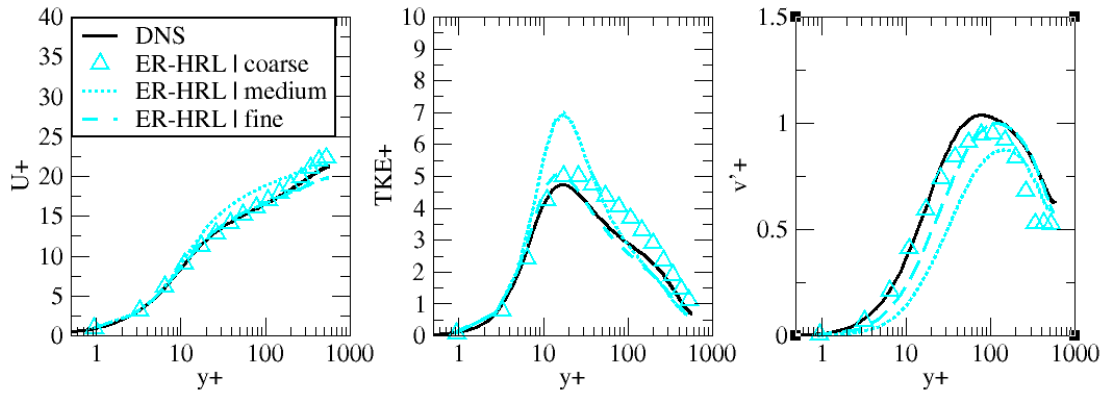
Figure 4.6 – Mesh sensitivity: Comparison of mean streamwise velocity profile (left), turbulent kinetic energy (middle), and wall-normal RMS velocity (right) for ER-HRL model against DNS data at $Re_\tau = 590$. Black thick lines represent DNS from (Lee and Moser, 2015), red dashed-lines show pure RANS, while Cyan up-triangles are own data for ER-HRL model.
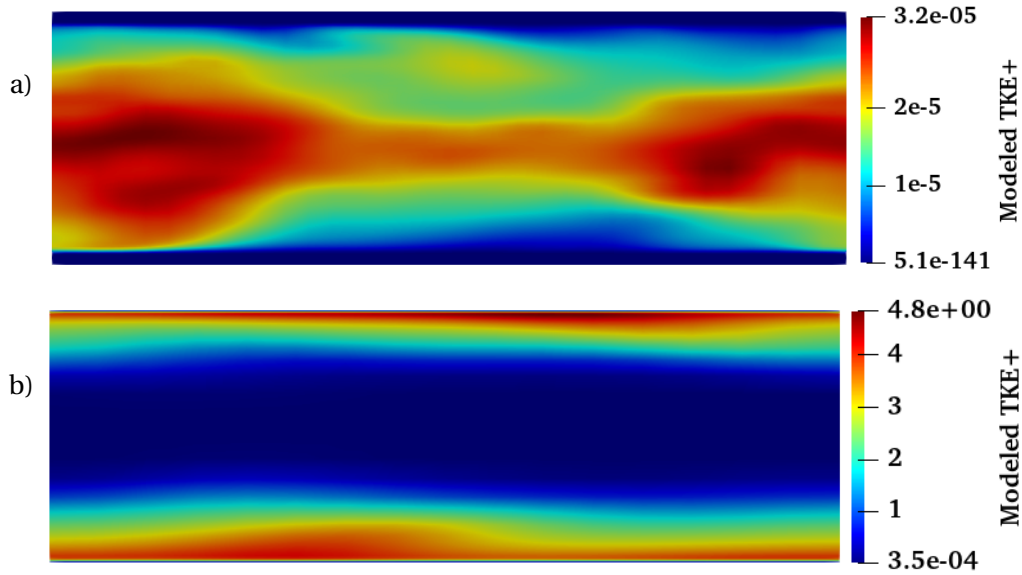
Figure 4.7 – Modeled part of the instantaneous turbulent kinetic energy normalized by friction velocity ($\frac{k}{u_\tau^2}$) predicted by the ER-HRL model at a) $Re_\tau = 150$ and b) $Re_\tau = 590$.

It is important to point out that for low turbulence levels such as $Re_\tau = 150$, WMLES models work with the same resolution as LES, but then the effect of wall-modeling is felt when going to higher Reynolds numbers Menter, 2015. It is therefore worth mentioning that results in Figure 4.4 are obtained with the *baseline* elliptic relaxation model (i.e. with no reconstruction for the wall-normal SGS velocity).

Unlike the case of $Re_\tau = 150$, the activation of RANS mode in the ER-HRL model is very significant at a higher Reynolds number (i.e. $Re_\tau = 590$), since it contributes the major part of TKE near the wall (see Figure 4.9). As a result, the model can tolerate much coarser grids in the spanwise and streamwise directions, translating into substantially lower computer expense relative to wall-resolved LES. It must be pointed out that the particle SGS model is significant here since it carries the bigger part of the fluid wall-normal velocity fluctuation (through Eq. 20).

From Figure 4.10 it can be noticed that the mean streamwise velocity and the TKE are well recovered by both the ER-HRL and the RANS $k - \epsilon - \zeta - F$ models. Although small deviations occur in the bulk region due to the coarse mesh used, the wall-normal velocity fluctuations are satisfactorily captured. It should be also highlighted that the ER-HRL model is superior to pure RANS in predicting the wall-normal velocity fluctuations in the near-wall region. This is particularly important because this very component (i.e. wall-normal RMS of velocity) is the key factor for particle deposition, and hence is deemed the main contributor to particle accumulation near the wall.
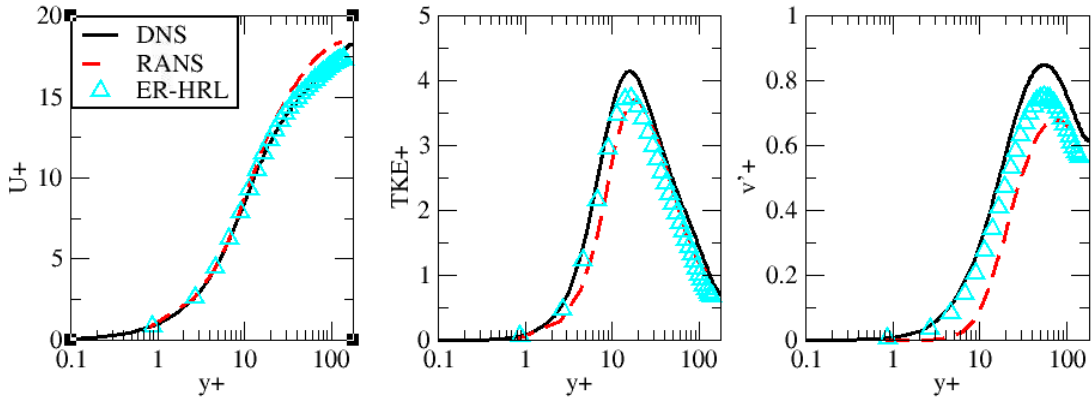
Figure 4.8 – Comparison of mean streamwise velocity profile (left), turbulent kinetic energy (middle), and wall-normal RMS velocity (right) for ER-HRL model against DNS data at Re_τ = 180. Black thick lines represent DNS from (Moser et al., 1999), red dashed-lines show pure RANS, while Cyan up-triangles are own data for ER-HRL model.

The most adequate meshes used in $Re_\tau = 590$ for both fluid and particle statistics are reported in Table 4.5. As shown in Fig. 4.11, the AWMLES model over-predicts the turbulent kinetic energy and misses up to almost 50 % of wall-normal RMS values in the near-wall region. On the other hand, the ER-HRL model shows a very good match with DNS data.
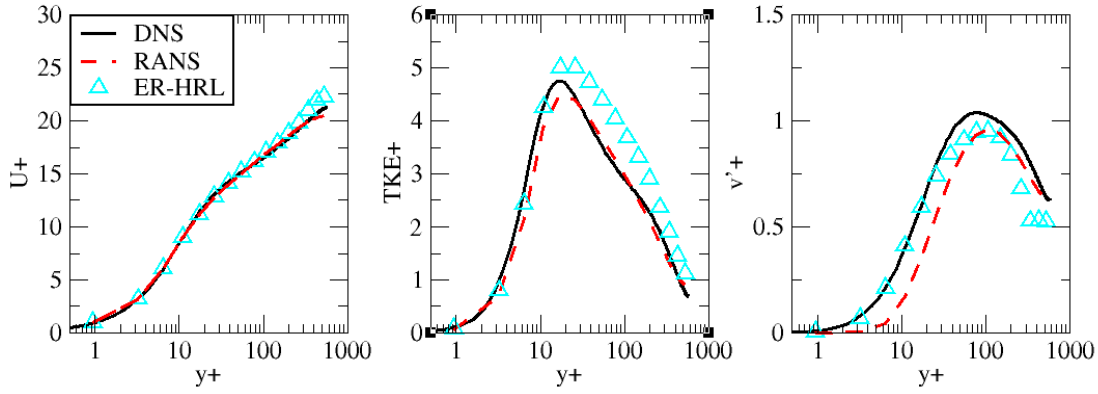
Figure 4.9 – Comparison of mean streamwise velocity profile (left), turbulent kinetic energy (middle), and wall-normal RMS velocity (right) for ER-HRL model against DNS data at $Re_\tau =$ 590. Black thick lines represent DNS from (Lee and Moser, 2015), red dashed-lines show pure RANS, while Cyan up-triangles are own data for ER-HRL model.
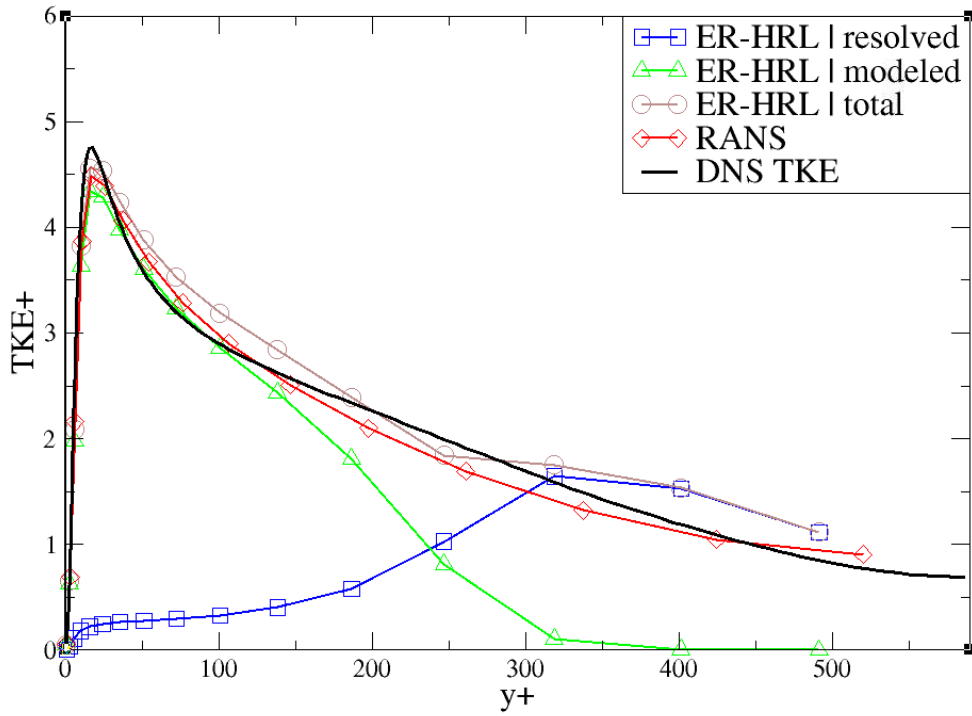
Figure 4.10 – Fluid flow turbulent kinetic energy split-up at $Re_\tau = 590$ normalized by friction velocity ($k/u_\tau{}^2$). Plots represent the resolved component from LES mode (blue squares), the modeled one resulting from the TKE transport equation while in RANS mode (green triangles), the total as a summation of both contributions (brown circles), pure RANS prediction (red diamonds), and DNS data from (Lee and Moser, 2015) is represented by black solid line
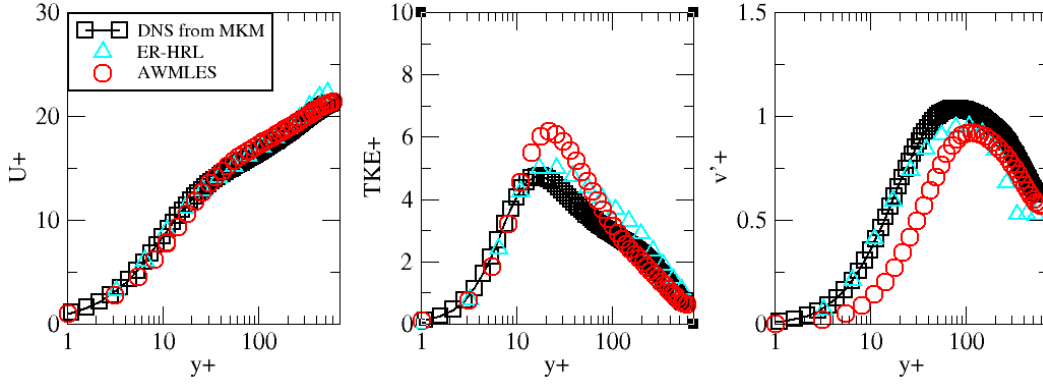
Figure 4.11 – Comparison of mean velocity profile (left), turbulent kinetic energy (middle), and wall normal rms velocity (right) for each of AWMLES and ER-HRL models against DNS data at $Re_\tau = 590$. Square symbol represents DNS from Lee and Moser, 2015, while Cyan up-triangles and red circles are own data for ER-HRL model and AWMLES respectively. Mesh used for each of AWMLES and ER-HRL models are indicated in Table 4.5

Table 4.5 – Grid resolutions for both ER-HRL and AWMLES particle simulations at $Re_\tau = 590$

Model	N_x	N_y	N_z	α	$D_x{}^+$	$D_y{}^+$	$D_z{}^+$	$N_{tot}x10^4$	$y_1{}^+$
ER-HRL	16	32	32	0.922	214.96	53.74	1.808 - 94.258	1.64	0.904
AWMLES	80	60	80	0.971	54.77	27.383	1.79 - 29.718	38.4	0.895

4.4.2 Particle Dispersion statistics

In this section, we show particle dispersion results for two Reynolds numbers i.e. $Re_\tau = 150$, 590. For each Reynolds number, we validate both hybrid RANS/LES models against DNS and well-resolved LES databases. Statistics were gathered for particles starting from t+ = 742 to t+ = 1192 for $Re_\tau = 150$ case, and from t+ = 1000 to t+ = 3000 for $Re_\tau = 590$ case (where t+ the ratio of physical time and fluid timescale i.e. t+ = t/τ_f). The starting time for initiating particle statistics is counted from the moment they were released in the domain. We analyzed the statistics for different swarm counts i.e. 20000, 50000, and 100000. It was found that there is no significant change in results when increasing particles count above 20000. Therefore, we report all the statistics in this study for only 20000 particles except for preferential concentration analyses where 10^5 particles were considered for each swarm. As seen from Table 4.2, it was ensured that Nyquist criterion (Marks, 1991) is fulfilled throughout the whole range of the particle timescales studied in this paper (i.e. dt $\leq \tau_p/2$). For this sake, the global fluid time step is divided into an integer number of particle time steps to match the stability criterion. In what follows, we provide quantitative and qualitative particle analyses for the above-mentioned two Reynolds numbers.

Low-turbulence flow ($Re_\tau = 150$)

At this Reynolds number, we report number density profiles, particle mean streamwise velocities, streamwise, spanwise, and wall-normal RMS velocity profiles by both ER-HRL and AWMLES models (Fig. 4.12 - 4.18). For particle central moment statistics, results match quite well the DNS data by Marchioli et al., 2007 for low and mid-inertia particles (Fig. 4.12 - 4.16). While in the case of very high inertia particles, it can be seen (Fig. 4.17) that RMS profiles deviate slightly from DNS data for both models. This is attributed to the fact that the particle timescale is too big to keep up with the instantaneous changes in the ever-decreasing turbulent motion scales near the wall (i.e. the dissipation range of energy cascade). This was reported by Picciotto et al., 2005; Rouson and Eaton, 2001. On the other hand, low-to-mid-inertia particles are more responsive to the dissipation scales near the wall, so their statistics match more closely to the DNS in which all scales of motion are fully resolved. It can also be seen from Fig. 4.12 - 4.17 that the mean streamwise velocity, in particular, is well captured for all particle sizes, while higher moment statistics deviate slightly from DNS data. This deviation becomes more pronounced when increasing particle inertia. However, particle statistics are deemed to be globally well predicted by both models at this Reynolds number.

As shown in Fig. 4.18, number density (i.e. particle concentration) profiles are reported to all particle sizes at two time instances. These concentration plots represent the instantaneous number densities divided by their initial values (n_o at $t^+ = 0$), and are denoted as "n_b" for simplicity. It should also be pointed out that at this Reynolds number, we used the baseline AWMLES and ER-HRL models without any SGS scheme. Data points are plotted starting from $y^+ = 0.86$ (i.e. y_1^+). It can be seen that predictions from both models are in good agreement with DNS profiles for all particle sizes. The preferential clustering of particles in the laminar sublayer where TKE is small is well reproduced (due to turbophoresis). This differential in particle dispersion rates is mainly driven by the sharp gradients of the flow turbulent intensity Caporaloni et al., 1975, which is caused by the no-slip and no-penetration conditions at the wall. Therefore, particles migrate from higher to lower turbulent intensity regions, yielding high concentration in the viscous sublayer Marchioli and Soldati, 2002; Sikovsky, 2014.

In the framework of the present study, it was shown in Sayed et al., 2021-b that the turbophoresis effect can be substantially suppressed by the coarseness of the employed grid. In that paper, turbophoresis effects on particles were investigated at the two shear Reynolds numbers $Re_\tau = 150, 590$. At low-turbulence level (i.e. $Re_\tau = 150$), it was confirmed that particles of mid-inertia i.e. St = 15 are the most responsive to the buffer layer turbulent intensity variations, clustering in the low TKE region (See Fig. 4.19). This is due to the comparable time scale of particles and the local fluid time scale causing particles to be more adaptive to near-wall turbulent structures. This finding was also observed by Nowbahar et al., 2013. On the other hand, small inertia particles remain instantaneously fully mixed in the domain, and act as fluid tracers (i.e. following the well-mixed criterion). These conclusions are also well documented in the DNS works of Marchioli and Soldati, 2002; Picciotto et al., 2005.
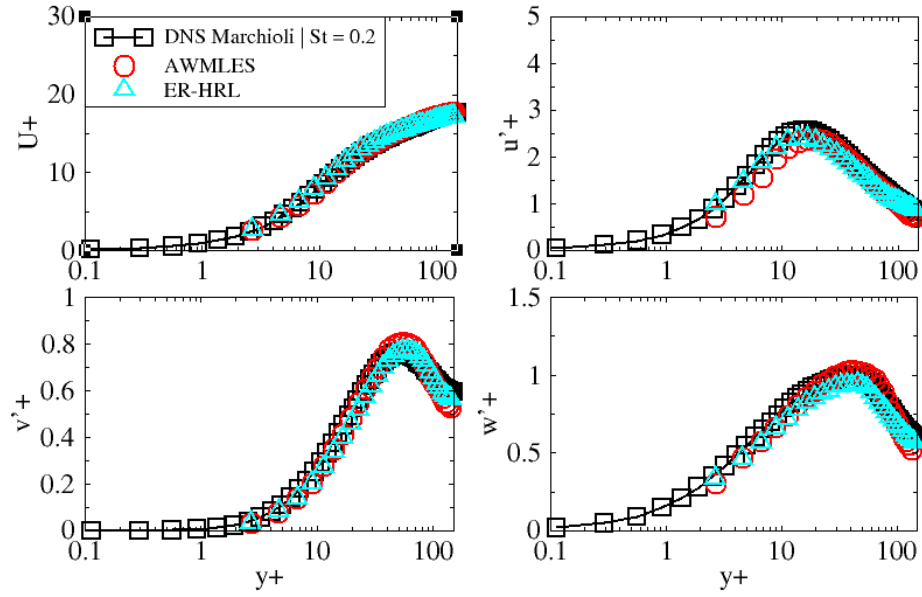
Figure 4.12 – Comparison between both AWMLES and ER-HRL models against DNS data from Marchioli et al., 2007 for mean velocity profiles, rms velocities for St = 0.2 over non-dimensional time span between t+=742 to t+=1192 at Re_τ = 150.
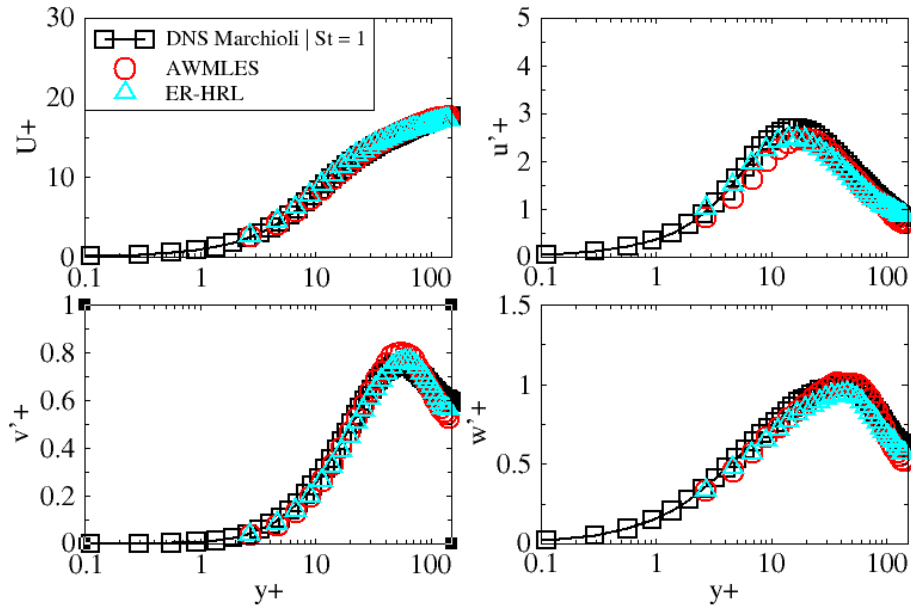
Figure 4.13 – Comparison between both AWMLES and ER-HRL models against DNS data from Marchioli et al., 2007 for mean velocity profiles, rms velocities for St = 1 over non-dimensional time span between t+=742 to t+=1192 at Re_τ = 150.
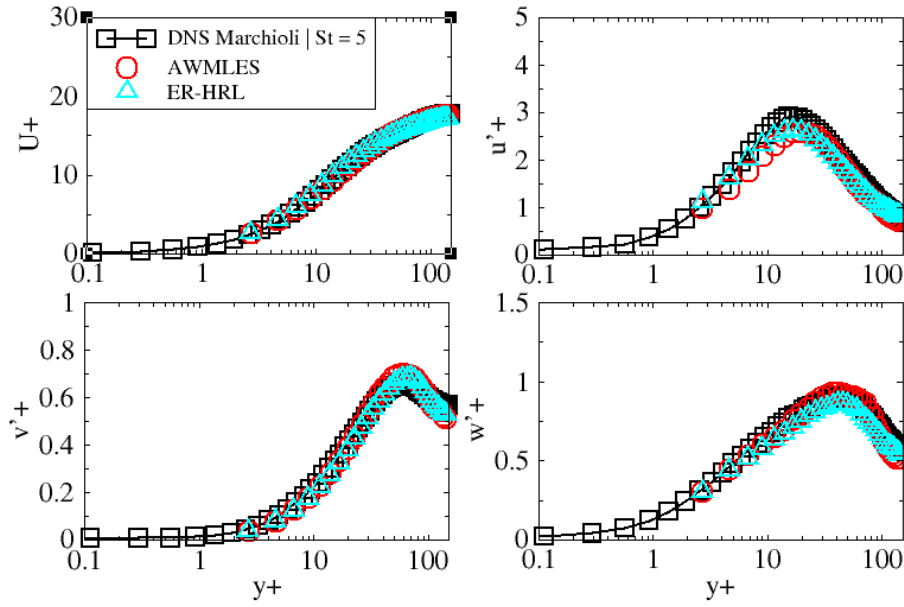
Figure 4.14 – Comparison between both AWMLES and ER-HRL models against DNS data from Marchioli et al., 2007 for mean velocity profiles, rms velocities for St = 5 over non-dimensional time span between t+=742 to t+=1192 at $Re_\tau = 150$.
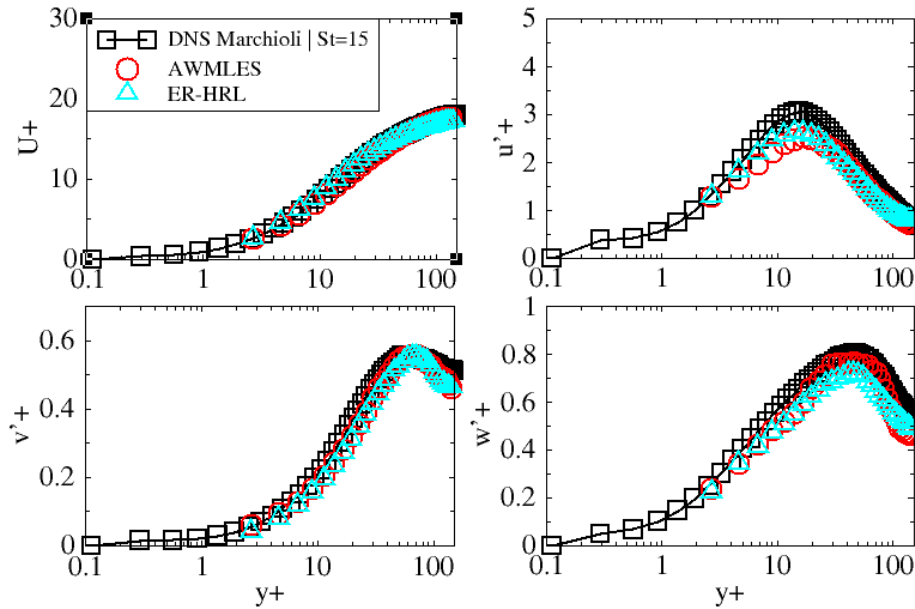
Figure 4.15 – Comparison between both AWMLES and ER-HRL models against DNS data from Marchioli et al., 2007 for mean velocity profiles, rms velocities for St = 15 over non-dimensional time span between t+=742 to t+=1192 at $Re_\tau = 150$.
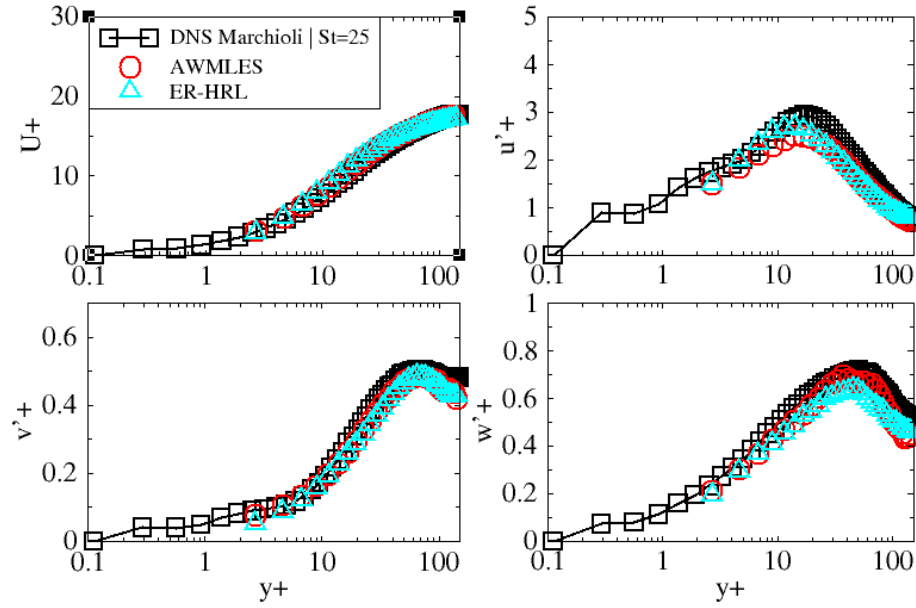
Figure 4.16 – Comparison between both AWMLES and ER-HRL models against DNS data from Marchioli et al., 2007 for mean velocity profiles, rms velocities for St = 25 over non-dimensional time span between t+=742 to t+=1192 at $Re_\tau = 150$.
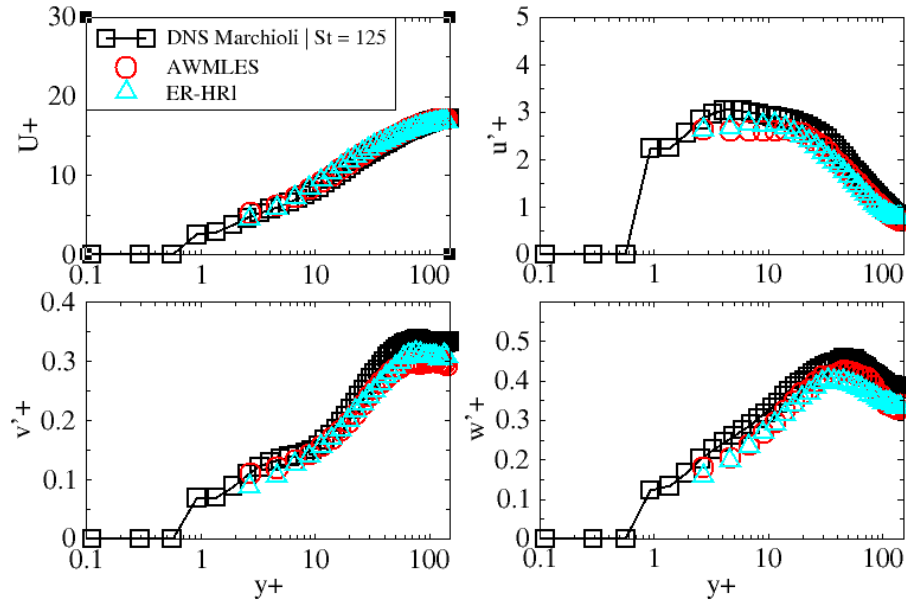
Figure 4.17 – Comparison between both AWMLES and ER-HRL models against DNS data from Marchioli et al., 2007 for mean velocity profiles, rms velocities for St = 125 over non-dimensional time span between t+=742 to t+=1192 at $Re_\tau = 150$.
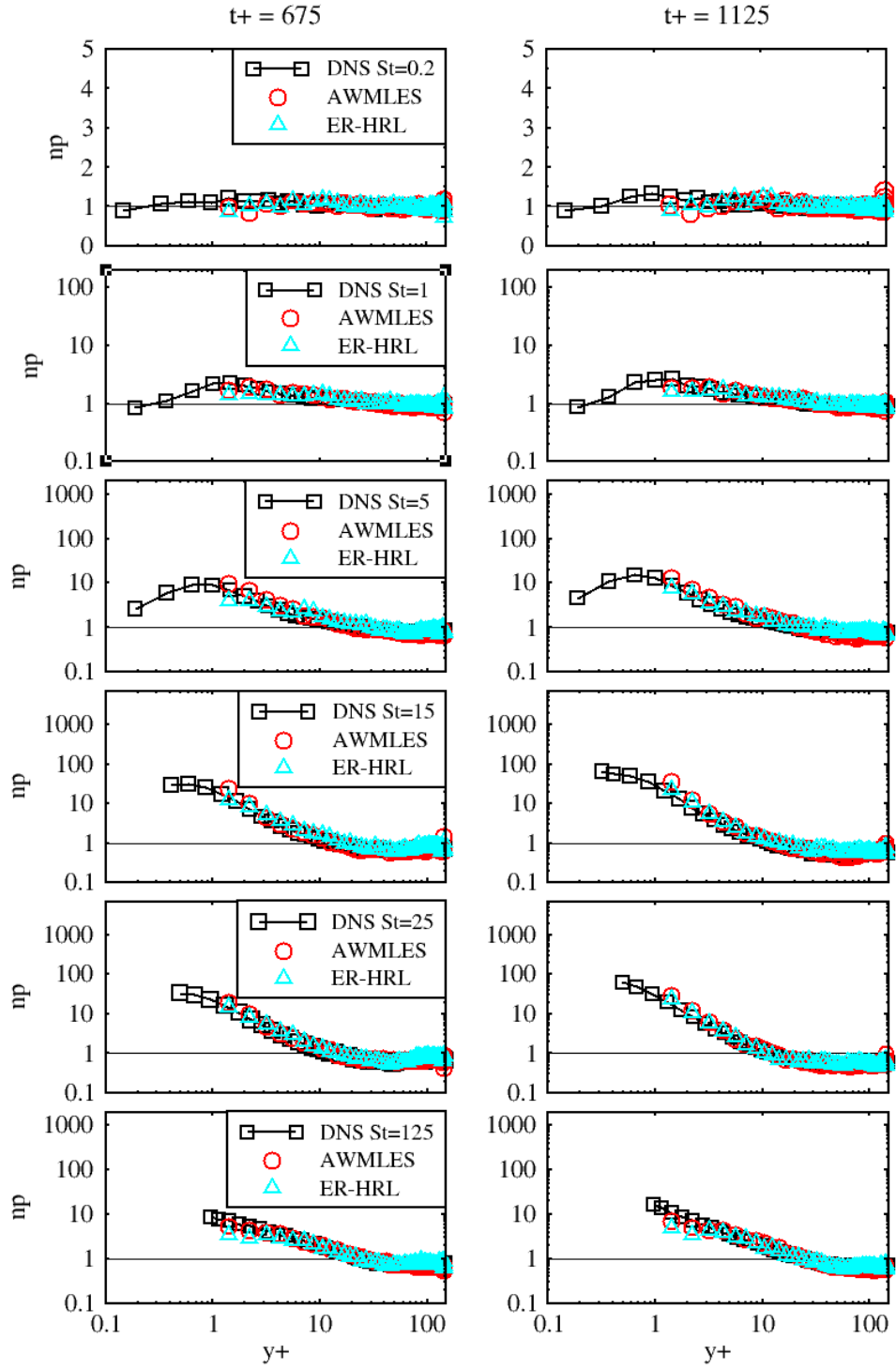
Figure 4.18 – Instantaneous particle number density, np, as a function of wall normal distance, y+ at $Re_\tau = 150$. Black diamonds represent DNS data from Marchioli et al., 2007 red circles represent own data by AWMLES model, while cyan up-triangles represent the profiles predicted by ER-HRL model. Counting was carried out in a non-cumulative fashion (i.e. particles are counted at each bin separately) though 64 bins across half of the channel height.
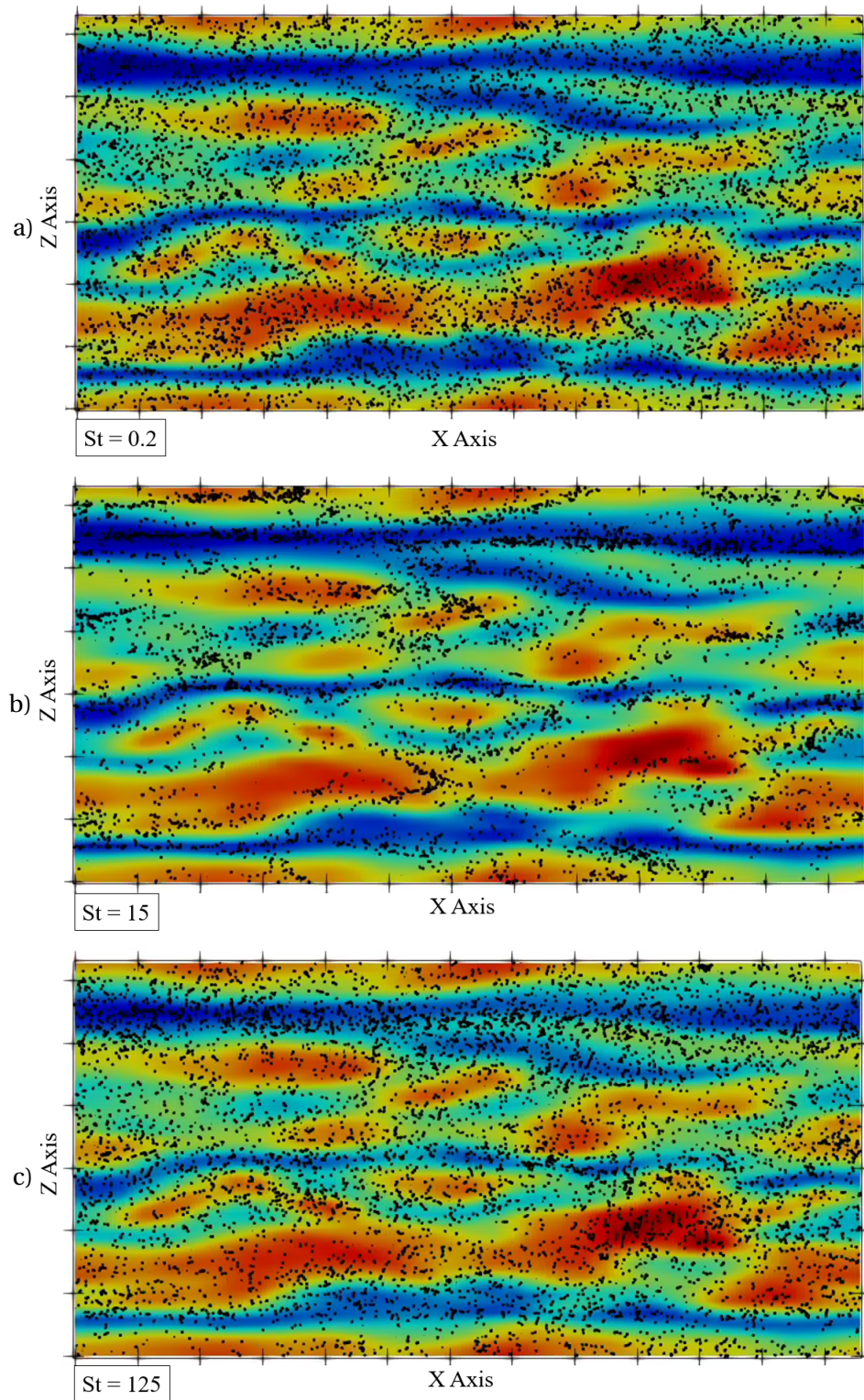
Figure 4.19 – Snapshot of a wall-parallel "x-z" plane at y+= 15 at Re_τ = 150. Black dots represent particles in the slab $15 \le y+ \le 30$ at different Stokes numbers i.e. a) St = 0.2, b) St = 15 and c) St = 125. The colors indicate the magnitude of the fluctuating stream-wise velocity component, red being highest and blue lowest. From Sayed et al., 2021-b, p.13

Moderate-turbulence flow ($Re_\tau = 590$)

To assess the SGS model prediction of particle dispersion, we increase shear Reynolds number to four times higher i.e. $Re_\tau = 590$. As was shown earlier in Figure 4.9, the model represents the flow statistics correctly using coarse grids (as in Table 4.5).

In the works of Zamansky et al., 2011, the authors adopted LES-SSAM (Subgrid Stochastic Acceleration Model) to account for the SGS effect of non-resolved flow acceleration in standard LES on particle dynamics (as proposed in Zamansky et al., 2010). The study was conducted in turbulent channel flow at $Re_\tau = 590$. The authors concluded that LES-SSAM gives a better prediction for particle mean velocity and RMS values than classical LES with no particle SGS model. We, therefore, compare our results to their LES-SSAM, classical LES, and DNS data to appraise our proposed ζ-SGS model.

In Figure 4.20, we show results for particle mean streamwise velocity for five non-dimensional particle timescales i.e. St = 1 - 125. Each profile is shifted by 10 units on the vertical axis for readability. Discrete phase statistics are gathered between t+=1000 and 2000. We also analyzed particle statistics for t+=3000, 4000. However, there was no significant difference compared to the results obtained at t+=2000. It can be seen that the mean streamwise velocity of low-to-mid inertia particles is better predicted by the ER-HRL model compared to the AWMLES at the wall region. Although the ER-HRL results match classical LES results at a much lower computational cost, profiles deviate slightly from LES-SSAM and DNS in the bulk region. This can be attributed to the strong streamwise acceleration variations experienced by particles. It is reported by Zamansky et al., 2011 that this effect is more pronounced for high-inertia particles, which agrees with our observation. The authors suggest that such an effect can be remedied by including the streamwise non-filtered velocity in the particle subgrid-scale model (ζ-SGS). In contrast, the AWMLES prediction matches the reference data more closely in the outer region of the boundary layer i.e. $y^+ > 30$. In the near-wall region, it is obvious that the AWMLES deviates from the correct behavior. The reason for this is that the effect of the missing SGS motions becomes more prominent on particles near the wall (since the particle is incapable of carrying the history of TKE as we go from mid to high inertia).

In Figure 4.21, we show results of particle wall-normal velocity fluctuations, v_p'. Five particle timescales are presented top to bottom from low to high inertia i.e. St = 1 - 125 shifted vertically by one unit. For low-to mid-inertia particles, profiles show better agreement with DNS data than all classical LES, LES-SSAM, and AWMLES models. However, for high-inertia particles i.e. St = 125, the filtering effect is more amplified for this velocity component. Consequently, a strong particle agitation in the channel may be noticed, especially away from the wall (where turbulence can be assumed isotropic and homogeneous). This results in the over-prediction of wall-normal RMS values for particle profiles as shown in the same Figure. It should be mentioned that the Fukagata et al., 2004 SGS model didn't significantly enhance the particle results comparatively with ζ-SGS model's contribution to the ER-HRL model. For this reason, it must be pointed out that the choice of particle SGS model is very crucial for higher Reynolds

numbers, especially when using such a coarse grid (as in Table 4.5). Unlike the Fukagata SGS model, ζ-SGS model is a very cost-effective approach. This can be illustrated by comparing the wall-normal RMS velocity prediction by the ER-HRL to the case where the ζ-SGS model is switched off. As an example, we show the effect of the ζ-SGS model wall-normal RMS values of particle statistics at Stokes number St = 1 (Figure 4.22). It can be seen that the SGS model accounts for the majority of the wall-normal RMS velocity component, especially in the near-wall region where the resolved scales are almost non-existing.

Referring to particle preferential concentrations mentioned in the previous section, a similar qualitative analysis was done by (Sayed et al., 2021-b) at Re_τ = 590. High inertia particles (i.e. St=125) were observed to accumulate the most at low RMS velocity regions. For low to mid inertia particles (St = 0.2-15), it can be noticed that particles are centrifuged out of high-TKE to low-TKE near-wall regions. It is obvious that low inertia particles i.e. St=0.2 do not behave as fluid particles - deviating from the well-mixed criterion. Instead, they cluster in aggregate patterns. This obviously departs from the expected physical behavior. As shown in Fig. 4.23, it was reported that the ER-HRL model fails to reproduce the expected behavior for the instantaneous particle concentrations. It was argued in the LES literature that such feature is due to the much coarser grids used compared to the Kolmogorov spatial scales. Given that our hybrid model is designed to perform better with very low mesh counts, it was concluded that it inherently cannot predict fine details such as instantaneous preferential particle concentrations at higher Reynolds numbers.

In their LES simulations at Re_τ = 644, Q. Wang and Squires, 1998 reported a similar observation and argued that the cause for this discrepancy can be attributed to the coarse grid size used in the computation. At the higher Reynolds number, the range of motion scales is wider. Therefore, particular attention should be given to the grid cell size to accurately predict particle preferential concentration. In this light, using much coarser grids relative to the Kolmogorov length scale in the experiments and DNS will affect particle clustering substantially.

Our hybrid modeling framework of the ER-HRL method is specifically designed to significantly reduce mesh density compared to LES while being able to accurately compute particle deposition rates (velocity and RMS of velocity). Therefore, increasing mesh density towards the Kolmogorov spatial scales is not warranted nor justified in our approach. As a result, one has to accept that within the bounds of the modeling strategy used here, gaining more detailed information such as instantaneous preferential concentration is not possible for the higher Reynolds numbers. Another argument put forth by Zamansky et al., 2010 is the missing SGS streamwise component of velocity in our particle SGS model, which was shown to have an important effect on particle transport. This can be remedied by additional modeling, but the more important argument of the grid coarseness cannot be corrected without jeopardizing the aim of our modeling strategy, which is to use mesh counts that are comparable to those of a RANS calculation.
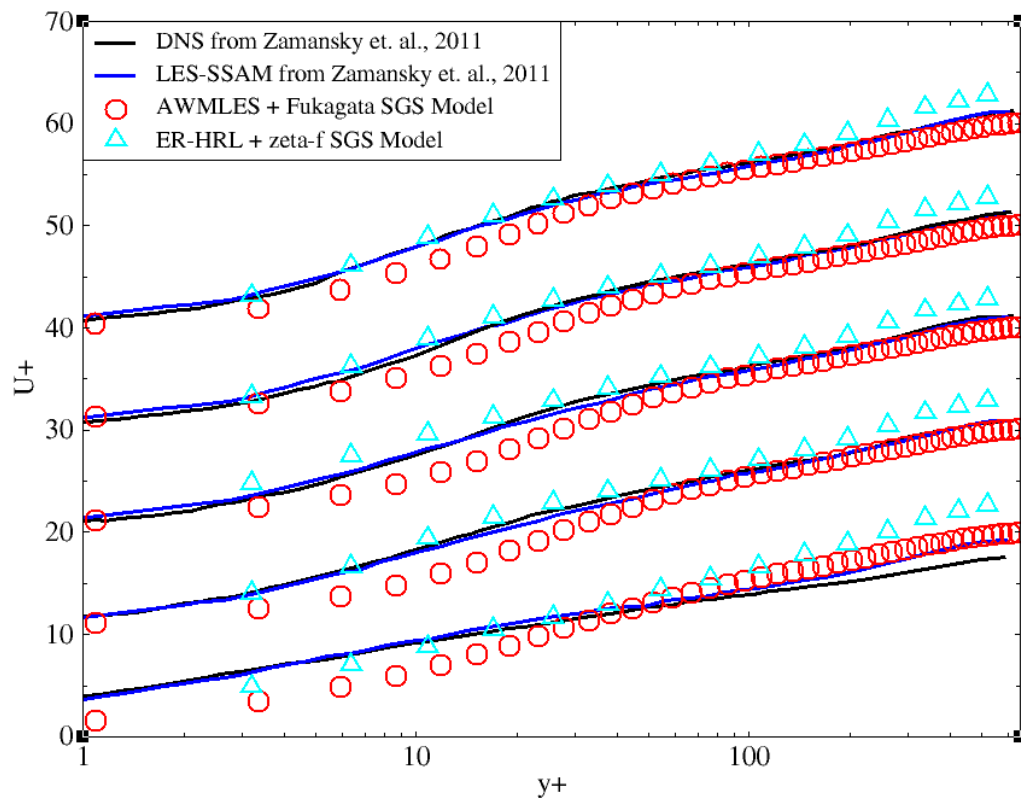
Figure 4.20 – Comparison for particle mean sreamwise velocity profiles at Stokes numbers St=1, 5, 15, 25, 125 from top to bottom. Black lines represent DNS data, blue lines represent LES-SSAM model, red circles represent AWMLES model with SGS Fukagata model and cyan up-triangles represent ER-HRL with ζ-SGS model.
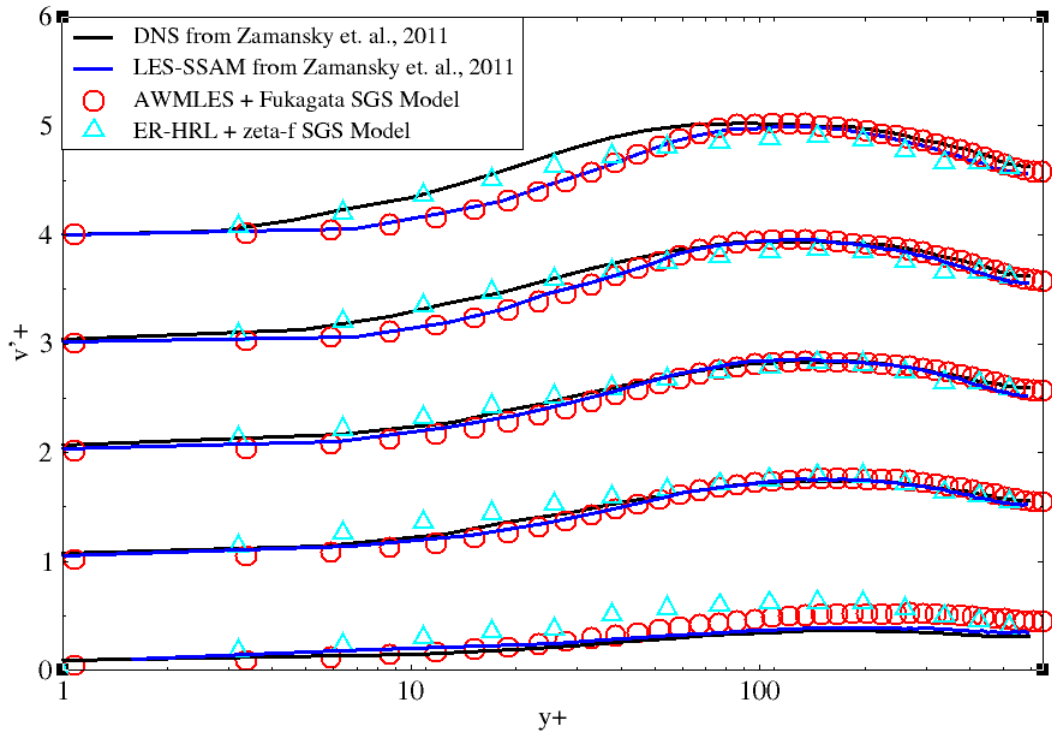
Figure 4.21 – Comparison for particle wall-normal rms velocity profiles at Stokes numbers St=1, 5, 15, 25, 125 from top to bottom. Black lines represent DNS data, blue lines represent LES-SSAM model, red circles represent AWMLES model with SGS Fukagata model and cyan up-triangles represent ER-HRL with ζ-SGS model.
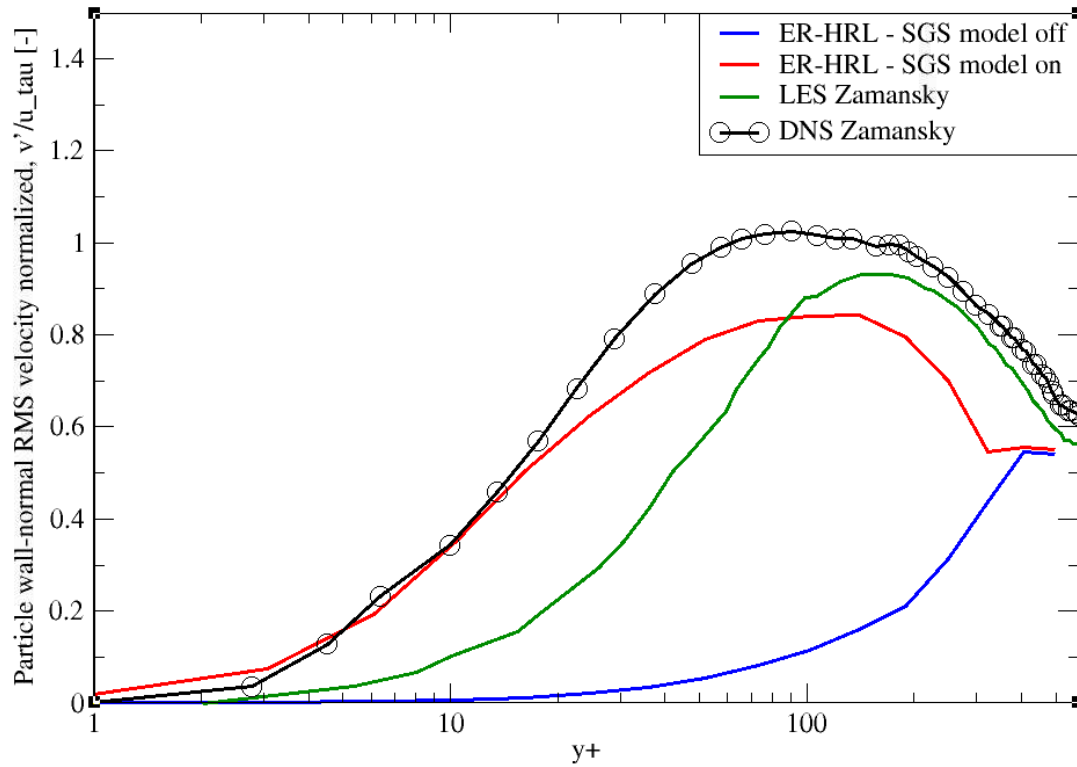
Figure 4.22 – Comparison for particle wall-normal RMS velocity profiles at St = 1. Black line with circles represents DNS data, green line refer to the classical LES, red and blue lines represent the ER-HRL model prediction with the ζ-SGS model switched on and off respectively.
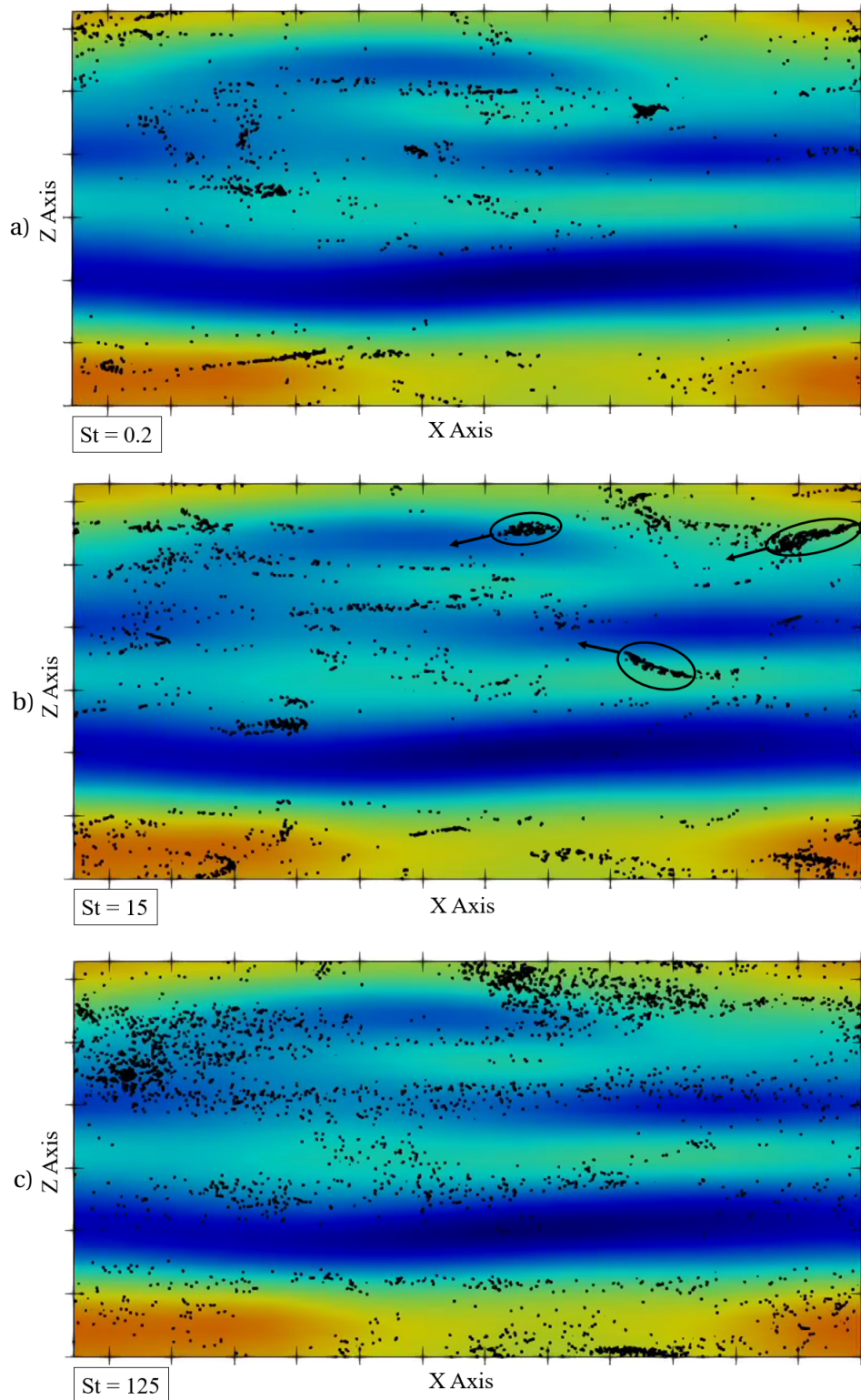
Figure 4.23 – Snapshot of a wall-parallel "x-z" plane at y+= 15 at Re_τ = 590. Black dots represent particles in the slab $15 \le y+ \le 30$ at different Stokes numbers i.e. a) St = 0.2, b) St = 15 and c) St = 125. The colors indicate the magnitude of the fluctuating stream-wise velocity component, red being highest and blue lowest. From Sayed et al., 2021-b, p.14

4.5 Conclusions

Particulate channel flow has been investigated using two hybrid RANS/LES models: AWMLES and ER-HRL. Results are reported at two shear Reynolds numbers i.e. $Re_\tau = 150, 590$. To assess each model, predictions of the primary (carrier) flow were first computed at both Reynolds numbers. All of the mean streamwise velocity profiles, TKE, and wall-normal RMS values were compared against reference LES and DNS data. To reveal the wall modeling of the ER-HRL approach, in particular, predictions were compared to ones obtained by its RANS component i.e. the $(k - \epsilon - \zeta - F)$ model. Turbulent statistics obtained by the ER-HRL were shown to exhibit better convergence than the AWMLES model to the reference DNS data at a much lower computational cost than conventional LES. In addition, it was noted that the wall-normal RMS velocity is better predicted by the ER-HRL model compared to pure RANS using the same mesh, especially in the near-wall region.

The novel particle ζ-SGS model was tested versus the AWMLES complemented by the Fukagata SGS model (Fukagata et al., 2004). The new model is based on the wall-normal transport equation (ζ) which is mainly activated in the RANS region. The ζ-SGS model accounts for the most dominant subgrid motion scales by retrieving the non-filtered velocity field in the wall-normal direction through turbulent kinetic energy and the wall-normal velocity variance. This very component is most influential on particle deposition rates on the wall. The model prediction of particle statistics was investigated alongside the AWMLES with the Fukagata SGS model. Both models were validated against DNS data for a wide range of particle inertia i.e. St= 0.2, 1, 5, 15, 25, 125. For each particle timescale, first and second-moment statistics, as well as number density profiles, were reported.

The obtained particle statistics at low turbulence level ($Re_\tau = 150$) from both models are in excellent agreement with DNS data. For the moderate Reynolds number case ($Re_\tau = 590$), results were compared to LES with subgrid stochastic acceleration model (LES-SSAM) as well as DNS from Zamansky et al., 2011. It was shown that the ER-HRL with ζ-SGS model is superior to both AWMLES with Fukagata SGS model and LES-SSAM. This is rather more obvious in particle wall-normal RMS values at low-to-mid inertia particles in the wall region. The present investigation shows that for low to mid-inertia particles, the ER-HRL model gives a very good agreement with classical LES, yet at a much lower CPU cost. However, very high inertia particles (St=125) show some deviation from LES-SSAM and DNS data, especially in the wall-normal RMS profile. The author suggests that such an effect could be remedied by correcting for the Stokes number filtering in further works. In addition, it was shown that the AWMLES model supplemented with the Fukagata SGS model matched more closely the reference data in the outer region of the boundary layer. We conclude that the contribution of the subgrid-scale model is very significant at higher Reynolds numbers, especially on coarse grids.

The findings of this study will serve as a new platform for studying dispersed flows at a lower computational cost, and an accurate open-source database against which researchers in hybrid RANS/LES multiphase flow can validate their models. After a global analysis of 24 swarms of 10^5 particles each, we conclude that the ER-HRL model is very robust and cost-effective for studying particle dispersion. It should be also emphasized that the ER-HRL model is capable of accurately recovering turbulent kinetic energy at even higher Reynolds numbers with coarse grids Sayed et al., 2020. On that account, it will be used to address more complex dispersed flows in the next chapters of the present project.

5 | Differentially Heated Cavity
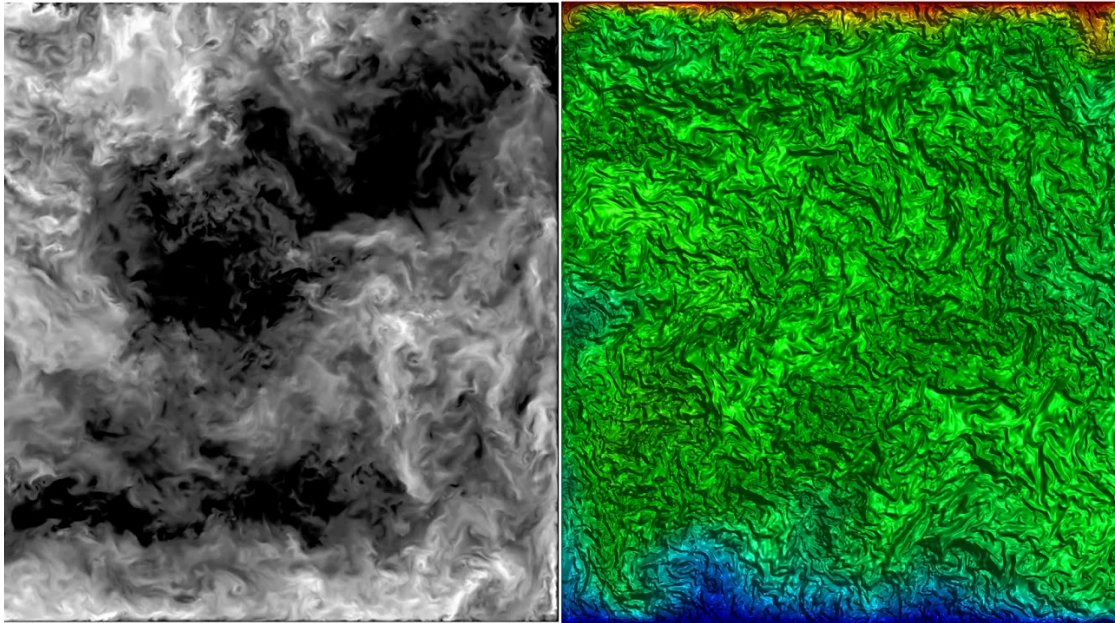
Figure 5.1 – Natural convection due to thermal stratification in a differentially heated cavity. Picture is taken from: *F. Xavier TRias*.

5.1 Overview

Particle dispersion and deposition in enclosures is of a big importance in myriad of applications. Some of these are medical, environmental and industrial. Therefore, it is vital to develop a credible tool to predict the behaviour of such particulate flows, their dispersion statistics and deposition rates.

Motivated by investigating a feasible modeling strategy for particulate flows in complex 3D flows, the dispersed flow inside a differentially heated cavity is investigated. The main focus of this chapter is the response of the subgrid-scale models and their ability to predict the particulate flow in the differentially heated 3D cavity when the mesh resolution is coarse and below optimal LES standards. As URANS and hybrid RANS-LES models fail to reproduce the flow accurately due to difficulty to model subtle physical mechanisms such as laminarization and three-dimensional effects, the alternative is LES applied on a coarse mesh.

This chapter is organized in two sections; the first part is dedicated to the investigation of Sub-Grid Scale (SGS) model influence on flow prediction using Coarse Large Eddy Simulation (CLES). The widely used sub-grid scale models namely the standard and the dynamic Smagorinsky models were tested in a simulation of the flow in a differentially heated 3D cavity at turbulent Rayleigh number $Ra = 10^9$. The cubical cavity of 0.7m side-length is set to have a temperature difference of 39 K between the two facing cold and hot vertical walls. Measured temperature profiles by the DIANA (DIfferentially heated cavity with Aerosol in turbulent NAtural convection) experiment (Kalilainen et al., 2016) for both the top and bottom walls were imposed as Dirichlet boundary conditions to implicitly account for wall-to-wall radiation effects. In the second part, the model with the better performance is used to study particle depletion (total wall-deposition) rates under the influence of gravity, Stokes drag and thermophoresis. Results of both the continuous and dispersed phases are compared in qualitative and quantitative manners to the reference well-resolved LES and experimental databases (Dehbi et al., 2017; Kalilainen et al., 2016).

5.2 Introduction

Particle transport in closed spaces is crucial for many engineering, medical and environmental applications, from flow inside hospital rooms and the transport of air-borne pollutants in clean rooms to radioactive particulate flows in nuclear plants and aircraft-related applications Jones and Kissane, 2000; Kam et al., 1998; Morrison et al., 2006; Poussou et al., 2010; Wana et al., 2007. Having a reliable design-based tool for predicting such flows can significantly improve the process of prototype-based analyses. A typical example is thermally-driven flow in a parallelepiped cavity. Such configuration is referred to as a Differentially Heated Cavity (DHC), where two opposite vertical walls are kept at two different temperatures and the rest of the walls are adiabatically insulated. Over the last few decades, numerous studies have investigated the DHC flow both numerically and experimentally (Ampofo and Karayiannis, 2003; Baïri

et al., 2007; Bejan, 1995; Betts and Bokhari, 2000; Briggs and Jones, 1985; Colomer et al., 2004; De Vahl Davis, 1968; Frederick and Valencia, 1989; Mallinson and De Wahl Davis, 1977; Mergui and Penot, 1996; Nansteel and Grief, 1984; Salat et al., 2004; Y. Tian and Karayiannis, 2000a, 2000b; Trias et al., 2010a, 2010b; Trias et al., 2007; Xin and Le Quéré, 1995). In particular, the first numerical simulation of flow inside a DHC dates back to 1968, when De Vahl Davis, 1968 conducted a study on 2D square cavities with laminar flow. With the growth of computer power, researchers endeavor 2D and 3D simulations/computations of turbulent flows inside DHC with moderate to high Rayleigh numbers with both Large Eddy Simulation (LES) and Direct Numerical Simulation (DNS), Bosshard et al., 2013; Kim et al., 2018; Puragliesi, 2010; Sebilleau et al., 2018; Trias et al., 2007 among others. Currently, the DHC serves as one of the main CFD benchmarks to validate models for internal turbulent buoyancy-driven flows.

To properly predict particle dispersion, the underlying carrier flow must be well-predicted. Despite being a simple geometry, DHC poses a big challenge for CFD models to accurately capture the flow behavior in a 3D turbulent regime. The main challenge for both the unsteady RANS and hybrid RANS-LES models is the simultaneous existence of both laminar and turbulent regions and the underlying transition from laminar to turbulent flow. It is known that eddy-viscosity-based turbulence models cannot capture laminar-turbulence transition accurately due to simplified strain-stress relation. Another disadvantage of the RANS approach is the requirement of complicated stochastic models for particles that are needed to take the effect of turbulence into account. For this sake, LES stands as a common tool for simulating the flow inside 3D cavities. However, to properly resolve the boundary layer, LES has stringent resolution requirements that scale with powers of the Grashof number (Benjamin and François, 2017).

The hybrid LES/RANS models emerge as a promising alternative. The RANS-LES approach activates RANS mode near the wall – tolerating much coarser meshes near the wall – while LES is deployed when cell size is sufficient to resolve local motion scales in the far-wall region. In this light, Abramov and Smirnov, 2006 studied the square cavity at a Rayleigh number of 1.58 x 10^9 using Detached Eddy Simulation (DES) based on the one-equation model for the turbulent kinetic energy (TKE) transport. It was found in this study that although the mean flow was reasonably represented, the flow was poorly predicted in the near-wall region. Recently, Ali et al., 2021 proposed a dual-mesh hybrid RANS-LES approach to DHC. The idea behind this approach is to use two overlapping computational domains, one for LES mode and the other to solve RANS equations. The main motivation was to avoid a mismatch between LES and RANS at the interface when a single mesh is used. It was reported that this approach yields a satisfactory accuracy in comparison with standard LES or RANS tested within the same study. The obvious disadvantage is the need to compute both LES and RANS for a single case.

In both works, (Abramov and Smirnov, 2006; Ali et al., 2021), periodic boundary condition was imposed in the depth direction, implying an infinitely long domain. Two configurations: one with solid boundaries (same set up used in this publication) and another with periodic boundaries in the depth direction implying an infinitely long domain, which helps to sustain

the modeled energy. Each of those configurations produces a very different outcome when the hybrid LES/RANS method is used. In this context, the hybrid LES/RANS approach results in a zero modelled energy when applied to the flow in the domain surrounded by solid walls, reducing the simulation to a coarse DNS. This is not the case when the periodicity is imposed in the depth direction. The main reason is that the two configurations produce different turbulent time and length scales, and the wall blocking effect is more significant for the domain surrounded by solid boundaries. These differences lead to a different performance of the hybrid LES/RANS approach which is most likely linked to the different levels of the modelled turbulent kinetic energy production in the near-wall region.

In this chapter, the two commonly used LES subgrid-scale models i.e. the standard and dynamic Smagorinsky models are employed, but on a mesh whose resolution is coarser than generally accepted LES standards (hereinafter: Coarse LES (CLES)). As will be shown below, at first the flow field is extensively investigated through both qualitative and quantitative results. The aim is to assess the SGS-model influence on the main flow central moments (Eulerian statistics) and therefore investigate the feasibility of LES simulations for particulate DHC flows when a mesh resolution is coarse.

In view of particulate flows in closed cavities, only a few studies have investigated particle tracking in DHC. Some of these studies focused on laminar flow like the work of Akbar et al., 2009 who reported the dispersion of particles of diameter 50 nm to 1 μm. In another study Bagheri et al., 2012, particle motion was investigated in a 2D DHC cavity flow at a Rayleigh number up to 10^8. In a turbulent flow regime, both of Puragliesi et al., 2011 and Bosshard et al., 2014 have studied particle transport at Ra = 10^9 using pseudo-spectral DNS and spectral-element LES codes respectively alongside Lagrangian Particle Tracking (LPT). As a result of the massive CPU requirement, the smallest particle considered in these simulations had 10 μm in diameter – which is relatively large for most of relevant engineering applications. To the best of our knowledge, the only experimental investigation that provides extensive details for both carrier flow and particle dispersion is the one conducted by Kalilainen et al., 2016. As will be shown later, this experimental data will be used in the exhaustive validation of the primary flow statistics as well as the discrete phase dynamics. Following that study, well-resolved LES was used in the work of Dehbi et al., 2017 to predict particle deposition rates for the range of aerodynamic diameters d_p = 0.5 - 10 μm. In accordance, we use this LES database as a reference for our predictions.

In this light and due to a better model performance, the dynamic Smagorinsky subgrid-scale (SGS) model was employed in a second step of particle tracking. In systematic fashion, six swarms of different particles sizes were computed using the accurately predicted Eulerian statistics once a fully developed flow was reached. Point particles are treated as solid spherical elements in a one-way coupling with the primary flow field, where: gravity, Stokes drag and thermophoretic forces where considered. In a quantitative fashion, temporally-local particle concentration histories of small-to-medium inertia particles (i.e. d_p= 1.4 – 3.5 μm) were compared to LES and experimental databases. The simple "stirred settling" model was used

as a reference for the depletion rates of high inertia particles (i.e. d_p= 5 – 14 μm).

The rest of the chapter is arranged as follows: in Section 5.3, the numerical setup and thermal boundary conditions are reported. In Section 5.4, results of both fluid flow and discrete phase are reported and finally in Section 5.5, we give a summary and future recommendations for this benchmark.

5.3   Numerical setup

A cubical cavity (x: horizontal, y: depth, z: vertical) with a side length of 0.7m is considered where all walls are set to the no-slip boundary condition. The flow inside the cavity is buoyancy-driven whereby the vertical walls are held at two different temperatures with ΔT=39.18 to have a Rayleigh number of Ra = 10^9. As in the fine LES study by Dehbi et al., 2017, the front and back walls were set to adiabatic (passive) walls in all studied cases. Reference temperature ($T_{ref} = \frac{T_H - T_C}{2}$) and mass density of fluid flow were set to 292.74 K and 1 kg/m^3 respectively. The used physical properties used for air are reported in Table 5.2.

As reported in the literature, it is crucial to account for wall-to-wall radiation (between the bottom and top walls) Ali et al., 2021; Ibrahim et al., 2013; Sergent, Joubert, et al., 2013; Sergent, Xin, et al., 2013; Xin et al., 2013. We therefore implicitly account for such effect by imposing the measured temperature profiles from the experiment as Dirichlet boundary conditions as suggested by Dehbi et al., 2017. It should be pointed out that in that publication, authors used the Dynamic Kinetic Energy SGS model which solves one additional equation for modeling the SGS TKE, and preserves the history of the unresolved motion scales.

To examine each of the SGS models in a quantitative fashion, flow first and second-order statistics i.e. mean and RMS velocity profiles as well as mean temperature profiles at different locations across the cavity are reported. Results are compared against reference LES predictions by Dehbi et al., 2017 and experimental measurements by Kalilainen et al., 2016. In particular, the high-quality particle image velocimetry (PIV) experimental measurements produced by Kalilainen made it possible to quantitatively validate the obtained results. In a qualitative manner, the main characteristics of the flow circulation at the cavity corners – where the flow is turbulent, as well as other flow coherent structures are shown.

As schematized in Fig. 5.2, the left vertical wall (x = 0) is assigned to be the hot wall (at temperature T = 330.54K), while the cold wall is at x = 0.7m (with T = 291.36K). For turbulent heat flux calculation, the standard values in both Fluent and T-Flows of the turbulent Prandtl number were used (i.e. Pr_t = 0.85, 0.91 respectively). It was mentioned by Kalilainen et al., 2016 that the isothermal walls in DIANA experiment was carried out within 0.4K uncertainty margin. Also, due care was taken to reduce heat losses from passive walls to the surroundings - for which limit, the adiabatic wall assumption can still hold. To implicitly emulate wall-to-wall radiation effects, we set the temperature of bottom and top walls independently of the spanwise direction (y-axis). This is done by imposing the measured temperature profiles (from

the DIANA experiment) as Dirichlet boundary conditions on the horizontal walls as in Fig. 5.3. This set of boundary conditions are called Intermediate Realistic Conditions (IRC) as first coined by Xin et al., 2013. In that study, the authors showed that IRCs represent the right physics of the turbulent flow field in the DHC.
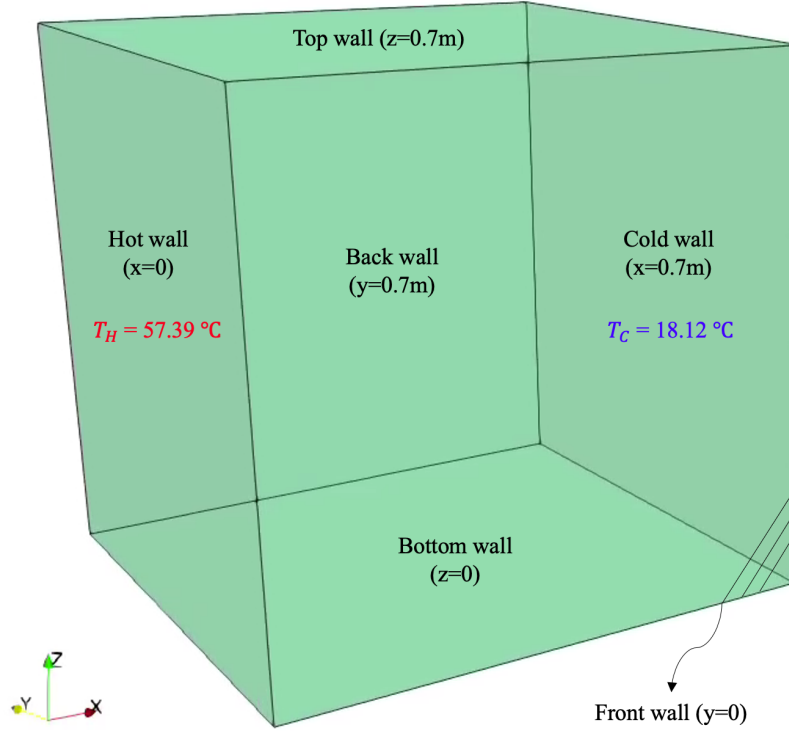
Figure 5.2 – Schematic of the cubical cavity indicating the flow-driving boundary conditions as well as the insulating walls

As indicated in Table 5.1, the fluid parameters used for all simulations are fixed. For pressure momentum coupling, we use the SIMPLE scheme and for time integration, we use the parabolic scheme. The central differencing scheme was used for the momentum equation while the SMART scheme was used for the energy equation. The turbulent heat flux model has been set to the Simple Gradient Diffusion Hypothesis (SGDH). It should be noted that for Fluent solutions below reported in this Chapter, the Bounded Central Differencing (BCD) scheme was used for the momentum equation while the second order upwind scheme was used for the energy equation. This is the recommended and default setup by ANSYS Fluent as it provides the least dissipative solution providing the highest resolution accuracy for the smallest scales.

Once a statistically-stationary flow is reached, particles are initially distributed in random positions covering the whole domain Fig. 5.4, and released from rest. Since we are aiming at the collective behavior of particle dispersion, we track particles under simplified conditions
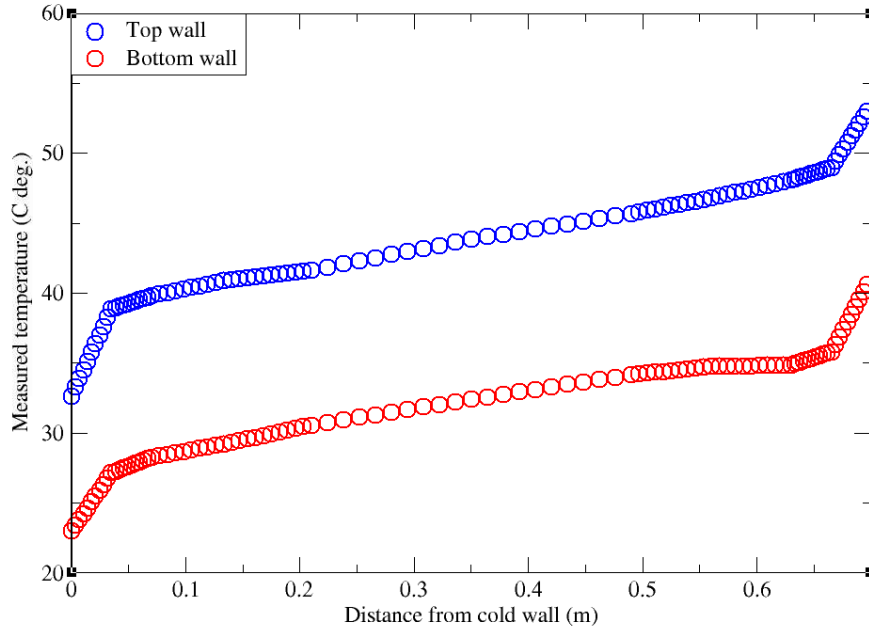
Figure 5.3 – Measured temperature profiles for bottom and top walls from the experiment Kalilainen et al., 2016

in which particle size and concentration are small enough to assume very dilute flow. This implies that particle-particle collision is neglected, and that particle has no feedback on the carrier fluid. As shown in Table 5.1 below, six sets of mono-dispersed silica (SiO_2) particles with Aerodynamic Mean Mass Diameter (AMMD) of 1.4 – 14 μm were considered where physical particle density is 2000 kg/m^3. Particle inertia is usually characterized by Stokes number which is defined as the ratio of particle relaxation time to the fluid time scale (Eq. 5.1).

$$St = \frac{\tau_p}{\tau_f} \tag{5.1}$$

where particle timescale (relaxation time) τ_p is defined as:

$$\tau_p = \frac{C_c \rho_p d_p^2}{18\mu} \tag{5.2}$$

Above, C_c is the Cunningham slip-correction factor which is calculated as follows:

$$C_c = 1 + \frac{\lambda}{d_p}\left(2.34 + 1.05 exp\left[-0.39\frac{d_p}{\lambda}\right]\right) \tag{5.3}$$
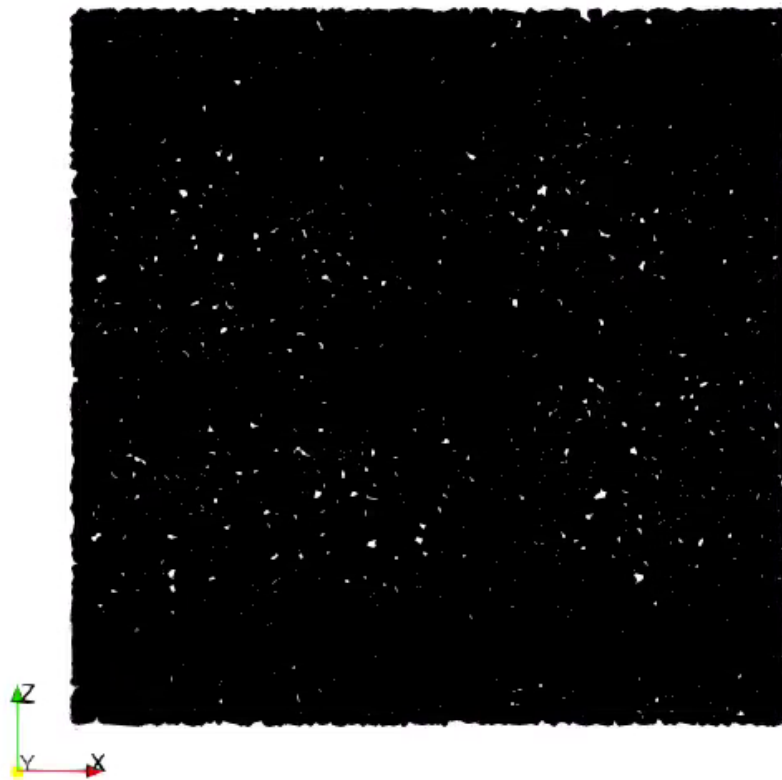
Figure 5.4 – Visualisation of randomly distributed particles at t = 0. Sample size is 50,000 particles

Table 5.1 – Input values for fluid parameters

d_p [μm]	D_{AMMD} [μm]	C_c [-]	τ_p (10^{-5}) [s]	St (10^{-5}) [-]	V_{TS} (10^{-5}) [m/s]	Δt_p (10^{-5}) [s]
0.35	0.5	1.466	0.11	0.18	1.08	0.2
1.0	1.4	1.155	0.72	1.17	7.06	1.0
2.5	3.54	1.062	4.12	6.7	40.42	2.0
3.54	5.0	1.044	8.12	13.21	79.68	3.0
6.0	8.49	1.026	22.94	37.3	225.04	6.0
8.0	11.31	1.019	40.50	65.86	397.31	8.0
10.0	14.14	1.015	63.04	102.5	618.42	10.0

Table 5.2 – Input values for fluid parameters

Variable	ρ	λ	β	ν	c_p
Values	1.0	2.434 x 10 $-$ 5	0.00319	1.728 x 10 $-$ 5	1.0

To achieve time-accurate solution for particle motion, the particle time step (Δt_p) must be of the same order of magnitude as particle time scale. For this sake, a pre-defined value for sub time steps is assigned for each particle size so that particle time step can fill in the flow (global) time step. As a result, particle time step for sub-micro particles becomes very tiny, and hence, only few time realizations could be obtained for smaller particles i.e. d_p = 0.35 μm. As seen from Table 5.1, T-Flows was set to make the necessary adjustments so particle time step stays $\leq$ ($\tau_p/2$).

In Fluent case, we used the range of particle sizes d_p = 1.0 - 14.14 μm - clipping out the sub-micron particle size to avoid extensive CPU run time. The time integration was performed by the so-called Automatic Tracking Scheme Algorithm (ATSA) which, for computational efficiency alternates between the first order implicit Euler scheme to the second order Trapezoidal scheme, depending on the local fluid dynamics. An embedded error function tracing particle trajectory is enforced, such that particle time step is sufficiently reduced until the predicted error in the trajectory drops below a certain tolerance. To guarantee a time-accurate solution for particles, this tolerance is set to a very low value of 10^{-7} m, which is 100 times smaller than the smallest particle diameters considered (d_p 1.4 μm) as shown in Table 5.1.

Although the flow is quite turbulent, typical velocities are small (not exceeding a few tens of cm/s), so that particles will be assumed to be removed from the fluid stream upon impact with the walls. For this, all walls were assumed to be perfectly absorbing. Once the particle center of mass is past the wall closest cell center, it is considered deposited and removed automatically from the domain.

LES is a transient approach whose solution depends on the grid employed. For this reason, one should only seek grid sensitivity in terms of turbulent statistics predictions. As mentioned by Pope, 2000, a mesh that captures 80% of the total turbulent kinetic energy (TKE) is deemed sufficient for a well-resolved LES. In the works of Dehbi et al., 2017, it was shown that a 2.4

Table 5.3 – Meshes used for grid-sensitivity test

Index	N_x	N_y	N_z	N_{tot}	α	y_1	y_1^+	$max(\Delta X_i)$
Coarse mesh	55	55	55	166,375	-0.9	0.00255	1.5	0.02453
Fine mesh	70	70	70	343,000	-0.914	0.00292	2.1	0.01694

million-cell mesh (in comparison with 5.1 million-cell mesh) is sufficient for producing a well-resolved LES. We use relatively coarse grids to solve the flow. As in Table 5.3, two meshes are used to assess grid sensitivity on flow statistics. The fine mesh has 71 nodes in each direction with a total number of 343,000 cells, while the coarse mesh has only 56 nodes (166,375 cells). Since the aim is always to place the first computational cell in the viscous sublayer (i.e. $y^+ <$ 3), the mesh coarseness can be judged by the maximum cell size, $max(\Delta X_i)$. This happens to be in the bulk region in this flow configuration. In our case, the coarse mesh has $max(\Delta X_i)$ of 0.035 L_c compared to 0.014 L_c in Dehbi et al., 2017 and 10^{-5} L_c in Puragliesi et al., 2011. As seen from Fig. 5.5-5.6, the mean velocity profiles of both horizontal and vertical components show very small differences between the meshes, and therefore, we proceed further with the coarser mesh.
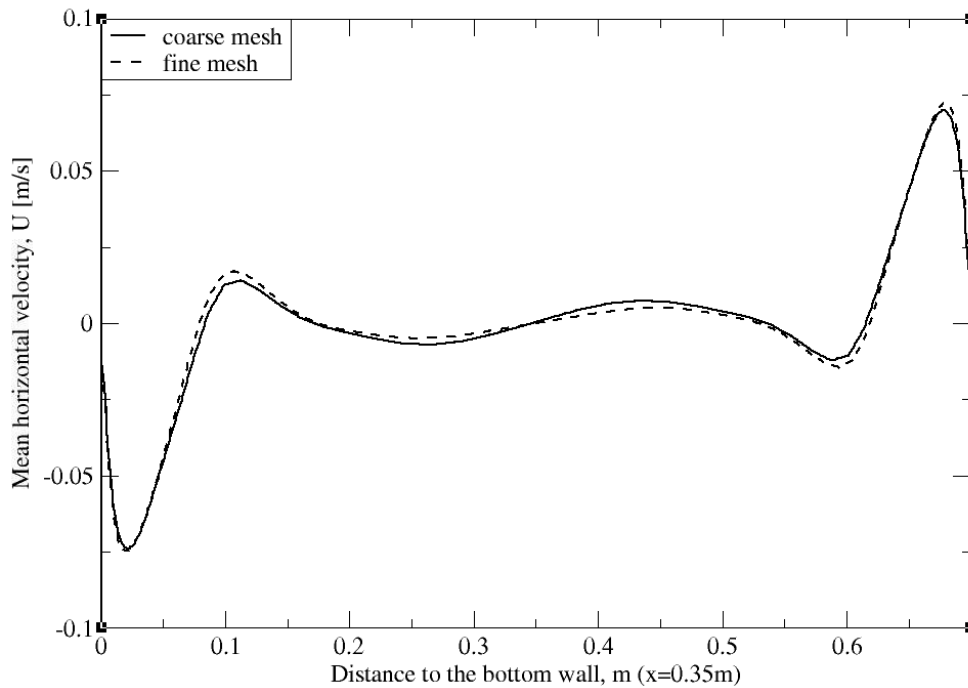
Figure 5.5 – Mean horizontal velocity component by the dynamic model at x = 0.35m.
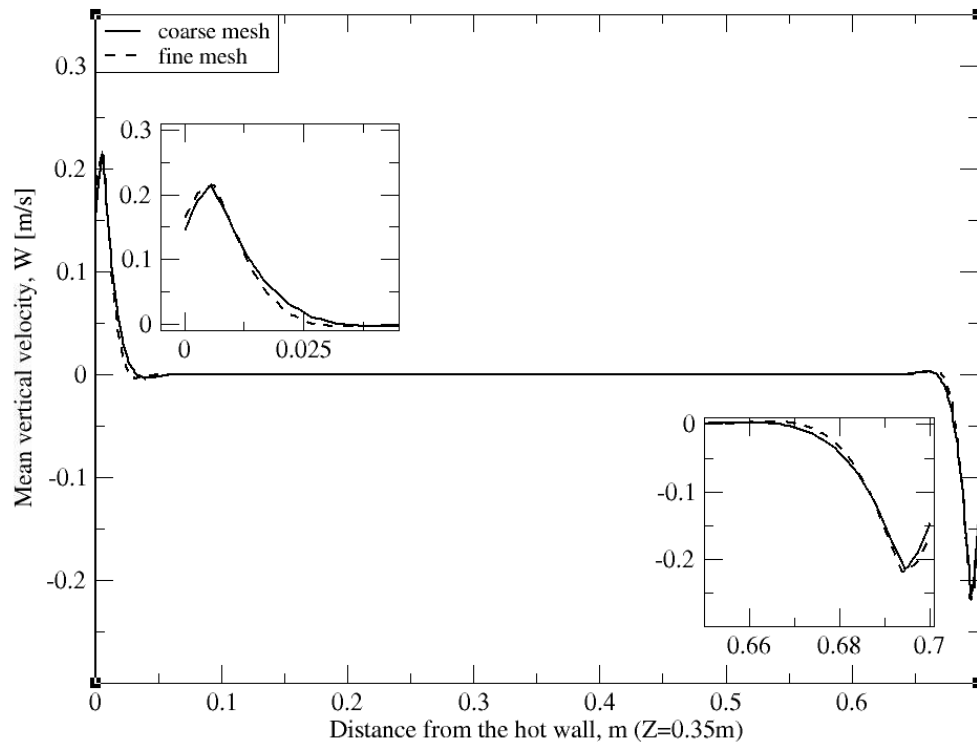
Figure 5.6 – Mean vertical velocity component by the dynamic model at z = 0.35m.

Table 5.4 – Turbulence models used and the corresponding first cell size and total CPU hour needed for each simulation | $2400\tau_c$

Turbulence model	y_1^+	y_1	CPU
Standard Smagorinsky	1.5	0.00255	07:31:59
Dynamic Smagorinsky	1.7	0.00255	10:08:00

5.4 Results

5.4.1 Fluid flow

In this section, we show and discuss the results from the standard and the dynamic Smagorinsky models. It is usual to judge the predictions of the flow statistics collected after a certain number of flow time units, τ_c. In this flow configuration, the time unit is defined in terms of cavity length and circulation speed as follows:

$$V_r = \frac{\alpha \sqrt{Ra}}{L_c} \tag{5.4}$$

$$\tau_c = \frac{L_c}{V_r} \tag{5.5}$$
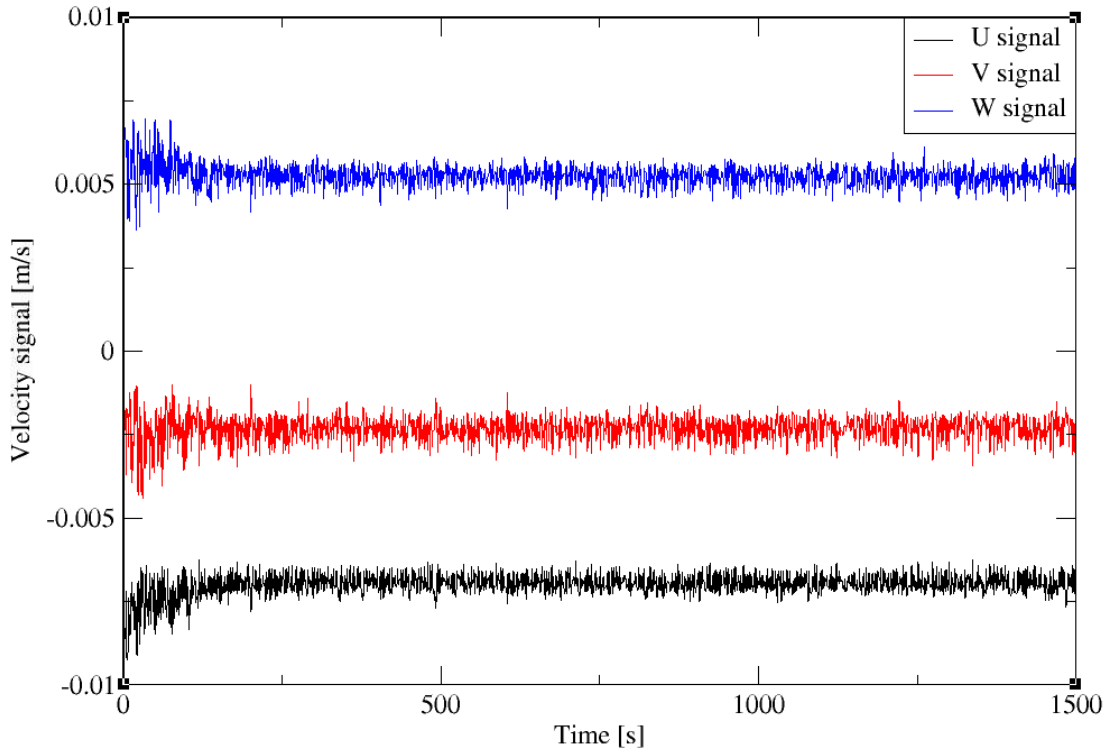
Figure 5.7 – Velocity signal as a function of time in the three orthogonal directions recorded at the center of the domain (0.35, 0.35, 0.35). Turbulent statistics were gathered over the 1500 seconds (2400 time units with time step size of 0.01sec) to guarantee statistically stationary flow.

In the LES study of Puragliesi, 2010, authors consider 450 time units to assume statistically stationary (fully developed) flow conditions, while both studies by Dehbi et al., 2017; Sergent,

Xin, et al., 2013 quote 600 time units. In this study, a double of the latter time-span was adopted, where turbulent statistics were initiated after 1200 time units from the beginning of the simulation, then results were averaged over another 1200 time units. This time-averaging interval was found to ensure full representation of the flow realizations. For our simulations, the circulation velocity and the time unit have values of 1.1 m/s and 0.637 s respectively. Considering the time step size of 0.01s, this translates to approximately 153,000 time steps to cover the whole simulation (see Fig. 5.7)

Using the LES data from Dehbi et al., 2017 as a reference, results are assessed by comparing the resolved part of TKE at three different sections across the cavity height as in Fig. 5.8-5.10. It can be noticed that at the mid-plane (z = 0.35 m and y = 0.35m) the dynamic Smagorinsky model is capable of predicting the majority of the TKE in the near-wall region. On the other hand, the SGS effects are more pronounced close to the top and bottom corners of the cavity where thermal stratification is prominent. However, it can be observed that overall, the dynamic Smagorinsky model is significantly better than the standard model close to the wall.

For the near-wall grid spacing, we use 0.00364 L_c for the first cell size. As shown in Table 5.4 below, the corresponding y^+ values for both SGS models are shown. The same coarse mesh was used for both models (with 55 cells in each direction). To guarantee a time-accurate solution, the time step size was assigned in each case so that the maximum Courant–Friedrichs–Lewy number (CFL) is less than one throughout the simulation in all reported cases. It can be noticed from Table 5.4 below that the dynamic Smagorinsky model takes about 33% extra CPU time compared to the standard Smagorinsky model. This is mainly due to the additional loops designed for the dynamic calculation of the Smagorinsky coefficient.

The DHC has a unique flow configuration with two distinctive thermal and velocity boundary layers developing on the vertical (active) walls. The thickness of these boundary layers scales with $Ra^{-1/4}$ (Puragliesi et al., 2011). This special flow regime can be observed from both the temperature and velocity contours (Fig. 5.11 - 5.12) where the highest velocity is located near the active hot and cold walls, while in the bulk region the fluid velocity is almost stagnant. This can also be observed from the velocity contours shown in Fig. 5.12, where two main counter-currents co-exist at the outer region of the vertical boundary layers. The reason for this particular flow organization is due to the buoyancy force emerging from thermal stratification (see Fig. 5.11). In addition, the centro-symmetric property can be identified from the velocity and temperature fields (Fig. 5.11, 5.12). It is important to highlight that the turbulent flow structures are more dampened in our flow field representation compared to the reference LES from Dehbi et al., 2017. This is mainly due to the relatively coarse mesh employed which accounts for bigger eddies according to the cut-off length (i.e. Δ).

On another note, it can be observed qualitatively from Fig. 5.13 that the TKE is well resolved by the dynamic Smagorinsky model in comparison with the reference standard LES. It can also be noted that velocity gradients are higher at the cavity corners due to the strong flow recirculation pockets as seen from the velocity vectors (Fig. 5.14, 5.15) as well as the coherent
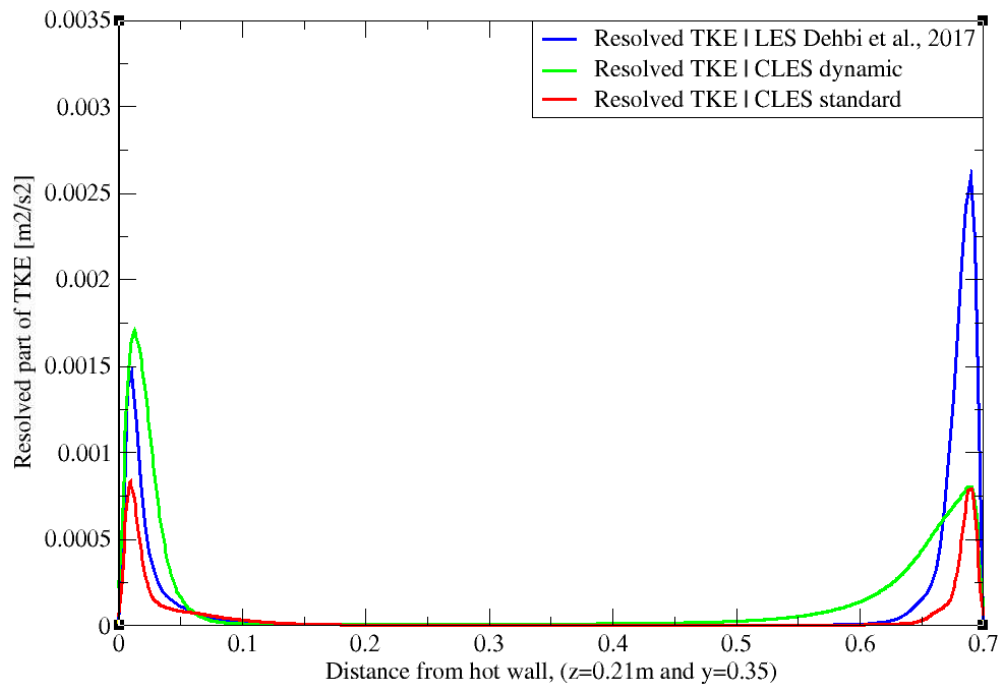
Figure 5.8 – TKE profiles from Dehbi et al., 2017 (blue), CLES dynamic (green) and CLES standard (red). Profiles are reported at z= 0.21m
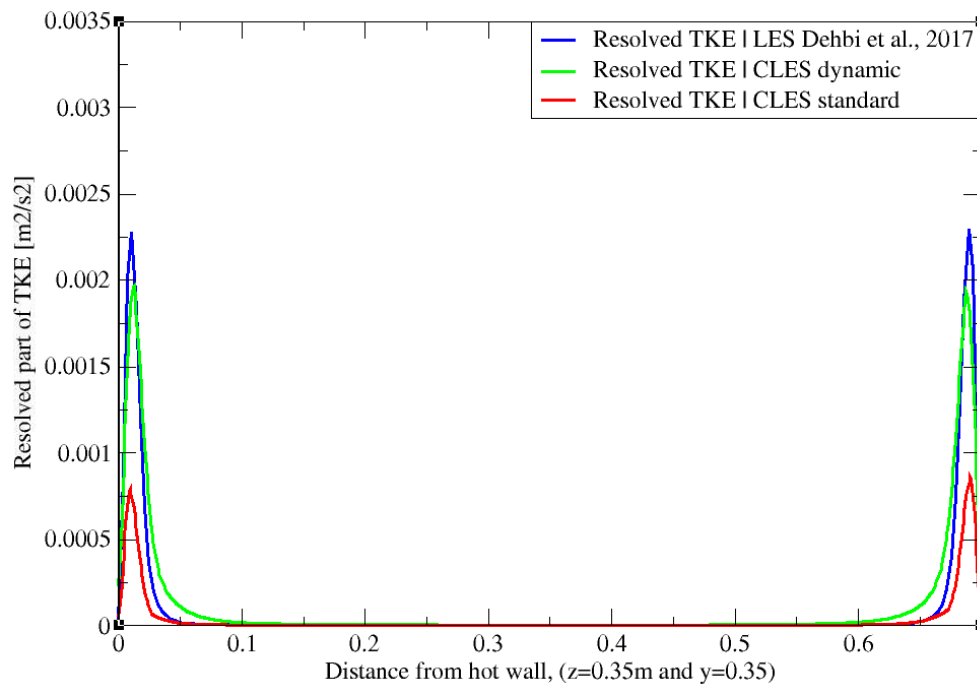
Figure 5.9 – TKE profiles from Dehbi et al., 2017 (blue), CLES dynamic (green) and CLES standard (red). Profiles are reported at z= 0.35m
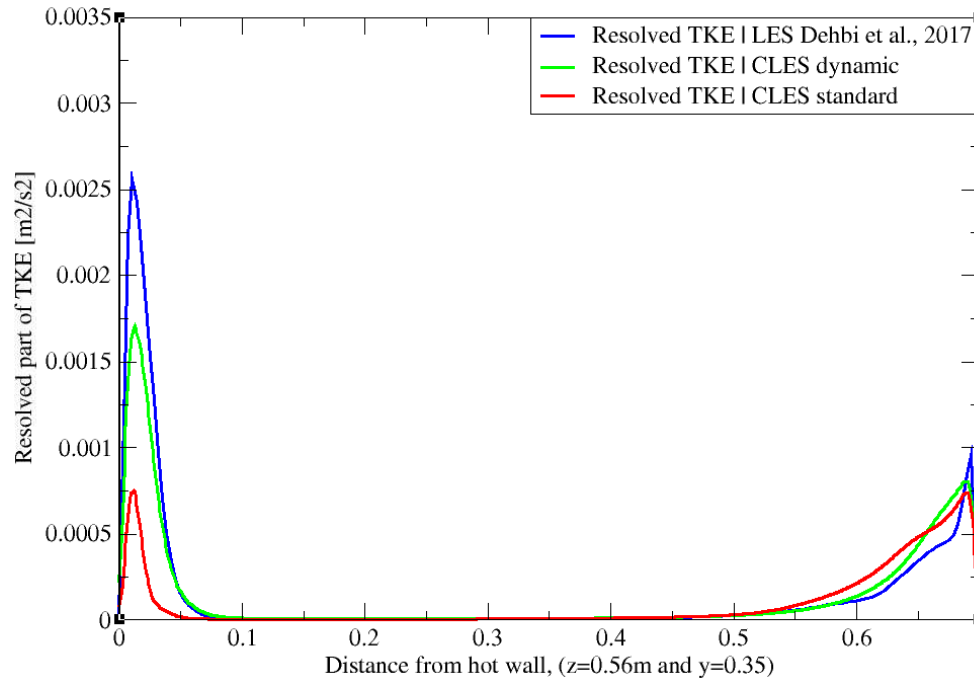
Figure 5.10 – TKE profiles from Dehbi et al., 2017 (blue), CLES dynamic (green) and CLES standard (red). Profiles are reported at z= 0.56m

turbulent structures in Fig. 5.16. This particular flow regime makes the choice of the sub-grid scale model for wall treatment quite crucial. For this sake, we study with scrutiny the capability of both the standard and dynamic Smagorinsky SGS models to predict the turbulent statistics in this benchmark

Time-averaged temperature contours produced by the dynamic Smagorinsky model reveal the hook-like structures as shown in Fig. 5.17. Temperature iso-contours are normalized by the reference temperature (T/T_{ref}). These flow structures (also known as "corner eddies") are identified by high-intensity recirculation zones that stem at the cavity corners and diffuse in the direction normal to horizontal walls. This behavior was also observed by Puragliesi et al., 2011. In agreement with previous literature observations, velocity streamlines in XZ-plane (Fig. 5.18) show the formation of counter-rotating secondary flows in the core region. The development of such flow patterns can also be noticed from the instantaneous velocity contours in Fig. 5.12.

In addition to the above qualitative assessment, an extensive quantitative analysis of flow mean and root mean square (RMS) profiles is reported for temperature and velocity fields. Profiles are plotted for both the Smagorinsky standard and the dynamic models to reveal the effect of the SGS model on flow prediction in the near-wall region – which is our main interest for the further particulate cavity investigation. To have a one-to-one comparison with reference LES and experimental databases, flow statistics have been plotted at four different
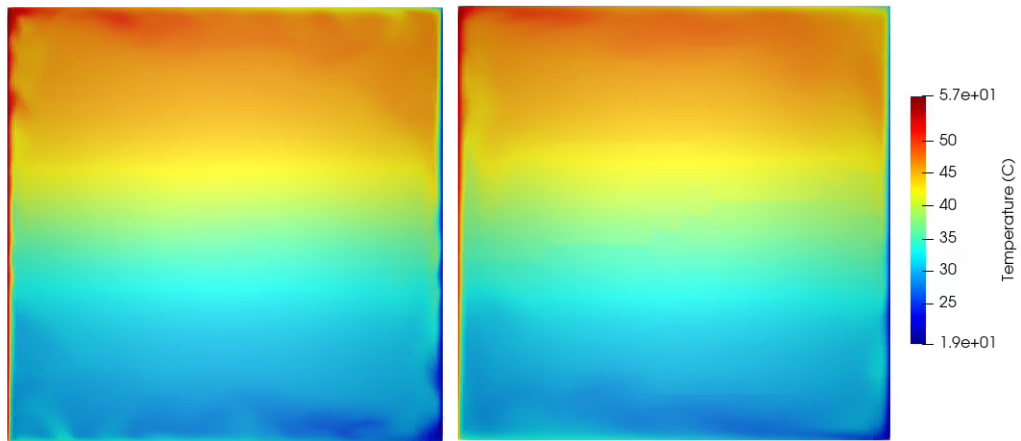
Figure 5.11 – Instantaneous temperature field from well-resolved LES from Dehbi et al., 2017 (left) and own CLES dynamic results (right) at the cavity mid-plane (x=0.35m) by the Smagorinsky dynamic model after 2400 τ_c.
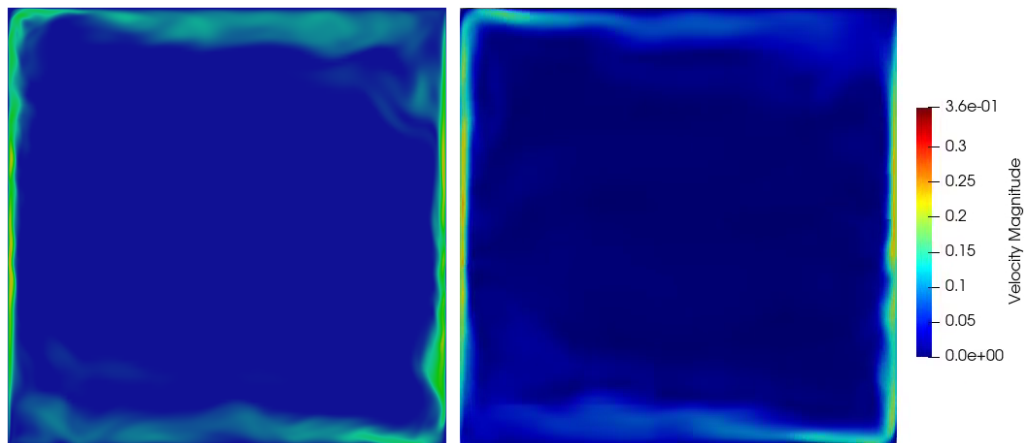
Figure 5.12 – Instantaneous velocity field from well-resolved LES from Dehbi et al., 2017 and own CLES dynamic results (right) at the cavity mid-plane (x=0.35m) by the Smagorinsky dynamic model after 2400 τ_c.
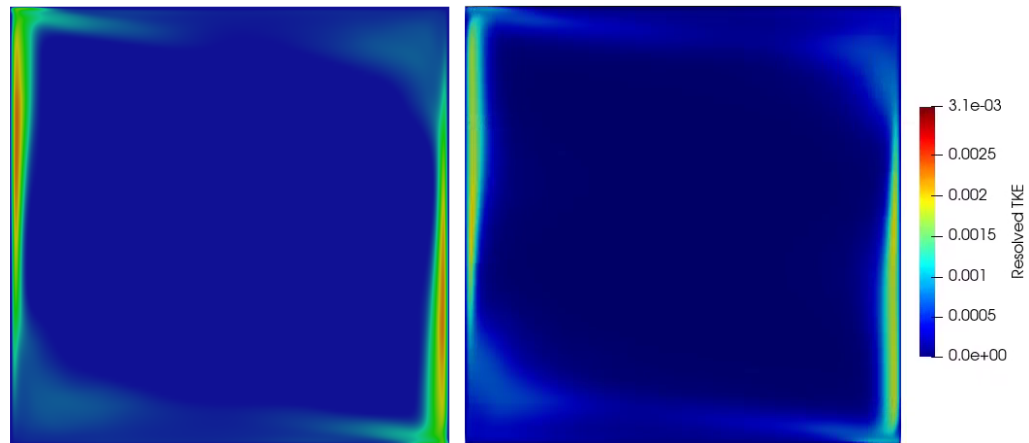
Figure 5.13 – Resolved part of turbulent kinetic energy at the mid-plane (y=0.35) from both reference LES by Dehbi et al., 2017 (left), and own CLES dynamic results (right).
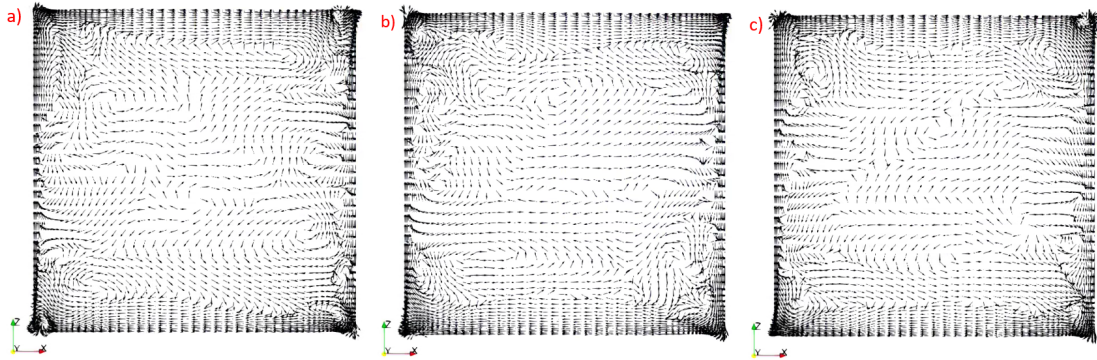
Figure 5.14 – Velocity vectors at different sections across the cavity spanwise direction (XZ parallel-planes: a) Y=0.21m, b) Y=0.35m and c) Y=0.56m). Velocity field is obtained using the Smagorinsky Dynamic model after 2400 time units to ensure statistically stationary turbulence. Velocity vectors are scaled by factor of 0.02.
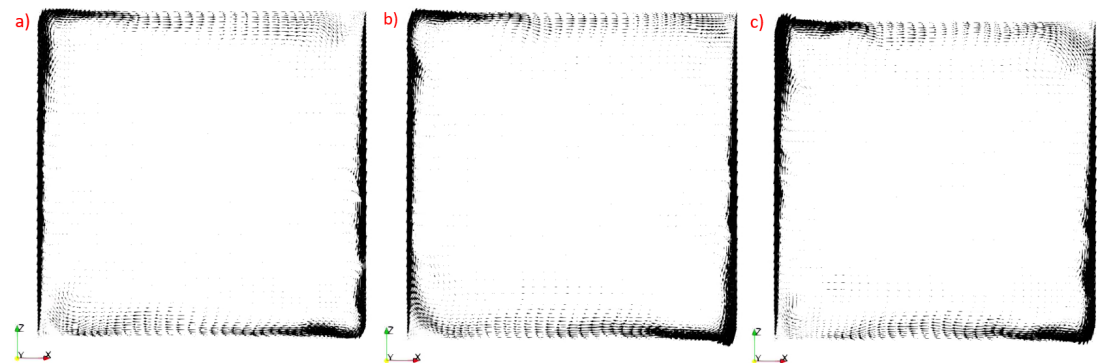
Figure 5.15 – Velocity vectors at different sections across the cavity spanwise direction (XZ parallel-planes: a) Y=0.21m, b) Y=0.35m and c) Y=0.56m). Velocity field is obtained using the Smagorinsky Dynamic model after 2400 time units to ensure statistically stationary turbulence. Velocity vectors represent velocity magnitude in XZ plane - scale factor is 0.2.
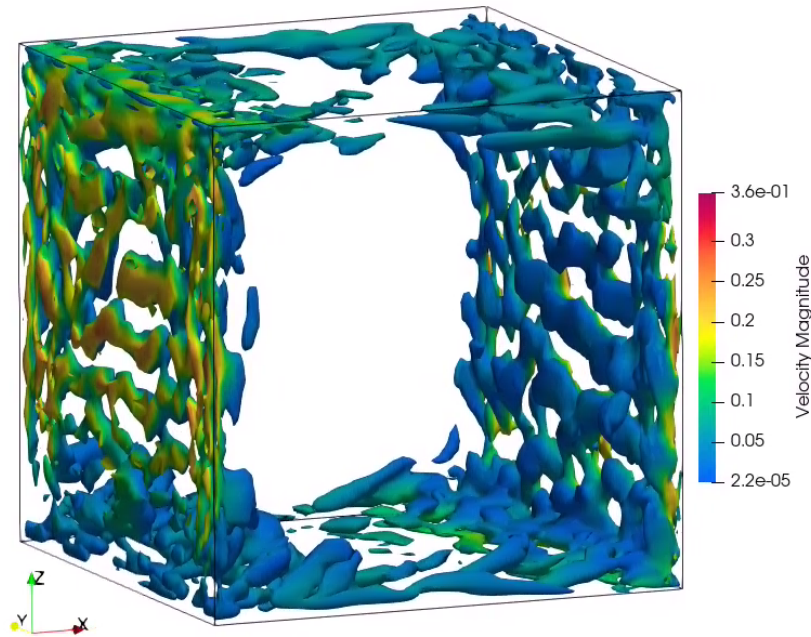
Figure 5.16 – Iso-surfaces of normalized Q-criterion at $2400\tau_c$, for a value of Q = 0.65. The vortices are colored by velocity magnitude. Turbulent structures are produced by the dynamic Smagorinsky model.

locations across the cavity (x=0.35, 0.56 m between the horizontal walls, and Z=0.35, 0.56 m between vertical active walls).

As can be noticed from Fig. 5.19, 5.20, the mean temperature profiles for both the horizontal and vertical centerlines (x=0.35m and z=0.35m) show a very good match with the reference data. However, for velocity profiles, the SGS model effect is more pronounced. As seen from Fig. 5.21, mean vertical velocity profiles predicted by both SGS models match the reference LES and experimental data at the cavity mid-plane. Yet, closer to the top wall (z=0.56m) where the thermal stratification is more prominent, the dynamic model is more accurate near the hot wall compared to the standard Smagorinsky model (Fig. 5.22). For the horizontal velocity component, it can also be noticed that the dynamic model gives a better prediction near the wall than the standard model as shown in Fig. 5.23, 5.24. On the other hand, the standard Smagorinsky model overpredicts somewhat the velocity profile in the boundary layer of both top and bottom walls. As expected, profiles of both models are slightly out of phase in the bulk region which is explained by insufficient mesh resolution. It is worth mentioning that the dynamic model with TKE transport in Fluent yields similar results to the ones obtained by the standard dynamic Smagorinsky. Therefore, the dynamic Smagorinksy model was deemed sufficient in this case for an efficient particle tracking analysis.

Similarly, for higher moment statistics we report velocity fluctuations i.e. RMS values of
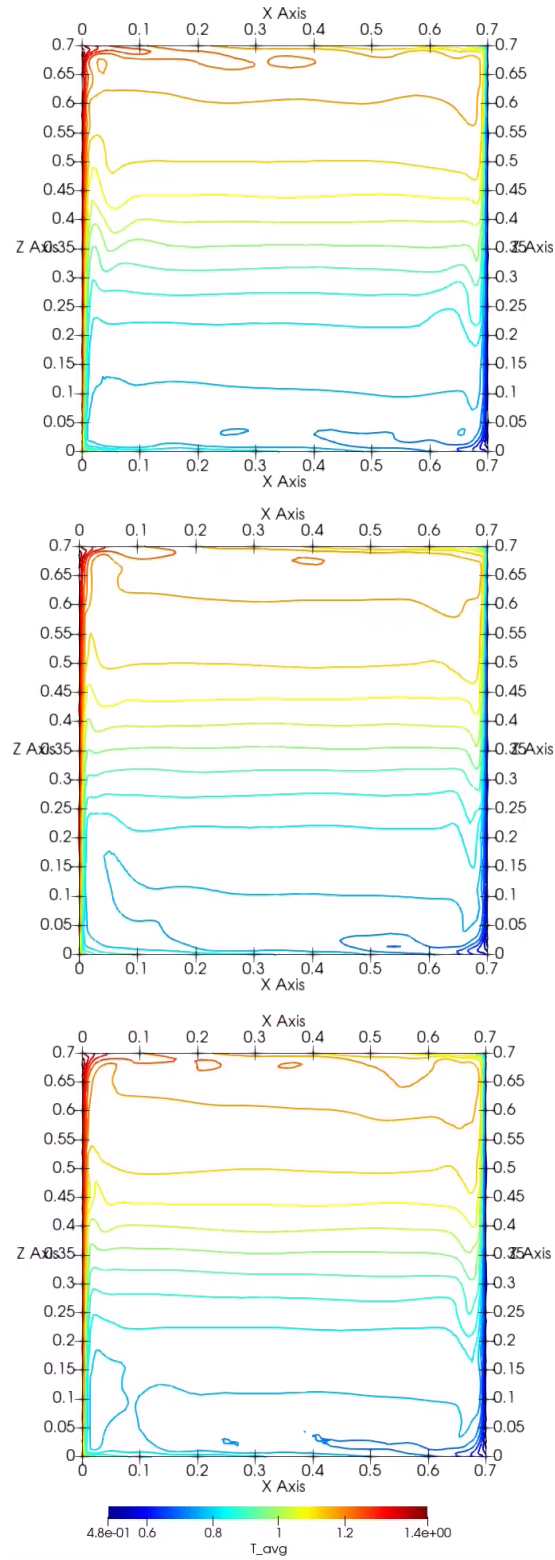
Figure 5.17 – Dimensionless mean temperature iso-contours (T/T_{ref}) produced by the dynamic Smagorinsky model at three XZ-parallel planes across the spanwise direction (y=0.21m, 0.35m and 0.56m from top to bottom) at $Ra = 10^9$.
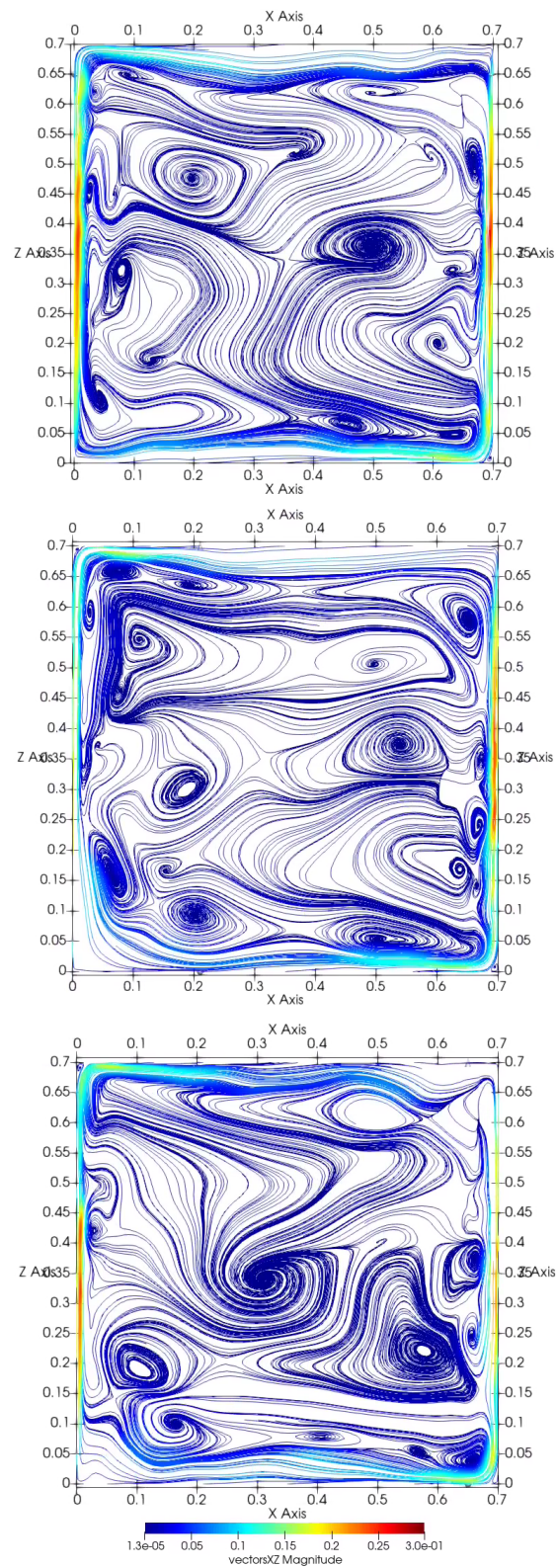
Figure 5.18 – Instantaneous velocity streamlines produced by the dynamic Smagorinsky model at three XZ-parallel planes across the spanwise direction (y=0.21m, 0.35m and 0.56m from top to bottom) at $Ra = 10^9$.

116
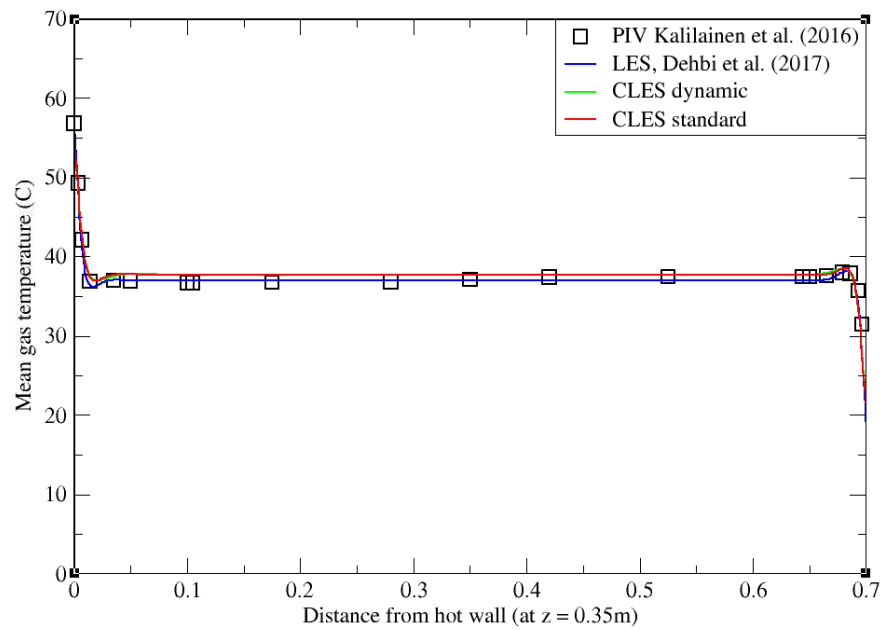
Figure 5.19 – Comparison for mean temperature profiles between hot and cold walls from both Smagorinsky models against reference LES and experimental databases. Profiles are obtained at (z=0.35m) using same mesh after 2400 time units.
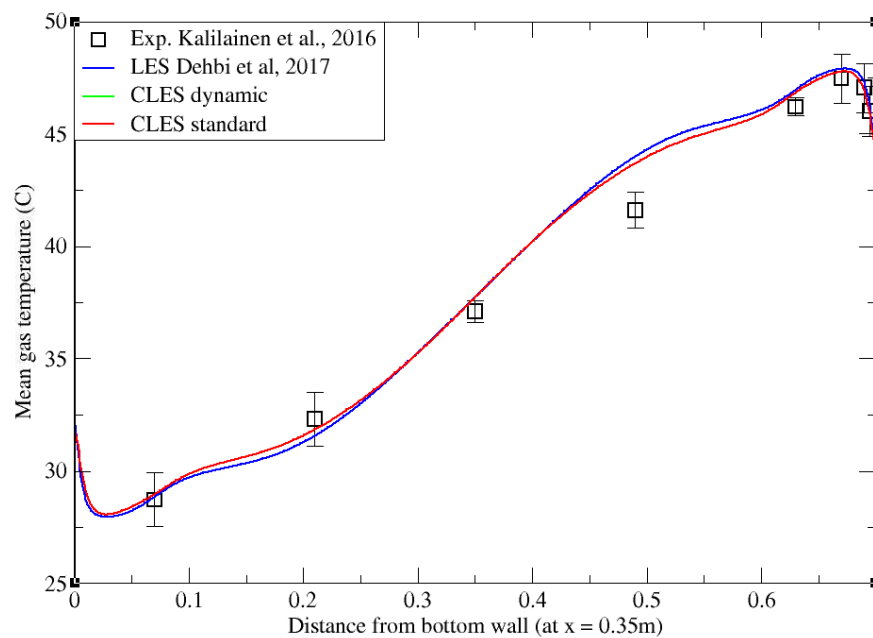
Figure 5.20 – Comparison for mean temperature profiles between bottom and top walls from both Smagorinsky models against reference LES and experimental databases. Profiles are obtained at (x=0.35m) using same mesh after 2400 time units.
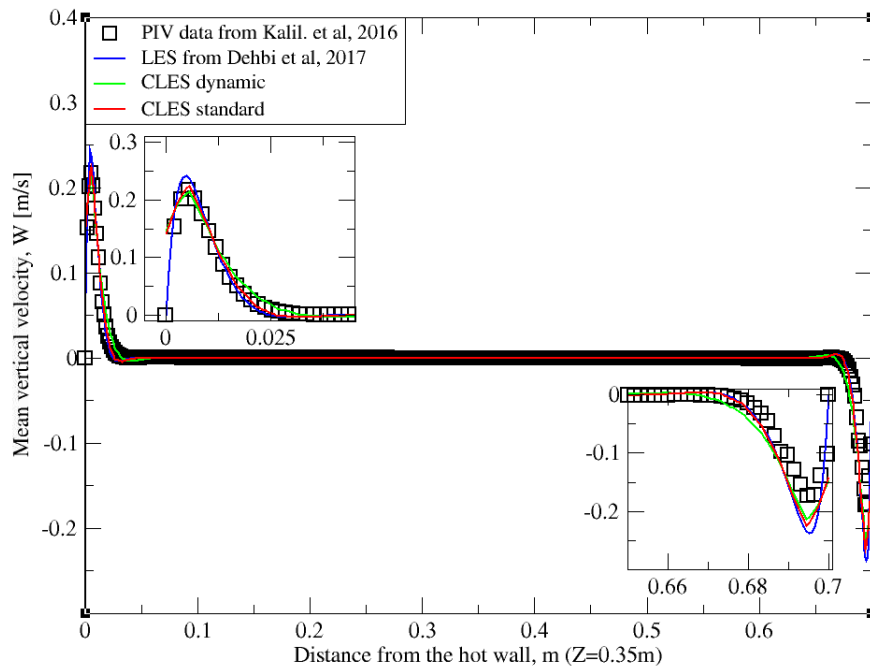
Figure 5.21 – Comparison for mean vertical velocity profiles between hot and cold walls from both Smagorinsky models against reference LES and experimental databases. Profiles are obtained at (z=0.35m) using same mesh after 2400 time units
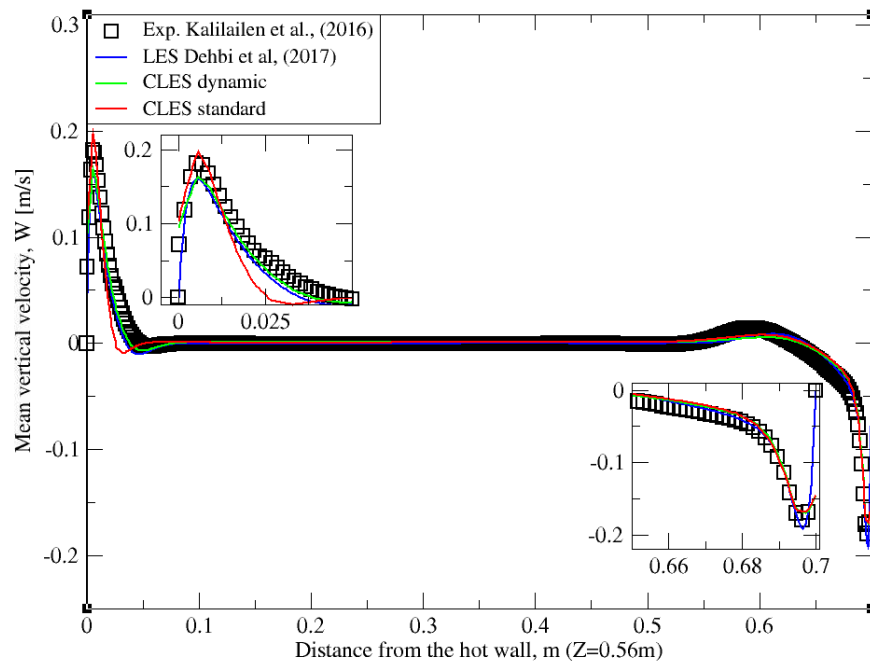
Figure 5.22 – Comparison for mean vertical velocity profiles between hot and cold walls from both Smagorinsky models against reference LES and experimental databases. Profiles are obtained at (z=0.56m) using same mesh after 2400 time units.
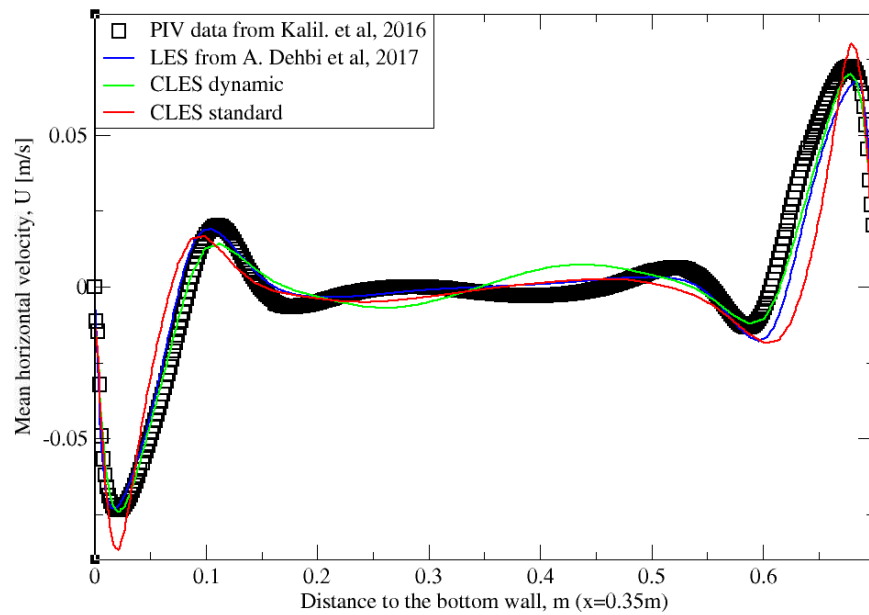
Figure 5.23 – Comparison for mean horizontal profiles between bottom and top walls from both Smagorinsky models against reference LES and experimental databases. Profiles are obtained at (x=0.35m) using same mesh after 2400 time units.
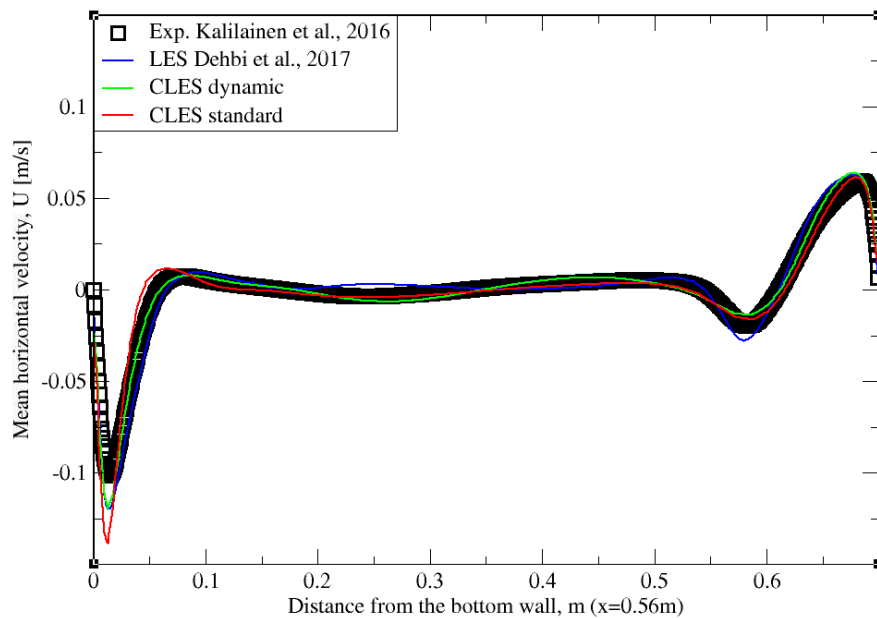
Figure 5.24 – Comparison for mean horizontal profiles between bottom and top walls from both Smagorinsky models against reference LES and experimental databases. Profiles are obtained at (x=0.56m) using same mesh after 2400 time units.

both horizontal and vertical velocities (Fig. 5.25-5.28) for both models. For the RMS of the horizontal component, it was observed that the standard Smagorinsky underpredicts values of velocity fluctuations substantially on both planes i.e. z = 0.35m, 0.56m. The dynamic model in contrast is shown to slightly overpredict the RMS of the horizontal velocity component (Fig. 5.25, 5.26). However, it shows a very good match with the vertical component. This can be seen in vertical RMS profiles at z=0.35m (Fig. 5.27) where the dynamic model captures 93% of the peak value of the velocity fluctuations, while the standard Smagorinsky model predicts only about 67% of the reference value near the wall. Closer to the top wall (z=0.56m), the dynamic model captures 85% versus 58% peak values at the wall relative to the reference LES (Fig. 5.28).
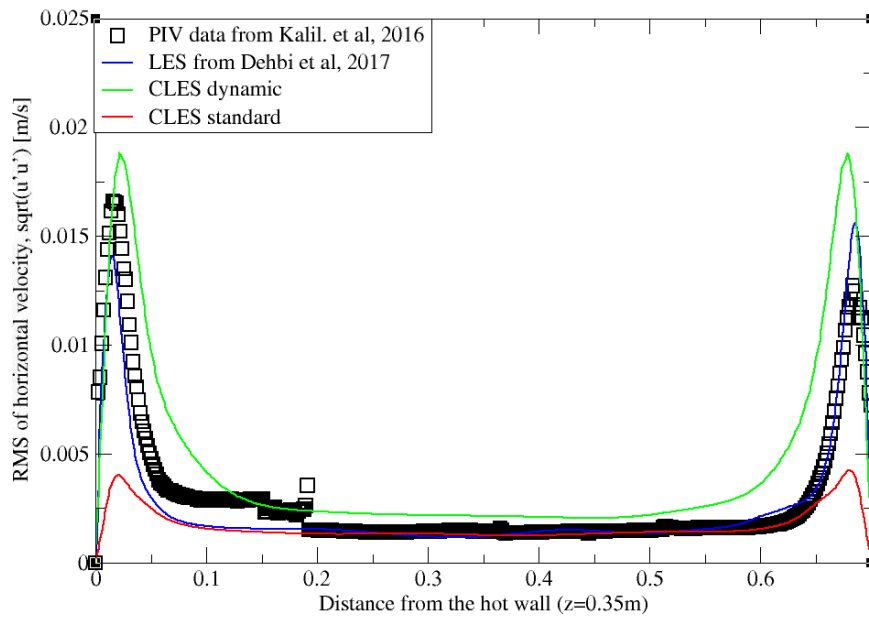
Figure 5.25 – Comparison for RMS horizontal velocity between hot and cold walls from both Smagorinsky models against reference LES and experimental databases. Profiles are obtained at (z=0.35m) using same mesh after 2400 time units.

The reason for the improved performance of the dynamic model is a better representation of unresolved motion scales. Unlike the standard model, varying the Smagorinsky coefficient in time and space allows the turbulent viscosity to be more accurately predicted. This in turn gives a better representation for the SGS model, especially in the near-wall region where strong turbulence anisotropy is expected. The differences in the sub-grid scale representation can be clearly seen from the eddy-over-molecular-viscosity ratio plotted for each SGS model (Fig. 5.29, 5.30). It can be noticed from the plots that the eddy viscosity produced by the dynamic model is approximately 4 times higher than the one predicted by the standard model with a fixed Smagorinsky constant. This returns more correct turbulent fluctuations near the wall in the case of the dynamic model and hence better prediction of the second-order statistics.

Even though the two models produce similar results for the first-order statistics (velocity and
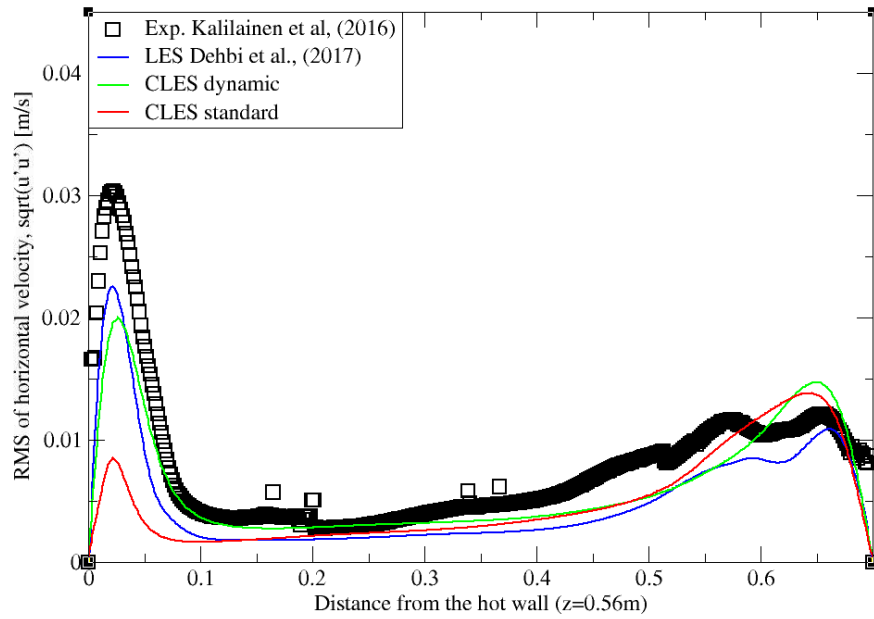
Figure 5.26 – Comparison for RMS horizontal velocity between hot and cold walls from both Smagorinsky models against reference LES and experimental databases. Profiles are obtained at (z=0.56m) using same mesh after 2400 time units.
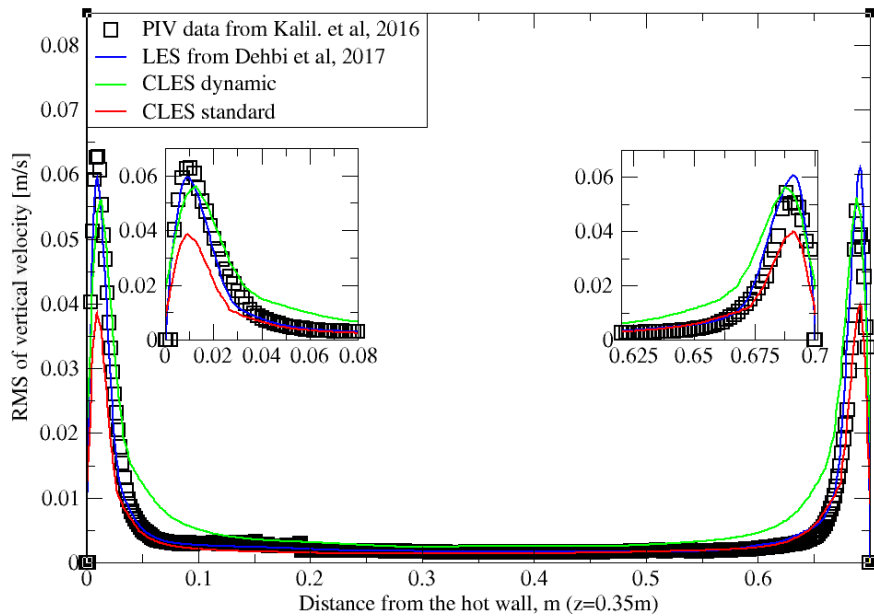
Figure 5.27 – Comparison for RMS vertical velocity between hot and cold walls from both Smagorinsky models against reference LES and experimental databases. Profiles are obtained at (z=0.35m) using same mesh after 2400 time units.
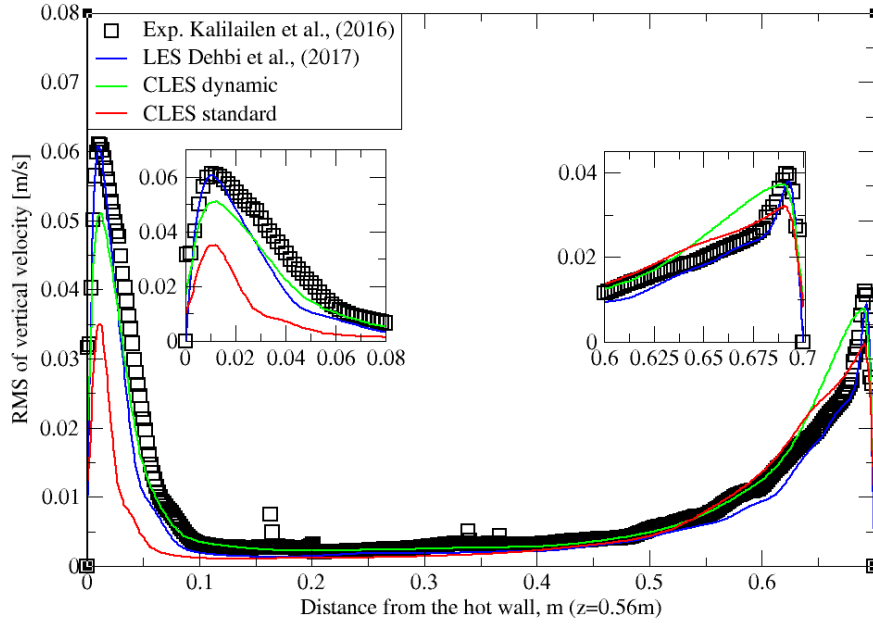
Figure 5.28 – Comparison for RMS vertical velocity between hot and cold walls from both Smagorinsky models against reference LES and experimental databases. Profiles are obtained at (z=0.56m) using same mesh after 2400 time units.
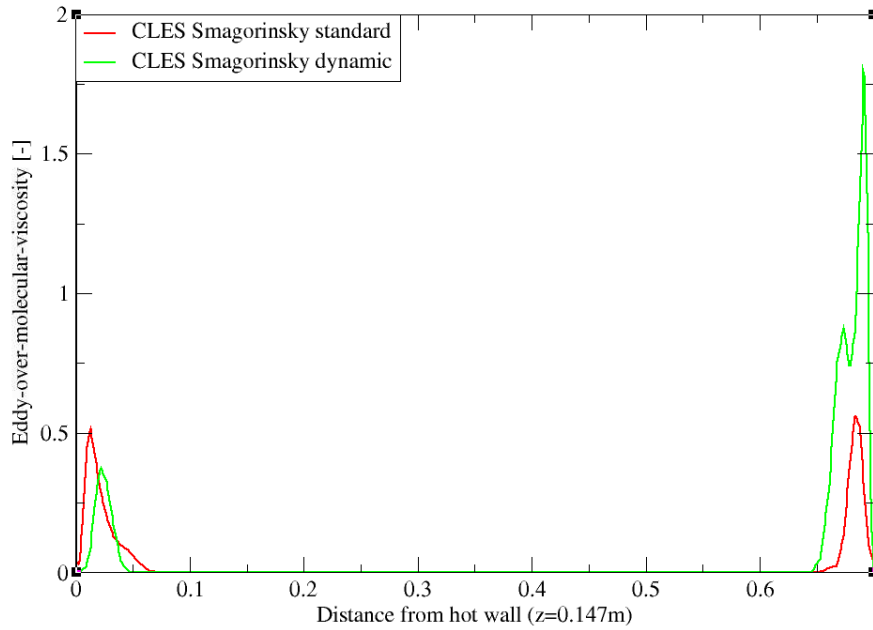
Figure 5.29 – Ratio of eddy over molecular viscosity probed along the horizontal line Z = 0.147m between hot and cold walls. Values from both the standard Smagorinsky and dynamic models at 2400 time units.
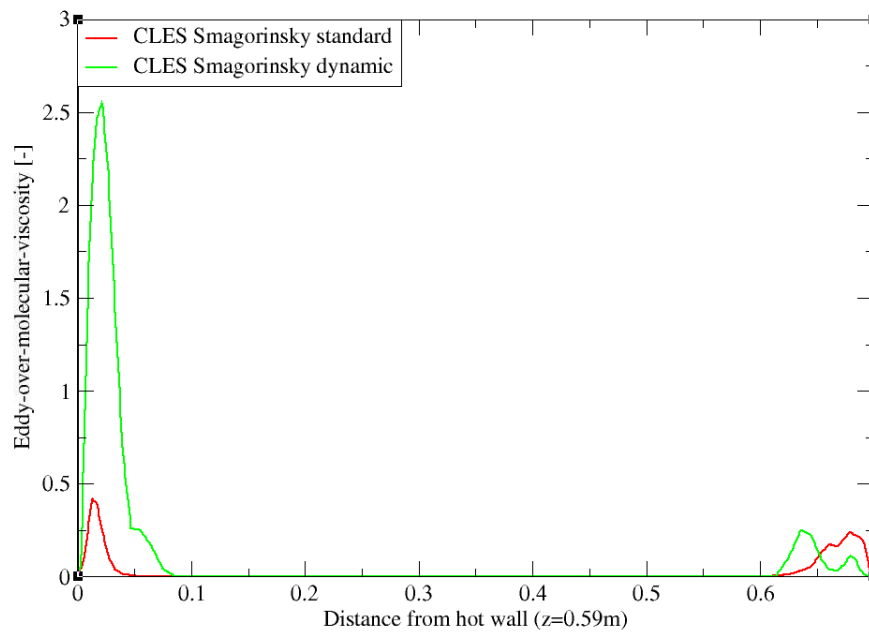
Figure 5.30 – Ratio of eddy over molecular viscosity probed along the horizontal line Z = 0.59m between hot and cold walls. Values from both the standard Smagorinsky and dynamic models at 2400 time units.

temperature fields), the results of the second-order statistics reveal quite a different picture. The peak values of the normal stresses, and consequently of the turbulent kinetic energy are predicted significantly better by the dynamic model. These differences are expected to be smaller for the fine mesh as the impact of the sub-grid scale is waning with the better mesh resolution. However, for the parametric study of the DHC flows where a large number of runs are needed, the fine-mesh resolution can only be afforded with substantial CPU resources. The presented results confirm that reasonable accuracy can be achieved on the much smaller mesh, but the choice of the sub-grid scale model has a significant implication on the LES ability to predict the second-order statistics. According to this finding and as will be shown in the next section, the dynamic model was chosen for with the particle dispersion analysis.

5.4.2 Lagrangian statistics

In the following, we focus on the particle depletion predicted by the LES dynamic model on a coarse mesh. Following the studies by both Dehbi et al., 2017 and Kalilainen et al., 2016, we investigate the local relative concentration of airborne particles in the cavity as a function of time. As reported in Table 5.1, six swarms of 10^5 particles each were considered as in Fig. 5.31 Since LPT is a Monte Carlo process, the solution converges to a narrow uncertainty margin when a larger sample size is used (convergence scales with $N^{1/2}$). As a preliminary simulation, the two sample sizes of 10^5 and 2×10^4 particles did not show a significant change in results (Fig. 5.32). However, it must be stressed that in such flow configuration, small deviations get amplified over time, and therefore, deposition time can be huge for small particles. For this reason, the sample comprising 10^5 particles was considered sufficiently large for obtaining credible results.
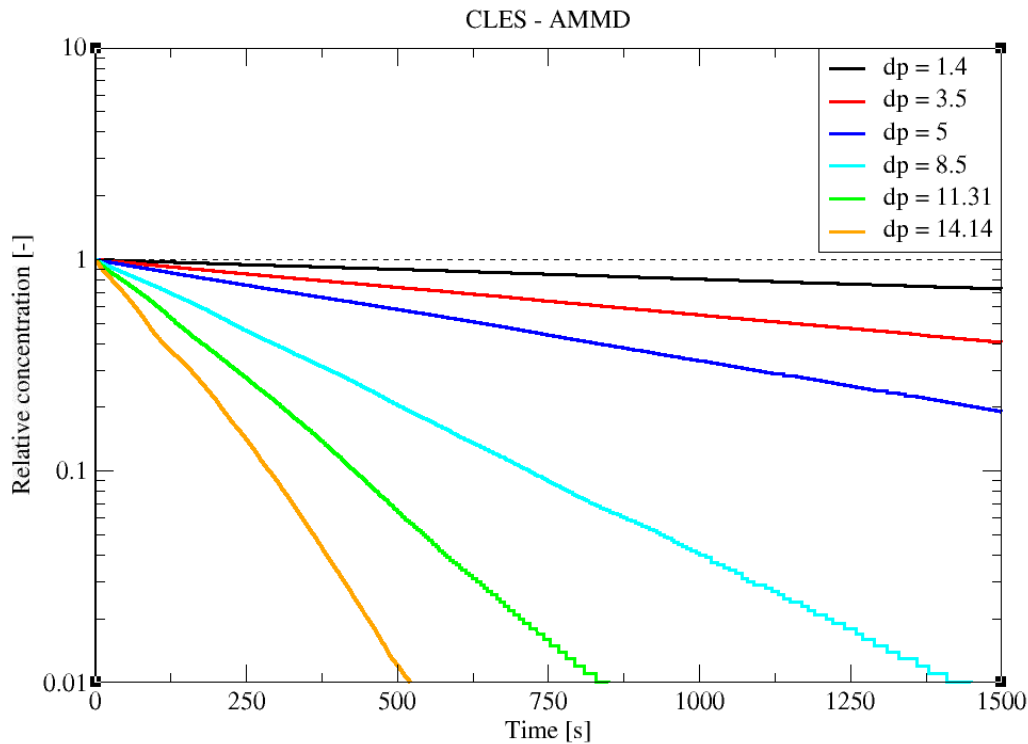
Figure 5.31 – CLES predictions of relative concentration for the reported particle sizes. Each symbol represents a different AMMD.

Since particle depletion rate in DHC takes place at a very small rate, the following results are obtained in a statistically developing manner. As shown in Fig. 5.31, local particle concentration in time is reported where only the active particles are accounted for at each time. Following the analysis of both Kalilainen et al., 2016 and Dehbi et al., 2017, the stirred settling model Hinds, 1999 is used as another reference to estimate particle depletion rate inside the cavity. The model assumes a perfect spatial uniformity of particle distribution at any moment post

injection, which is approximately the case if a mechanical tool was used to "stir" the particles. The model also assumes that particles have a net velocity equal to the gravitational terminal speed V_{TS} and therefore, only horizontal surfaces are considered to compute depletion rates. With such definition, temporally local concentration has an exponential relation with time as follows:

$$C(t) = C(0) exp\left(\frac{-t}{L_c/V_{TS}}\right) = C(0) exp\left(\frac{-t}{L/(\tau_p g)}\right)$$ (5.6)
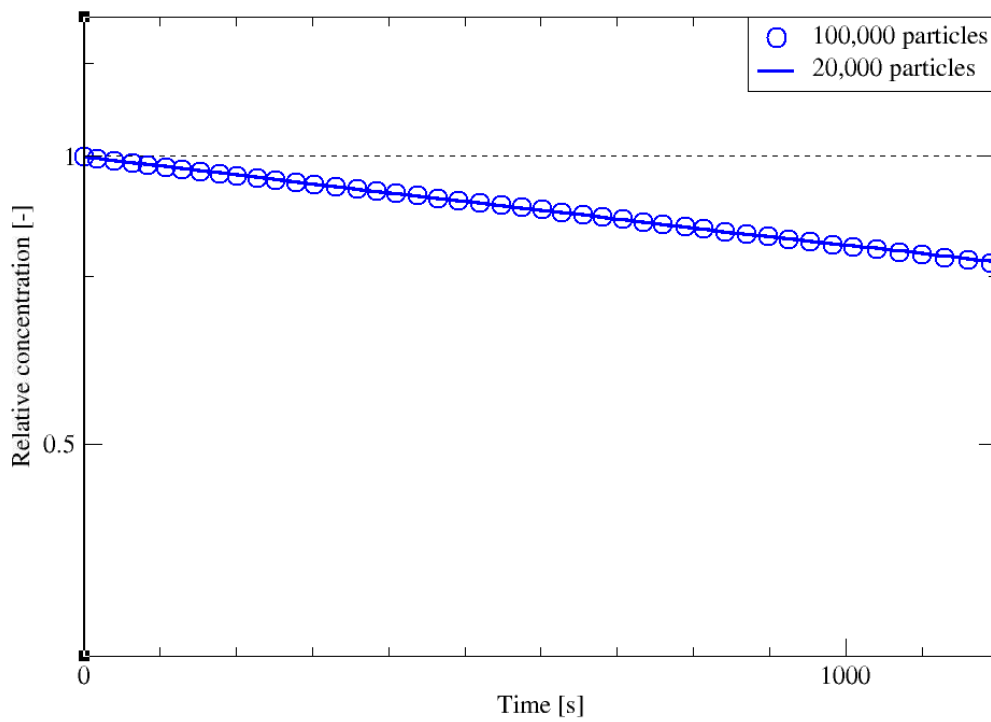
Figure 5.32 – Relative concentration for two different particle counts obtained by CLES. Plots are reported for $d_p = 1.4 \, \mu$m

Despite providing a good picture about inertial particle depletion, the stirred settling model is considered a rough approximation for relatively small inertia particles where the timescale of the particle is comparable to the typical eddy fluctuation in the domain (Fig. 5.33). This is due to the rapid response of low-inertia particles to the carrier flow, and therefore, the model assumption of terminal speed does not hold. This finding was confirmed in the study of Dehbi et al., 2017 using well-resolved LES.

Comparing the predictions of CLES against both of LES and the reference experimental data, it can be seen that there is a small deviation in relative concentration for 1.4 μm particles (Fig. 5.33). However, this deviation is not significant given that depletion rates are plotted over a

large time interval. Looking at the spatial distribution of the deposited particles of size 1.4 μm (as in Fig. 5.34), it could be shown that SGS has also little effect on the deposition pattern over the cavity walls. As can be seen from the histogram representation, the spatial distribution of deposited particles is in line with the reference LES results with less than 5% deviation. It must be stressed that the inclusion of the thermophoretic force is the main drive on this unique deposition pattern. This is shown through the two sensitivity computations of the spatial distribution of particle deposition (Fig. 5.34 - 5.37). It should be noted however that thermophoresis has little effect on the depletion rates of particles in general. This is due to the strong turbulent diffusion which is the overriding cause for the significant deposition rates of smaller particles. This conforms with the observation obtained by Dehbi et al., 2017 who used well-resolved LES.
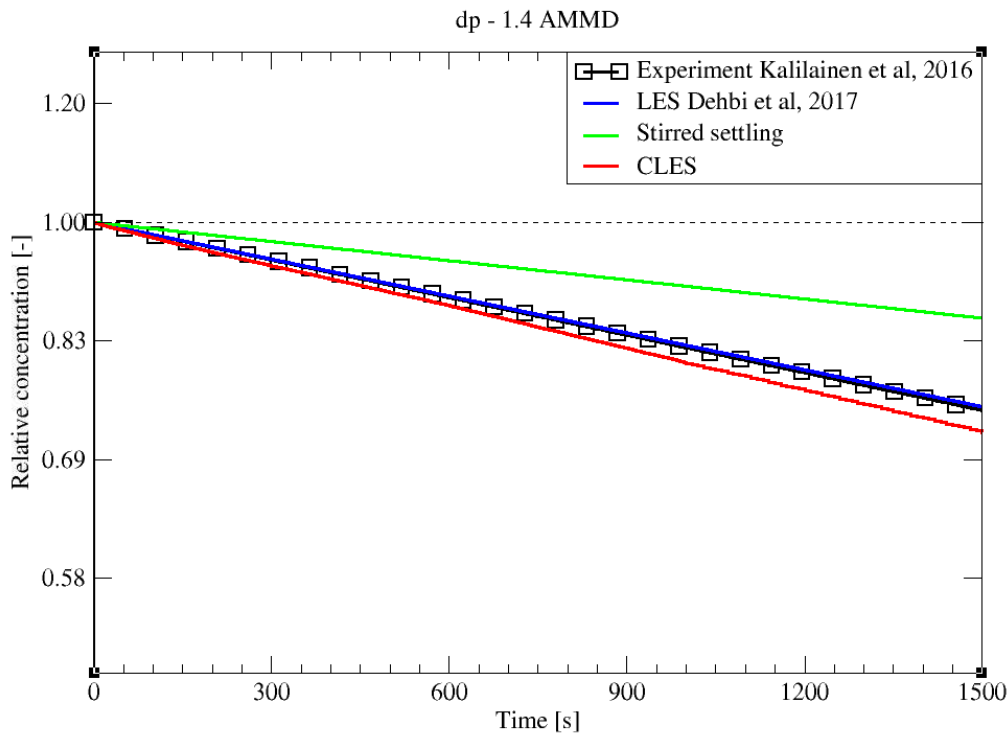
Figure 5.33 – Comparison for particle relative concentration of $d_p = 1.4\mu$m versus time. Predictions by CLES are plotted against all of LES from Dehbi et al., 2017, experimental data by Kalilainen et al., 2016, and the stirred settling model (Hinds, 1999).

For a bigger particle diameter i.e. d_p = 3.5, 5 μm, it could be noticed from Fig. 5.35 - 5.36 that CLES prediction is still in very good agreement with both LES an experimental data. As mentioned above, it could also be seen that the stirred settling model approaches the experimental trend as particle size gets bigger (Fig. 5.35). Similar to the spatial deposition for 1.4 μm particles, it can be seen from (Fig. 5.37) that for higher-inertia particles i.e. 5 μm, gravity force is more dominant than both drag and thermophoretic forces. This can be inferred from the better agreement in deposition pattern between CLES and the reference LES relative

Deposition spatial distribution - 1.4μm
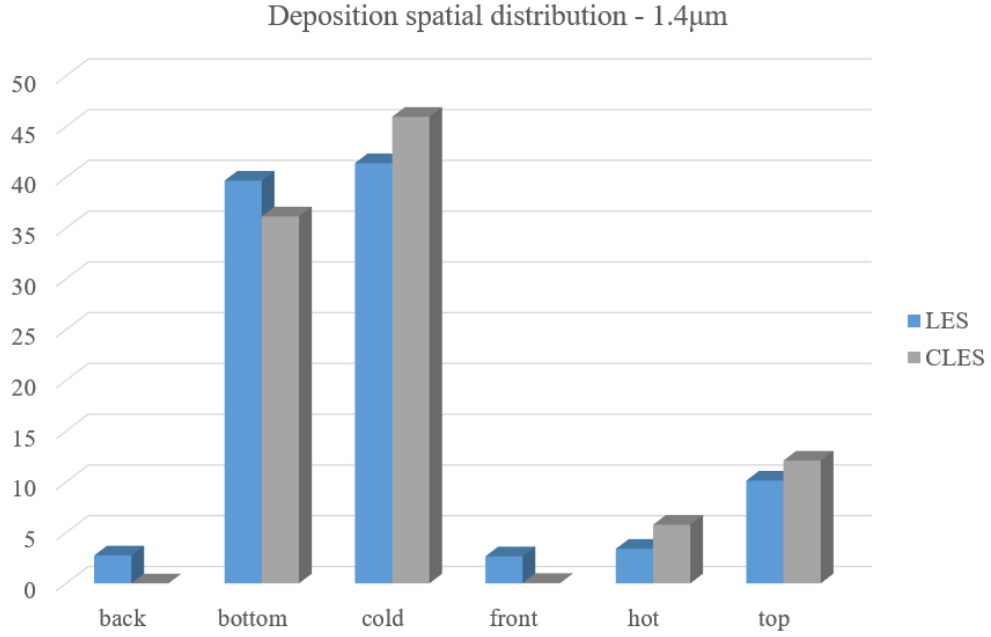
Figure 5.34 – Representation of spatially deposited particles on each wall at t=10.2s (Thermophoretic force included) . Predictions by CLES for particle size $d_p = 1.4$ μm are compared against LES from Dehbi et al., 2017.

to the smaller-inertia particle size.

In order to have a more quantitative picture, the decay constant was calculated for each particle diameter against LES predictions. The decay constant β_D is defined as the inverse of time constant for particle depletion. (Eq. 5.9 - 5.10).

$$\beta_D = \frac{1}{\tau_{rem}} \tag{5.7}$$

$$\tau_{rem} = \frac{-ln(\eta)}{T'} \tag{5.8}$$

where η is particle relative concentration at the corresponding time instant, T'. As can be seen from Fig. 5.38, such comparison reveals that due to SGS effects the decay constant is slightly underestimated below 3.5 μm. In contrast, bigger particles decay rates align perfectly with the correct depletion rate since they are less affected by turbulent fluctuations.

It must be pointed out that particle results obtained by T-Flows were unsatisfactory (see Section A.3.1 in Appendix B). This was mainly concluded from the prediction of the decay constant plot. As could be seen from Fig. 5.39, the decay constant is not only missing the value for low-inertia particles but also for larger ones. such comparison with Fluent reveals that some code development optimization of numerics need to be done in T-Flows in the future.
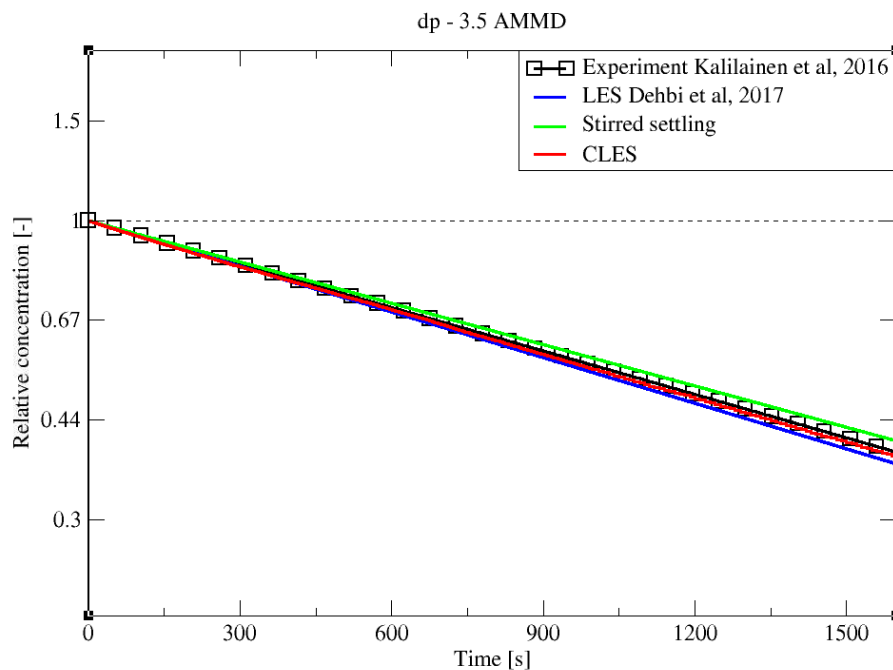
Figure 5.35 – Comparison for particle relative concentration of d_p = 3.5 μm versus time. Predictions by CLES are plotted against all of LES from Dehbi et al., 2017, experimental data by Kalilainen et al., 2016, and the stirred settling model (Hinds, 1999).
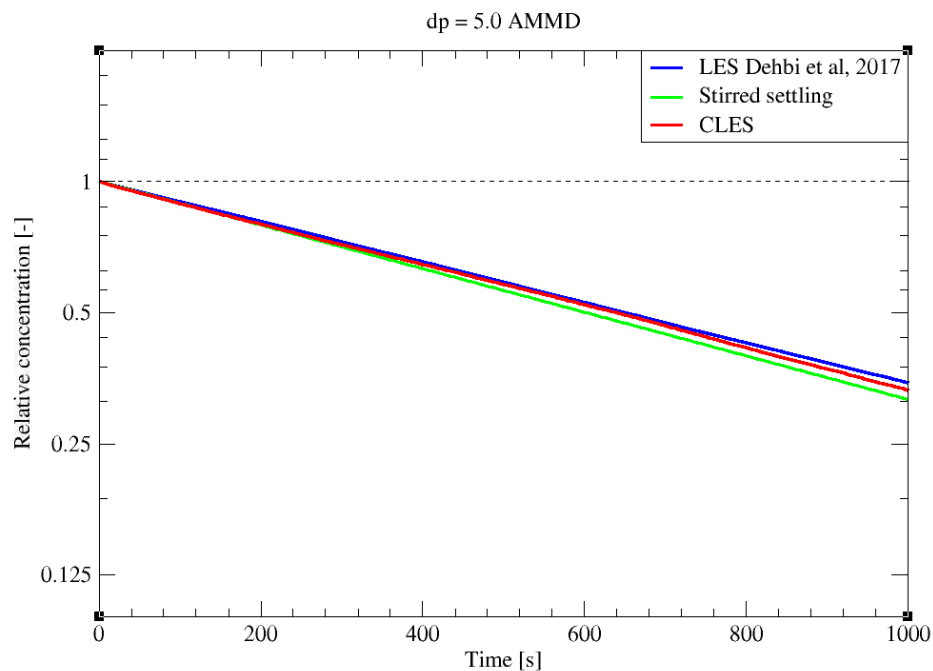
Figure 5.36 – Comparison for particle relative concentration of d_p = 5.0 μm versus time. Predictions by CLES are plotted against both of LES from Dehbi et al., 2017 and the stirred settling model (Hinds, 1999).
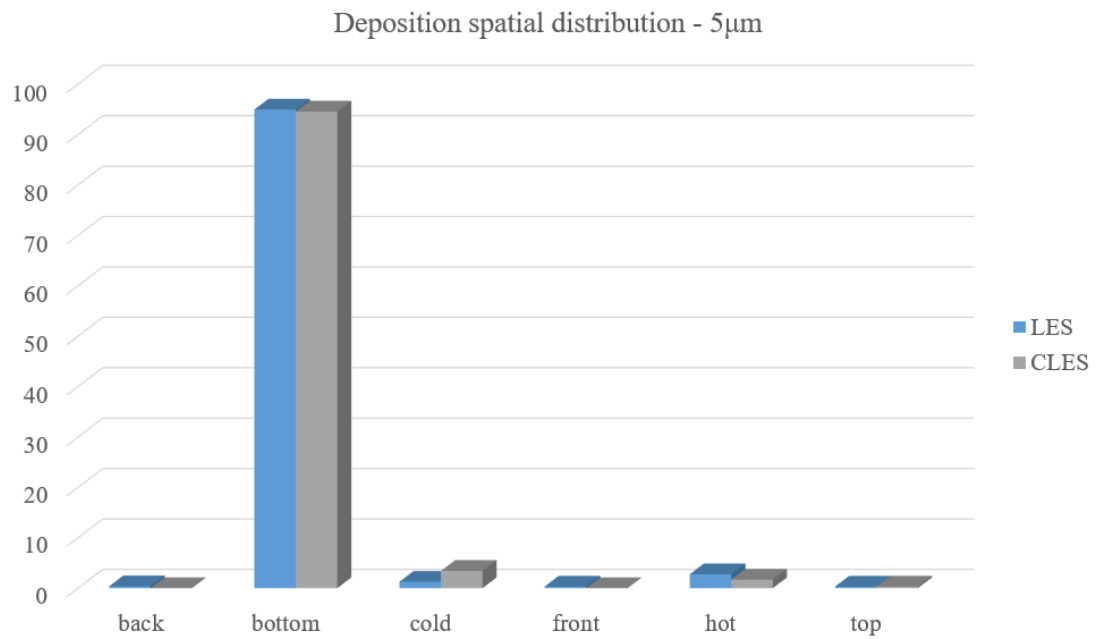
Figure 5.37 – Representation of spatially deposited particles on each wall at t=10.2s (Thermophoretic force included) . Predictions by CLES for particle size $d_p = 5.0\mu$m are compared against LES from Dehbi et al., 2017.
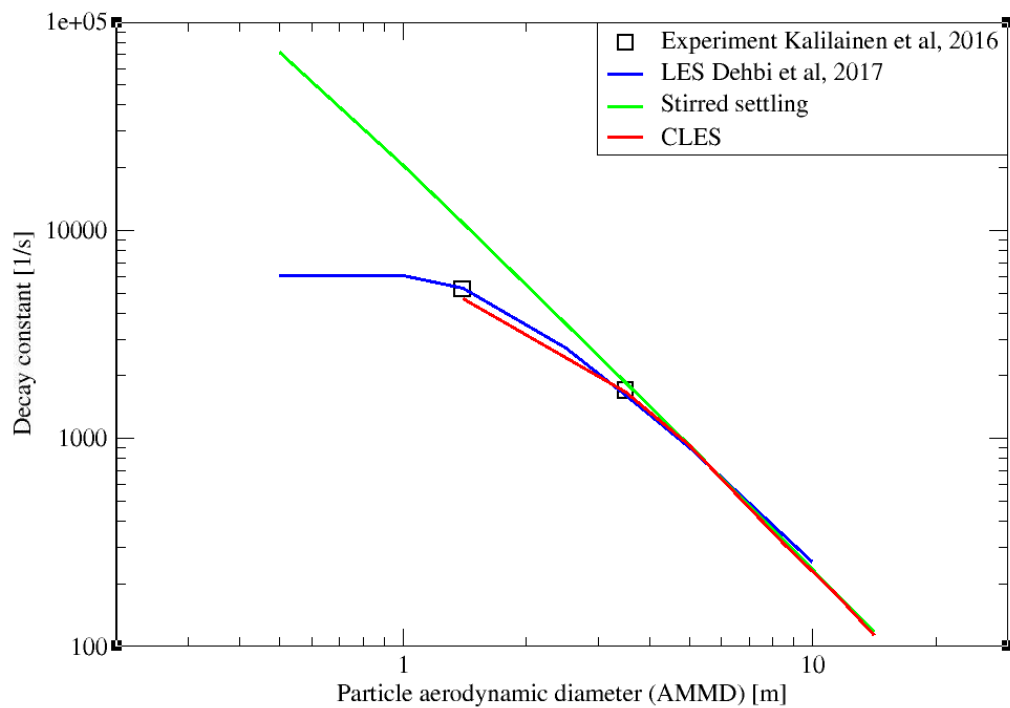
Figure 5.38 – Comparison for particle decay constant obtained by ANSYS Fluent, 2015

This is laid out with other perspectives and recommendations as will be shown next in the Summary Section (Section 5.5).
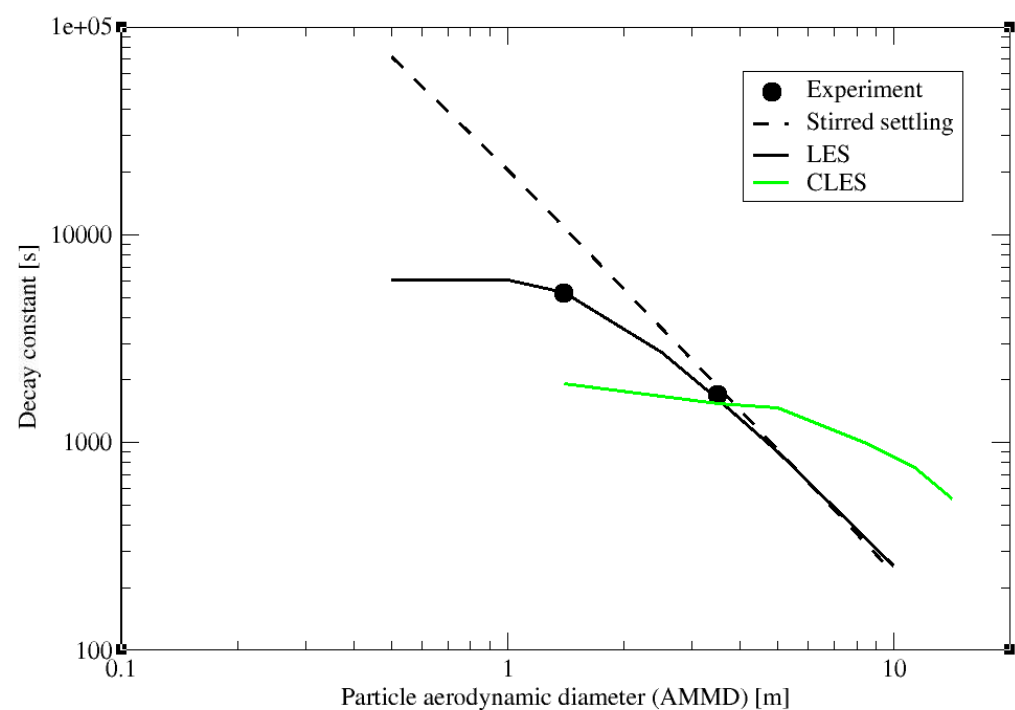
Figure 5.39 – Comparison for particle decay constant obtained by T-Flows - Ničeno, 2001

5.5 Conclusions

The flow field inside a three-dimensional, wall-bounded, differentially heated cavity (DHC) has been investigated using Large Eddy Simulations on a mesh significantly coarser than used in a previous research at Rayleigh number of Ra = 10^9. In particular, two LES models have been used, the Smagorinsky standard and dynamic models. Wall-to-wall radiation effects have been implicitly taken into account by imposing the measured temperature profiles of bottom and top walls as Dirichlet BCs in all simulations. An extensive quantitative analysis is reported for the fluid flow where first and second-moment statistics are reported. The results are compared against both well-resolved LES by Dehbi et al., 2017 and the experimental database by Kalilainen et al., 2016 at different locations across the domain. On a qualitative level, mean and instantaneous fields of both fluid temperature and velocity have been shown to capture the correct physics. Temperature iso-contours were shown to produce the well-known hook-like structures due to very high curvature at the cavity corners. Noticeable findings of centrosymmetric temperature and velocity fields as well as counter-rotating secondary flow structures in the core region have been reported.

It was shown that both coarse LES models can predict the mean flow properly. However, for high moments i.e. RMS values for horizontal and vertical velocity fluctuations, a significant underprediction of the flow statistics was observed in the near-wall region by the standard Smagorinsky model. On the other hand, the dynamic model predictions match the reference LES and experimental databases very well. The main reason behind this difference is that the eddy viscosity values are better predicted near the wall by the dynamically adjusted model coefficient, and hence the flow is well represented compared to the standard model.

The first and second central moment statistics by the coarse dynamic Smagorinsky model are globally in very good agreement with reference LES and experimental measurements at a fraction of CPU cost relative to LES by Dehbi et al., 2017. The obtained results agree on both qualitative and quantitative levels with the results obtained by LES of Dehbi et al., 2017, DNS of Puragliesi et al., 2011, and the experimental measurements of Kalilainen et al., 2016. Good performance of coarse dynamic LES simulation with less than 0.2 million compared to the 2.4 million-cell-mesh of well-resolved LES confirms that for coarse LES of cavity flow with the right SGS model can still be used for further fluid flow investigations.

In a second step, the accurate predictions of the fluid flow were used to feed particle tracking in an Euler/Lagrange frame. In a systematic study, seven swarms of 10^5 particles each were computed to investigate a wide range of particle aerodynamic diameters $d_p = 1.4 - 14 \ \mu$m. In particular, predictions of particle depletion rates for $d_p = 1.4, 3.5 \ \mu$m obtained by coarse LES were compared to reference LES and experimental databases. Results show a considerable deviation from the trend of depletion rate in a way that particle sizes below 3.5 μm have an overpredicted deposition rate, whereas above that limit it becomes underpredicted. This effect is more justified in sub-micro and low-inertia particles where turbulent fluctuations are more relevant. However, mid-to-high inertia particles still showed a considerable deviation from

the reference data for particle deposition. This discrepancy is mostly resorted to the low-order integration scheme used for LPT in T-Flows. It must be also pointed out that insufficient time interval obtained by T-Flows due to the huge CPU needed for a prolonged simulation prevents us from drawing a safe conclusion about the accuracy of integration scheme from the lack of thereof.

To eliminate all sources of error, a similar systematic investigation was done using ANSYS Fluent, 2015 code. The aim of such analysis is to compare the results of the same code (i.e. Fluent) to compare the prediction of low-to-high resolution meshes against reference data. Fluent results showed that the mesh resolution has a pronounced effect only on smaller particles, where the under-resolved motions are more relevant (Sayed et al., 2022). On the other hand, Fluent showed a very good agreement with the reference data for high-inertia particles. It was also found that the mesh resolution in the near-wall region is quite significant for accurate particle depletion results.

Good performance of coarse dynamic LES simulation using ANSYS Fluent with less than 0.125 million cells compared to the 2.4 million-cell-mesh of well-resolved LES confirms that for the cavity simulation, CLES with the right SGS model can still be used to predict accurately the motion of a specific band of particle sizes. Authors consider the finding of the present study a promising step for further complex particulate flow investigation using coarse LES.

Through a sensitivity computation of two particle sizes, it was found that the inclusion of the thermophoretic force is the main driver for the unique spatial deposition pattern. It was be noted however that thermophoresis has little effect on the depletion rates of particles in general. This is due to the strong turbulent diffusion which is the overriding cause for the significant deposition rates of smaller particles. This comes in alignment with the observations reported by Dehbi et al., 2017. As will be shown in the Summary Chapter, we give some perspectives recommendation for future investigations of particulate flow inside DHC.

6 High-efficiency Dust Separator

Figure 6.1 – A schematic showing particle dispersion across gas cyclone at different time instances. The simulation is performed using the dynamic Smagorinsky model in T-Flows.

6.1 Introduction

Gas cyclone separators have been for a long time used in many industrial sectors, varying from agro and pharma services to mining and petrochemical projects. In particular, reverse flow cyclones are the most commonly used high-efficiency separation devices. Despite their simple configuration, the shape optimization of gas cyclones is far from being a simple task. In addition, the associated flow dynamics inside the cyclone is extremely sophisticated due to the inherent instability and high anisotropy levels of its swirling flow. In contemplation of tackling this complexity, CFD simulations have been used to give a comprehensive inspection of the turbulent flow field, and therefore assess the performance of cyclone separators. This has been reported in both experimental and numerical investigations across the literature, some of which are Azadi et al., 2010; Bhaskar et al., 2007; Brar et al., 2015; Chuah et al., 2006; Derksen, 2003; Derksen et al., 2006; Derksen et al., 2008; Erol et al., 2019; Hoekstra, 2000; Hoekstra et al., 1999; Jiao et al., 2006; José de Souza et al., 2012; Kepa, 2010; Raoufi et al., 2008; Sayed et al., 2021-a; Schuetz et al., 2004; Shi and Bayless, 2007; Wan et al., 2008; B. Wang et al., 2006. The first cyclone CFD-based predictions go back to the early numerical simulations of a turbulent flow field in 1982 Boysan et al., 1982.

In order to accurately predict the performance of gas cyclones, the choice of the turbulence model is very crucial to the prediction of collection efficiency. Out of many turbulence models reported in the literature, the Re-normalization group k-epsilon (RNG $k - \epsilon$) and the Reynolds Stress (RSM) turbulence models coupled with Lagrangian Particle Tracking (LPT) seem to have been the most preferred choice when investigating separation efficiency Azadi et al., 2010; Bernardo et al., 2006; Bhaskar et al., 2007; Chuah et al., 2006; Derksen, 2003; Elsayed and Lacor, 2012, 2011-b, 2011-a; Gimbun et al., 2005; Griffiths and Boysan, 1996; Hoekstra, 2000; Jiao et al., 2006; Kepa, 2010; Ma et al., 2000; Masoud and Shahidzadeh, 2011; Narasimha et al., 2007; Qiu et al., 2012; Raoufi et al., 2008; Safikhani et al., 2011; Schuetz et al., 2004; Shi and Bayless, 2007; Shukla et al., 2011a; Su et al., 2011; Valverde et al., 2011; Wan et al., 2008; B. Wang et al., 2006; Zhao et al., 2006. In the context of particle separation prediction, most reported studies use the common Discrete Random Walk (DRW) as a dispersion model. Despite being easy to implement in CFD codes, the DRW method suffers from a static nature where the integral timescale for particles has to be pre-assigned by the user as an input parameter. This in turn makes the model quite cumbersome to use for different flow configurations. In addition, the used input parameters are usually missing from most publications which hinder the reproducibility of results.

In such high-level of flow anisotropy like in a gas cyclone - which can be easily spotted from the tangential velocity being one order of magnitude higher than the axial velocity and two orders higher than the radial component - standard Reynolds Average Navier Stokes (RANS) models fail to describe the flow turbulent quantities. In that light, it was shown by Hoekstra et al., 1999; Kaya and Karagoz, 2008 that the RNG $k - \epsilon$ model gives unrealistic predictions for both the tangential and axial velocity components. In particular, it was reported by Elsayed and Lacor, 2011-a; Hoekstra, 2000; Kaya and Karagoz, 2008 the standard $k - \epsilon$ and RNG $k - \epsilon$

turbulence models give nonphysical representation of the axial velocity profiles close to the wall. This is mainly caused by the co-existence of highly-anisotropic and swirling motions that are not accounted for by these models.

In contrast, the Reynolds stress models (RMS) - owing to the fact that they employ one transport equation for each component of the Reynolds stress tensor (τ_{ij}), are naturally more suited for swirling flows with dominant anisotropic effects. This was comprehensively shown in several studies, some of which are Jiao et al., 2006; R.B. Xiang and Lee, 2005; Shukla et al., 2011b; Slack et al., 2000; B. Wang et al., 2006. However, it was demonstrated in Gronald and Derksen, 2011; Martignoni et al., 2007; Pisarev et al., 2011 that, for higher-moment Eulerian statistics, velocity fluctuations are considerably underpredicted by RSM. In that regard, {José de Souza et al., 2012 raises the question: How do results from the RSM alongside the DRW models fit the experimental data very well, when the main feed for the DRW are considerably underpredicted RMS velocity values Azadi et al., 2010; Bhaskar et al., 2007; Chuah et al., 2006; Gimbun et al., 2005; Raoufi et al., 2008; Safikhani et al., 2011; Su et al., 2011; Wan et al., 2008; B. Wang et al., 2006. In response to that question, the author of the present work suggests that in spite of the importance of the turbulent fluctuations on particle movement, the driving force for predicting cyclone performance is the strong swirling motion which is the main source of the centrifugal force pushing particles towards the walls. Another claim could be that the authors might have tuned the input parameters for the turbulent dispersion model to achieve such good agreement with the measured grade efficiency in the experiment.

In spite of the RSM models' capability of providing good results regarding the separation efficiency of cyclone separators, it is still unequivocally better to use LES for two reasons. The first one is that the flow inside gas cyclones is inherently unstable and therefore LES being a transient approach is more suited to represent the flow, whereas RSM can be very difficult to converge. The second reason is that since RANS models are based on temporal averaging, they always need to be complemented by stochastic Eddy Interaction Models (SEIM) (also known as turbulence dispersion models) for particles to sense turbulence. LES, on the other hand, provides by default the flow instantaneous field seen by particle, for which one does not require any additional dispersion models - removing one layer of modeling from the LPT process (i.e. adding artificial stochasticity). This is usually the case, especially since the smallest resolved motion scales are the minimum ones affecting the dispersion of the corresponding particle size. In that regard, it is no wonder that a finer mesh will already imply less contribution from the sub-grid scale (SGS) model on particle motion. In view of the LES simulation of cyclone separators, there are plenty of publications that demonstrated the superiority of LES to RANS in predicting both the carrier gas flow and the particle collection efficiency. Some of those contributions are: Derksen, 2003; Derksen et al., 2006; Derksen and Van den Akker, 2000; Elsayed and Lacor, 2014; Jang et al., 2018; José de Souza et al., 2012; Martignoni et al., 2007; Wasilewski et al., 2019.

Given the privilege of having a time-dependent solution that is pertinent to the inherently-transient highly-swirling flow inside the cyclone and the better resolution obtained for both

continuous and dispersed phases, it might sound intuitive that LES is the best choice for approaching the flow inside gas cyclones. However, it must be acknowledged that LES still suffers from the computational expense that can be significant in such complex flows, especially at high Reynolds numbers. As an alternative, the hybrid RANS/LES methods can be used as a trade-off between RANS-like grid resolutions and LES accuracy. In this chapter, we investigate the Elliptic Relaxation hybrid RANS/LES (ER-HRL) approach to assess its capability for predicting cyclone performance at a relatively lower cost than LES. As mentioned in Chapter 4, the model is based on an explicit RANS formulation close to the wall while accounting for wall-anisotropy and switches to LES in the bulk region. The model was shown to be an impressive prediction of channel flow, proved to be robust and cost-effective in both canonical and complex industrial benchmarks Hadziabdic and Hanjalic, 2020; Sayed et al., 2021-b with a considerable reduction in CPU power relative to traditional LES - and without considerably compromising the accuracy. Such advantages were the main impetus to use the model for the present investigation of the reversed flow gas cyclone.

The ER-HRL model was used for the first time to solve the fluid flow inside the cyclone separator in Sayed et al., 2021-a where a high Reynolds number of Re = 280,000 was investigated. As a continuation of that work, this chapter outlines a further investigation of cyclone performance through particle separation prediction. As will be shown later, the fluid flow prediction is first compared against the reference LES and experimental databases Derksen, 2003; Hoekstra, 2000 at Reynolds number Re = 280,000. Secondly, a chosen volume flow rate i.e. Q = 40 l/min was computed where twelve swarm simulations were performed to cover a wide range of particle Stokes numbers (i.e. St = 2.3 x 10^{-4} - 3.3 x 10^{-2}). Grade efficiency prediction of the ER-HRL model will be compared to LES and experimental data from José de Souza et al., 2012; Xiang et al., 2001.

6.2   Geometry and numerical setup

A typical geometry layout that corresponds to the Stairmad high-efficiency cyclone separator was adopted (Fig. 6.2). As shown below, we consider the reversed flow cyclone configuration used in José de Souza et al., 2012. In such a configuration, the tangential inlet creates the swirling motion of the gas flow which then forces particles to be centrifuged out towards the cyclone's outer walls. As a result, particles are finally collected in the dust bin collector (also known as the dust hopper), or they escape out of the dipleg (vortex finder) according to their sizes.
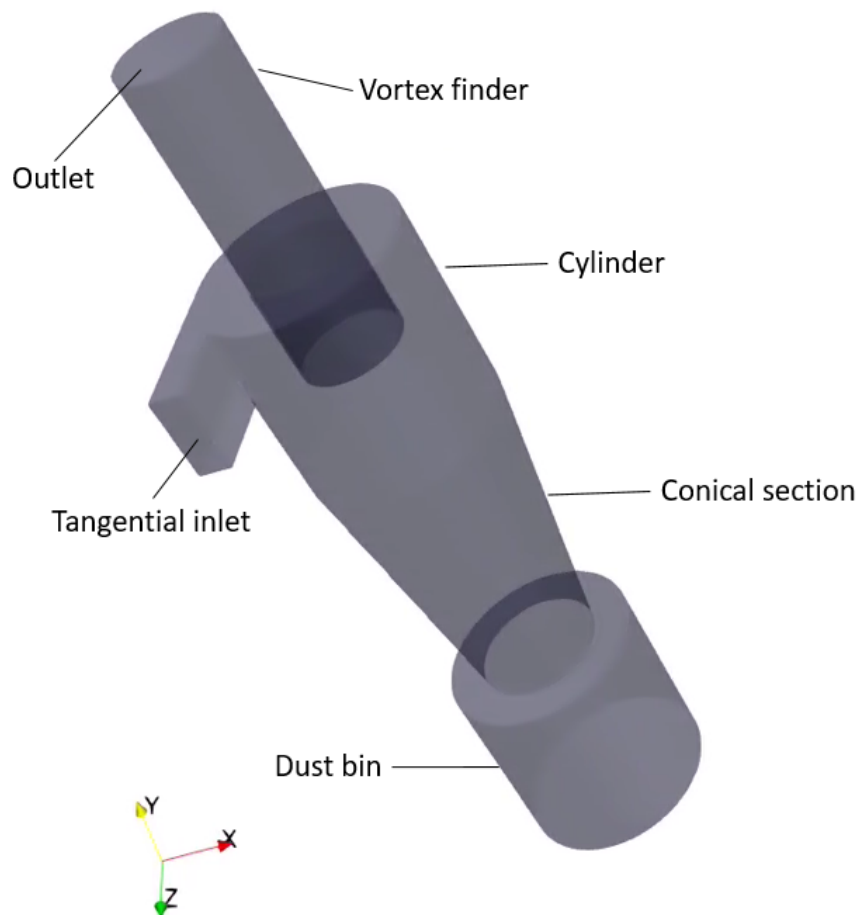
Figure 6.2 – Schematic diagram of the used cyclone separator

As shown in Fig. 6.3, the cyclone geometry is prescribed by ten parameters (as in Table 6.1). The unique flow inside the cyclone incorporates two main interwoven sources that affect particle movement: turbulent structures and the flow swirl. Although both of those competing factors affect particle dispersion, the swirling motion is considered the driving force behind separation (due to the attributed centrifugal force). Turbulence on the other hand is more significant in diffusing particles which enhances the likelihood of light particles getting caught in the exit stream (through the vortex finder).

As mentioned in Derksen, 2003, results of the gas cyclone are insensitive to the specific inlet velocity profile: comparing simulations with uniform and parabolic inlet profiles shows hardly any differences in terms of the average velocities and fluctuation levels in the body of the cyclone. It was argued that this insensitivity is likely due to the virulent region where the inlet flow merges with the swirling gas already present (at the cylindrical part of the cyclone body). In this region, the gas quickly forgets the history (dynamics) in the inflow tangential channel. Based on this, the inlet velocity was set to have a flat profile of 16.1 m/s. The Reynolds number achieved for the fluid flow validation is Re = 280,000 based on the inlet velocity and cyclone cylinder diameter. The exit is set as pressure outlet, and the no-slip condition is imposed on the walls. For the pressure velocity coupling, we use the semi-implicit method pressure-linked equations (SIMPLE) algorithm. For both momentum and turbulent transport equations, the SMART advection scheme was used. The time step size was prescribed to achieve a time-accurate solution with the maximum Courant number (CFL) ≤ 1 throughout all the simulations. For this, the time step size used for the unsteady flow simulation is $5x10^{-6}s$. The air fluid density and viscosity were set to be 1.125 kg/m^3 and 1.789 x 10^{-5} $kg \cdot m^{-1} \cdot s^{-1}$.

As will be shown in the Results Section, the ER-HRL model is validated against the reference experimental data Hoekstra, 2000 that consist of velocity profiles measured by Laser Doppler Anemometry (LDA). To have a one-to-one comparison with the chosen LES and experimental databases i.e. Derksen, 2003; Hoekstra, 2000; José de Souza et al., 2012, we probe mean and RMS velocity profiles at three positions across the cyclone axis (as in Fig. 6.3) as a function of the barrel diameter (D_c). Distances are measured from the dustbin entrance where the y coordinates of each are position 1 = $1.015D_c$, position 2 = $1.16D_c$ position 3 = $1.52D_c$ (i.e. y_1 = 0.031456 m, y_2 = 0.03596 m, y_3 = 0.04712 m). As mentioned above, the flow inside the cyclone geometry is naturally unstable due to anisotropic and swirling effects. This makes it quite challenging for the solver to converge. For this sake, we use a standard RANS model first to develop the flow across the cyclone axis. The model is then swiftly switched from the RANS to the desired hybrid turbulence model once (at least) one flow-through time is achieved. The turbulence transport equations $k - \epsilon - \zeta - F$ have been initialized by the values 0.005, 0.001, 0.1, 0.1 respectively.

As shown in Fig. 6.4, a 570,000 element fully hexahedral block-structured grid was used in all simulations. It is worth mentioning that the cell count of the employed mesh is similar to the ones used in the literature for porous LES. The grid resolution has been refined in the near-wall region to have a first cell height of 1mm. Such resolution ensures a smooth convergence of the solution but also a well-treated boundary layer. It was mentioned by Derksen, 2003 that the convergence of flow statistics can be reached around 25 units of integral timescale δ_v (i.e. $\delta_v = D_c/U_{in}$). In this work, we report 40 units to be a good instance to start collecting turbulent statistics. Once engaged, the Eulerian statistics were gathered over the span of 80 other time units where the flow was assumed statistically stationary. It should be noted that the velocity field seen by the particle, in this case, is purely the resolved motion scales, whereas the SGS effects were not included. This is because the $\zeta - SGS$ model was originally implemented to account for flat-wall-bounded turbulent flows. Therefore, a further generalization of the

model can be an interesting perspective to encompass curved walls and arbitrary geometries.

For particle analysis, we compute the flow at a volume flow rate of Q = 40 L/min, to compare with the results obtained by José de Souza et al., 2012. Once the primary flow was considered to be statistically stationary, 5000 particles with a mass density of 6085 kg/m^3 were injected at the inlet section in a random Gaussian distribution. The interaction force between particles is usually ignored due to the negligible particle-particle collisions Elghobashi, 1994. This is usually the case since the dispersed phase occupies a low volume fraction (i.e. of the order of $10^{-4} - 10^{-5}$) in most particle-laden flows). That said, we assume one-way coupling as well as non-colliding particles throughout this case. This simplification is not only motivated by computational considerations but also justified by the nature of high-efficiency cyclones. In contrast to high-throughput cyclones, high-efficiency cyclones separators are usually located in the final stage of the separation process (i.e. when the volume fraction of the dispersed phase is relatively very small, and only fine particles are left in the gas stream).

The particles are treated as point-mass solid spherical elements spanning a range of sizes i.e. d_p = 5 - 60 μm. For particle collection, walls were assumed to be "sticky" i.e. particles are deposited once they touch the wall surface. Also, particles are removed from the computational domain upon deposition. It must be pointed out that the particle time step was adjusted according to the Nyquist criterion to guarantee temporal accuracy for particle transport. In this configuration, particle time step size was assigned to be less than or equal to half of the particle relaxation time (i.e. $\leq \tau_p/2$) as shown in Table 6.2.

Table 6.1 – Cyclone design parameters with the used dimensions

Design Parameters	Dimensions(m) Jose et al., 2012	Dimensions(m) Sayed et al., 2021
Body diameter, Dc	0.031	0.276
Gas outlet diameter, De	0.0155	0.138
Inlet height, a	0.0125	0.112
Inlet width, b	0.005	0.045
Cyclone height, H	0.077	0.687
Cylinder height, h	0.031	0.276
Gas outlet duct length, S	0.0155	0.138
Vortex finder extension, V	0.0325	0.29
Cone bottom opening, B	0.005	0.045
Bin collector height, C	0.03	0.27
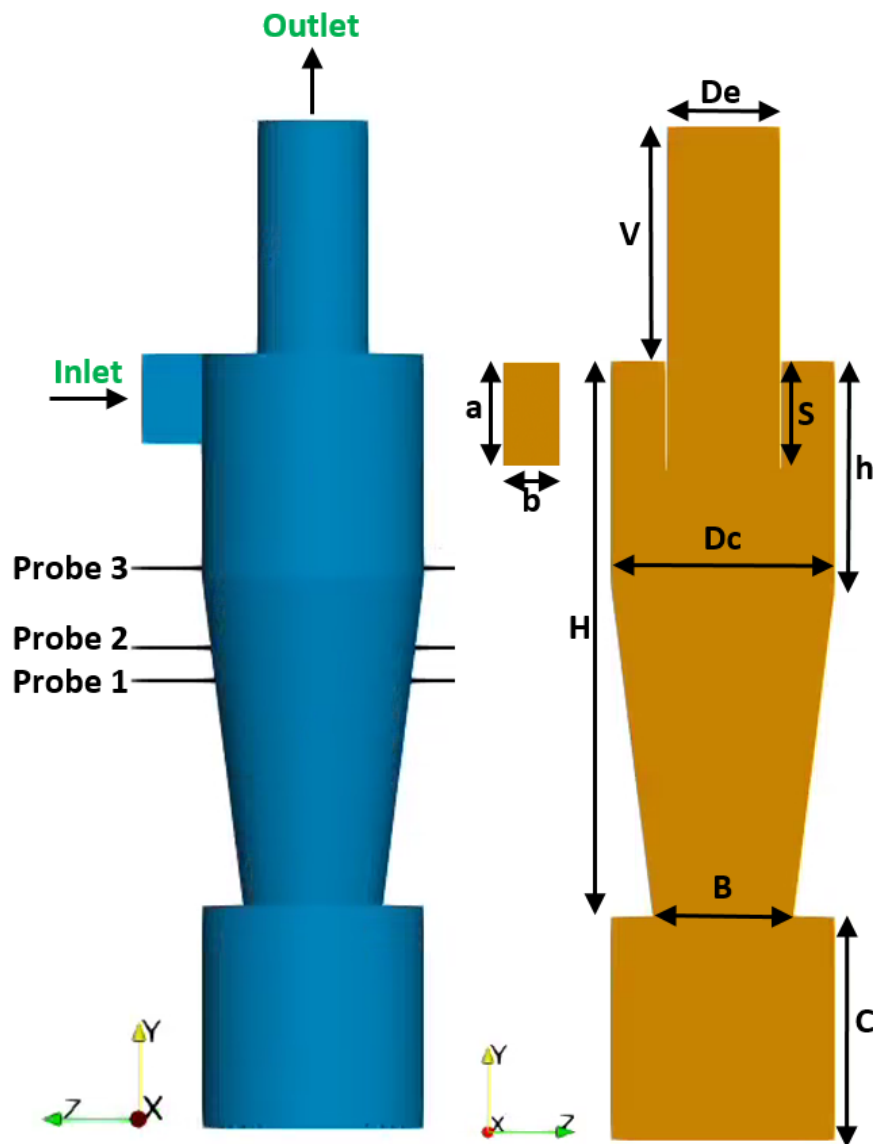
Figure 6.3 – Schematic showing the used gas cyclone separator with the main geometrical parameters (right), and measuring locations (left).

Figure 6.4 – Block-structured hexahedral mesh for cyclone 1. Mesh has 570,000 elements and wall refinement of 1mm for first cell size.

6.3   Primary flow results

In this section, we show the results of the fluid flow at Reynolds numbers i.e. $Re = 280,000$ based on cyclone barrel diameter and inlet velocity ($Re = U_{in}D_c/\nu$). It must be noted that the geometry was up-scaled by a factor of 8.9 to stay in the incompressible flow zone (Mach number < 0.3). To assess the accuracy of the ER-HRL model, we validate the obtained results by comparing tangential and axial velocity profiles to the experimental data by Hoekstra, 2000. The comparison is also held against LES predictions of both Derksen, 2003 and José de Souza et al., 2012. Quantitatively, both mean and RMS velocity profiles are reported at the above-mentioned three positions. As shown in Fig. 6.5, the model results produced by a similar coarse mesh to José de Souza et al., 2012 are closer to the fine LES by Derksen, 2003. While the mean flow is indicated to be captured properly, it can be seen that RMS values are underpredicted at the cyclone barrel i.e. position 3 (where the flow dynamics are the most challenging).

It should be mentioned that both reference LES and experimental data show pronounced levels of fluctuation at the center of the cyclone. This is due to the Precessing Vortex Core (PVC) which is believed to link the gradients of the average velocity to the RMS fluctuations (Derksen, 2003). This argument is based on the presupposition that the fluctuations induced by PVC at a point can be viewed as the result of the precessing motion of averaged velocity profiles over that point. It should also be pointed out that experimentally measured tangential RMS profiles show a local minimum at the center of the cyclone. This minimum is explained by the slight decrease of the average tangential velocity at the center plane. This feature is largely missed by the ER-HRL model as well as both LES predictions. As a consequence of this missed local minimum, some slight deviations from experimental data can be observed in the averaged tangential component from all ER-HRL and the LES results.

Similarly, by comparing the axial velocity component for both mean and RMS values, it could be seen that bigger deviations exist. From Fig. 6.6, it can be seen that the mean axial velocity predicted by the ER-HRL model is relatively close to LES predictions at the barrel section of the cyclone. However, more deviations tend to appear in the direction of the dust bin i.e. the magnitude is considerably missing at position 3 (at the conical section). Similarly, it can be noticed from the RMS profiles that, despite missing the amplitude, the trend of the RMS of axial velocity is well reproduced at the cylindrical section - whereas it departs from LES prediction and the experimental measurements at the conical part. It is worthwhile mentioning that, to realistically model the flow in the cyclone, the dust bin collector collection is needed to be included into the cyclone model. In the context of comparing LES predictions to the experimental measurements, it was shown by Derksen, 2003 that in the absence of the dust bin, strong deviations take place throughout the cyclone. In addition, the swirl intensity at the core of the main vortex is significantly amplified which reflects on the axial velocity profiles (departing from the expected behavior).
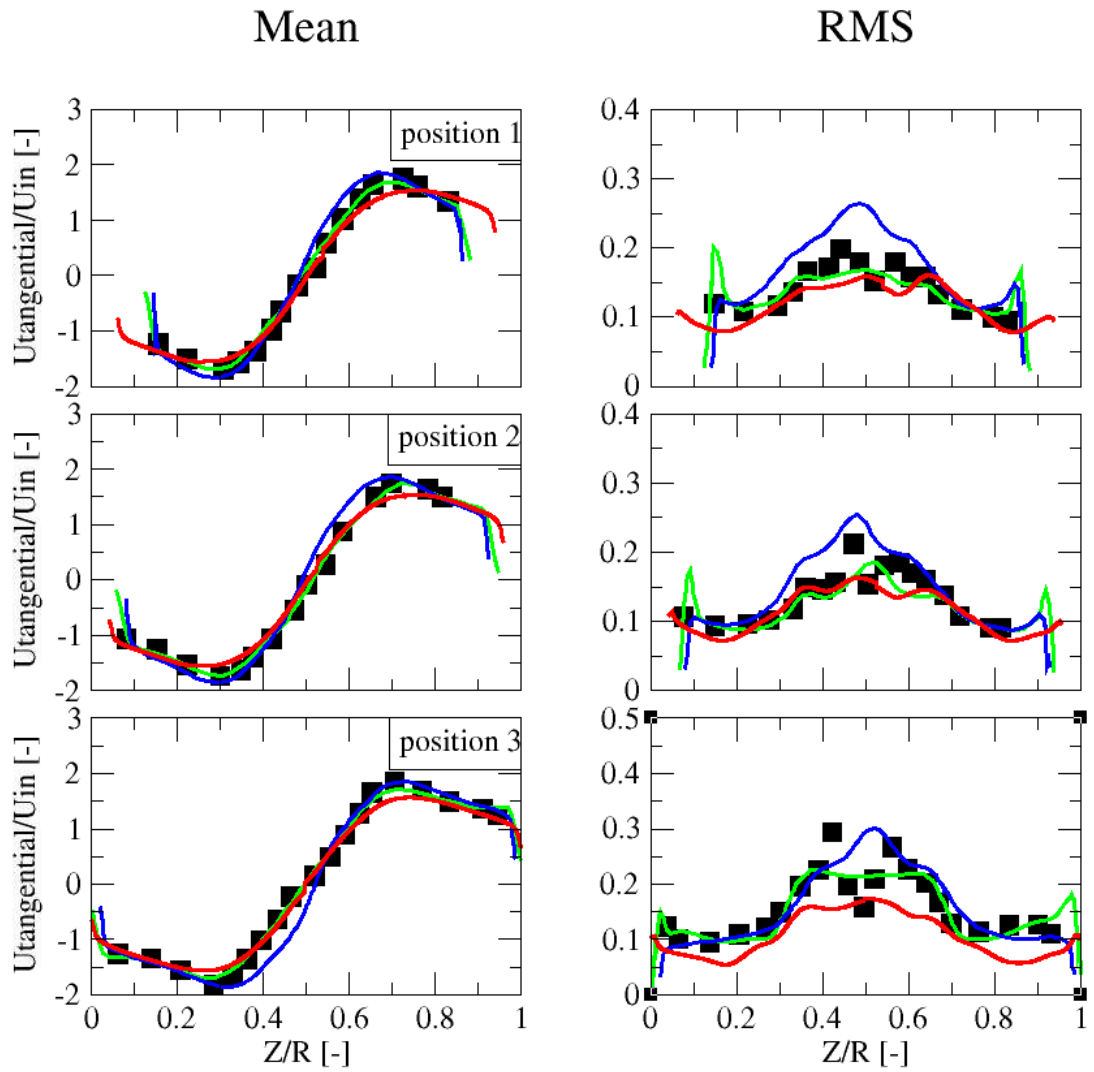
Figure 6.5 – Mean tangential velocity profiles at three different locations across the cyclone axis. Colors indicate results obtained from different sources; green represents LES from Derksen, 2003, blue shows results by José de Souza et al., 2012, red is our results obtained by the ER-HRL at Re=280,000, while black squares refer to the experimental measurements by Hoekstra, 2000.

In a qualitative fashion, we show a snapshot of the instantaneous velocity magnitude in Fig. 6.7. It can be anticipated from the velocity field at the mid-plane that the core vortex has a dominant effect on the flow dynamics inside the cyclone. Due to the high turbulent activity close to the wall, the subgrid-scale TKE has the highest values on the walls (Fig. 6.8). These results agree with the qualitative assessment by Derksen, 2003 where SGS TKE was reported to be one order of magnitude higher than the resolved one. In this light, it can be seen that both modes of the ER-HRL model (RANS-LES) are activated in the domain. This can be seen from Fig. 6.8, where the eddy viscosity has a peak near the wall where RANS is meant to be working.

Fig. 6.9 shows the energy spectrum based on the axial velocity at distance y=0.1m. The Figure highlights the inertial range of the energy cascade reported by Kolmogorov, 1991 where the -5/3 slope was successfully reproduced. The unique flow field inside the cyclone is significant for the analysis of core vortex motion. To visualize the flow in a better resolution, we show the stream-traces diagram within the cyclone as illustrated in Fig. 6.10. Such streamlines of fluid elements are important to understanding the main vortex structure.

As exhibited in Fig. 6.10-d, the double-layer vortex consisting of the outer vortex and the inner vortex observed by Gao et al., 2022 was reproduced from the stream-traces diagram. The gas entering the cyclone from the inlet section undergoes a downward spiral motion under the centrifugal force and is constrained by the barrel wall. This downward flow is considered the outer vortex flow, whereas the inner vortex flow is formed at the bottom of the conical section. This inner vortex flow stems from the pressure difference between the increasing pressure at the outer wall due to the decrease in cone diameter, and the relatively lower pressure at the central zone of the cone section. This inner flow is eventually discharged from the outlet section through the vortex finder.

With a closer look into the flow movement inside the cyclone, it can be inferred from Fig. 6.11 that both turbulence and swirling effects coexist throughout the domain. A large number of small vortices can be spotted near the wall. As illustrated in Fig. 6.11, this is more pronounced at two zones: the inlet section and the cone bottom (indicated as (a) and (b)). Such flow topology can explain the complexity of such three-dimensional flow. At the bottom of the vortex finder Fig.6.11-a, both the short-circuit flow and the secondary vortex phenomenon mentioned in previous studies were reproduced in the velocity vector diagram. As could be seen from Fig. 6.10, the flow inside the cyclone separator is a double-layer swirling turbulent flow. However, in addition to outer vortex flow and inner vortex flow, there are several coexisting transversal vortices. Such structures affect the flow symmetry in multiple ways such as the longitudinal circulation flow of the annular space, the short-circuiting flow near the outlet of the vortex finder, and the eccentric circulation flow near the bottom of the cone. As a consequence, such influences would propagate to affect separation efficiency and pressure drop.
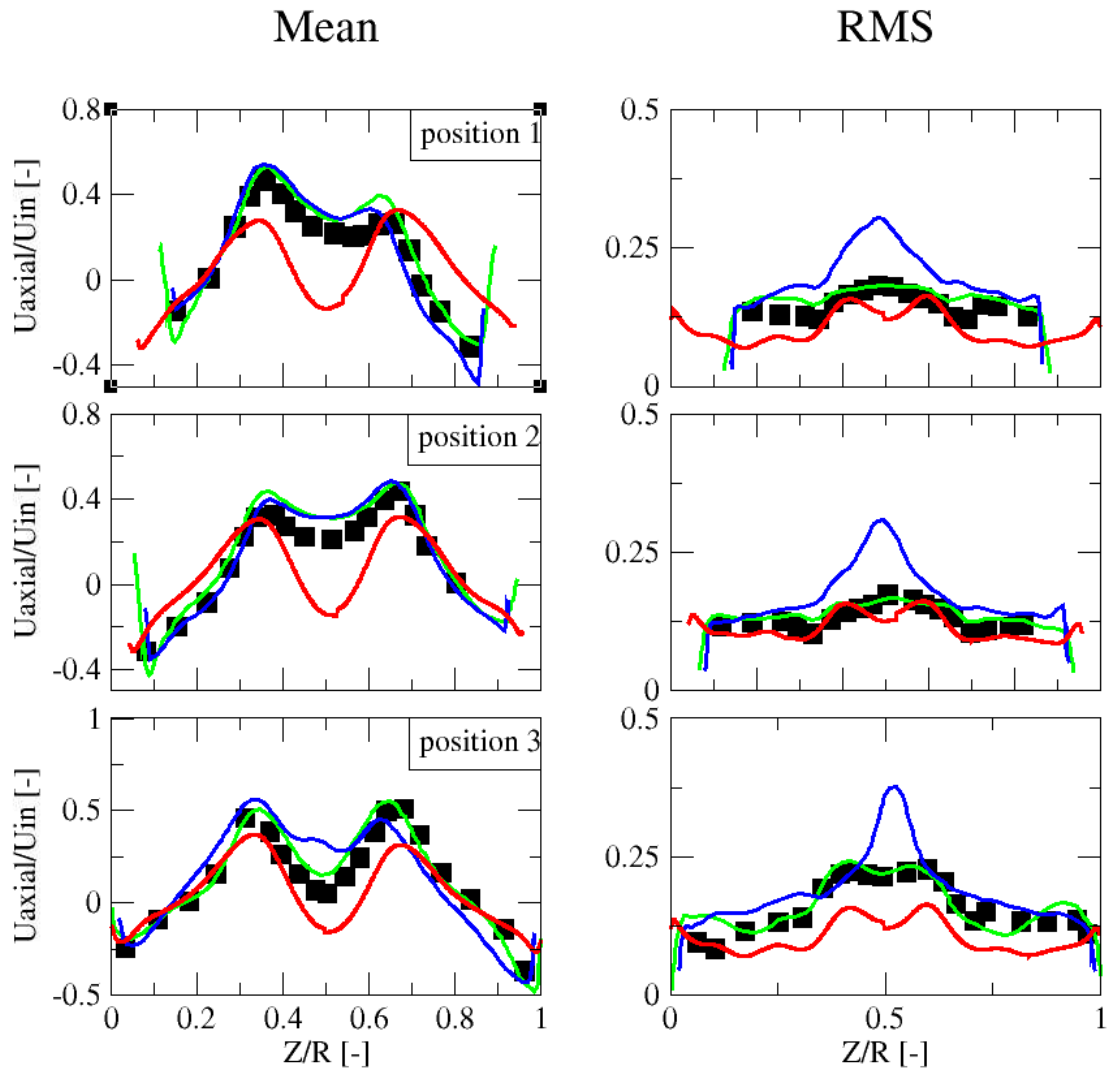
Figure 6.6 – Mean axial velocity profiles at three different locations across the cyclone axis. Colors indicate results obtained from different sources; green represents LES from Derksen, 2003, blue shows results by José de Souza et al., 2012, red is our results obtained by the ER-HRL model at Re=280,000, while black squares refer to the experimental measurements by Hoekstra, 2000.
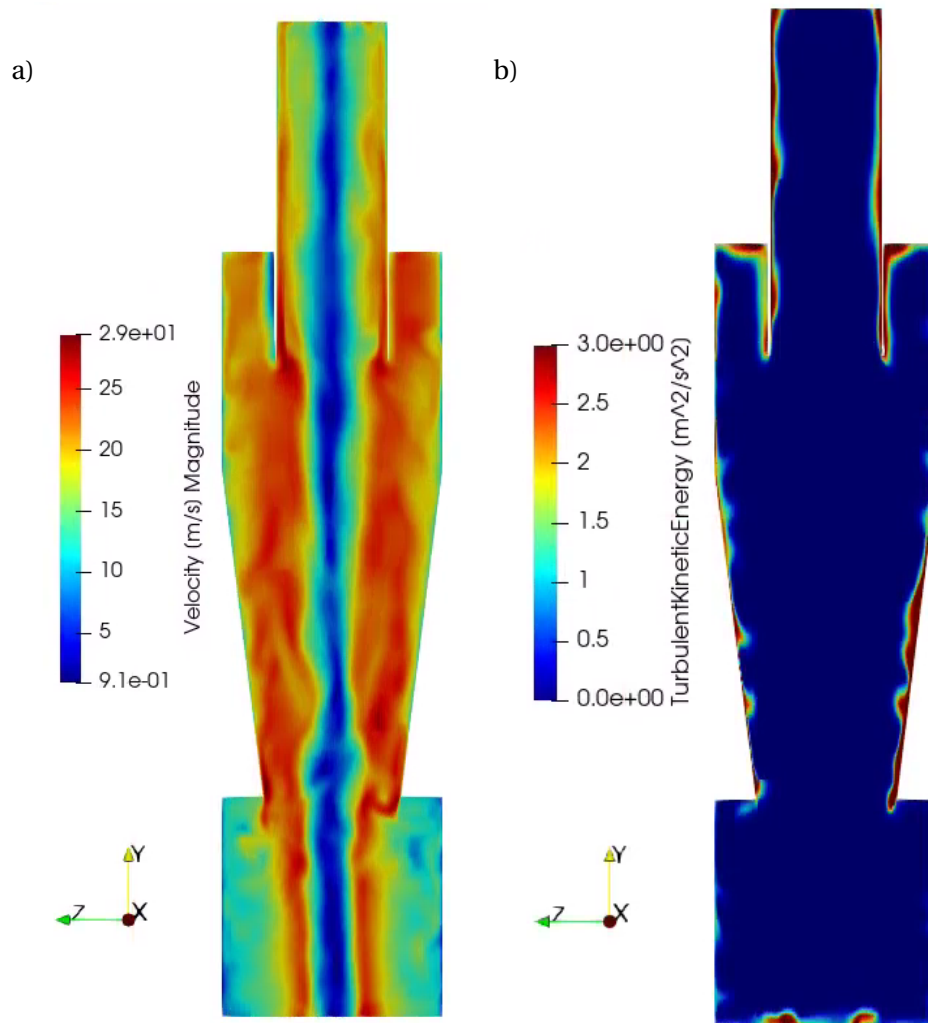
Figure 6.7 – Instantaneous velocity magnitude at mid-plane predicted by ER-HRL at t+ = $14\delta_v$
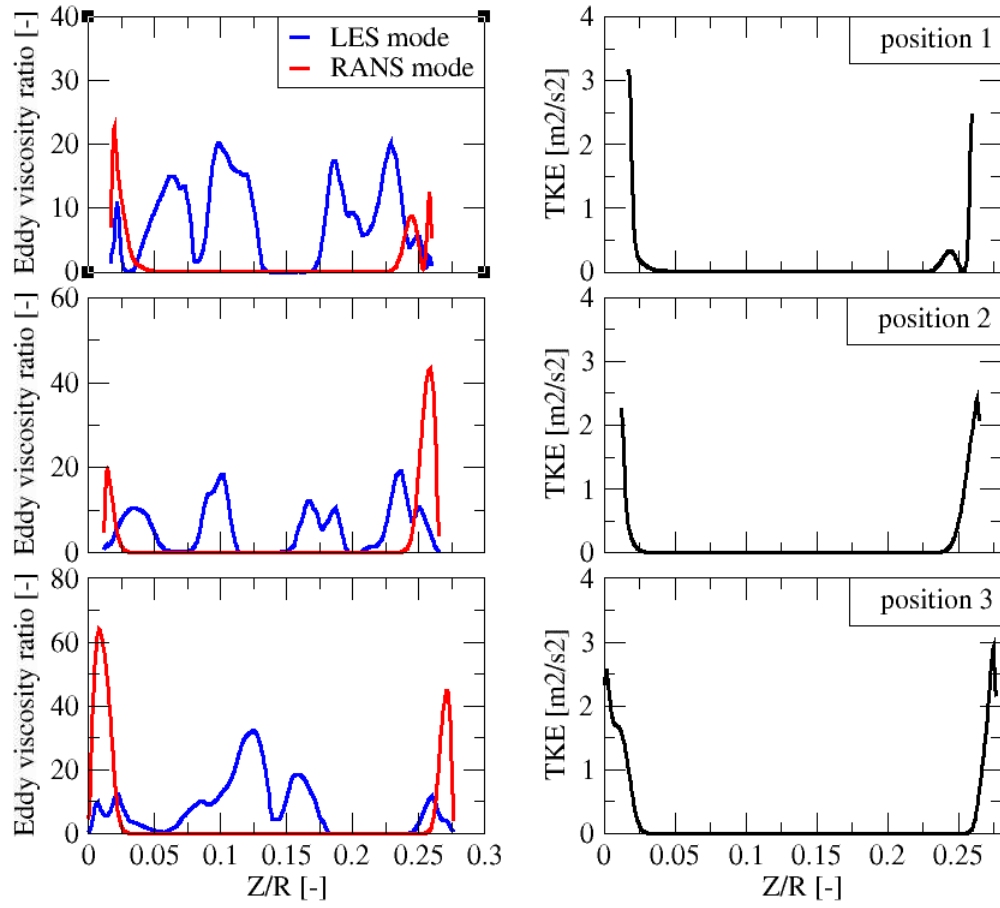
Figure 6.8 – Turbulent kinetic energy and eddy viscosity ratio measured at the three pre-specified locations at Cyclone 1.
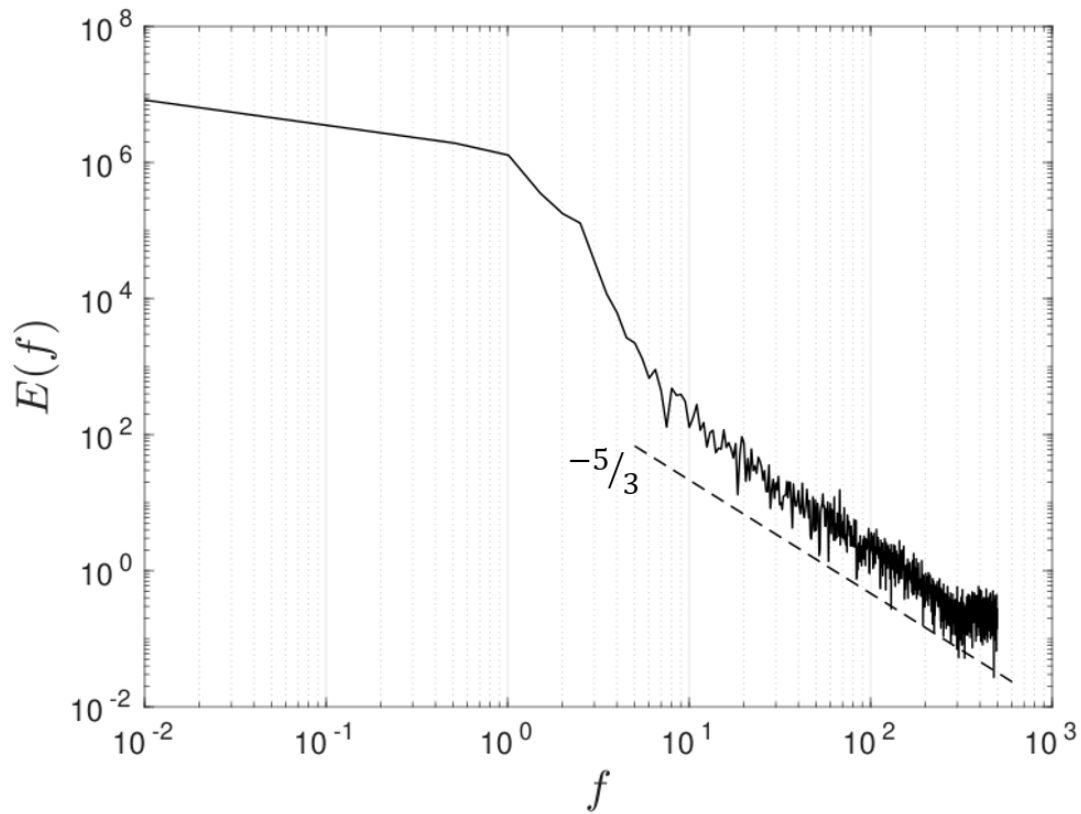
Figure 6.9 – Power spectra as a function of cyclone local frequency. The plot reproduces the theoretical slope of -5/3 (dashed line) at the inertial range of energy cascade Kolmogorov, 1991
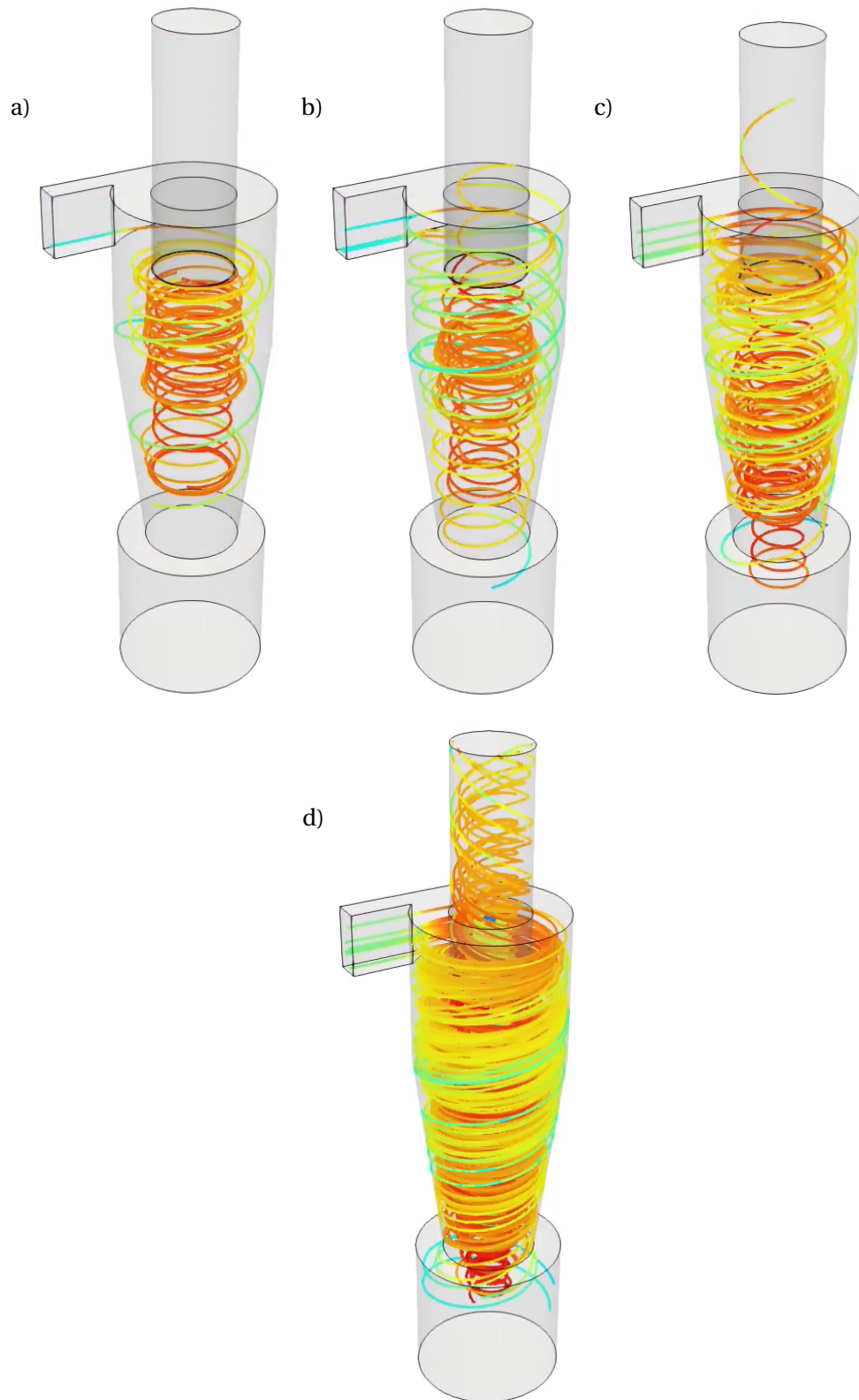
Figure 6.10 – Stream-tracers within the cyclone separator with equally spaced sampling points: a) 20 points; b) 50 points; c) 100 points; d) 500 points.
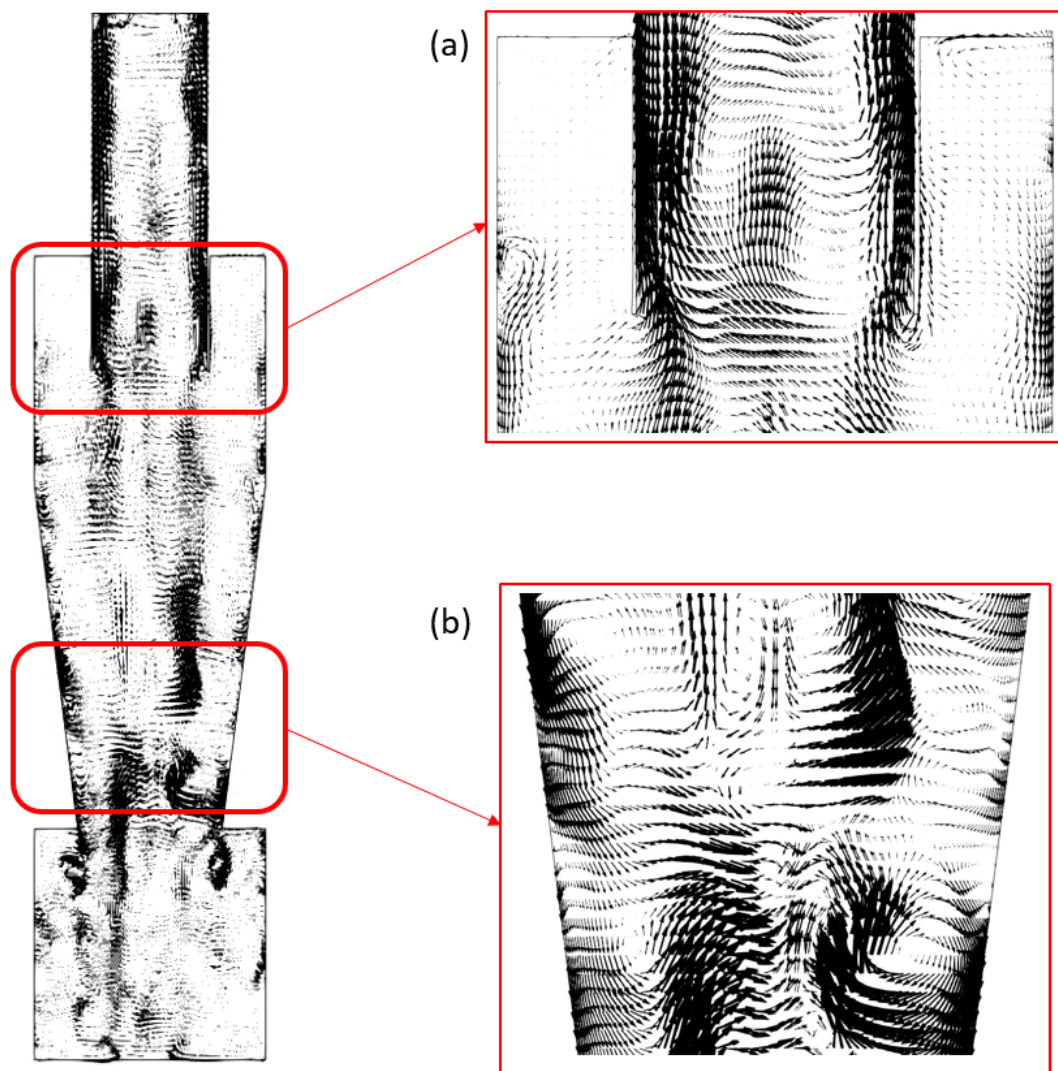
Figure 6.11 – Instantaneous velocity vectors scaled by the magnitude of the projected velocity at Y-Z mid-plane. The close-up of the inlet and cone bottom zones reveal the complex flow structures inside the cyclone.

6.4   Solid particle results

To study the collection efficiency of the Stairmand high-efficiency cyclone, twelve sets of different particle sizes were released in domain (as characterized in Table 6.2). The particles were considered to be non-colliding, spherical elements that experience gravity and Stokes-drag. One-way coupling was assumed, albeit that mass loading effects on cyclone separation performance have been witnessed for mass loadings as low as 1% (Ontko, 1996), that is, at very low particle volume fractions of the order of 10^{-5}. These assumptions imply that, given the flow geometry, the particulate flow problem is fully defined by three dimensionless numbers: the gas flow Reynolds number (defined above), and the particle Stokes number (i.e. $St = \frac{\tau_p}{\tau_f} = \frac{\rho d_p^2 D_c}{18\mu U_{in}}$), and the Froude number ($Fr = \frac{U_{in}^2}{D_c|g|}$ where g is the gravitational acceleration vector).

Following the analysis of José de Souza et al., 2012 which reported three flow rates (i.e. Q = 30, 40, 50 l/min) for the cyclone grade efficiency analysis, we choose one flow rate (Q = 40 l/min at Re= 22,000 and Fr = 374) to compare our model results against their LES as well as the experimental data from Xiang et al., 2001. All particle-wall collisions were considered to be non-elastic by setting the restitution coefficient to zero (i.e. particle is considered collected upon touching the wall). In addition, once a particle crossed the plane x = 3.5D i.e. the outflow boundary, it was considered to be exhausted.

Table 6.2 – Particle response time and Stokes number for each studied particle diameter. The volume flow rate is 40 l/min

$d_p(\mu$m)	particle Stokes number (-)	particle relaxation time (10^{-4}s)	particle time step (s)
5.0	2.29×10^{-4}	4.72	0.0002
10.0	9.15×10^{-4}	18.9	0.0005
15.0	2.06×10^{-3}	42.52	0.001
20.0	3.67×10^{-3}	75.59	0.0015
25.0	5.72×10^{-3}	118.1	0.003
30.0	8.24×10^{-3}	170.1	0.003
35.0	1.12×10^{-2}	231.5	0.003
40.0	1.46×10^{-2}	302.3	0.003
45.0	1.85×10^{-2}	382.7	0.003
50.0	2.29×10^{-2}	472.4	0.003
55.0	2.77×10^{-2}	571.6	0.003
60.0	3.30×10^{-2}	680.3	0.003

A set of twelve swarms of 5000 particles each spanning two orders of magnitude was investigated systematically and was computed to assess the model prediction of cyclone efficiency (as in Table 6.2). As shown in Fig. 6.12, grade efficiency was reported at different time instances during the simulation to check the convergence history of particle separation. The convergence history plots show that the 30 seconds can be deemed sufficient to assess particle statistics. This corresponds approximately to 1100 units of integral time scale δ_v.
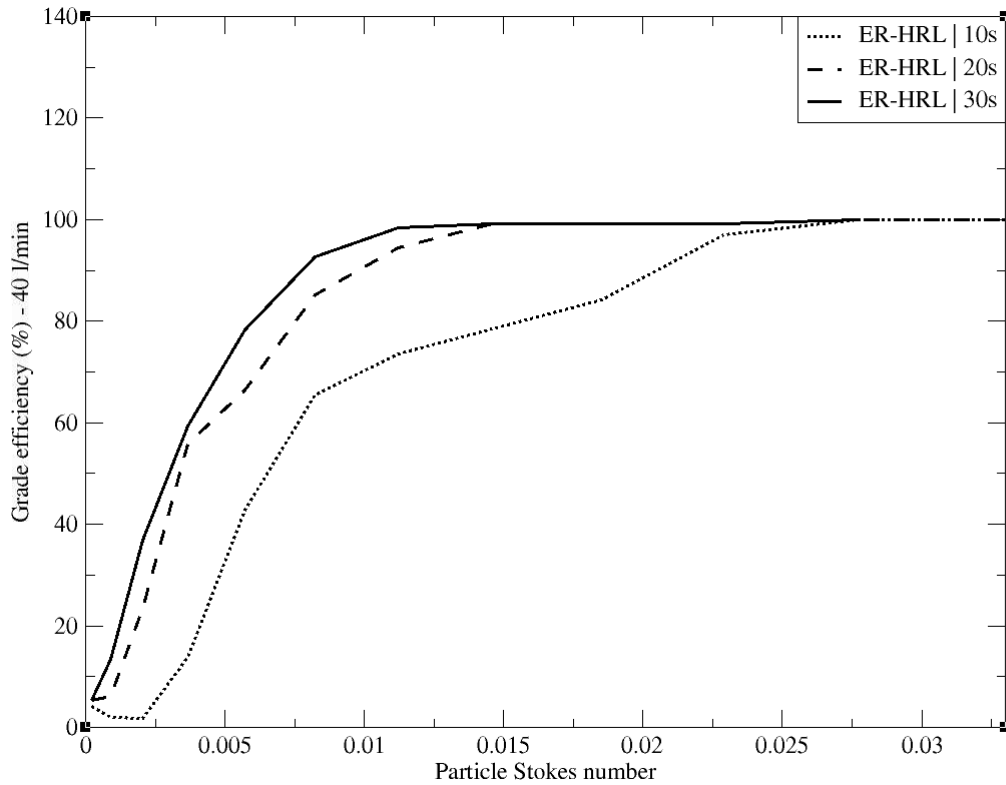
Figure 6.12 – Cyclone grade efficiency for 40 l/min using the ER-HRL model. Results are reported at several time instances showing the separation convergence history.

As seen from Fig. 6.13, cyclone separation efficiency obtained by the ER-HRL model is reported versus LES and experimental measurements. The cutoff diameter was estimated to be at $d_p = 20\mu m$. It can be seen from the figure that the ER-HRL model has a closer prediction to the experimental measurements than the LES by José de Souza et al., 2012. It can be noticed that lower-inertia particles have some deviation from the reference measurements. This is mainly due to the absence of SGS motions which are most influential on particle motion at the cylindrical section of the cyclone. It is important here to recall that the uncertainty of the experiment is relatively large in this range, with the 95% confidence interval varying from -6% to +6%. Therefore, such deviations are tolerable. It can also be seen from Fig.6.13 that, smaller deviations are exhibited for bigger-size particles, which conforms with the observation of José de Souza et al., 2012. Qualitatively, the predicted behavior of the numerical curves is consistent since they are sigmoid-shaped, as observed by Hoffmann and Stein, 2008. The average simulation time (for both continuous and discrete phases) is 65 hours which corresponds to 1040 CPU hours. This is a good improvement in terms of required computational power compared to the one needed to perform traditional LES by Derksen et al., 2008 who used 3600 CPU hours for each simulation.
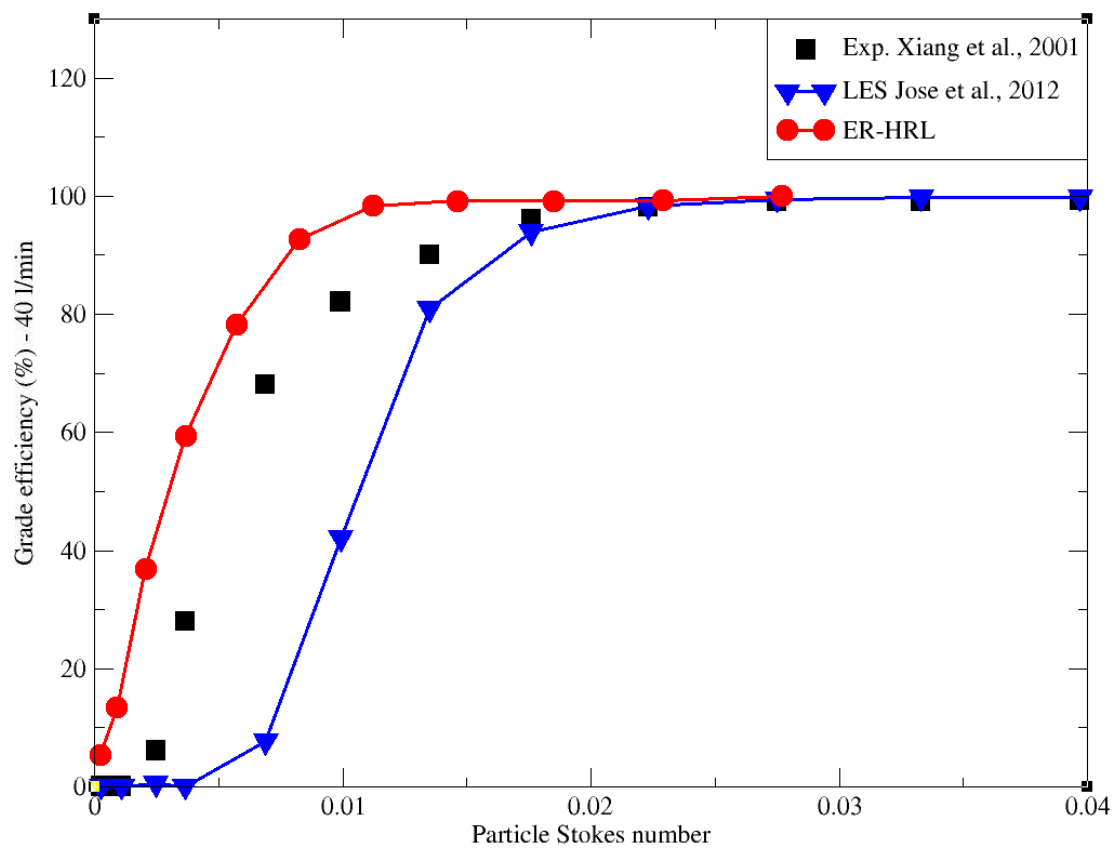
Figure 6.13 – Cyclone grade efficiency for 40 l/min using the ER-HRL model.

6.5   Conclusions

In this study, the ER-HRL model was investigated in a stairmand high-efficiency gas cyclone modeled with a dust bin collector at a high Reynolds number of Re = 280,000. The model predictions were compared to LES and experimental databases (Derksen, 2003; Hoekstra, 2000; José de Souza et al., 2012). Mean and RMS velocity profiles of both axial and tangential components are reported at different locations across the cyclone axis.

Results show that the model can predict the mean tangential velocity profiles fairly well. However, mean axial velocity predictions show a considerable deviation from reference data, especially at the conical section of the cyclone. Although the axial RMS values are following the same trend of the experiment, their magnitudes were also shown to be underpredicted. On the other hand, the RMS values of the tangential component give a relatively better prediction. The swirl intensity at the core of the main vortex was significantly amplified, which may have been reflected in the axial velocity profiles (departing from the expected behavior). Even though the ER-HRL model accounts for part of the wall anisotropy (through ζ transport equation), the author claims that it might be not sufficient to rely on RANS models based on linear eddy viscosity models in handling swirling flows with very strong anisotropic effects at the wall region. Given such flow configuration, the discrepancies in RMS profiles can be attributed to the missing two other variances (i.e. $\overline{u'u'}, \overline{w'w'}$).

Depending on the fact that higher-moment statistics are secondary to particle motion since the particulate flow, in this case, is impaction driven, a systematic analysis of twelve particle swarms was conducted to assess the model prediction of the cyclone separation efficiency. A wide range of particle sizes spanning two orders of magnitudes of Stokes number i.e. St = 2.3 x 10^{-4} - 3.3 x 10^{-2} was considered. Cyclone grade efficiency show better agreement with the experimental results by Xiang et al., 2001 than the ones obtained by LES of José de Souza et al., 2012. As will be shown later in the Summary Chapter, some recommendations are given to motivate a further continuation of this work.

7 Gas Droplet Separator: the ARTIST project - phase VI
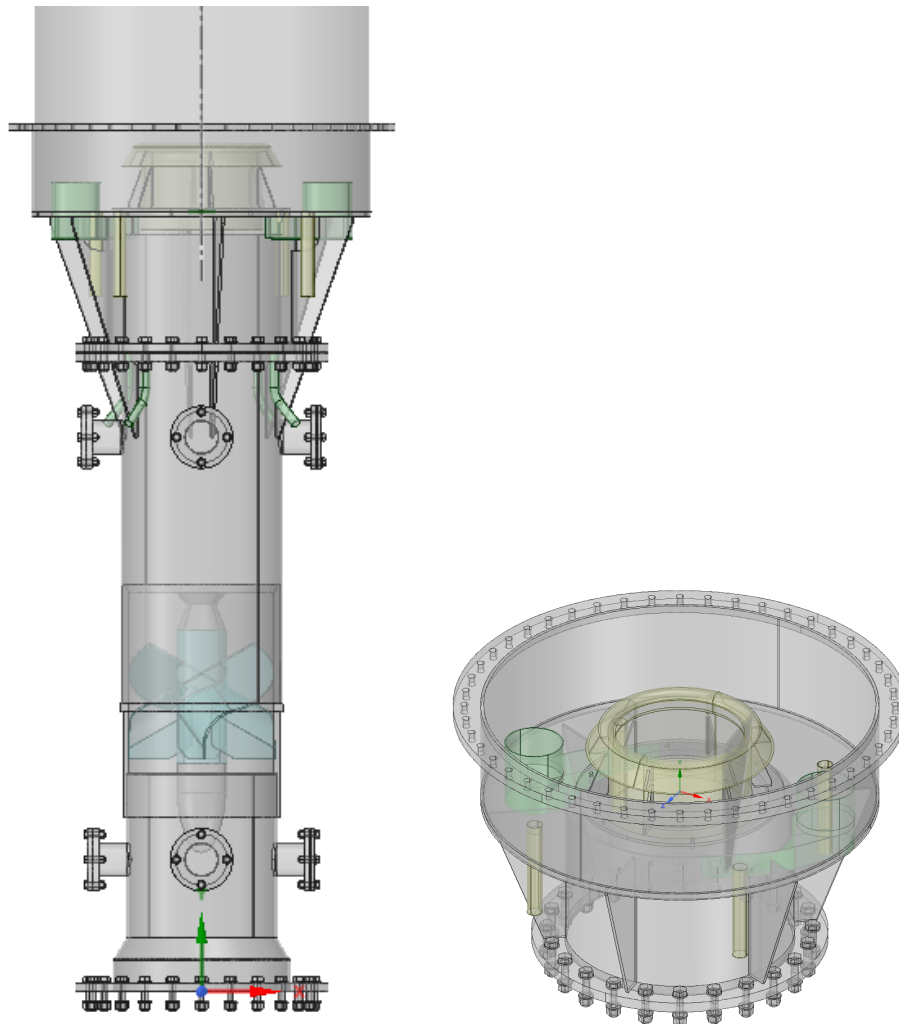
Figure 7.1 – CAD schematic of phase VI of the steam generator device - ARTIST.

7.1   Background and motivation

The international experimental program ARTIST (AeRosol Trapping In a STeam generator) addresses the fraction of liquid and/or solid aerosol borne radioactive material that could be retained in a steam generator (SG) due to interaction between the flows and internal structures. The ARTIST project was established by Paul Scherrer Institut (PSI) in 2002 in Switzerland. Through a five-year-time-span (i.e. 2002 - 2007), the project was designed to be a cost share international program that aimed at investigating the aerosol and droplet retention during a Steam Generator Tube Rapture (SGTR). Due to the lack of available data, probabilistic safety assessments (PSA) typically take little or no account of any retention of fission products in the secondary side, i.e. mainly the SG, although the complex geometry of the tube bank, support plates, separators and dryers in a SG provides a large surface area on which fission products may be trapped. In this light, a set of experiments were performed by Kapulla, 2008 addressing the velocity field and the droplet retention in the separator. All experiments were conducted in full scale (1:1) for both the SG and the dryer unit, see Fig. 7.2. The performed SGTR tests had helped to construct a reliable database for several operating conditions of the steam generator, as well as the simulation of specific accident procedures. The ARTIST benchmark is a seven-phase project where each phase highlights a specific flow phenomenon depending on the location across the SG where it occurs.

For the sake of relevance, we focus in this chapter on the investigation of droplet retention in swirl vane separator (SVS) and dryer sections (Phase VI) under dry conditions. This particular phase deals with Design Basis Accident (DBA)-type phenomena, i.e. the potential for "primary bypass", whereby a break at the top of the tube bundle sprays fine primary liquid droplets that might find their way to the environment through, for example, a stuck-open safety valve. Air–liquid nozzles that create droplets with prototypical diameters have already been tested (Dehbi, Knasiak, et al., 2001; Dehbi, Suckow, and Güntay, 2001). Carrier gas flow rates and droplet sizes are varied to match prototypical Stokes numbers. It was shown in Güntay et al., 2008 that droplet retention in the separator and dryer increases with increasing droplet size and with decreasing carrier gas mass flow rate. The trend was similar for the retention in the swirl vane. The droplet retention in the upper part of the droplet separator was observed to be significantly smaller than in the swirl vane, and relatively independent of the droplet size or carrier gas mass flow rate.

In the context of this project, the ARTIST benchmark is considered the most challenging particulate flow due to the high level of geometrical complexity and the associated swirling effects on particle dispersion. The main goal of this chapter is therefore to extensively assess the prediction capabilities of WMLES to retention efficiency. For efficiency and robustness reasons, we use the commercial code ANSYS Fluent, 2015 to investigate this case. The employed turbulence model chosen to match our WMLES methodology is the Delayed Detached Eddy Simulation model (DDES). The model activates a two-equation Realizable $k - \epsilon$ $(Rk - \epsilon)$ RANS mode in the boundary layer and switches to LES in the separation region. As will be shown below, we study both the primary fluid flow and particle retention under simplified

conditions. This in turn will help build a reliable but cost-effective design tool for optimizing steam generators in the future. In addition, our obtained results are intended to serve as a self-contained open-source database for researchers in hybrid RANS/LES modeling of complex particle-laden flows.
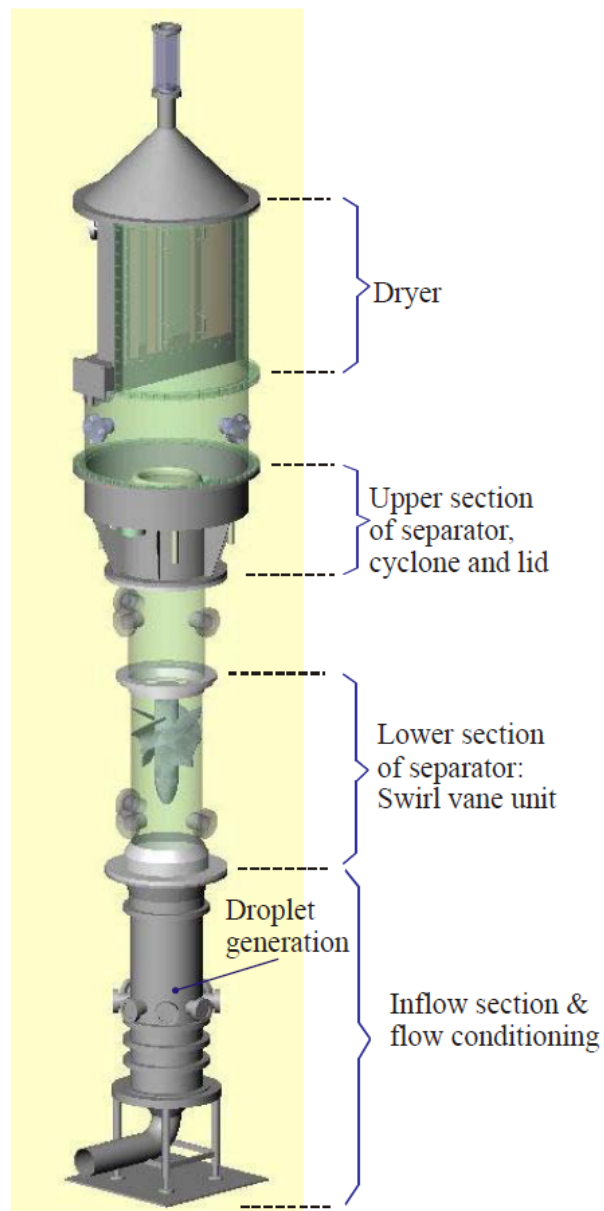
Figure 7.2 – A schematic showing the several stages of the ARTIST facility.

7.2   Physical geometry and computational domain

As shown in Fig. 7.3, the physical domain has been cleaned from irrelevant parts to the CFD simulation. To have one-to-one comparison with the reference experimental data, two geometrical models have been considered in this study: configuration D and configuration E. As seen from Fig. 7.4, the main difference between these configurations is the dryer section. In accordance with the experiment and to have a solid validation case, we employ two sets of simulations; one for configuration D (without dryer section), and another set for configuration E (with dryer). As described in Fig. 7.5, the geometry of the device is characterized by six main dimensions. For a systematic investigation, we keep these six dimensions fixed throughout all simulations for each configuration (Table 7.1). It should be pointed out that the dryer height was originally designed to be 1117 mm, then it was extended to 2120 mm in order to prevent reversed flow at the outlet section.
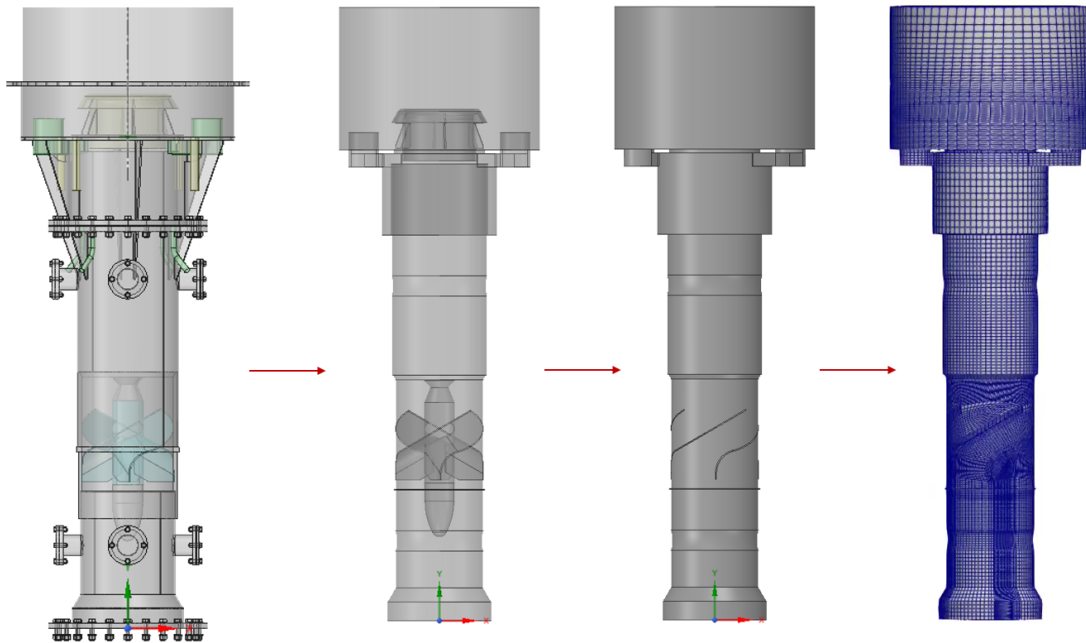
Figure 7.3 – Schematic showing the geometry extraction and mesh of the Swirl Vane domain. From left to right, the ARTIST facility - phase VI, the faceted-body, the negative shape solid domain, and the computational grid.

Table 7.1 – Table 1: Dimensions of the ARTIST facility - phase VI

Parameter	Config. D (mm)	Config. E (mm)
Inlet diameter, A	582	582
Device base height, B	2633	2633
outlet section height, C	800	968.5
Outlet diameter, D	1124	1124
Dryer height, E	-	2120
Total device height, F	3433	5721.5
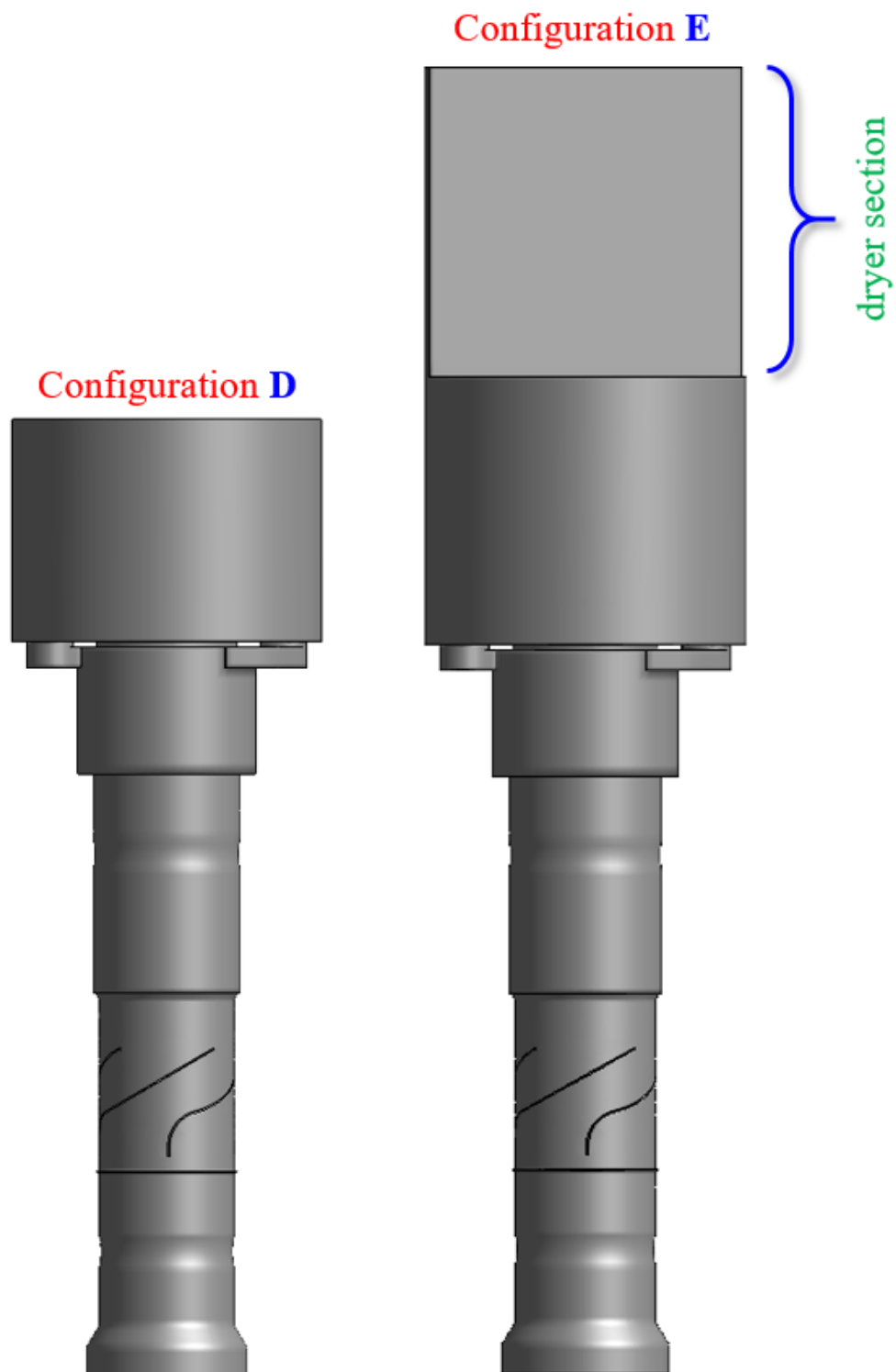
Figure 7.4 – Schematic of the used two configurations; configuration D (left), and configuration E (right). Each configuration is characterized by the geometrical parameters specified in Fig. 7.5 with the corresponding dimensions as in Table 7.1
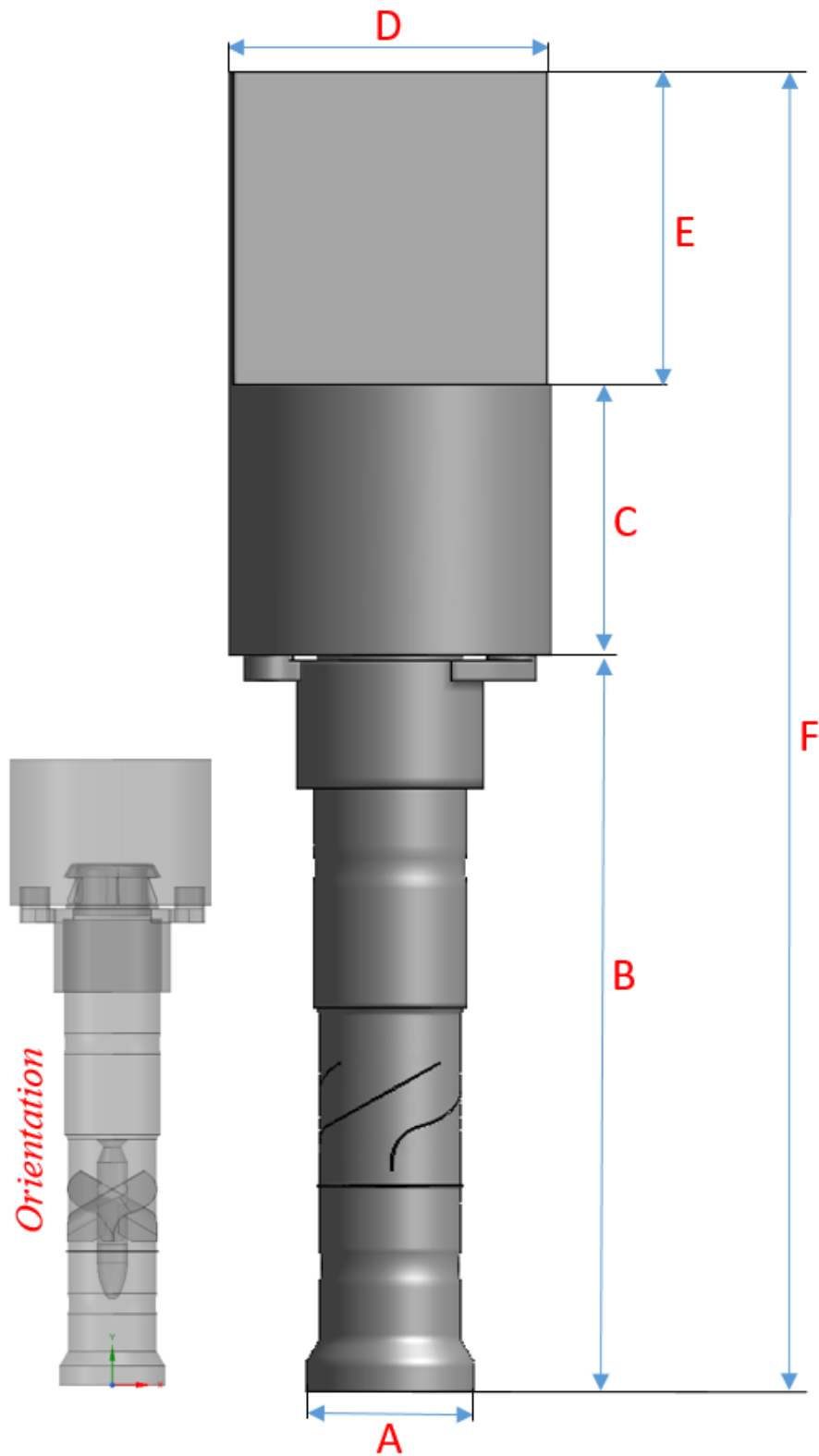
Figure 7.5 – Schematic of phase VI of the ARTIST facility with the main parameters characterizing each configuration i.e. config. D & E as in Table 7.1

Once the negative shape was constructed, a block-structure fully-hexahedral mesh (Fig. 7.6) was obtained using the commercial package Pointwise, 2021 V18.4 R4. In this mesh, the focus has been put into obtaining a fully-structured mesh that aligns with the flow stream from inlet to outlet - to reduce numerical diffusion. The near wall region was not considerably refined considering that we deal with wall-modeled LES in this case. That said, modeling the wall has been tasked to the RANS model employed near the wall in case of DDES and to the standard wall-functions in case of RSM.

7.3   Numerical set-up

Due to the complexity of the SVS configuration and since research codes are not robust enough to tackle such flow topologies, ANSYS Fluent (V 2020-R1) was chosen to solve this case. The Delayed-Detached Eddy simulation was employed with the realizable $k - \epsilon$ RANS model ($DDES/k - \epsilon$) in a hybrid transient mode. For the sake of simplicity, the $DDES/k - \epsilon$ model is referred to hereinafter as DES. In addition to DES, Reynolds Stress Model (RSM) and LES Smagorinsky models have been used to compute some cases in order to assess the prediction of higher moment statistics relative to DDES. The carrier fluid (air) was considered as perfect gas with density $\rho = 1.225 kg/m^3$ and dynamic viscosity $v = 1.789 * 10^{-5} kg/(ms)$. Turbulent statistics were gathered after 5 flow through times - starting from initial conditions - for another 5 flow times (till statistical convergence was achieved). In this case, flow through time (also known as viscous time scale) is defined as follows:

$$\delta_v = \frac{L_o}{U_o} \qquad (7.1)$$

where L_o is the characteristic length (which is different for each configuration), and U_o is the characteristic velocity (inlet velocity in this analysis). As shown in Fig. 7.7, two measurement locations have been chosen to have one to one comparison between the obtained results and the reference experimental measurements (i.e. MP3A, MP4A). The two position are located at the xz-plane $y_1 = 1.881$ m and $y_2 = 3.2015$ m for MP3A and MP4A respectively. As in Fig. 7.8, the azimuthal orientation of MP4 locations is 90, 0 degrees for MP4A and MP4B respectively, which is a crucial position for judging the flow prediction at the dryer section. As mentioned above, two configurations for the SVS were considered: one without dryer section, and the other configuration contains a dryer section. The dryer was modeled as an extension of half the outlet section with a pressure outlet boundary condition at the exit. For each configurations we perform five mass flow rates i.e. $\dot{m} = 100, 200, 400, 600, 800$ kg/hr. Each flow rate is based on the inlet cross-sectional area and inlet velocity ($\dot{m} = \rho A_{in} U_{in}$). As in Table 7.2, the used five mass flow rates are reported as well as the corresponding inlet velocities and time step size used in each case.

Once the flow is fully converged, particles are injected during one through time, then five more flow times were computed where particles are advanced without introducing new ones. As will be shown below, 12 particle swarms - spanning a wide range of Stokes numbers were
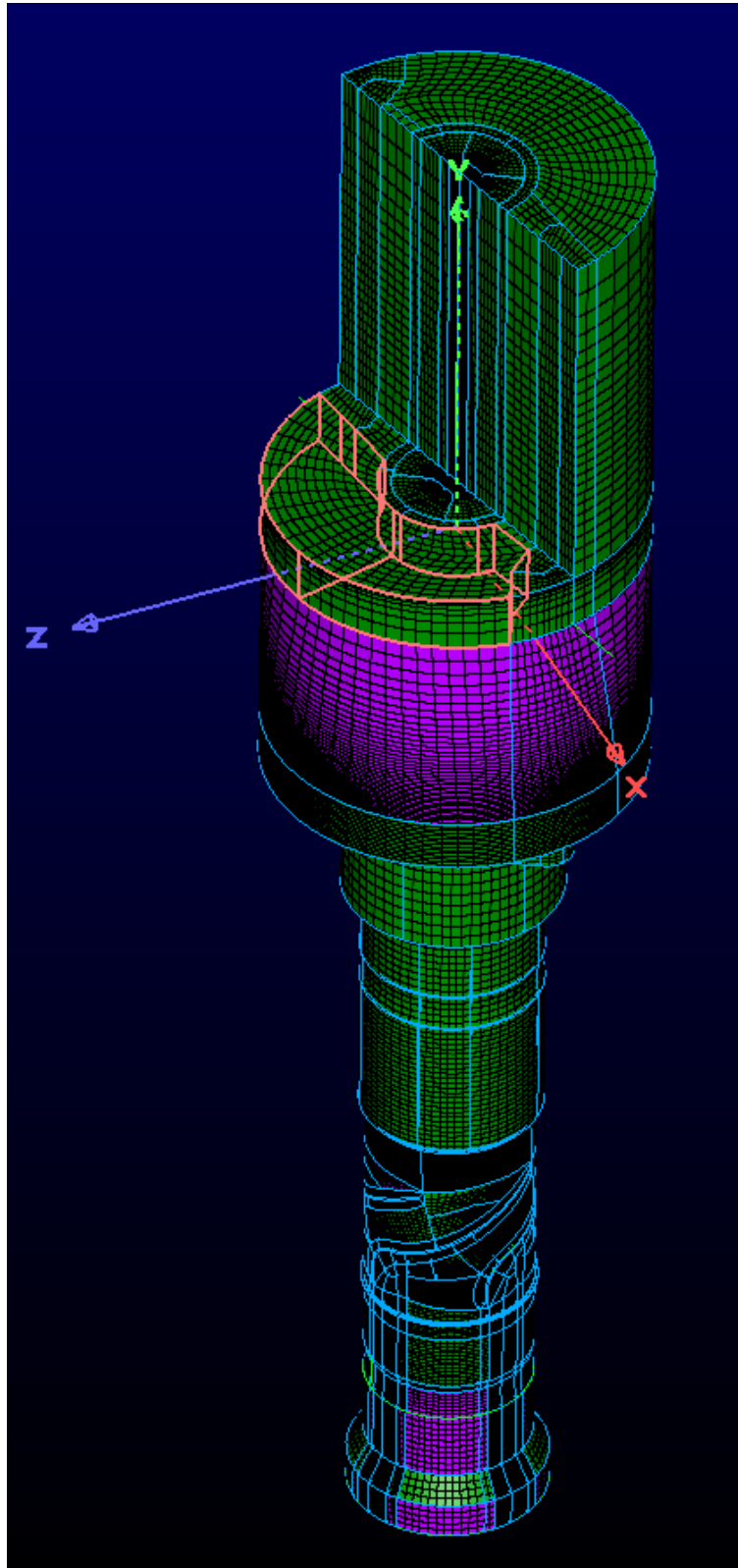
Figure 7.6 – A block-structured fully hexahedral mesh created by Pointwise.
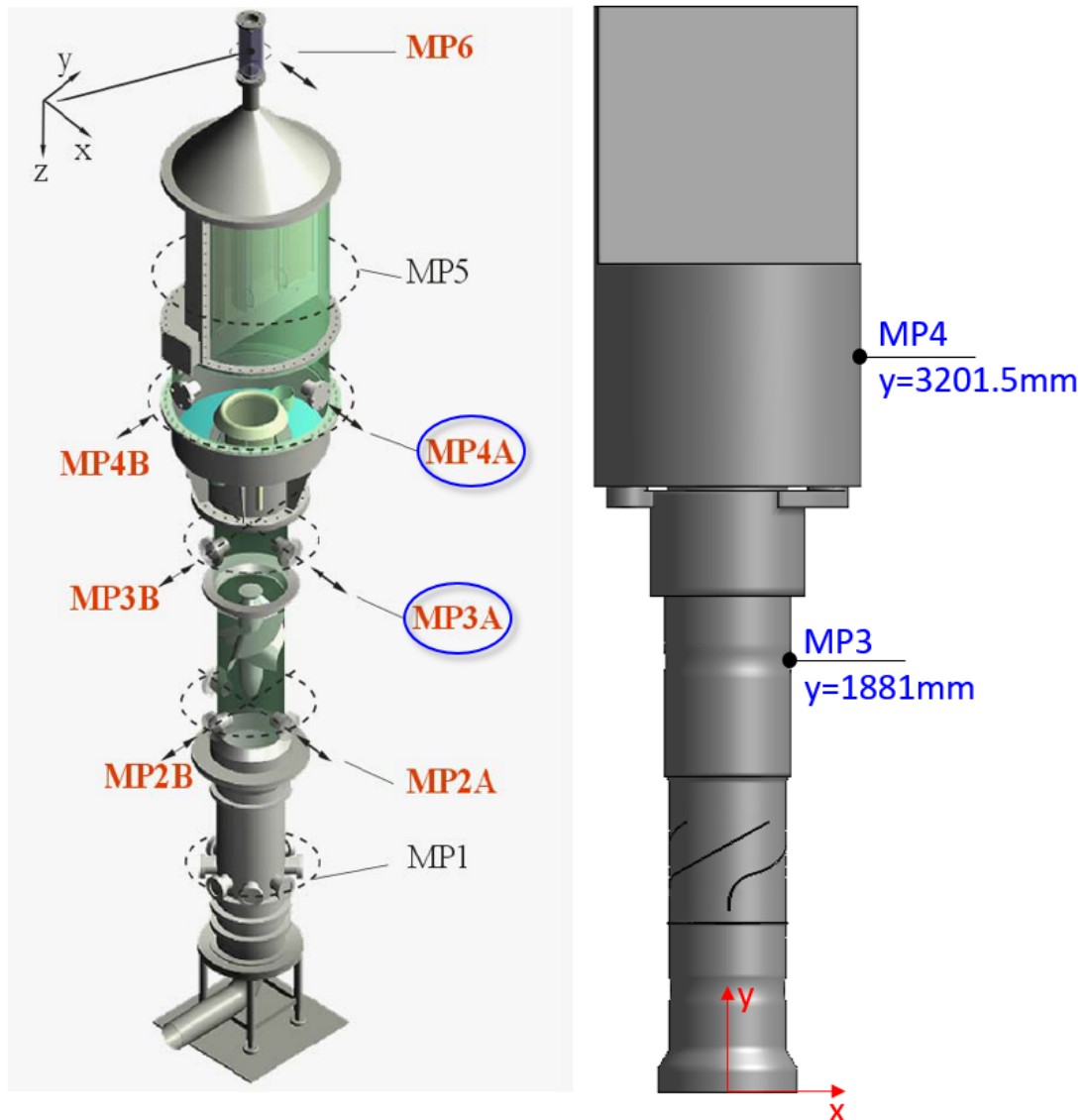
Figure 7.7 – A schematic showing the different measuring positions where experimental data is available. As indicated, the obtained results from our CFD simulations are compare against the reference data at those two locations: MP4A and MP3A.

Table 7.2 – Table 2: Input parameters for the considered cases

Mass flow rate [kg/hr]	Inlet velocity [m/s]	Time step [s]
100	0.085	0.03
200	0.1705	0.007
400	0.341	0.006
600	0.5114	0.005
800	0.682	0.0035

considered for each mass flow rate. To achieve accurate particle trajectory computations, the time steps for the integration of the Lagrangian ODE's must be of the order of the particle relaxation time (τ_p), and hence are much smaller than the fluid time-steps. Therefore the code makes the necessary adjustments such that an integer number of particle time steps correspond to one fluid time step. The time integration of the coupled ODE's is performed by the so-called Automatic Tracking Scheme (ATS) which shuttles between the first order implicit Euler scheme and the second order Trapezoidal scheme, depending on the local flow dynamics. An embedded error control on the trajectory is enforced, that is, the particle time step is sequentially reduced until the predicted error in the trajectory is below a certain tolerance. In the current simulations, this tolerance is set to a low value of 10^{-5} with a maximum number of 20 refinements. To compute the total particle retention efficiency, all walls are assumed to be perfectly absorbing. Therefore, particle is considered to have deposited when the particle center of mass happens to be at a distance less than the particle radius.
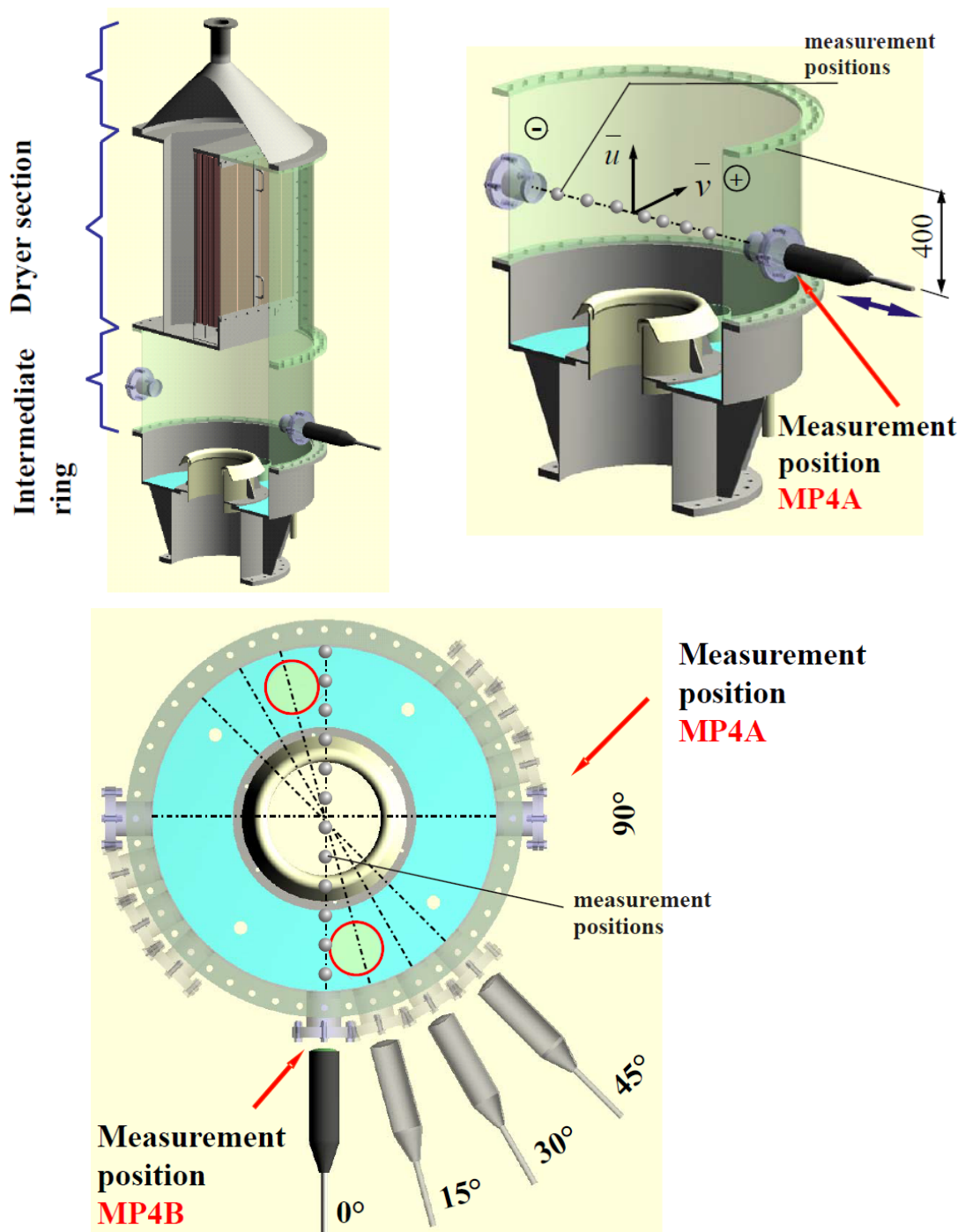
Figure 7.8 – A close up of the measuring location MP4 which lies at the intermediate ring of the outlet section.

7.4 Fluid flow prediction

As mentioned above, the flow is computed in both configurations (i.e. D and E) at several mass flow rates. In the following we show results for both mean and RMS velocity profiles using several turbulence models. We assess each model's prediction of turbulent flow quantities first in order to have a reliable pathway for the discrete phase simulation. Predictions of fluid flow at the considered mass flow rates are validated by the experimental data provided for each SVS configuration.

7.4.1 Configuration D (without dryer section)

As demonstrated below, we show at this section the primary flow prediction of all of the standard Smagorinsky model, RSM and DES at two different mass flow rates i.e. $\dot{m}$ = 400, 600 kg/hr. Fig. 7.9 shows the mean velocity of both the axial and transversal velocity component for $\dot{m}$ = 400 kg/hr at the measurement location MP4A. Looking at the axial velocity component, it can be seen from the Figure that out of the three turbulence models, the Reynolds stress model has the best match with the reference experimental data. The three-hump pattern is successfully reproduced by RSM capturing 70% of the peak or each hump as a minimum value. This comes as no surprise since RSM is proven to be efficient in predicting swirling flows. In addition, the flow dynamics inside the SVS configuration is similar to the one inside reversed gas cyclones (exhibited in Chapter 6), in which sense RSM is known to produce the mean flow the best. All three models however predict a similar profile for the transversal velocity component at this location. It was mentioned by Kapulla, 2008 that the upper bound for the overall statistical uncertainty for both the mean and the RMS-value estimator of the velocity is 5%. These errors are regarded as prototypically independent of the measurement location. That said, the mean flow is considered to be generally well-predicted by all three models at this flow rate.

To have better resolution on how the models behave at higher mass flow rates, the same set of simulations were performed at $\dot{m}$ = 600 kg/hr. As seen from Fig. 7.10 - 7.12, both mean and RMS velocity components are reported for each turbulence model at both mass flow rates i.e. $\dot{m}$ = 400, 600 kg/hr. It can be seen from this analysis that at the higher mass flow rate of $\dot{m}$ = 600 kg/hr, the middle hump of the mean axial velocity tends to disappear. This feature is most pronounced by the RSM predictions as in Fig. 7.12. In a more quantitative assessment, these predictions at $\dot{m}$ = 600 kg/hr are compared to the reference data (Fig. 7.13). It can be seen that mean velocity have similar trend and magnitude for both the axial and transversal components from the three models. However, it must be pointed out that the middle hump of the mean axial velocity is largely missed. In addition, the DES model is noticed to predict the mean transversal profile slightly better than LES and RSM. A similar observation can be spotted from the RMS of both axial and transversal velocities where the middle peak is missing. Despite of small deviations, it can be noticed from this configuration that both RSM and DES have globally a better prediction than LES with the standard Smagorinsky model. This is
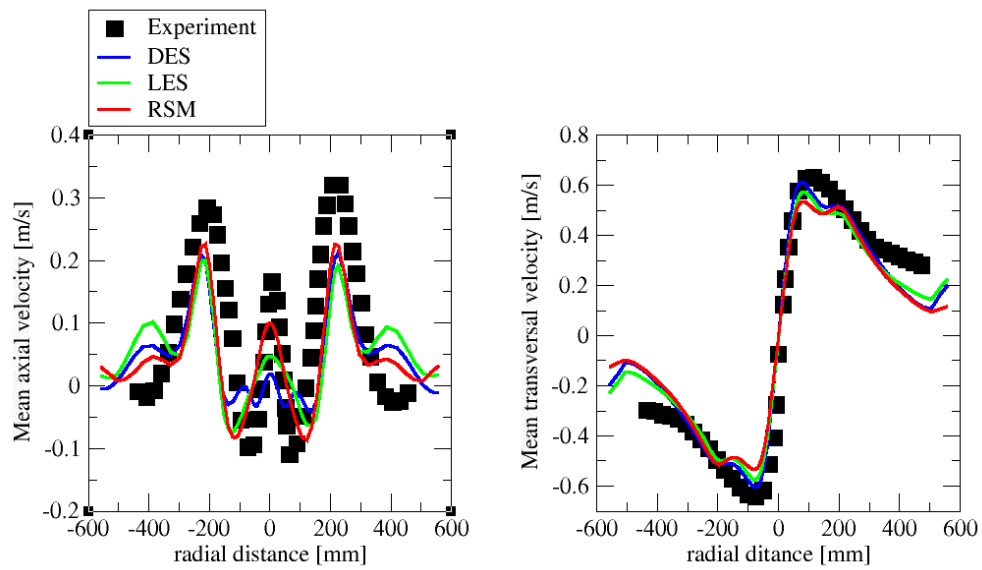
Figure 7.9 – A comparison of all of RSM (red), LES Smagorinsky (green) and DES (blue) turbulence models for mean axial and transversal velocity profiles at $\dot{m}$ = 400 kg/hr versus experimental data. Profiles are plotted at the measurement location MP4A.

intuitive given the fact that such a complex flow requires explicit wall-modeling for a better flow prediction. To this end, we only use RSM and DES for the assessment of configuration E (with dryer) as will be shown in the next section.
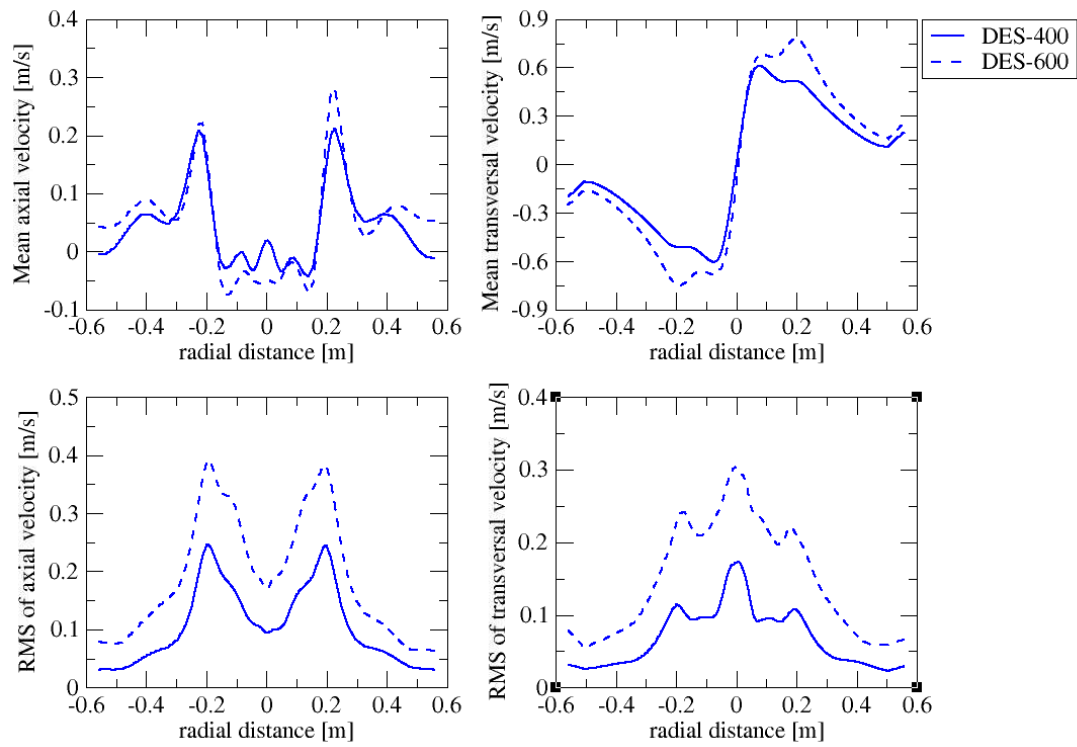
Figure 7.10 – Mean and RMS velocity profiles obtained by DES turbulence model for both axial and transversal components at $\dot{m}$ = 400, 600 kg/hr. Profiles are reported at the measurement location MP4A.
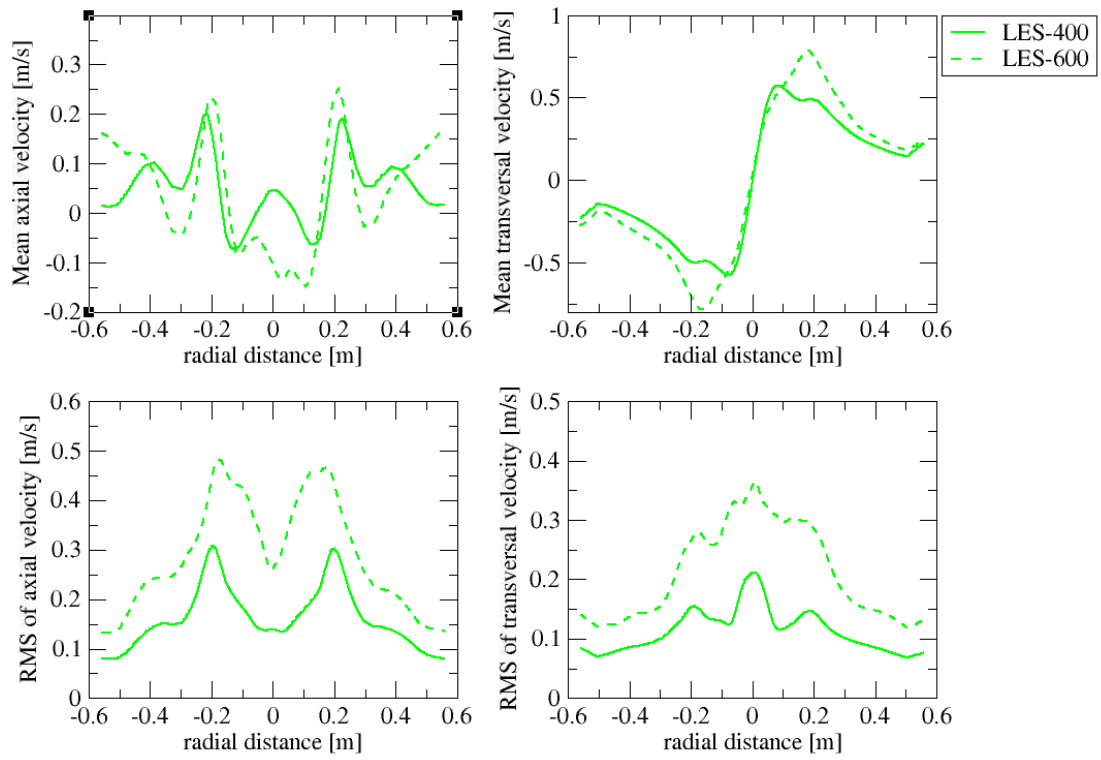
Figure 7.11 – Mean and RMS velocity profiles obtained by LES turbulence model for both axial and transversal components at $\dot{m}$ = 400, 600 kg/hr. Profiles are reported at the measurement location MP4A.
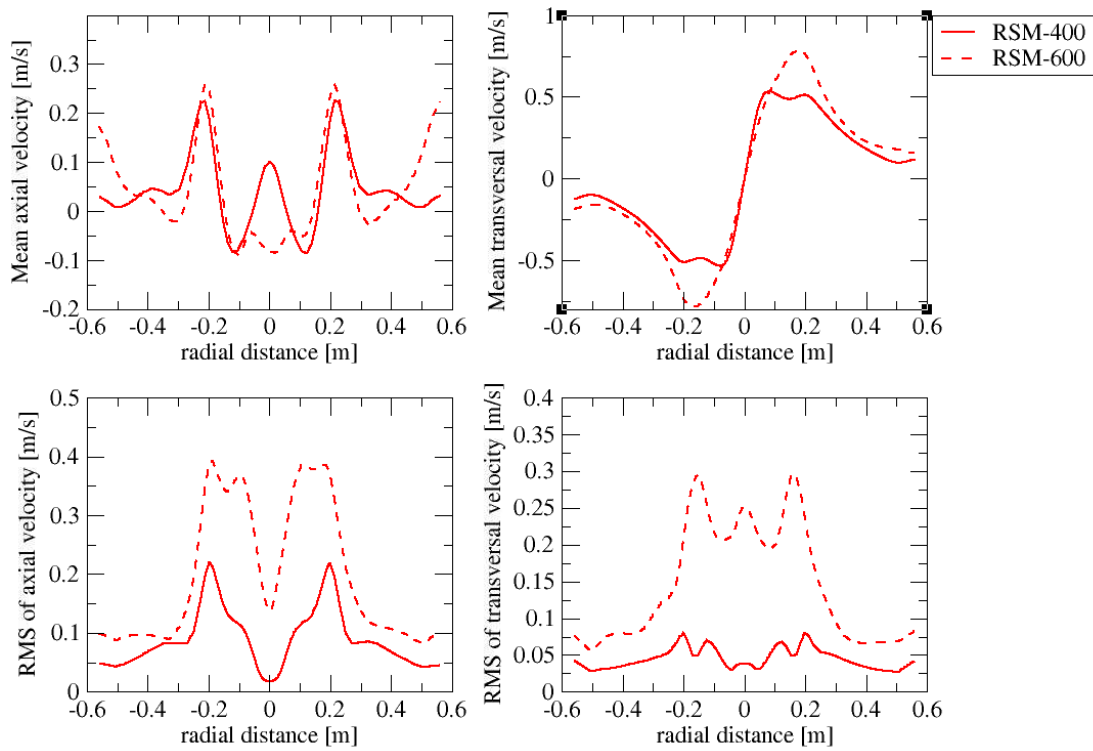
Figure 7.12 – Mean and RMS velocity profiles obtained by RSM turbulence model for both axial and transversal components at $\dot{m}$ = 400, 600 kg/hr. Profiles are reported at the measurement location MP4A.
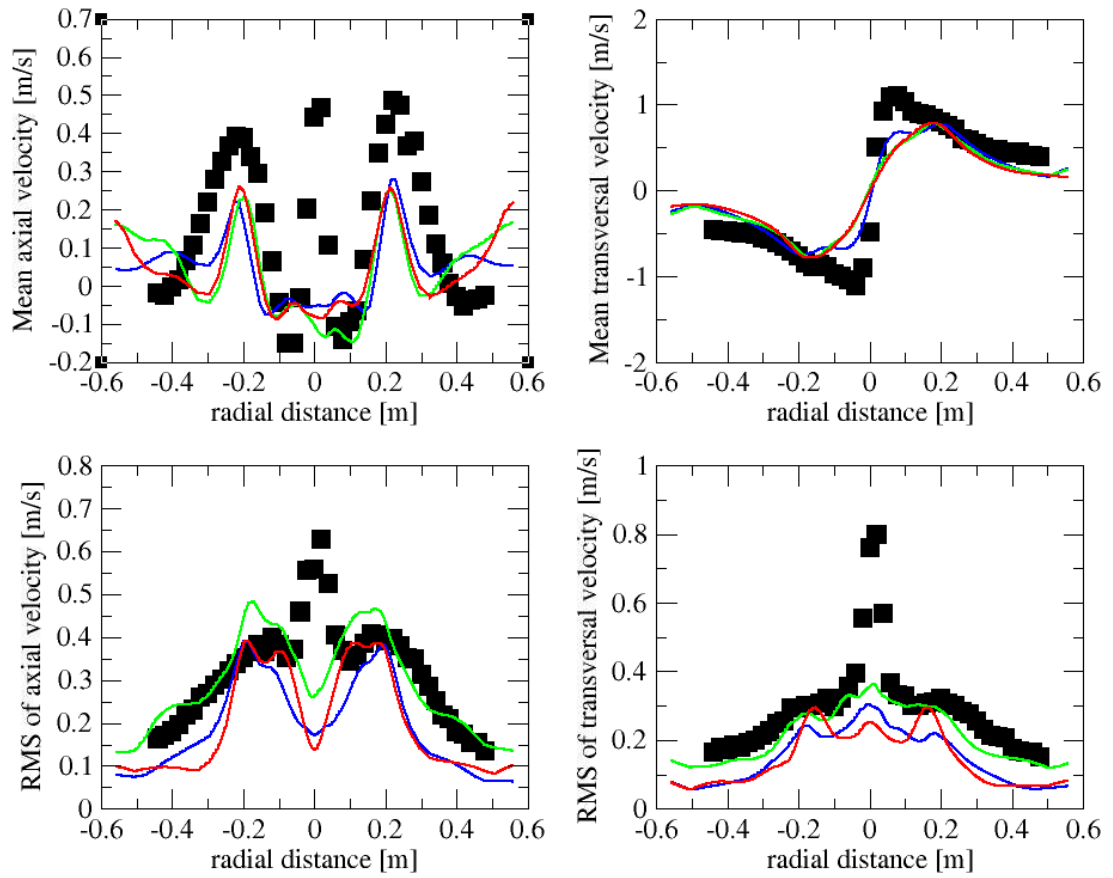
Figure 7.13 – Mean and RMS velocity profiles obtained by all of RSM (red), LES (green) and DES (blue) turbulence models for both axial and transversal components at $\dot{m}$ = 600 kg/hr. Profiles are reported at the measurement location MP4A.

7.4.2 Configuration E (with dryer section)

Unlike configuration D, there are available data for both the carrier flow and discrete particle retention for this configuration (i.e. config. E). As will be shown below, we consider the RSM and DES models to compute the primary flow at $\dot{m} = 600 \; kg/hr$. These comparisons are reported at both measurement locations i.e. MP3A and MP4A. As seen from Fig. 7.14, in spite of the underprediction of both mean axial and transversal profiles at MP3A, the trend of the experimental data is captured fairly well. However, the RMS values are not reproduced properly by both models. Moving further downstream of the vane, it can be noticed from Fig. 7.15 that both models fail to describe the mean axial velocity. Although the trend of the transversal component is captured, the magnitude is still considerably underestimated by both models. The RMS values are on the other hand completely missing.

To eliminate - as much as possible - the main sources of errors, two sanity checks were performed, one on the inflow conditions and the other is on mesh resolution. In order to have a more realistic inlet velocity profile, a 20L/D precursor domain with a diameter identical to the SV inlet diameter was created. The pipe flow was prescribed such that a flat profile is assigned to the pipe inlet and zero gauge pressure to the outlet. Once the pipe flow became fully-developed, the velocity profile at the pipe outlet was patched to the inlet of the SVS domain. As seen from Fig. 7.16, despite of some small differences in RMS of both axial and transversal velocity components, the inlet profile does not seem to have a big influence on downstream flow (especially for mean flow quantities).

The second check is mesh resolution: it is known that implicit LES is mesh-dependent by nature. This is due to the fact that the smallest resolved motion scales are obtained by the mesh cut-off length. For this sake, only mesh sensitivity should be sought in this study of hybrid RANS/LES. The mesh used to obtain the results below is 699,734 elements in size. To check mesh sensitivity, a finer mesh was used (i.e. 4,898,082 cells) to compare first and second moment statistics at both MP4A and MP3A locations with respect to the reference experimental data. As in Fig. 7.17 - 7.18, it can be noticed that the difference between both meshes is negligible, especially for the mean flow. Therefore, we proceed with the coarser mesh to investigate particle retention efficiency.

It is important to mention that in this study, the most significant turbulent statistics for particle motion are the first-moment central statistics. On the other hand, RMS values and higher moment come as a secondary point of interest from particle dispersion viewpoint. In addition, it must be stressed that the majority of particle retention takes place at the vane section of the SVS device (Kapulla, 2008) where the mean flow is fairly captured at this point (MP3A location).
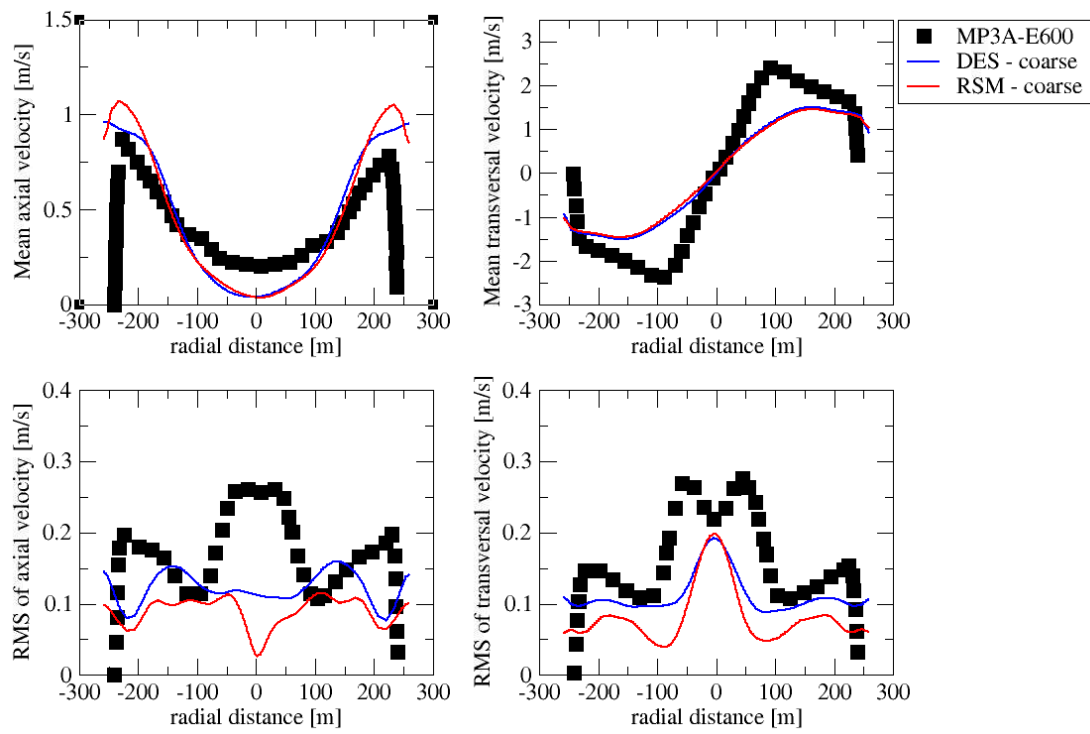
Figure 7.14 – Mean and RMS velocity profiles obtained by RSM (red) and DES (blue) turbulence models for both axial and transversal components at $\dot{m}$ = 600 kg/hr. Profiles are reported at the measurement location MP3A.
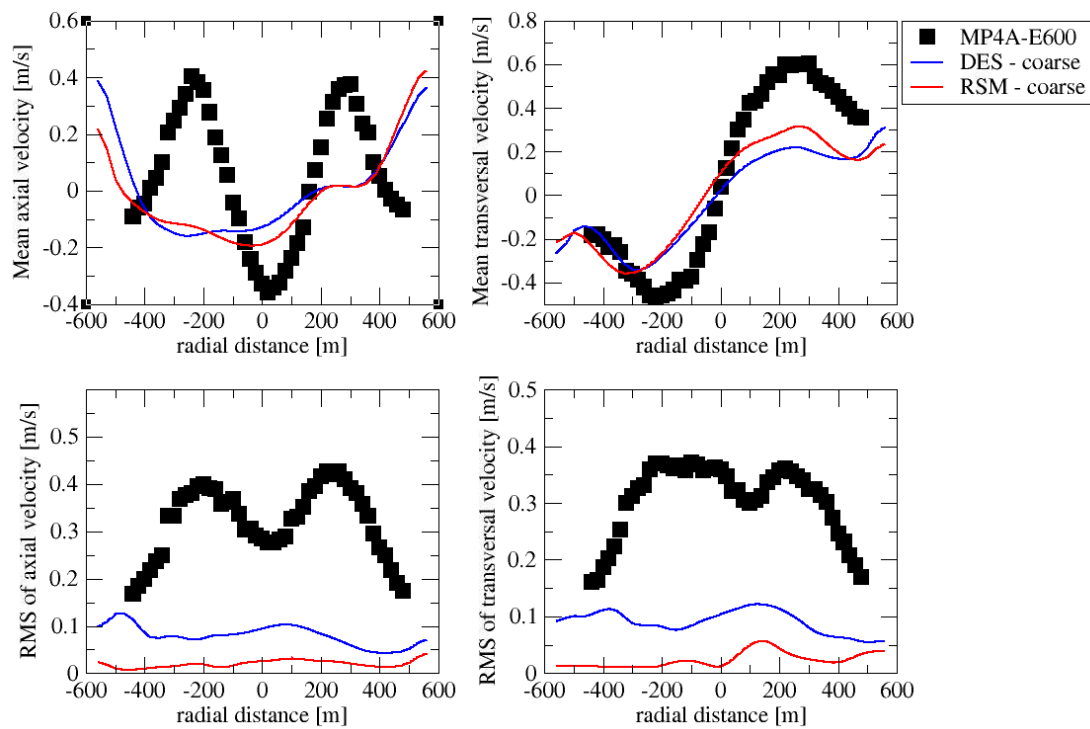
Figure 7.15 – Mean and RMS velocity profiles obtained by RSM (red) and DES (blue) turbulence models for both axial and transversal components at $\dot{m}$ = 600 kg/hr. Profiles are reported at the measurement location MP4A.
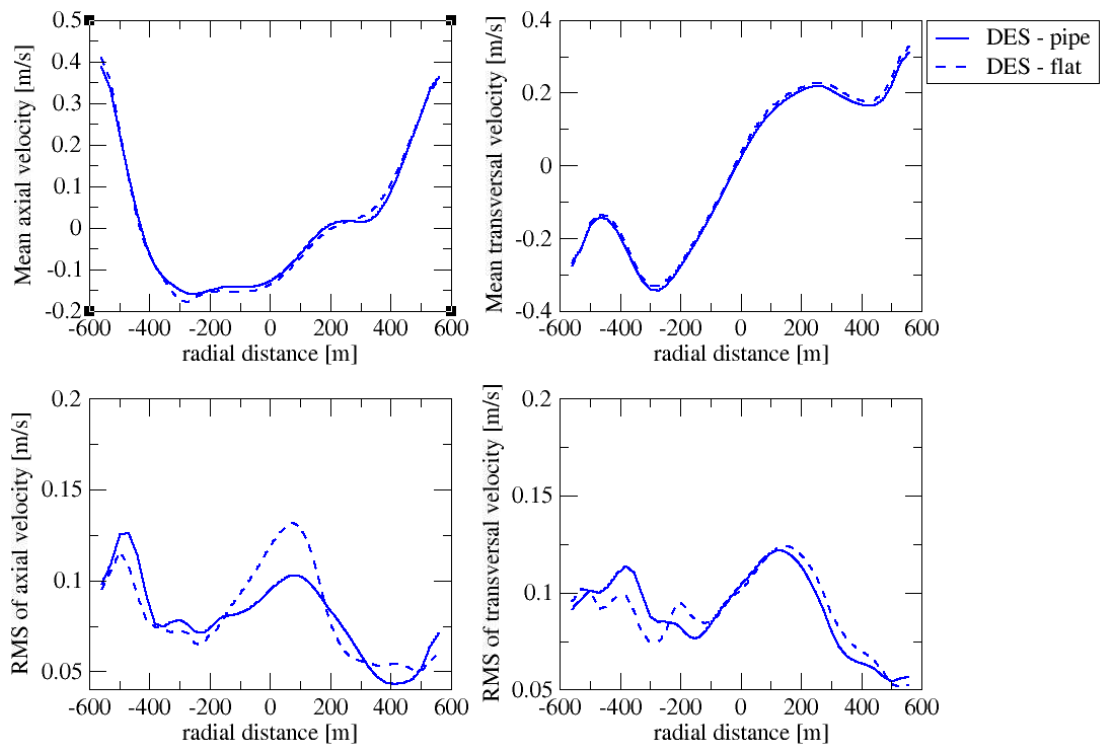
Figure 7.16 – Mean and RMS velocity profiles obtained by DES for both inlet conditions i.e. flat and fully developed pipe flow profiles. Profiles are reported for $\dot{m}$ = 600 kg/hr at the measurement location MP4A.
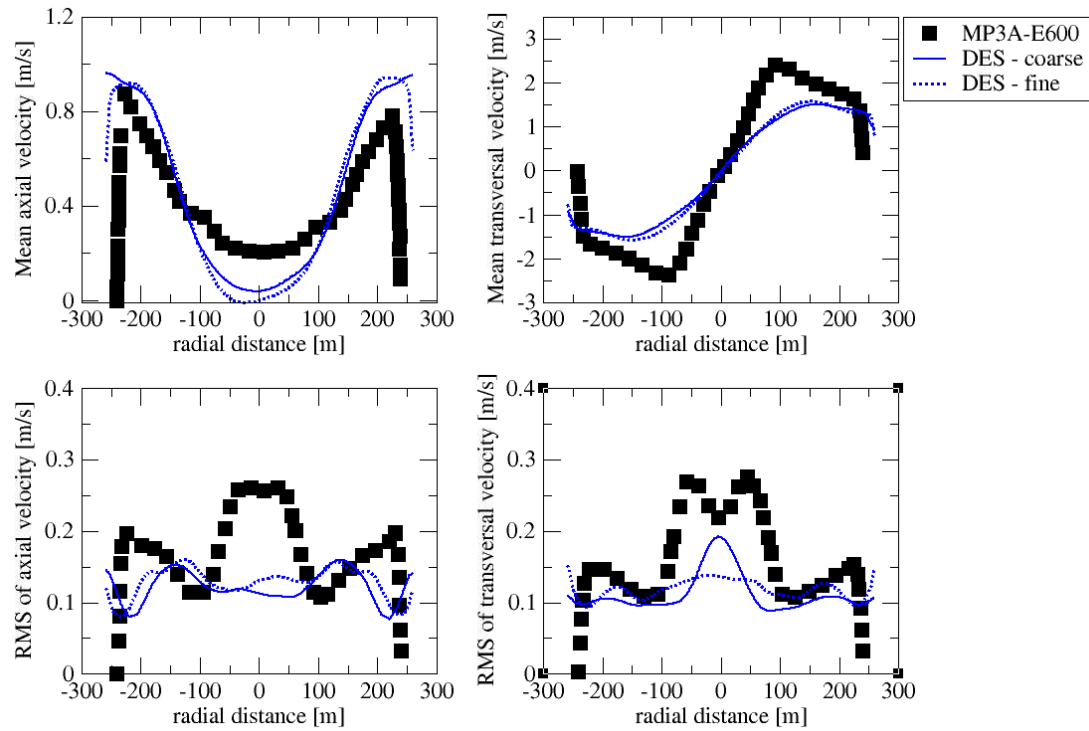
Figure 7.17 – Mean and RMS velocity profiles obtained by DES for both coarse and fine meshes used. Profiles are reported for $\dot{m}$ = 600 kg/hr at the measurement location MP3A.
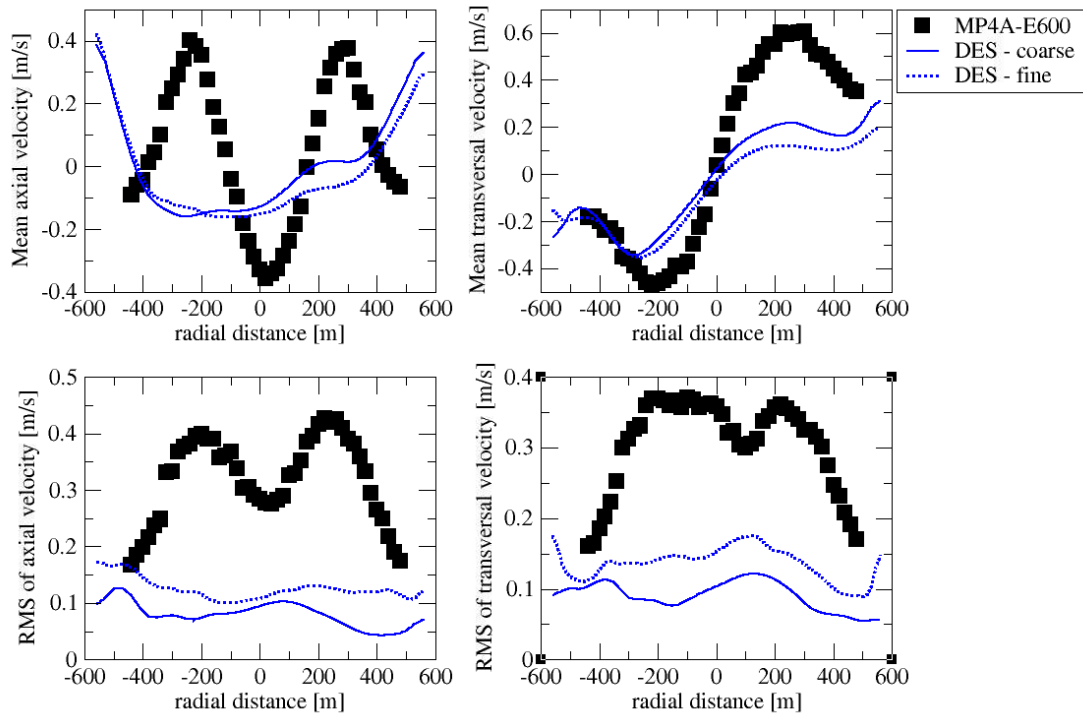
Figure 7.18 – Mean and RMS velocity profiles obtained by DES for both coarse and fine meshes used. Profiles are reported for $\dot{m}$ = 600 kg/hr at the measurement location MP4A.

7.5   Particle retention prediction

In the following, particle retention efficiency (η) is investigated through a set of 12 swarms of different particle sizes with nominal AMMD of $d_p = 5 - 60 \mu$ m. As mentioned in earlier chapters, the particle curvliniear motion is characterized by the Stokes number which relates the particle momentum response time (or particle relaxation time) to continuous fluid response time:

$$St = \frac{\tau_p}{\tau_f} \tag{7.2}$$

where particle time scale is calculated from

$$\tau_p = \frac{\rho_p d_p^2}{18\mu} \tag{7.3}$$

where ρ_p is particle density, which was set to and $915 kg/m^3$ in all cases. The primary flow time scale is then computed from the characteristic velocity and characteristic length as follows:

$$\tau_f = \frac{L_o}{U_o} \tag{7.4}$$

where U_o and L_o correspond to the inlet velocity (U_{in}) and the length F in the current configuration (Table 7.1).

The particulate simulations are performed for five mass flow rates ($\dot{m}$ = 100, 200, 400, 600, 800 kg/hr) yielding a wide range of Stokes numbers i.e. St = 1.06 * 10^{-6} - 1.22 * 10^{-3}. Particle tracking is performed in a transient mode with the feed of the instantaneous velocity field from the DES model. Therefore, no particle dispersion model was needed since the stochasticity is inherently provided by the time-dependent turbulent carrier flow field. Similar to Kapulla, 2008, both drag and gravity forces were accounted for, while other forces like lift and electrophoretic forces were neglected.

Once the flow is fully converged, particles are injected in an unsteady fashion. The particles are introduced at each time step for one flow through time, then tracked for five more flow-through times to make sure that the majority of particles are either deposited or escaped. In all cases, the residual portion of particles inside the domain did not exceed 1% of the total number of the initially admitted particles. As a preliminary test on particle sample size, two sets of different particle counts injected per time step are simulated i.e. 37 particle and 217 particles. In both cases, particles are introduced at a small distance (y = 0.0125 m) from the inlet cross-section at fluid mass flow rate of 600 kg/hr (Fig. 7.19). As shown in Fig. 7.20, no

significant deviation in the retention efficiency curve is observed when using 37 particles than 217 particles sets. To save CPU cost, we use through all the following simulations only 37 particles per time step. The resulting number of particles introduced across the above mentioned mass flow rates varies between 10^5 - 10^6 particles for each swarm set across the different flow rates.
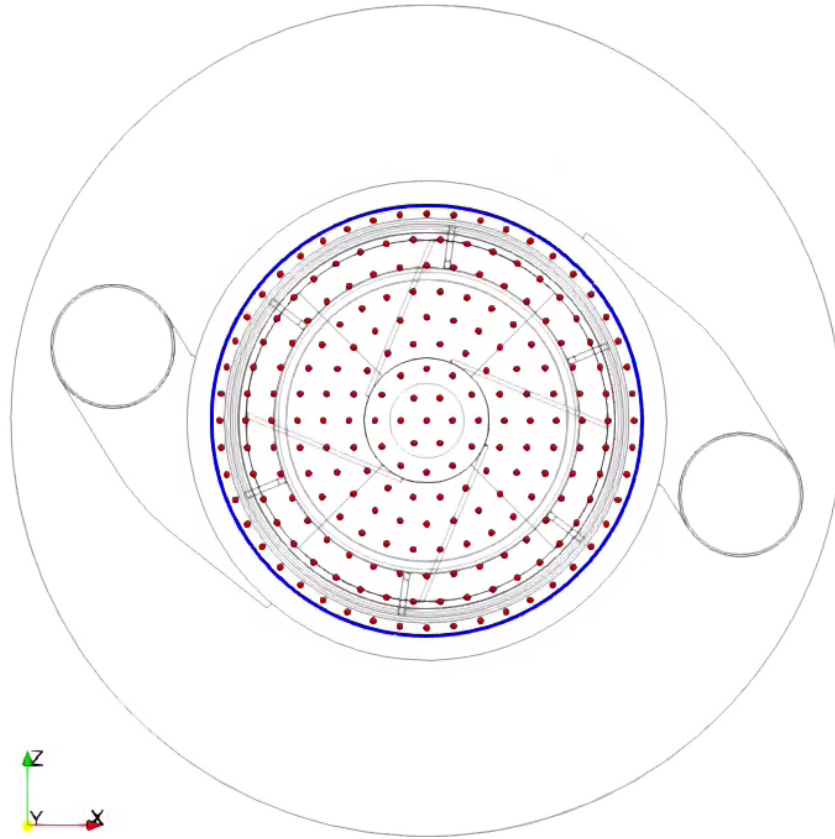
Figure 7.19 – Uniform distribution of 217 injected particles per time step at the inlet section

In accordance with the experiment, particles are then introduced on a much smaller area to represent the nozzle point-sprayer injection system as in Kapulla, 2008. The diameter of the spraying nozzle outlet was considered to be 0.056m (which is less than 1% of the diameter of the inlet section) as in Fig. 7.21. The particle retention efficiency of both injection methods were compared for the same mass flow rate (i.e. $\dot{m}$ = 600 kg/hr) to check the sensitivity. Although the comparison does not show a big difference in total retention efficiency Fig. 7.22, the nozzle sprayer injection is considered for the rest of the present work in order to match the right physical representation of the experiment.

For a decontamination system in which one injects a certain count of particles (N_{in}), a specific amount of particle should be retained given the carrier fluid flow rate. This percentage is defined as the retention efficiency i.e. $\eta = \frac{N_{retained}}{N_{in}}$. In a qualitative manner, Fig. 7.23 shows a
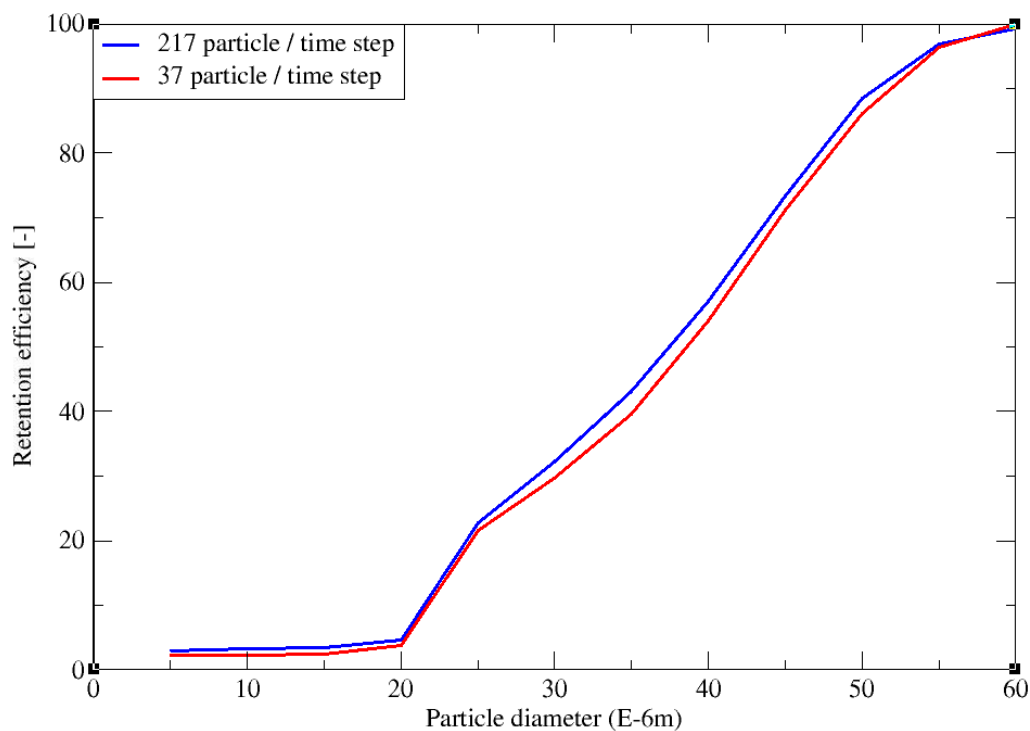
Figure 7.20 – Comparison of particle retention prediction obtained by different particle counts (i.e. 37, 217 particles per time step). Particles where injected at rest in both cases for a primary mass flow rate of 600 kg/hr.
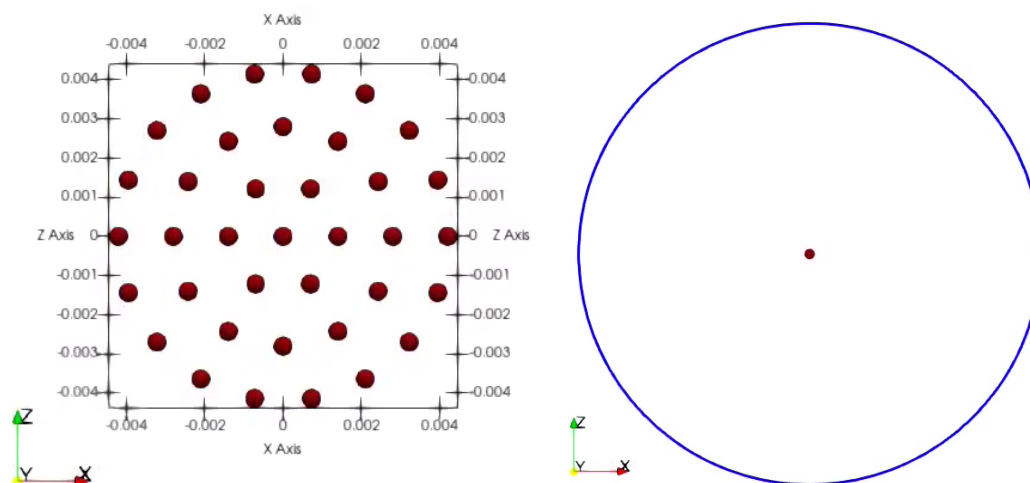
Figure 7.21 – Nozzle particle injection at aerosol mass flow rate 50kg/hr. 37 particles are introduced per time step at approximately 1% of inlet section diameter
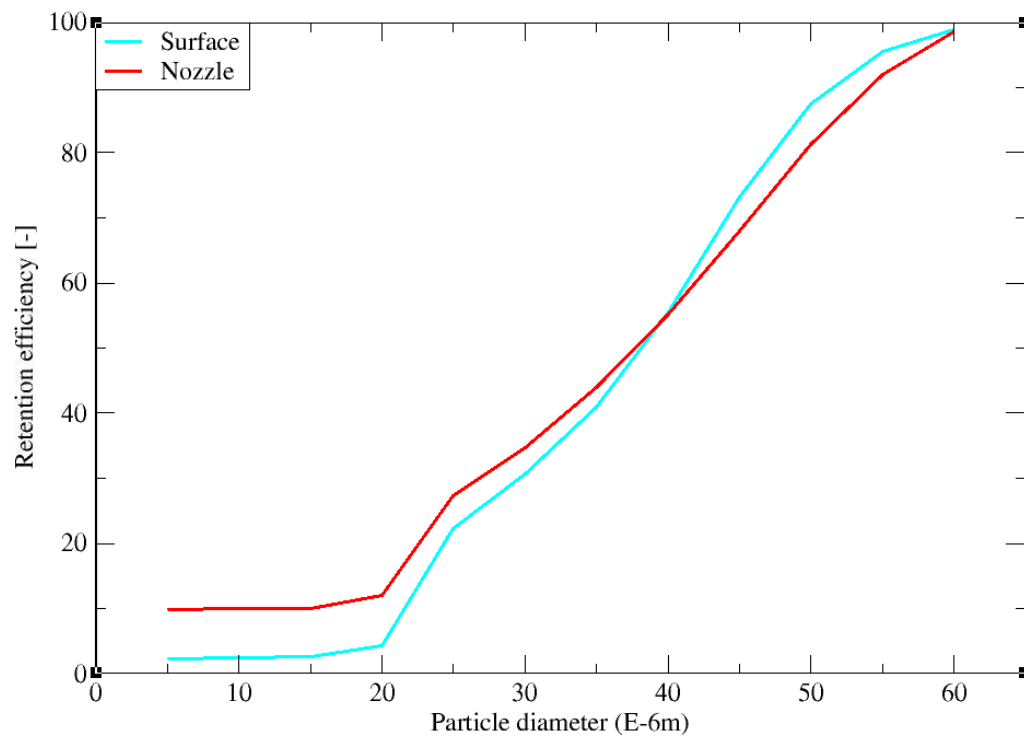
Figure 7.22 – Retention efficiency prediction by the two injection methods i.e. nozzle sprayer and surface injections. Particles where injected in both cases for a primary mass flow rate of 600 kg/hr.

snapshot of the dispersed flow inside the SVS at $\dot{m}$ = 600 kg/hr after one flow transient time from the instant particle were injected. The typical spiral-shape structures can be observed at the outer wall proximity. Such structures could be identified at the swirling flow inside high-efficiency gas cyclone separators Derksen, 2003. It can be clearly seen that the number of airborne particles decreases at higher particle inertia as expected. Moreover, it was observed that the majority of the depositions take place at the vane section, which agrees with the finding of Kapulla, 2008 at this flow rate. More quantitatively, it can be seen from Fig. 7.24, where five mass flow rates are considered, that particle retention is increased as mass flow rate decreases. This is more pronounced for relatively low-to-mid intertia particles ($d_p < 30\mu m$) where the changes in fluid time scale are more relevant.

In a comparison with the experimental data, particle retention efficiency at mass flow rates $\dot{m}$ = 100, 400, 800 kg/hr were noticed to have a considerable deviation. Although the DES results exhibit globally similar trends to the experiment, the values of retention efficiency is still largely missed. This can also be inferred from Fig. 7.26, where retention efficiency is reported for 30 μm particles versus all studied mass flow rates. The comparison of such plot with the reference data reveals that relatively mid-inertia particles have significantly lower depositions at high mass flow rates. Such deviations can be resorted to the inadequacy of the used DES model to predict the correct behaviour of particle dispersion in this case. Another argument can also be the poor representation of the dryer section in the current modeled geometry i.e. the cap of the dryer from the experimental facility was ignored in our simulations due to the lack of its dimensions. The author claims that this could have a noticeable and direct impact on the obtained axial velocity, which can be clearly viewed from the inaccurate predictions of the mean flow in Fig. 7.18.
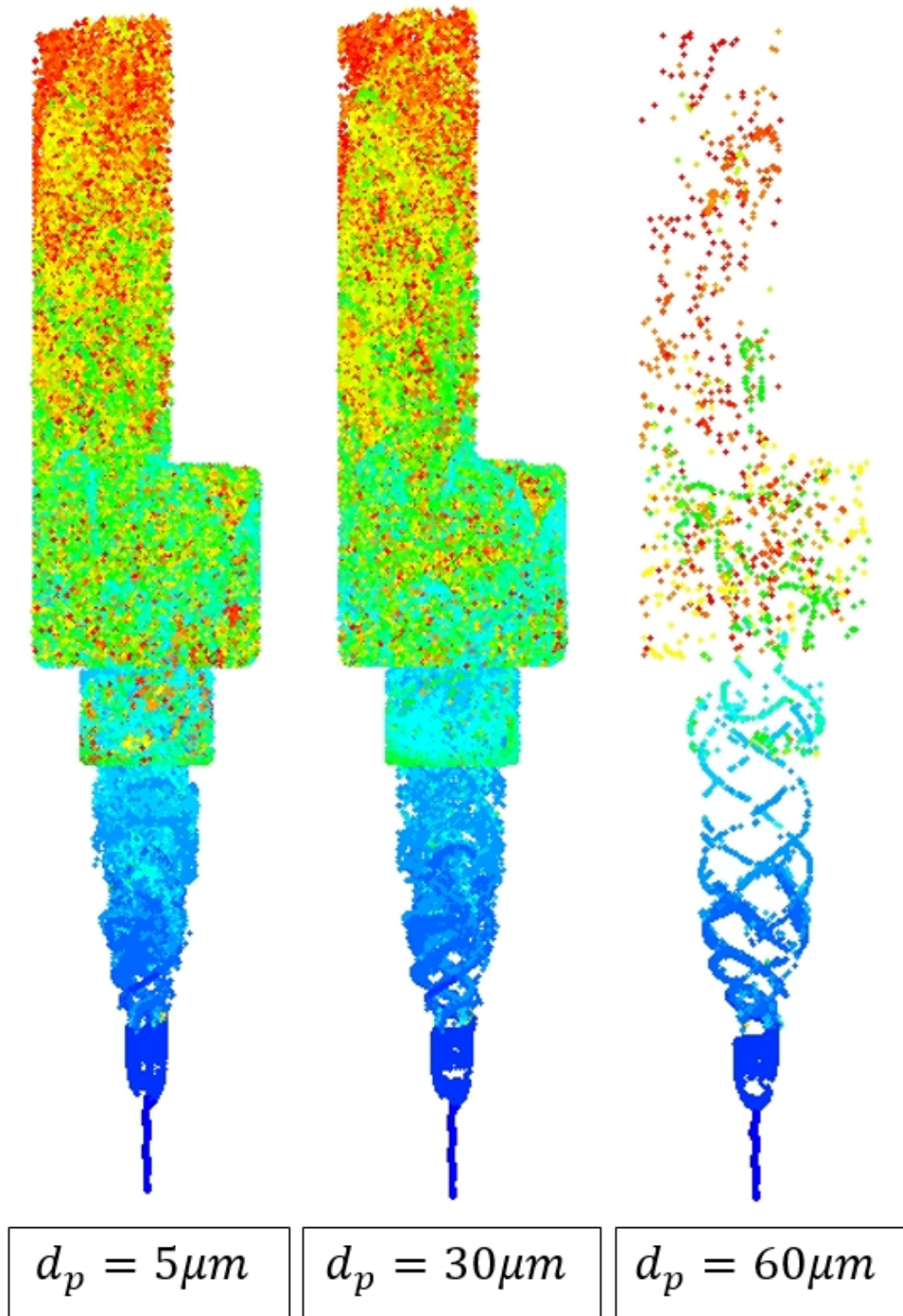
Figure 7.23 – Particle dispersion at $\dot{m}$ = 600 kg/hr for three particle sizes i.e. d_p = 5, 30, 60 μm. The Figure is a snapshot during the transient simulation after one flow through time of particle injection. Particles are colored by residence time red being the biggest residence time and blue is the smallest.
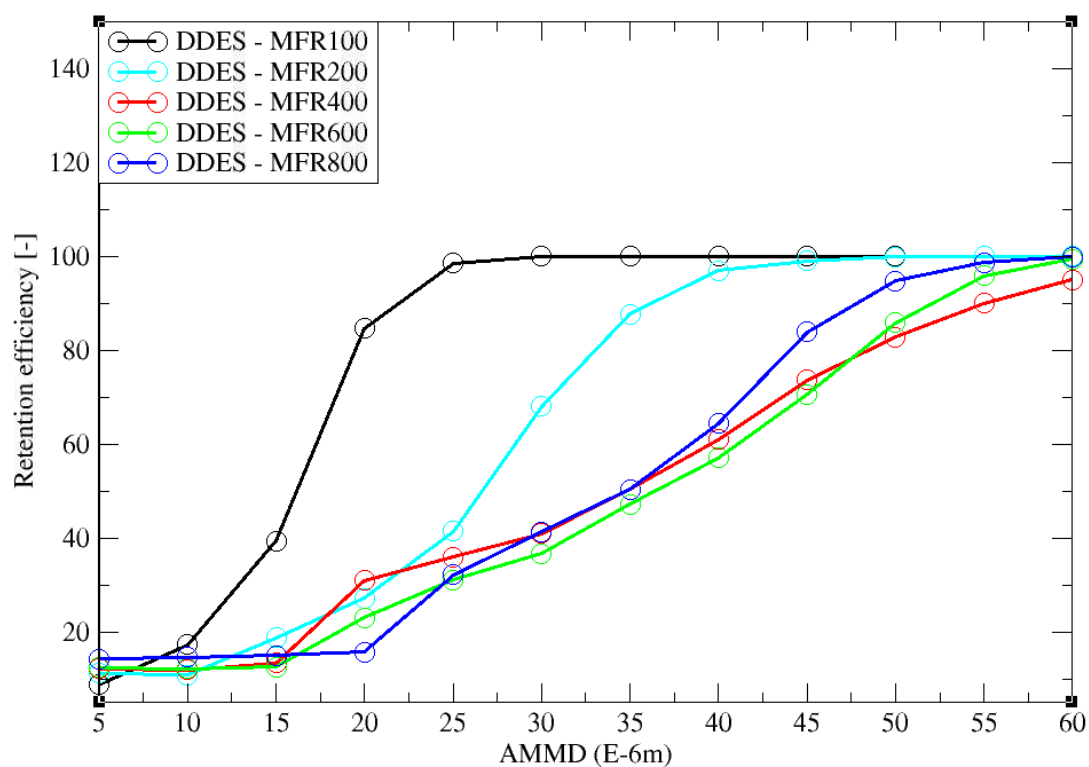
Figure 7.24 – Prediction of total retention efficiency by DDES model. Results are reported at five mass flow rates i.e. $\dot{m}$ = 100, 200, 400, 600, 800 kg/hr.
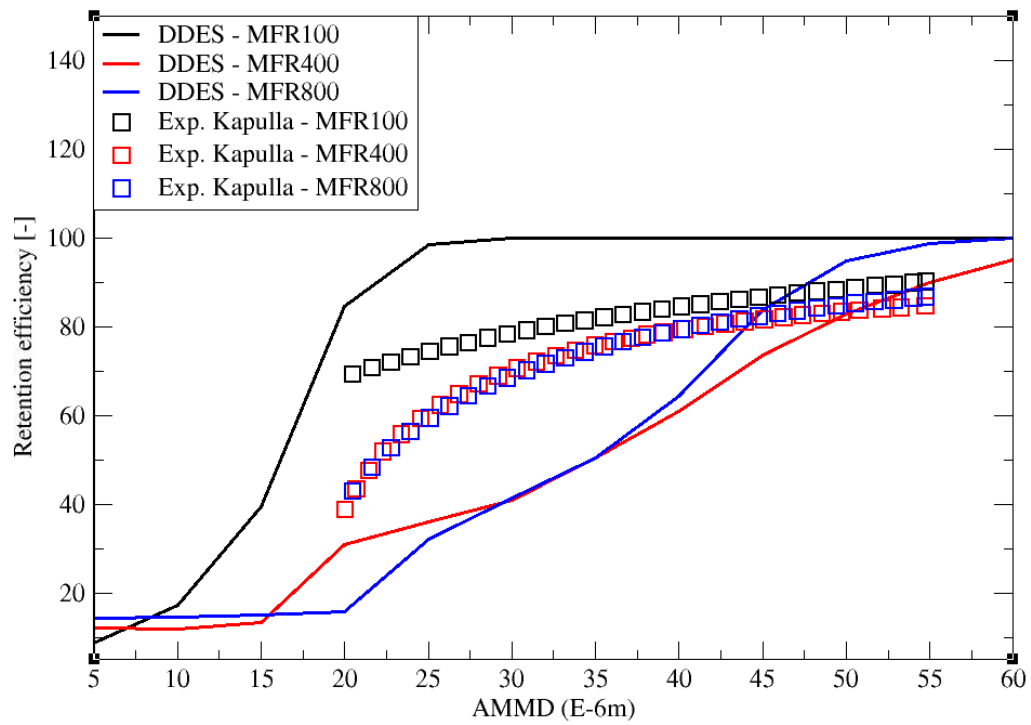
Figure 7.25 – comparison of retention efficiency prediction by DDES model against experimental results by Kapulla, 2008. Results are reported at 3 mass flow rates i.e. $\dot{m}$ = 100, 400, 800 kg/hr.
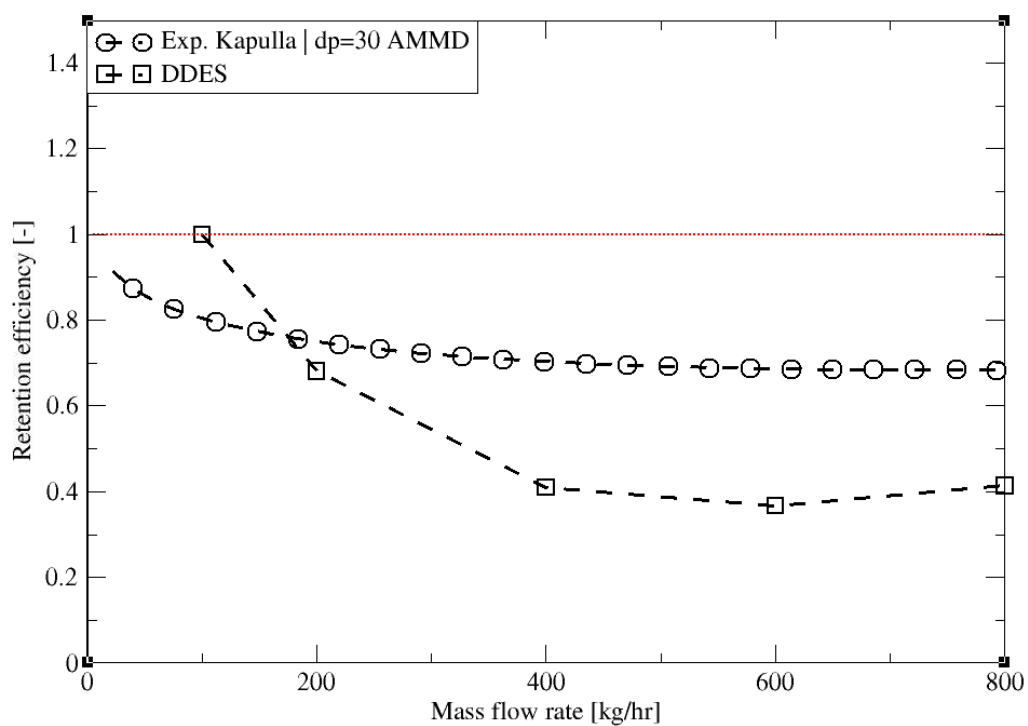
Figure 7.26 – Particle retention efficiency for particle size 30μ m AMMD for versus carrier fluid mass flow rate. Results obtained by the DDES model are compared to the experimental measurements from Kapulla, 2008.

7.6   Conclusions

Through this chapter, an extensive CFD analysis was conducted on phase VI of the ARTIST Benchmark which represents droplet retention in swirl vane separator (SVS) and dryer sections under simplified conditions. The main objective of this study is to assess the prediction of particle retention efficiency using Wall-Modeled LES. Due to the ER-HRL model limitations in T-Flows, the Delayed Detached-Eddy Simulation (DDES) with the Realizable $k - \epsilon$ RANS model in ANSYS Fluent was used. In a systematic fashion, two configurations of the swirl vane were considered (with and without a dryer section) at a range of mass flow rates were considered i.e. $\dot{m}$ = 100, 200, 400, 600, 800 kg/hr. For an accurate spatial resolution, a fully hexahedral block-structured mesh was constructed. Mesh sensitivity check was performed using two meshes comprising 699,734 and 4,898,082 elements - to judge the effect of SGS motions on turbulent flow prediction.

To analyse the contribution of wall modeling in DDES, two other models (i.e. LES Smagorinsky and RSM) were used as a preliminary step at two mass flow rates $\dot{m} = 400, 600 \, kg/hr$. Models predictions of both mean flow and higher moment statistics were reported for each case. Although the Reynolds Stress Model (RSM) has a better prediction for the mean flow, it was shown that the DES gives a better global picture for higher statistics. Results of both mean and RMS velocity profiles for both transversal and axial components were compared to the experimental data by Kapulla, 2008 at different locations across the SVS.

Results show that for configuration D (without dryer section), the DES exhibits a good prediction of the mean flow, whereas RMS values are considerably underpredicted. For configuration E (with dryer), although DES reproduces the global trend of the mean flow right after the swirl vane section, it fails to predict both the mean flow and higher moment statistics further away from the vane (i.e. close to the dryer entrance). The trend of mean transversal velocity profiles is in a fairly good match with the experiment. However, the magnitude is missing up to 40%. The author suggests that such big deviations from the experimental data in configuration E are mainly due to the poor modeling of the dryer geometry (since the cap of the dryer is completely missing). This can be seen to be directly reflected in mean and RMS axial velocity profiles that are predominantly affected at the dryer section relative to the first measuring point (close to the vane).

As a final step, particle retention efficiency was investigated where twelve particle swarms (i.e. $d_p = 5 - 60$) spanning three orders of magnitude of Stokes numbers were reported. All swarm sets were computed for each mass flow rate considered in this study in configuration E, where experimental data from Kapulla, 2008 is available. As a results of mean flow underprediction, the total retention efficiency is quite under-estimated, especially for particles with diameter below than 40 microns. This comes as no surprise since the mean flow was shown to be considerable underestimated by DES, and therefore, the accuracy of predicting particle statistics is compromised.

8 Summary

8.1 Numerical implementation, testing, verification and validation

In this thesis, we have addressed the capability of particle-laden flow prediction in complex turbulent flows using Wall-Modeled LES (WMLES). Keen on building an accessible platform for researchers in LES of dispersed flows, all developments have been implemented in the open-source general-purpose code T-Flows (Ničeno, 2001). The latest version of the code can be found on GitHub[I], which incorporates a powerful Control Version System (CVS) tool that can be used to reproduce the results of this thesis at any time.

As the first goal of this thesis is to construct a reliable particle tracking method by which dispersed flows can be simulated, a Lagrangian Particle Tracking (LPT) algorithm has been implemented. The algorithm consists of two main operations: a scanning step, and an interpolation one. In the scanning step, the algorithm browses through all cells to locate the injected particle's position. Once located, an optimized search process is employed for the next time step, where the particle is only searched for through the encapsulating cells to the particle's nearest node. The second operation of the algorithm is fluid velocity interpolation to the particle location. All particles are advanced through a post-processing step in a point-particle approach (i.e. the fluid velocity at the particle location is incorporated in the particle Lagrangian equation of motion as if the particle was not there). In addition, since we only consider low-concentration dispersed flows (also known as dilute flows), the particle has no feedback on the carrier (primary) fluid flow.

The LPT algorithm was verified through two flow configurations namely: T-junction flow, and 90-degree-bends. In the first case, a rectangular T-junction for laminar was considered. To ensure a sound analysis, fluid velocity profiles obtained by T-Flows were compared to the ones calculated by Fluent. Profiles are reported at different locations across the T-outlet branch. Qualitatively, particle tracks were reported in a symmetric flow configuration as a sanity check to make sure the Lagrangian equation of motion is properly computed. Followed

---

[I]https://github.com/DelNov/T-Flows

by this, a single-particle trajectory was compared between both codes to check any possible discrepancy in the deterministic behavior of the laminar flow. Results from LPT in T-Flows showed an excellent agreement with ANSYS Fluent.

To verify and validate the algorithm, the flow in a 90-degree bend was considered. At first, the flow statistics were investigated where both spanwise and wall-normal velocity profiles are reported. Similar to the T-junction case, predictions from T-Flows were compared to ANSYS Fluent to verify the case first. Then, the experimental data from Pui et al., 1987 was used to assess our results. As the key factor in this analysis, particle deposition efficiency was compared against the reference data in both laminar and turbulent flow regimes (i.e. Re = 1360, 4080). For the laminar case, T-Flows predictions match Fluent very well except for the particle size at the cut-off i.e. $d_p = 20\ \mu$m. This deviation is most probably linked to the different time-integration scheme used in Fluent. For the turbulent flow case i.e. Re = 4080, results from T-Flows show a global good agreement with the experimental data within a range of 20% of maximum deviation. Results are deemed very satisfactory to move further to test the code in more challenging forced and buoyancy-driven flows.

The second fold of the thesis is focused on the investigation of a wall modeling in turbulent flows. As a first step, the algebraic wall-modeled LES (AWMLES) by Shur et al., 2008 has been implemented in T-Flows, where its performance has been assessed in a turbulent channel flow across three shear Reynolds numbers i.e. $Re_\tau = 395, 590, 1000$ (Sayed et al., 2020). As in Chapter 4, the AWMLES model was validated alongside the pre-existing Elliptic Relaxation Hybrid RANS/LES (ER-HRL) model in T-Flows against DNS data from the literature. Results showed that the AWMLES model fails to properly predict the flow above moderate Reynolds number ($Re_\tau = 590$), whereas the ER-HRL was shown to be more robust and cost-effective across a wider range of Reynolds numbers i.e. $Re_\tau = 395 - 18,000$. This is well documented in both papers Sayed et al., 2020, 2021-b.

In the context of WMLES of particle-laden flows, recent studies however have shown that the unresolved scales of the fluid velocity can have significant effects on particles with relaxation times smaller than the Kolmogorov time scale (Bini and Jonesa, 2007; Cernick et al., 2015). For these particles, an SGS model is required in the particle equations of motion. Among all particle SGS models, two promising approaches which have been proposed recently to define the fluid velocity seen by the particle will be investigated: the first one is the Fukagata model (Fukagata et al., 2004), and the second one is the $\zeta - SGS$ model, which was proposed by the author during the course of this project (Sayed et al., 2021-b).

The Fukagata SGS model attempts to capture SGS influence through the inclusion of a stochastic SGS (Brownian) force in the particle equation of motion. Even though the model recovers enough of the SGS kinetic energy, it still shows limitations in predicting preferential particle clustering. This is due to the assumption of homogeneous isotropic SGS turbulence which is least accurate close to the walls. The second approach i.e. $\zeta - SGS$ model however, is based on feeding particles with wall anisotropic turbulence through the wall-normal velocity fluctua-

tions. Those fluctuations are merely extracted from the variance of wall-normal transport (ζ). Such deconvolution retrieves the modeled part of the most important velocity component for particle deposition (i.e. the wall-normal component). In Chapter 4, both models were investigated thoroughly in a periodic channel flow to assess their potential to proceed with accuracy in more complex flows. To judge the performance of each model, four benchmark cases have been considered: one canonical flow and three complex flow cases. As will be discussed below, the obtained results for each of these cases have been validated by either DNS or experimental measurements.

8.2 Canonical turbulent channel flow

The particulate channel flow has been studied using two WMLES models: the Algebraic WMLES (AWMLES) and the Elliptic Relaxation Hybrid RANS/LES (ER-HRL). Results were reported at two shear Reynolds numbers i.e. $Re_\tau = 150, 590$ for both the primary (carrier) flow and the dispersed phase. For each Reynolds number, all of the mean streamwise velocity profiles, turbulent kinetic energy (TKE), and wall-normal RMS values were first compared against reference LES and DNS data. To reveal the wall modeling capabilities of the ER-HRL approach, in particular, predictions were compared to ones obtained by its RANS mode (i.e. the $k - \epsilon - \zeta - F$ model). Turbulent statistics obtained by the ER-HRL were shown to exhibit better convergence than the AWMLES model compared to the reference DNS data at a much lower computational cost than conventional LES. In addition, it was noted that the wall-normal RMS velocity is better predicted by the ER-HRL model compared to pure RANS using the same mesh, especially in the near-wall region.

In the context of subgrid-scale (SGS) modeling, the novel particle ζ-SGS model was tested versus the AWMLES complemented by the Fukagata SGS model (Fukagata et al., 2004). The new model is based on the wall-normal transport equation (ζ) which is mainly activated in the RANS region. The ζ-SGS model accounts for the most dominant subgrid motion scales by retrieving the non-filtered velocity field in the wall-normal direction through turbulent kinetic energy and the wall-normal velocity variance. This very component is most influential on particle deposition rates on the wall. The model prediction of particle statistics was investigated in parallel to the AWMLES with the Fukagata SGS model. Both models were validated against DNS data for a wide range of particle inertia i.e. St= 0.2, 1, 5, 15, 25, 125. For each particle timescale, first and second-moment statistics, as well as number density profiles, were reported.

The obtained particle statistics at low turbulence level ($Re_\tau = 150$) from both models are in excellent agreement with DNS data. For high Reynolds number case ($Re_\tau = 590$), results were compared to LES with subgrid stochastic acceleration model (LES-SSAM) as well as DNS from Zamansky et al., 2011. It was shown that the ER-HRL with ζ-SGS model is superior to both AWMLES with the SGS Fukagata model and LES-SSAM. This is rather more obvious in wall-normal RMS values at low-to-mid inertia particles in the wall region. The present investigation

shows that for low to mid-inertia particles, the ER-HRL model shows a very good agreement with classical LES, yet at a much lower CPU cost. However, very high inertia particles (i.e. St = 125) show some deviation from LES-SSAM and DNS data, especially in the wall-normal RMS trend. The author suggests that such an effect could be remedied by correcting for the Stokes number filtering in further works. In addition, it was shown that the AWMLES model supplemented with the Fukagata SGS model matched more closely the reference data in the outer region of the boundary layer. We conclude that the contribution of the ζ-SGS model is very significant at higher Reynolds numbers, especially on coarse grids.

8.3   Complex turbulent flows

8.3.1   Differentially Heated Cavity

As a second benchmark to test the model implementations, a flow inside a three-dimensional, wall-bounded, differentially heated cavity (DHC) is considered at the Rayleigh number of Ra = 10^9. This benchmark has long been investigated using several turbulence modeling approaches. In particular, both RANS and hybrid RANS/LES were shown to produce poor results in the near wall region, in case a finite cavity length is used. This is mainly challenging due to the simultaneous existence of both laminar and turbulent regions and the underlying transition from laminar to turbulent flow. It is known that eddy-viscosity-based turbulence models cannot capture laminar-turbulence transition accurately due to simplified strain-stress relation.

To this end, LES stands as a common tool for simulating the flow inside 3D cavities. However, to properly resolve the boundary layer, LES has stringent resolution requirements that scale with powers of the Grashof number Dollet and Boulogne, 2017. For this reason, the flow field inside the cavity has been investigated using Large Eddy Simulations on a mesh significantly coarser than used in traditional LES. In particular, two LES models have been used, the standard and dynamic Smagorinsky models. Wall-to-wall radiation effects have been implicitly taken into account by imposing the measured temperature profiles of bottom and top walls as Dirichlet BCs in all simulations. An extensive quantitative analysis is reported for the fluid flow where first and second-moment statistics were reported. The results are compared against both well-resolved LES by Dehbi et al., 2017 and the experimental database by Kalilainen et al., 2016 at different locations across the domain. On a qualitative level, mean and instantaneous fields of both temperature and velocity have been shown to capture the correct physics. Temperature iso-contours were shown to reproduce the well-known hook-like structures which stem from the very high curvature at the cavity corners. Noticeable findings of centrosymmetric temperature and velocity fields as well as counter-rotating secondary flow structures in the core region have been reported.

From a quantitative point of view, it was shown that both coarse LES models can predict the mean flow properly. However, for high moments i.e. RMS values for horizontal and vertical

velocity fluctuations, a significant underprediction of the flow statistics were observed in the near-wall region by the standard Smagorinsky model. On the other hand, the dynamic model predictions match the reference LES and experimental databases very well. The main reason behind this difference is the better representation of eddy viscosity values near the wall by the dynamically adjusted model coefficient, and hence, the flow is well represented compared to the standard model.

The first and second central moment statistics by the coarse dynamic Smagorinsky model are globally in very good agreement with the reference data at a fraction of CPU cost relative to LES by Dehbi et al., 2017. The obtained results agree on both qualitative and quantitative levels with the results obtained by LES of Dehbi et al., 2017, DNS of Puragliesi et al., 2011, and the experimental measurements of Kalilainen et al., 2016. Good performance of coarse dynamic LES simulation with less than 0.2 million compared to the 2.4 million-cell-mesh of well-resolved LES confirms that coarse LES of cavity flow with the right SGS model can still be used for further fluid flow investigations.

In a second step, the accurate predictions of the fluid flow (using the dynamic Smagorinsky model) were used to feed particle tracking in an Euler/Lagrange frame. In a systematic study, seven swarms of 10^5 particles each were computed to investigate a range of different particle aerodynamic diameters $d_p = 1.4 - 14~\mu$m. In particular, predictions of depletion rates for $d_p = 1.4, 3.5~\mu$m particles obtained by coarse LES were compared to reference LES and experimental databases. Results show a considerable deviation from the trend of depletion rate in a way that particle sizes below 3.5 μm have an overpredicted deposition rate, whereas above that limit it becomes underpredicted. This effect is more justified in sub-micron and low-inertia particles where turbulent fluctuations are more relevant. However, mid-to-high inertia particles still showed a considerable deviation from the reference data for particle deposition. This discrepancy is likely due to the low-order integration scheme used for LPT in T-Flows. It must be also pointed out that insufficient time interval obtained by T-Flows due to the huge CPU needed for a prolonged simulation prevents us from drawing a safe conclusion about the accuracy of the integration scheme or lack of thereof.

To eliminate all sources of error, a similar systematic investigation was done using ANSYS Fluent, 2015 code. Such analysis aims to compare the results of the same code (i.e. Fluent) predicted by low-to-high resolution meshes against reference data. Fluent results showed that the mesh resolution has a pronounced effect only on smaller particles, where the under-resolved motions are more relevant. On the other hand and unlike T-Flows, Fluent showed a very good agreement with the reference data for high-inertia particles. It was also found that the mesh resolution in the near-wall region is quite significant for accurate particle depletion results. Through a sensitivity computation of two particle sizes (i.e. $d_p = 1.4, 3.5~\mu$m), it was found that the inclusion of the thermophoretic force is the main driver of the unique spatial deposition pattern. It was noted however that thermophoresis has little effect on the depletion rates of particles in general. This is due to the strong turbulent diffusion which is the overriding cause for the significant deposition rates of smaller particles. This comes in alignment with

the observations reported by Dehbi et al., 2017. The good performance of coarse dynamic LES using ANSYS Fluent with less than 0.125 million cells compared to the 2.4 million-cell-mesh of well-resolved LES confirms that for the cavity simulation, CLES with the right SGS model can still be used to predict accurately the motion of a specific band of particle sizes.

8.3.2   Gas Cylone Separator

As a second complex flow benchmark in this project, the ER-HRL model was investigated in a Stairmand high-efficiency gas cyclone modeled with a dust bin collector at a high Reynolds number of Re = 280,000. Mean and RMS velocity profiles of both axial and tangential components are reported at different locations across the cyclone axis. The model predictions were compared to both LES and experimental databases (Derksen, 2003; Hoekstra, 2000; José de Souza et al., 2012).

Results show that the model is capable of predicting the mean tangential velocity profiles fairly well. However, mean axial velocity predictions show some deviation from reference data, especially at the conical section of the cyclone. Although the axial RMS values are following the same trend of the experiment, their magnitudes were also shown to be underpredicted. On the other hand, the RMS values of the tangential component give a relatively better prediction. The swirl intensity was observed to be significantly amplified at the core of the main vortex which may have been reflected in the axial velocity profiles (departing from the expected behavior). Even though the ER-HRL model accounts for part of the wall anisotropy (through ζ transport equation), the author claims that it might be not sufficient to rely on RANS models based on linear eddy viscosity models in handling swirling flows with very strong anisotropic effects in the wall region. Given such flow configuration, the discrepancies in RMS profiles can be attributed to the absence of the two other variances (i.e. $\overline{u'u'}, \overline{w'w'}$).

Since the dispersed flow in this benchmark is impaction driven, higher-moment statistics are considered secondary to particle motion. In this light, a systematic analysis of twelve particle swarms was conducted to assess the model prediction of the cyclone separation efficiency. A wide range of particle sizes spanning two orders of magnitudes of Stokes number ranging between St = 2.3 * 10^{-4} - 3.3 * 10^{-2} was considered. Cyclone grade efficiency shows a better agreement with the experimental results by Xiang et al., 2001 than the ones obtained by coarse LES of José de Souza et al., 2012.

8.3.3   ARTIST project - Swirl Vane separator

As a final benchmark, an extensive analysis was conducted on phase IV of the ARTIST project which is considered the most complex flow in the presented thesis. This configuration represents the droplet retention in swirl vane separator (SVS) and dryer sections under simplified conditions. The main objective of this study is to assess the prediction of particle retention efficiency using Wall-Modeled LES. Due to the ER-HRL model limitations in T-Flows, the Delayed

Detached-Eddy Simulation (DDES) with the Realizable k-e RANS model in ANSYS Fluent was used. Systematically, two configurations of the swirl vane were considered (with and without a dryer section) at a range of mass flow rates were considered i.e. $\dot{m}$ = 100, 200, 400, 600, 800 kg/hr. For an accurate spatial resolution, a fully hexahedral block-structured mesh was constructed. A mesh sensitivity check was performed using two meshes comprising 699,734 and 4,898,082 elements - to judge the effect of SGS motions on turbulent flow prediction.

To analyze the contribution of wall modeling in DDES, two other models (i.e. LES Smagorinsky and RSM) were used as a preliminary step at two mass flow rates $\dot{m} = 400,600\,kg/hr$. Models' predictions of both mean flow and higher moment statistics were reported for each case. Although the Reynolds Stress Model (RSM) has a better prediction for the mean flow, it was shown that the DES gives a better global picture for higher statistics. Results of both mean and RMS velocity profiles for both transversal and axial components were compared to the experimental data by Kapulla, 2008 at different locations across the SVS.

Results show that for configuration D (without dryer section), the DES exhibits a good prediction of the mean flow, whereas RMS values are considerably underpredicted. For configuration E (with dryer), although DES reproduces the global trend of the mean flow right after the swirl vane section, it fails to predict both the mean flow and higher moment statistics further away from the vane (i.e. close to the dryer entrance). The trend of mean transversal velocity profiles is fairly a good match with the experiment. However, the magnitude is missing up to 40%. The author suggests that such deviations from the experimental data in configuration E are mainly due to the poor modeling of the dryer geometry (since the cap of the dryer is completely missing). This can be seen to be directly projected on both mean and RMS axial velocity profiles that are predominantly affected at the dryer section relative to the first measuring point (close to the vane).

As a final particulate flow study, particle retention efficiency was investigated through twelve particle swarms (i.e. $d_p = 5 - 60\mu m$) spanning three orders of magnitude of Stokes numbers. All swarm sets were computed in configuration E for each mass flow rate considered, where experimental data from Kapulla, 2008 are available. As a result of mean flow under-prediction, the total retention efficiency is underestimated, especially for particles with a diameter below 40 microns. This comes as no surprise since the mean flow was shown to be underestimated by DES, and therefore, the accuracy of predicting particle statistics was compromised.

8.4 Thesis conclusions

This thesis has addressed the prediction of particle-laden flow dispersion using Wall-Modeled LES (WMLES). A reliable platform for Lagrangian particle tracking (LPT) was implemented in the open-source research code T-Flows. An algebraic WMLES turbulence model based on Prandtl mixing length for implicit wall-modeling as well as two recent particle SGS models (i.e. the $\zeta - SGS$ Sayed et al., 2021-b and Fukagata et al., 2004 SGS models) were incorporated in the algorithm. In addition, a Discrete Random Walk (DRW) like the model has been added to

the code to provide stochasticity for particles in pure RANS simulations.

The proposed $\zeta - SGS$ model which is tailored for the ER-HRL turbulence model proved to be very robust and cost-effective in turbulent canonical flows (e.g. channel flow). It should be also emphasized that the ER-HRL model is capable of accurately recovering turbulent kinetic energy at even higher Reynolds numbers with coarse grids Sayed et al., 2020. However, the model rationale of using relatively coarse grids to explicitly activate the $k - \epsilon - \zeta - F$ RANS model is jeopardized by the lost finer details of fluid flow due (i.e. SGS motions). This was also shown to be the case in more complex flows like the Stairmand gas cyclone separator, where the swirling motion cannot be fully captured by linear eddy-viscosity (LEV) models. Through all simulations of forced convection flows done in this thesis, the implemented LPT was shown to be very efficient with a slight particle overhead. However, more optimization is needed in T-Flows for naturally convected flows (e.g. the DHC) in this thesis, as well as other improvements in the numerical scheme. In this light, some recommendations are suggested in the next section to develop the code further.

The findings of this study will serve as a new platform for studying dispersed flows at a lower computational cost, and an accurate open-source database against which researchers in hybrid RANS/LES multiphase flow can validate their models.

8.5 Remarks and perspectives

In the context of code development and the continuation of work on particle tracking in WMLES, we make some recommendations for future work and give a few remarks on possible improvements in the LPT of T-Flows.

8.5.1 Particulate flow in 90-degree-bends

1. Deposition efficiency can be sensitive to the spatial distribution of particles at the inlet section. It was noted that the Gaussian distribution of particles (in Fluent) influences the deposition curve (especially at the cut-off i.e. range of the mid-inertia particles). The reason for this is that when using the normal distribution, more particles are located at the core of the flow and hence have higher velocity, and therefore more particles tend to impact the bend-wall conjuring up higher deposition data. This in particular results in a higher deposition for inertial and mid-inertial particles.

2. Special attention is required for advection schemes in particulate flows. If the background flow is not properly solved, particle results cannot be trusted. In the scope of this work but also in a broader context, the first-order upwind scheme should always be avoided, especially in turbulent flow regimes with dispersed particles.

3. Particle deposition efficiency is very sensitive to the physical properties used in the simulation. Hence, due care must be given not only to matching the operating Reynolds

number with the reference data but also to match the same physical properties for the carrier flow (density and viscosity in this case). To avoid confusion, such analyses should always be based on the non-dimensional Stokes number (provided that the same definition for fluid timescale is incorporated).

4. Curvature ratio (defined by the ratio of the radius of curvature to the pipe diameter) is a key parameter in reproducing the deposition curve in 90-degree-bends. Using larger curvature ratios with the same operating Reynolds number might lead to flattening out the deposition curve. This is due to the extended timescale which renders cutoff length particle sized to have less Stokes number values (i.e. more time to adapt to the new flow direction).

5. It was noticed at the start of the simulations that the solver struggles to advance the flow through the bend. This is mainly caused by two reasons: the reversed flow forming at the outlet section and the nonphysical flat inlet velocity profile. To circumvent the first problem the user can switch between pressure outlet and convective outflow boundary conditions that are existing in the code to converge the solution. For a more physical velocity inlet, a precursor domain can be employed where a pipe flow is solved independently to develop the flow. Once the BL is established, the precursor domain is computed simultaneously with the main 90-degree-bend (i.e. outlet of the precursor domain is the new inlet of the 90-degree bend).

8.5.2   Particulate flow in DHC

- Particle depletion rates are highly sensitive to the boundary layer resolution (first cell height is crucial). For this sake, it is very useful to conduct a mesh sensitivity study before extensive particle analysis, especially when using coarse LES.

- Even though the mesh employed can be sufficient to represent the background flow properly, this does not omit the chance that particles might need a better mesh resolution for an accurate prediction. In this context, it is worth mentioning that particle deposition can be greatly affected by the under-resolved motion scales at the wall. This is easily spotted with small-inertia particles but it can also affect the prediction of bigger particles.

- Time integration scheme for particles might have some effect; in the present work, the Runge-Kutta fourth-order (RK4) scheme was used for velocity, while for calculating particle position, time advancement was done through Forward Euler scheme. In addition, the spatial interpolation of the fluid velocity at particle location is done by three-dimensional linear interpolation was used which could be slightly less accurate than higher order models. Such effect can be merely more pronounced on larger time intervals, which is the case in DHC flows. Nonetheless, it is worth noting that when using a higher order scheme, we must use a first-order method for the points adjacent to the boundary (which does not change the global error bounds).

197

- It must be emphasized that a sufficient number of time realizations are needed to draw a safe conclusion on particle predictions. This point can be spotted once the particle relative concentration shows an exponential decay trend (varies linearly on a log scale) with time.

- Small numerical artifacts can accumulate into a big margin of error in such flow configurations where the physical time required is relatively long. Since CPU time can be very long for smaller particles, it can be very useful to employ a simple neural network model (NN) as a posteriori to extrapolate the curve. In this way, the trend can be easily predicted within a small range of uncertainty - saving hundreds of CPU hours.

- The mesh resolution in the boundary layer and especially the first cell size is very crucial for an accurate prediction of particle depletion rates and decay constants. This was concluded from a sensitivity pre-analysis done by Fluent where several BL resolutions were used to predict the depletion rates of mid-to-high inertia particles.

- The use of the LES dynamic Smagorinsky model with TKE transport was found to add no noticeable enhancement to the results compared to the standard dynamic Smagorinsky model even in the case of coarse LES. That said, it is clear that using the standard dynamic model is more efficient in investigating particulate flow inside the cavity. Comparisons of both models' predictions of the primary flow (first and second-moment statistics) are reported in Appendix B.

8.5.3   Particulate flow in Gas Cyclone separators

- An implementation of a more efficient way of advancing particles transiently is highly encouraged. This is quite crucial for problems like the gas cyclone where particle injection is clustered into a relatively small control volume at the beginning of the simulation. Since this is the only way to introduce particles in reversed gas cyclones, the lack of an efficient concurrent simulation can lead to an undesirable bottleneck caused by a massive swarm overhead.

- Even though the current study revealed that SGS motions have relatively less effect on particle separation efficiency, it is recommended to include the particle SGS model to alleviate deviations from the trend for smaller particles. In that context, the $\zeta - SGS$ model can be extended to deal with curved walls and arbitrary geometries.

- Since fluid timescales have a wide range (especially in such highly turbulent flows with strong swirling motion) between LES and RANS zones, it is worth investigating the effect of these two different timescale zones on the particle advancement as a future analysis.

- It will be very interesting to perform a pure LES simulation using the dynamic Smagorinsky model and compare results to the ones obtained by the ER-HRL model using the same mesh.

- As impact velocities can be locally high, sub-models for particle bounce off the walls can be considered. In particular, the model of Minier et al., 1991 for the coefficients of restitution in cyclones as well as the well-known wall collision model of Thornton and Ning, 1998 may be implemented and looked at.

A Appendix A

A.1 Turbulence Modeling & Reynolds stresses

Consider an incompressible Newtonian fluid with uniform and constant molecular viscosity. Navier-Stokes equations read

$$\frac{\partial u_i}{\partial x_i} = 0 \tag{A.1}$$

$$\frac{\partial u_i}{\partial t} + u_j \frac{\partial u_i}{\partial x_j} = -\frac{1}{\rho}\frac{\partial p}{\partial x_i} + \frac{\partial}{\partial x_j}\left[\frac{2\mu}{\rho}S_{ij}\right] \tag{A.2}$$

where S_{ij} is the strain rate tensor that reads

$$S_{ij} = \frac{1}{2}\left[\frac{\partial u_i}{\partial x_j} + \frac{\partial u_j}{\partial x_i}\right] \tag{A.3}$$

By plugging this strain rate into equation 2, it yields

$$\frac{\partial u_i}{\partial t} + u_j \frac{\partial u_i}{\partial x_j} = -\frac{1}{\rho}\frac{\partial p}{\partial x_i} + \frac{\mu}{\rho}\left(\frac{\partial^2 u_i}{\partial x_i \partial x_j}\right) \tag{A.4}$$

In turbulent flows, the properties of the flow become randomly distributed in both time and space over a wide range of motion scales. In order to see the effect of the turbulent perturbations on the mean flow, we use Reynolds decomposition; such that each of the main flow parameters is a contribution of a long-time averaged mean value and a fluctuating one (as in Eq. A.5)

$$u_i = U_i + u'_i, \qquad p = P + p' \tag{A.5}$$

201

Taking time average for the streamwise velocity for instance:

$$U_1 = \frac{1}{T'} \int_{T'}^{T'+t} u_1 dt \tag{A.6}$$

where T' is the time period upon which the quantities are averaged and which by definition should be much larger than any fluctuation lifetime in the domain. For this reason

$$\frac{1}{T'} \int_{T'}^{T'+t} u_1' dt = 0 \tag{A.7}$$

By plugging (5), (6) and (7) into (2), we can obtain the general form of Reynolds-Averaged Navier-Stokes (RANS) equations.

$$\frac{\partial U_i}{\partial x_i} = 0 \tag{A.8}$$

$$\frac{\partial U_i}{\partial t} + U_j \frac{\partial U_i}{\partial x_j} = -\frac{1}{\rho} \frac{\partial P}{\partial x_i} + \frac{\partial}{\partial x_j} \left[\frac{2\mu}{\rho} S_{ij} - \overline{u_i' u_j'} \right] \tag{A.9}$$

where $\overline{u_i' u_j'}$ is referred to as **Reynolds stress tensor**, which stems from averaging the non-linear terms (convection part), while S_{ij} is the mean strain tensor, that is computed from the mean velocity gradients as follows

$$S_{ij} = \frac{1}{2} \left[\frac{\partial U_i}{\partial x_j} + \frac{\partial U_j}{\partial x_i} \right] \tag{A.10}$$

This Reynolds stress tensor (τ_{ij}) is a 9-component-symmetric tensor, and hence, one only has to compute six components (isotropic turbulence is assumed). The diagonal elements ($\overline{u_i' u_i'}$) represent the normal Reynolds stresses and off-diagonal ones ($\overline{u_i' u_j'}$) represent Reynolds shear stresses. Now the momentum equations read

$$\frac{\partial U_i^{\mathrm{I}}}{\partial t} + U_j \frac{\partial U_i}{\partial x_j} = -\frac{1}{\rho} \frac{\partial P}{\partial x_i} + \nu \frac{\partial^2 U_i}{\partial x_i \partial x_j} - \frac{\partial \overline{u_i' u_j'}}{\partial x_j} \tag{A.11}$$

As a consequence of averaging over time, we gained 3 new unknowns and no additional equations. This means we have a closure problem, meaning that we need to find additional equations to close the problem and start the solution. In the last 50 years, a number of turbulence models have been proposed for this sake. One of the most widely used models especially in LES is the Boussinesque approximation which is also used in PSI-Boil code. This is going to be explained below.

A.2   Smagorinsky-Lilly Model

In case of solving Large Eddy Simulation, we have a similar set of equations but with different significance, such that the flow variables are space filtered instead of temporal averaged. The filtered Navier-Stokes equations then read

$$\frac{\partial \overline{u_i}}{\partial x_i} = 0 \tag{A.12}$$

$$\frac{\partial \overline{u_i}}{\partial t} + \frac{\partial \overline{u_i u_j}}{\partial x_j} = -\frac{1}{\rho}\frac{\partial \overline{p}}{\partial x_i} + \nu \frac{\partial^2 \overline{u_i}}{\partial x_i \partial x_j} \tag{A.13}$$

where $\overline{u_i}$ is the filtered velocity, that represents the difference between the actual velocity and the sub-grid scale velocity

$$\overline{u_i} = u_i - u_i' \tag{A.14}$$

$$\frac{\partial \overline{u_i}}{\partial t} + \frac{\partial \overline{u_i}\,\overline{u_j}}{\partial x_j} = -\frac{1}{\rho}\frac{\partial \overline{p}}{\partial x_i} + \nu \frac{\partial^2 \overline{u_i}}{\partial x_i \partial x_j} - \frac{\partial \tau ij}{\partial x_j} \tag{A.15}$$

Where τ_{ij} is referred to as **SGS Reynolds stress tensor** and it reads

$$\tau_{ij}{}^{\mathrm{II}} = \overline{u_i'\bar{u}_j} + \overline{\bar{u}_i u_j'} + \overline{u_i' u_j'} = \overline{u_i u_j} - \overline{\bar{u}_i \bar{u}_j} \tag{A.16}$$

This stress accounts for the difference between non-filtered nonlinear terms in the advection part. Since τ_{ij} is computed ONLY from SGS (filtered) values which are unknowns, it will be bridged to the large scale field through Boussinesque hypothesis. In both (U)RANS and LES, the turbulent (or SGS) eddy viscosity arises from the Boussinesque approach by which the stress tensor (evaluated by statisticly averaged/ filtered velocity field) is linked to mean velocity gradients. Using this hypothesis, Reynolds stress tensor reads

$$\tau_{ij} = -\underbrace{\overline{u_i' u_j'}}_{\text{SGS stresses}} = \nu_t \underbrace{\left(\frac{\partial \overline{u_i}}{\partial x_j} + \frac{\partial \overline{u_j}}{\partial x_i}\right)}_{\text{Large-scale strain rate}} - \frac{2}{3}k\delta_{ij}{}^{\mathrm{III}} \tag{A.17}$$

[I]In fully established flow, the inertial term will be omitted from the above equations. The reason for this is that the statistical properties of the turbulent fluctuations are no longer time dependent. For such a state, the turbulence is said to be statistically stationary.

where k is the Turbulent Kinetic Energy (TKE)

$$k = \frac{1}{2} \overline{u_i' u_i'} \tag{A.18}$$

and ν_t is the turbulent viscosity which is in most cases computed algebrically (as an isotropic scalar quantity) to avoid the need of solving additional equations that would increase the computational expense which is already substantial in case of solving LES. Taking into account that solving the eddy viscosity as a scalar quantity is not "strictly" correct, and that's why the word *apprioximation* properly holds for this approach. In Smagorinsky-Lilly model, the eddy viscosity reads

$$\nu_t = (C_s \Delta)^2 \sqrt{2 S_{ij} S_{ij}} = (C_s \Delta)^2 \, |\, S \,| \tag{A.19}$$

where C_s is Smagorinsky constant, Δ is the filter width and $|\,S\,|$ is the strain rate magnitude. The length scale can have several formulations depending on the chosen low-pass filter. The one implemented in PSI-Boil reads

$$\Delta = min(V^{\frac{1}{3}}, \delta) \tag{A.20}$$

such that V is the volume of the computational cell and δ is the distance to the wall. Substituting from (16) into equation (15), we get the momentum equation in the final form.

$$\frac{\partial \overline{u_i}}{\partial t} + \frac{\partial \overline{u_i} \, \overline{u_j}}{\partial x_j} = -\frac{1}{\rho} \frac{\partial \overline{p}}{\partial x_i} + \nu_{eff} \frac{\partial^2 \overline{u_i}}{\partial x_i \partial x_j} \tag{A.21}$$

Where ν_{eff} is the effective velosity holding both contributions from laminar viscosity and eddy one.

$$\nu_{eff} = \nu + \nu_t \tag{A.22}$$

A.3   Wall Functions

In wall-bounded flows, the vicinity of the wall is either fully-resolved or modeled. For wall-resolved LES in PSI-Boil, wall functions approach (from Werner and wengle) is adopted as a brute modeling to the wall region. Best practice advises that the wall functions should be activated only if the first computational cell height is located beyond $y^+ = 30$ (when wall-adjacent cell falls within the logarithmic region of the boundary layer). This model is based on

---

[III] In Smagorinsky model, the turbulent kinetic energy term in Reynolds stresses is ignored, since it's not modeled

[III] Notice that as the grid is refined, τ_{ij} gets smaller and smaller untill it deminishes.

the power law which scales the dimensionless velocity as follows

$$u+ = \begin{cases} y+ & \text{if} \quad y+ \leq A^{\frac{1}{1-B}} \\ A(y+)^{B} & \text{otherwise} \end{cases}$$

If the power law is integrated over the height of the first cell, the following piece-wise function is obtained for the wall shear stress

$$\tau_w = \begin{cases} \mu \bar{u}_1 / y_1 & \text{if} \quad y+ \leq A^{\frac{1}{1-B}} \\ \rho u_1 / A[\mu / (\rho y_1)^B]^{\frac{2}{1+B}} & \text{otherwise} \end{cases}$$

A.4   Damping functions

- Piomelli damping function

$$f_d = 1 - exp[-(y^+ / 25)^3] \tag{A.23}$$

- Van-Driest damping function

$$f_d = \left[1 - exp[-(y^+ / 25)]\right]^2 \tag{A.24}$$
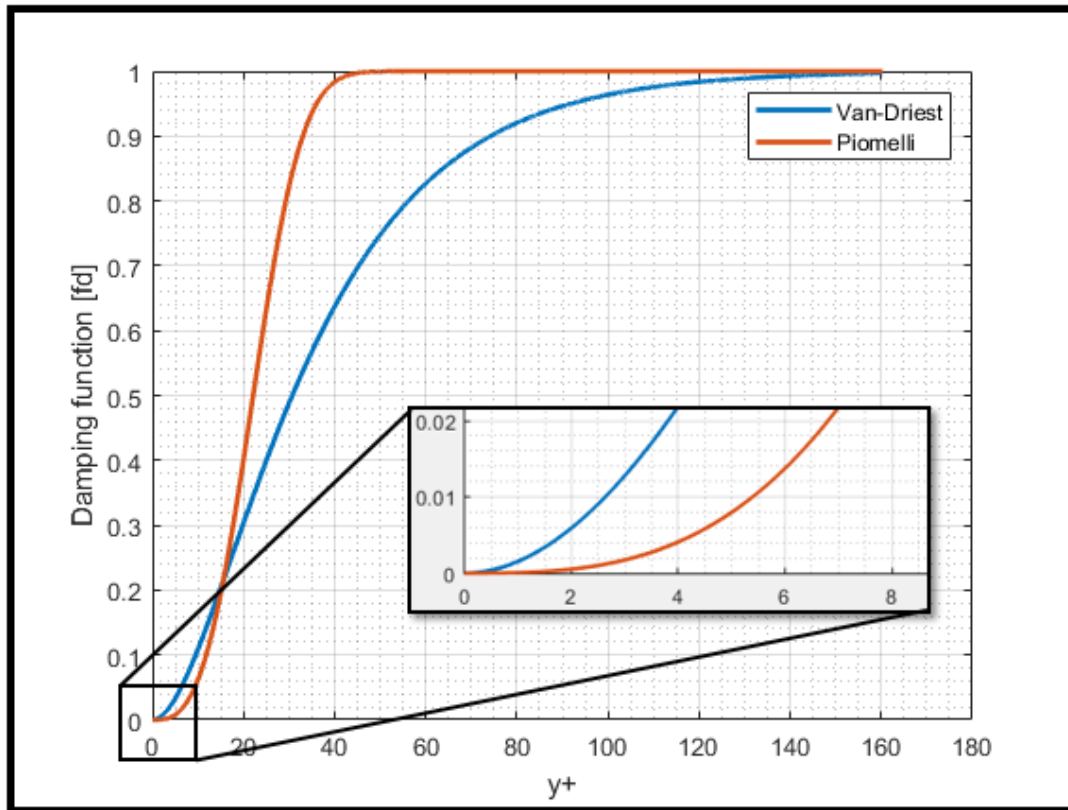
Figure A.1 – Comparison between Piomelli and Van-Driest Damping functions Vs. y+

A | Appendix B

In this section, we point out to some worth-mentioning observations in some of solved cases through this work. As shown below, some of these observations can be uses as preliminary results for the assessment of further model investigations.

A.1 90-Degree Bend

Due to over-damping of the solution, the 1st order upwind scheme can sometimes lead to inaccurate results. this can be seen from the following test in a 90-degree-bend flow where velocity profiles were plotted at the outlet section - obtained by different discretization schemes. it can be seen that the 1st order upwind flattens out the velocity profiles, causing the flow topology inside the domain to change. for this reason, it's recommended when dealing with medium-to-highly complex flows to use higher order schemes e.g. MUSCL, QUICK, 2nd order upwind. The upwind scheme implemented in T-Flows to the date of this thesis - is a first order, whereas the one Fluent uses is a second order. In order to have one-to-one comparison with Fluent (as code verification), we used QUICK scheme where identical profiles for the same mesh and same problem setup obtained. This can be clearly seen in A= Fig. A.1 - A.4
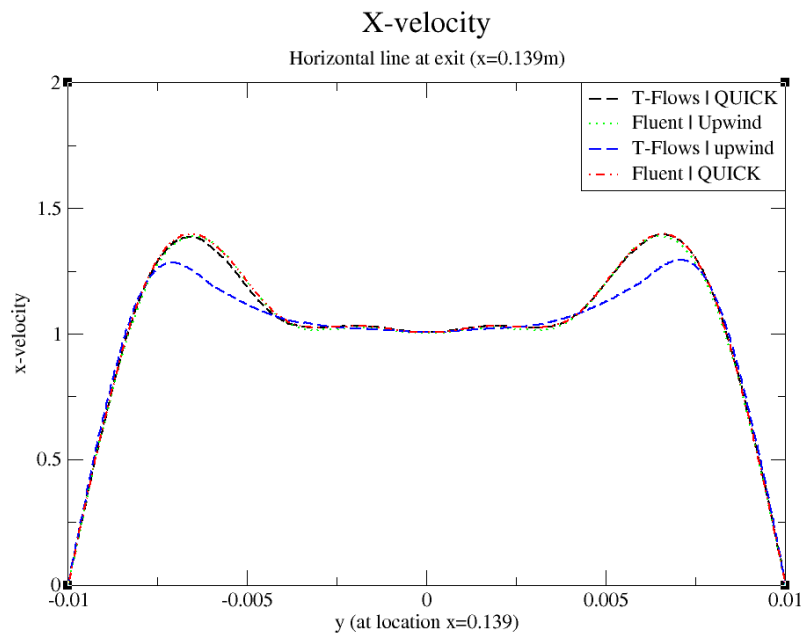
Figure A.1 – Streamwise velocity profiles measured on a horizontal line at the exit of bend (x = 0.139 m). profiles are reported from both T-Flows and ANSYS Fluent with both QUICK and upwind schemes
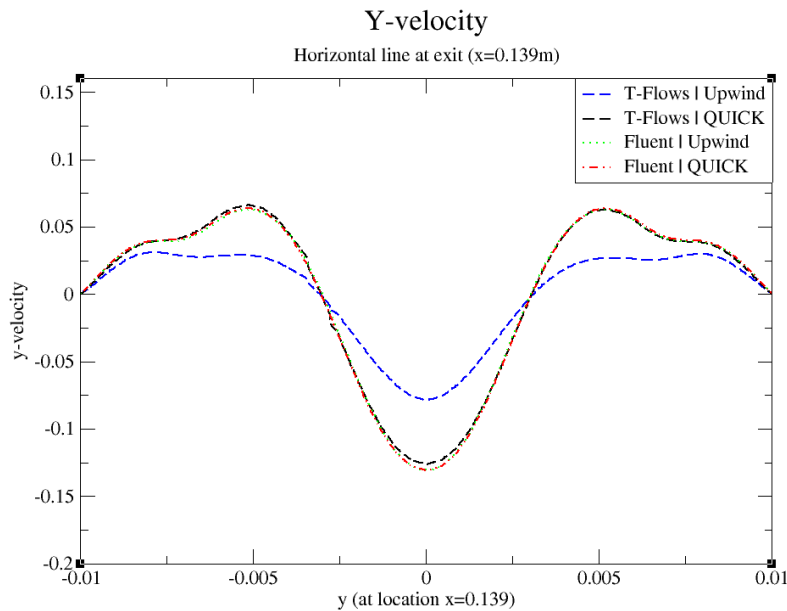
Figure A.2 – Spanwise velocity profiles measured on a horizontal line at the exit of bend (x = 0.139 m). profiles are reported from both T-Flows and ANSYS Fluent with both QUICK and upwind schemes
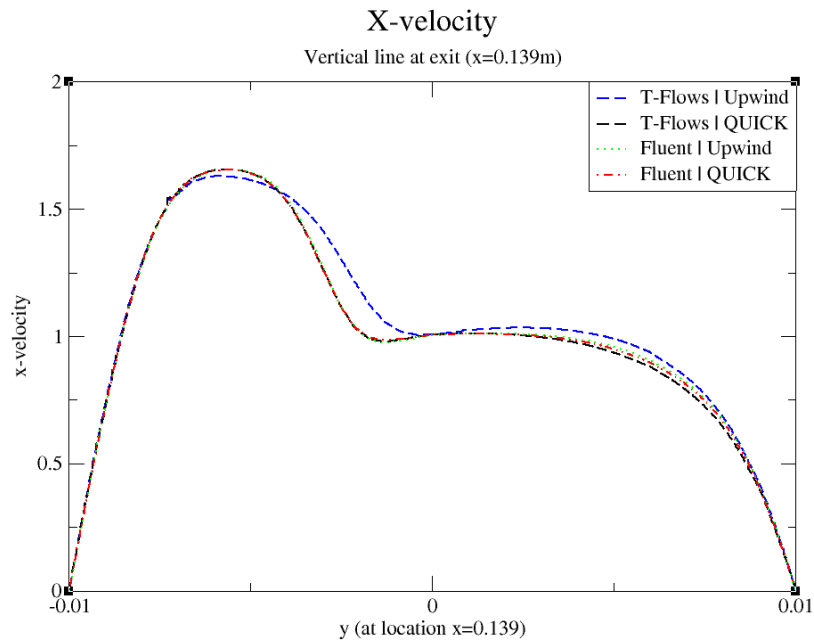
Figure A.3 – Streamwise velocity profiles measured on a vertical line at the exit of bend (x = 0.139 m). profiles are reported from both T-Flows and ANSYS Fluent with both QUICK and upwind schemes
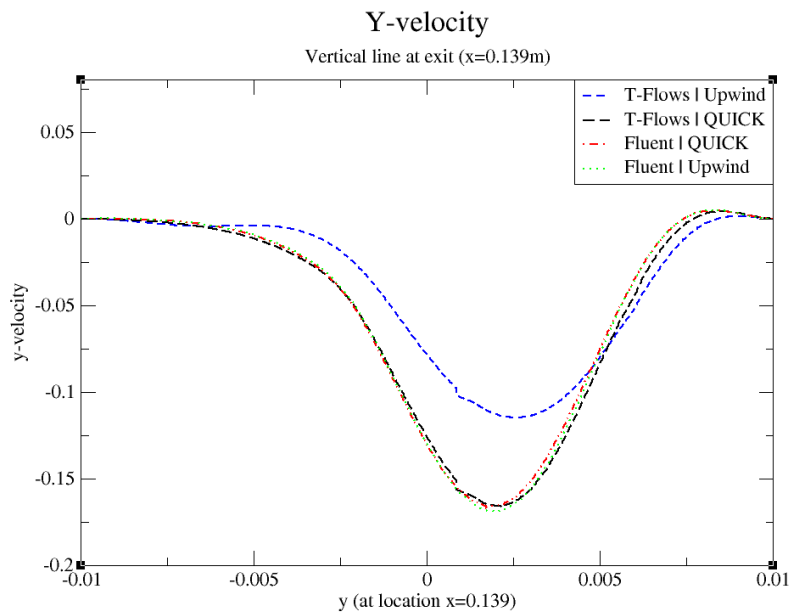
Figure A.4 – Spanwise velocity profiles measured on a vertical line at the exit of bend (x = 0.139 m). profiles are reported from both T-Flows and ANSYS Fluent with both QUICK and upwind schemes

A.2   Turbulent Channel FLow

To verify LPT algorithm for turbulent flow case, a qualitative analysis was conducted first to guarantee that every particle is advanced independently and separately - while seeing the turbulent fluctuations. This can be shown through thw following figures. In Fig. A.5, a single particle's velocities where recorded over some time interval. The time window shows the particle velocities in the three orthogonal directions, closing the first check point. As a second check to make sure particles are transported independently, 16 particles were introduced sequentially (particle by particle) at the inlet of the channel where an inlet-outlet boundary conditions were assigned. Each particle injection is distant from the previous one by 1/10 of the flow through time to make sure we have different behaviour for each particle (affected by the transient primary flow). The particles' Reynolds number in this case range between 0.005 and 0.02 which lies in the region of stokes flow, and hence, approving our one-way coupling approximation. Particles are mid-inertial that they have a Stokes number of 3.8, and the background flow is mildly turbulent with $Re_\tau = 150$. Each particle is treated as escaped once they reach the outlet. As shown in Fig. A.6 - A.7, both particles' trajectories and streamwise velocities give a sound qualitative indication about the anticipated behaviour.
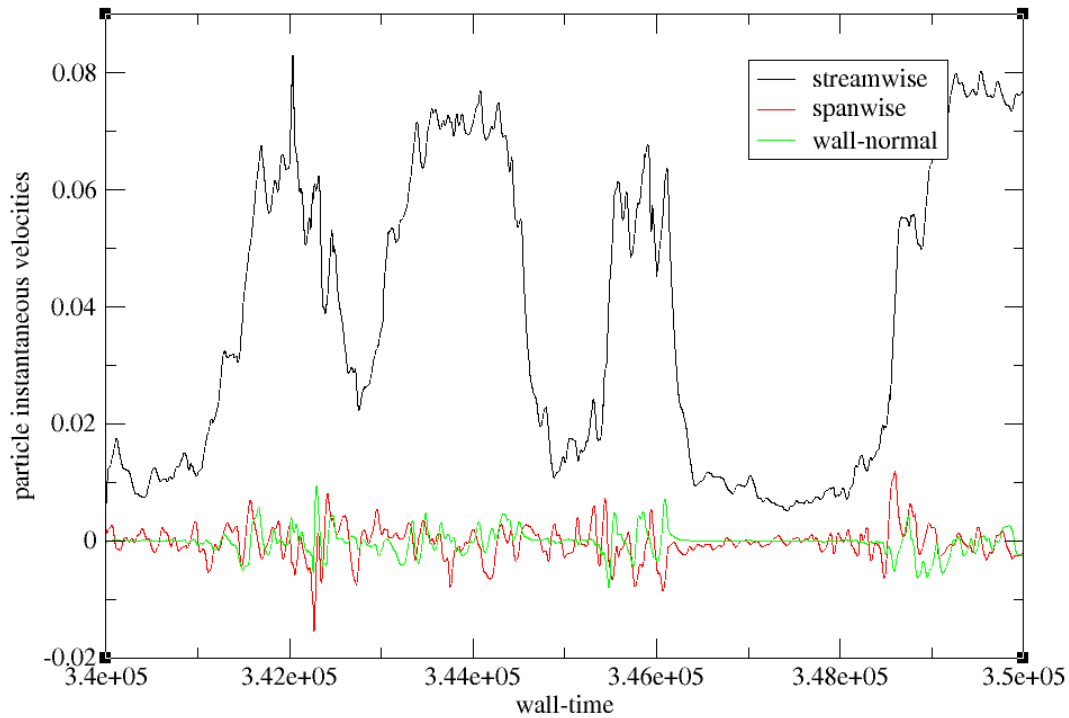
Figure A.5 – Eddy viscosity ratio for different Reynolds numbers predicted by LES/ $k\text{-}\epsilon\text{-}\zeta\text{-}f$
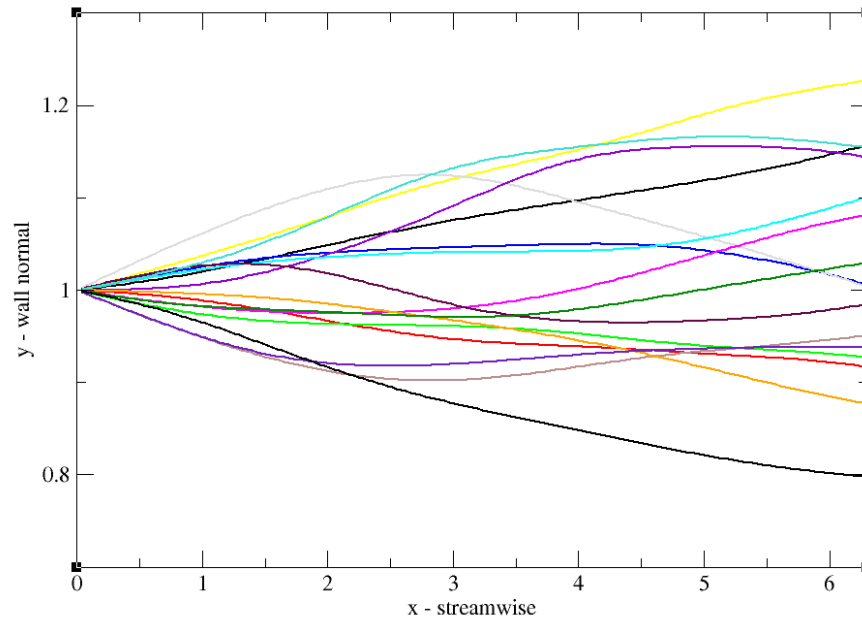
Figure A.6 – Trajectories of 16 particles imposed sequentially in the domain of plane channel
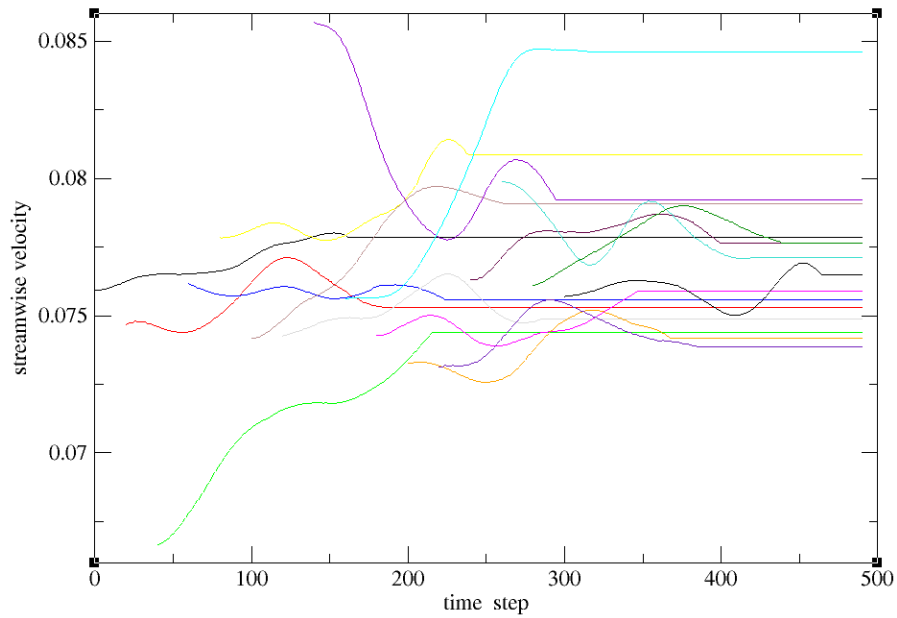
Figure A.7 – Instantaneous streamwise velocities of 16 particles imposed sequentially, the point at which each particle reach a plateau is the exact moment they leave the domain so the computations for the new velocities are not carried out anymore

A.3   DHC-related

A.3.1   Particulate DHC results by T-Flows

In the follwing, we show the results obtained by T-Flows in the Differentially Heated Cavity (DHC) case. As shown in Fig. A.8, only few time instances were obtained for sub-micron particles. This is because of the intense CPU required for smaller particles (due to the tiny time step size used). Although the CLES prediction deviates from the reference data at an early time history, a safe conclusion can only be made over much longer time windows (i.e. two order of magnitudes bigger). A similar observaion can be noted from $d_p = 1.4$ μm particles (as in Fig. A.9).
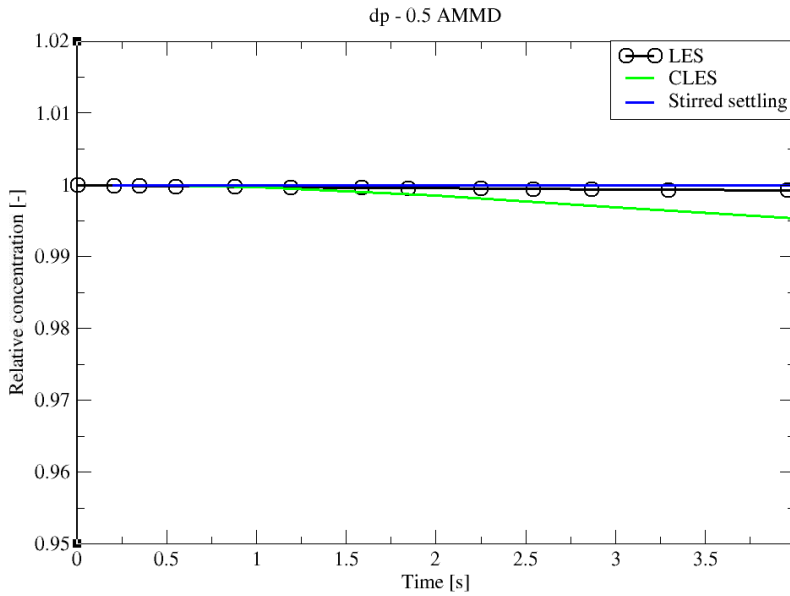
Figure A.8 – Comparison for particle relative concentration of $d_p = 0.5$ μm versus time. Predictions by CLES are plotted against both of LES from Dehbi et al., 2017 and the stirred settling model (Hinds, 1999).

Looking at the spatial distribution of the deposited particles of size 1.4 μm (Fig. A.10), it could be deduced that maybe SGS has little effect on particle depletion rate but a more pronounced effect on the deposition pattern over the cavity walls. As can be seen from the histogram representation, more than 35% of the particles deposit on the hot wall compared to as little as 4% obtained by the well-resolved LES, which is qualitatively a big margin of error. On the other hand, for a bigger particle diameter i.e. $d_p = 3.5$ μm, it could be noticed from Fig. A.11 that CLES prediction is in a better agreement with both LES an experimental data. For a higher inertia particles (i.e. $d_p > 3.5$ μm) the time needed for depleting particles increases (see Fig. A.12), rendering underprediction values from CLES to the removal rate compared to LES.
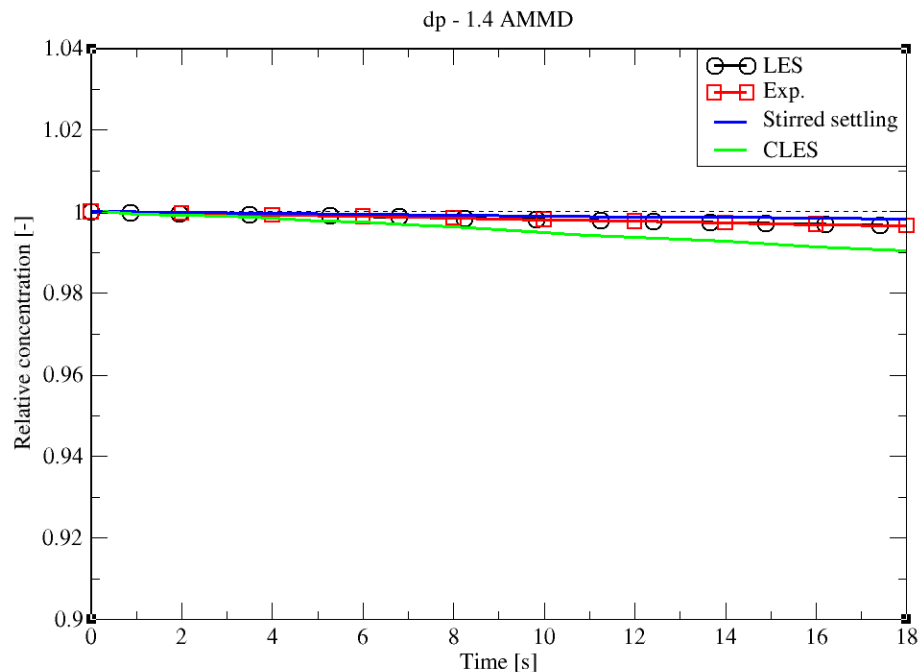
Figure A.9 – Comparison for particle relative concentration of $d_p = 1.4\mu$m versus time. Predictions by CLES are plotted against all of LES from Dehbi et al., 2017, experimental data by Kalilainen et al., 2016, and the stirred settling model (Hinds, 1999).
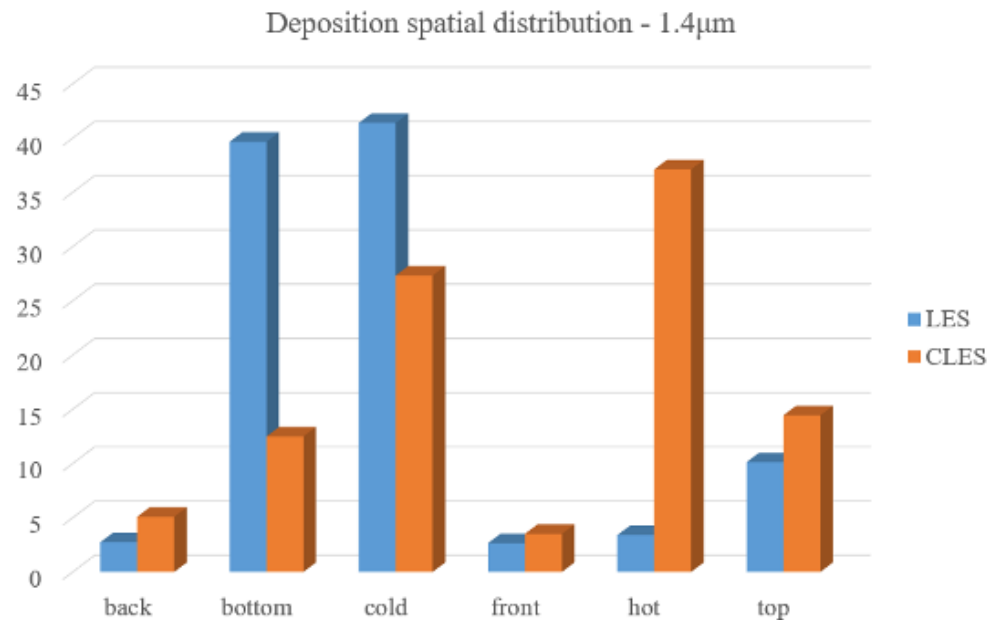
Figure A.10 – Representation of spatially deposited particles on each wall at t=10.2s (Thermophoretic force included) . Predictions by CLES for particle size $d_p = 1.4\ \mu$m are compared against LES from Dehbi et al., 2017.

It should be mentioned that the time interval reported by Dehbi et al., 2017 is much bigger than what we have in the current study. At this point, the discrepancy between the spatial distribution for 1.4 μm particles obtained by CLES and the one predicted by the reference LES could be due to either SGS effects on particle motion or that the number of time realizations is not enough for a safe judgement on the global behavior. In order to have a clearer picture, the decay constant was calculated for each particle diameter against LES predictions. The decay constant β_D is defined as the inverse of time constant for particle removal (Eq. A.1 - A.2). As shown from Fig. A.13, it is clear that the resolution used in the near-wall region is not sufficient to represent the right physics for mid-to-high inertia particles. This is usually the case if the discrepancy in results happen to be in inertial particles range as well as for smaller ones.

$$\beta_D = \frac{1}{\tau_{rem}} \tag{A.1}$$

$$\tau_{rem} = \frac{-ln(\eta)}{T'} \tag{A.2}$$

where η is particle relative concentration at the corresponding time instant, T'.
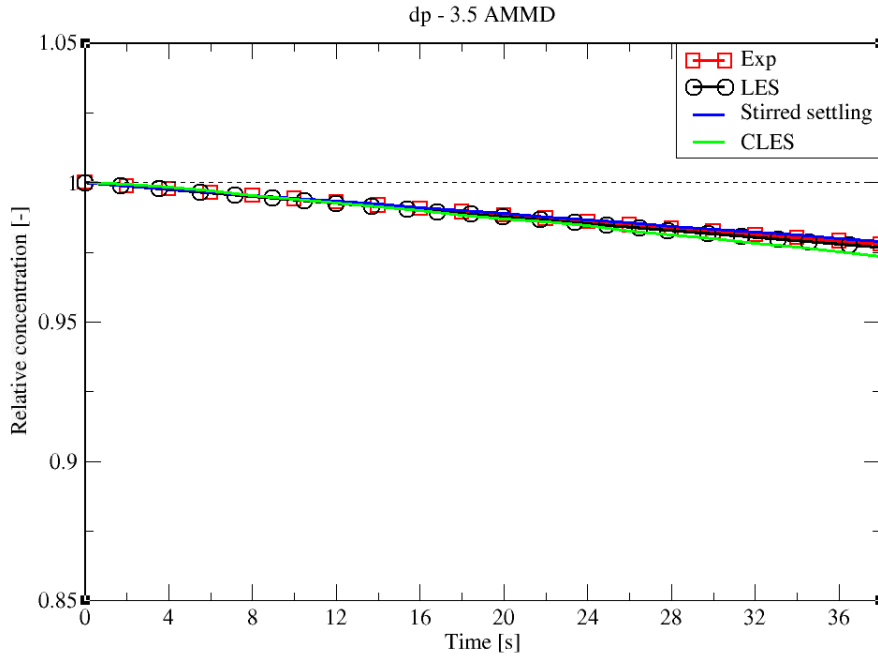
Figure A.11 – Comparison for particle relative concentration of d_p = 3.5 μm versus time. Predictions by CLES are plotted against all of LES from Dehbi et al., 2017, experimental data by Kalilainen et al., 2016, and the stirred settling model (Hinds, 1999).
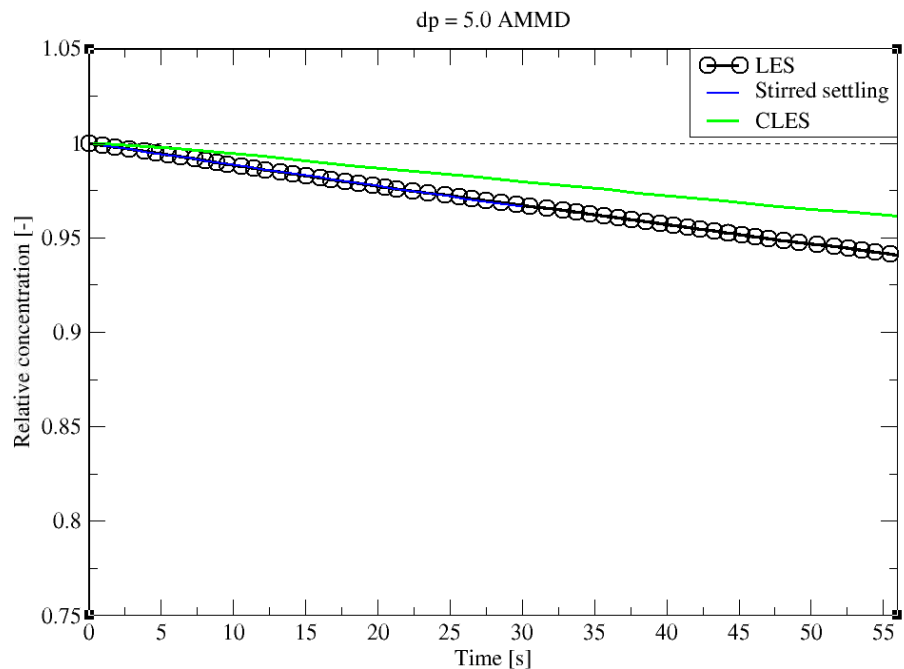
Figure A.12 – Comparison for particle relative concentration of d_p = 5.0 μm versus time. Predictions by CLES are plotted against both of LES from Dehbi et al., 2017 and the stirred settling model (Hinds, 1999).
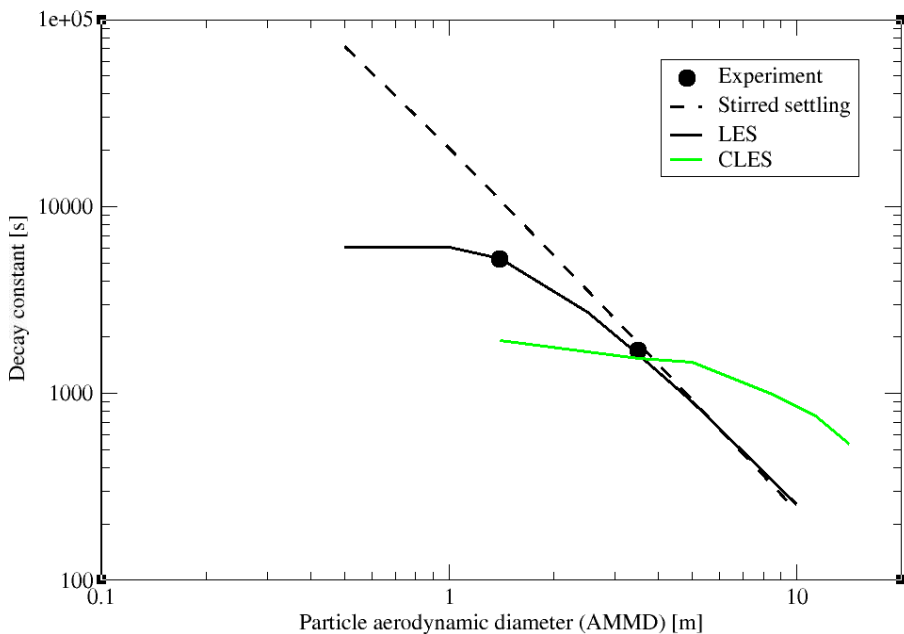
Figure A.13 – Comparison for particle decay constant obtained by CLES against all of experimental and LES data as well as the stirred settling model.

A.3.2 The dynamic Smagorinsky model with K-transport

In the following, the prediction of the dynamic Smagnorinsky model with k-transport is reported in comparison with the results obtained by the standard model. As will be shown below, the results show negligible effect between the two turbulence models, especially regarding particulate flow simulations.
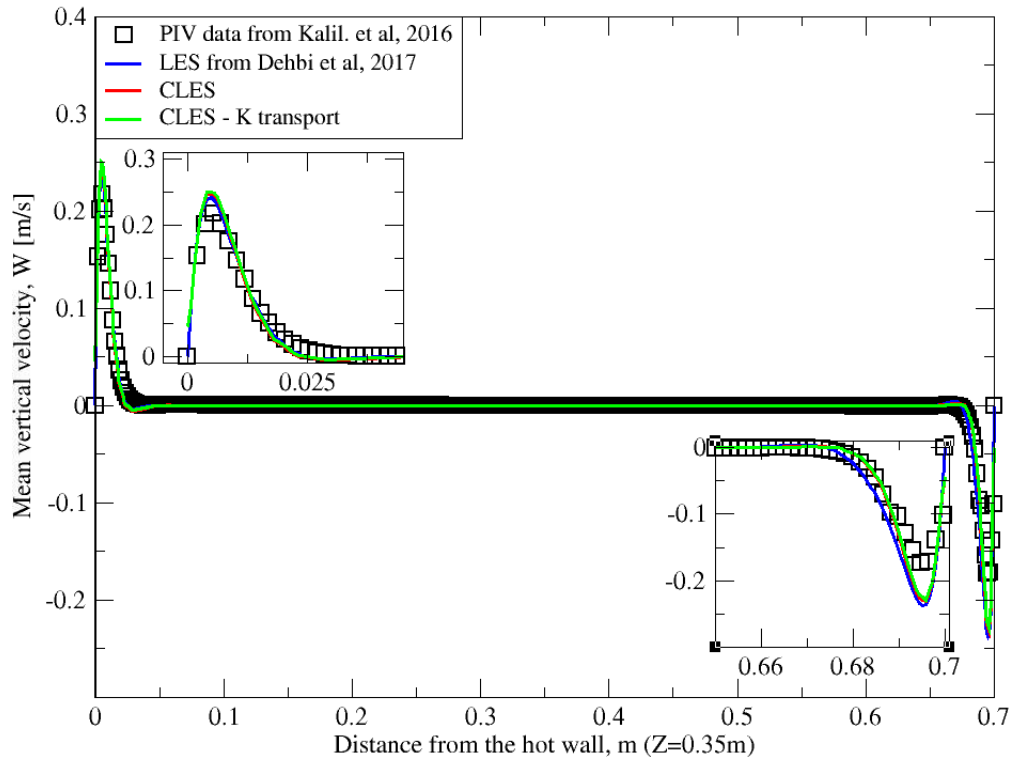
Figure A.14 – Comparison for mean vertical velocity profiles between hot and cold walls from both Smagorinsky models against reference LES and experimental databases. Profiles are obtained at (z = 0.35 m) using same mesh after 2400 time units
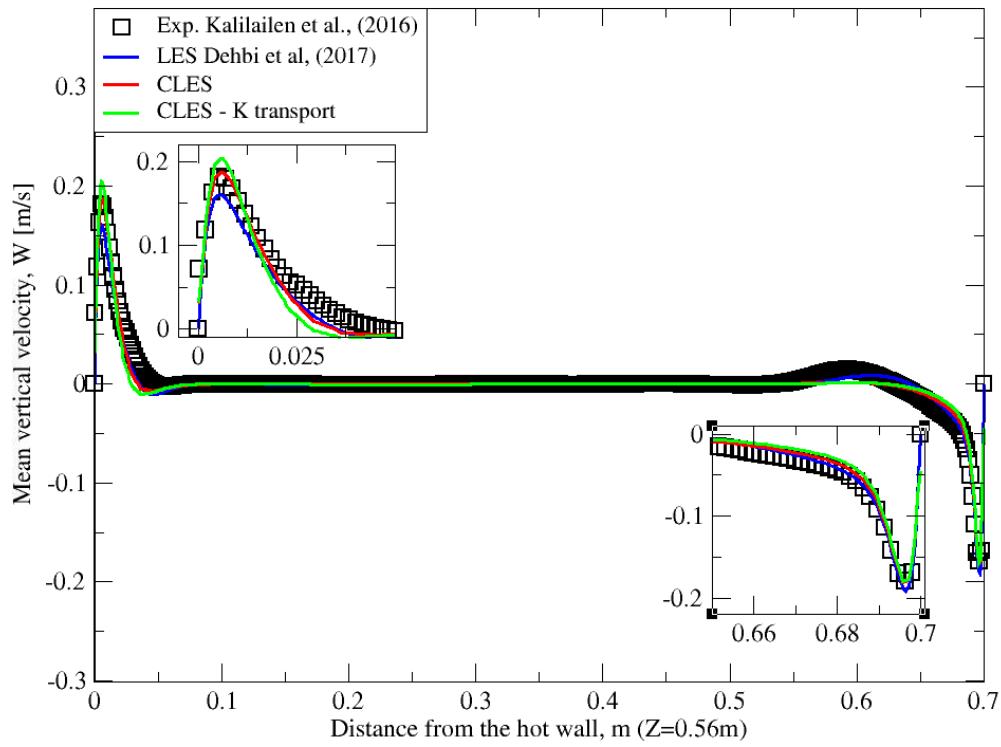
Figure A.15 – Comparison for mean vertical velocity profiles between hot and cold walls from both Smagorinsky models against reference LES and experimental databases. Profiles are obtained at (z = 0.56 m) using same mesh after 2400 time units.
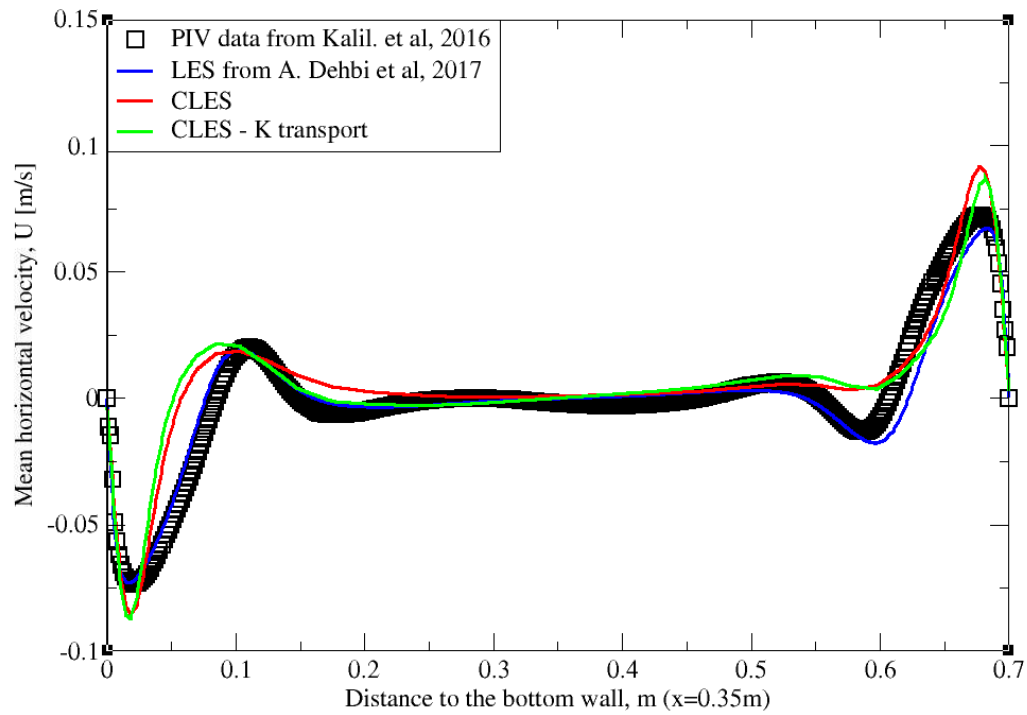
Figure A.16 – Comparison for mean horizontal profiles between bottom and top walls from both Smagorinsky models against reference LES and experimental databases. Profiles are obtained at (x = 0.35 m) using same mesh after 2400 time units.
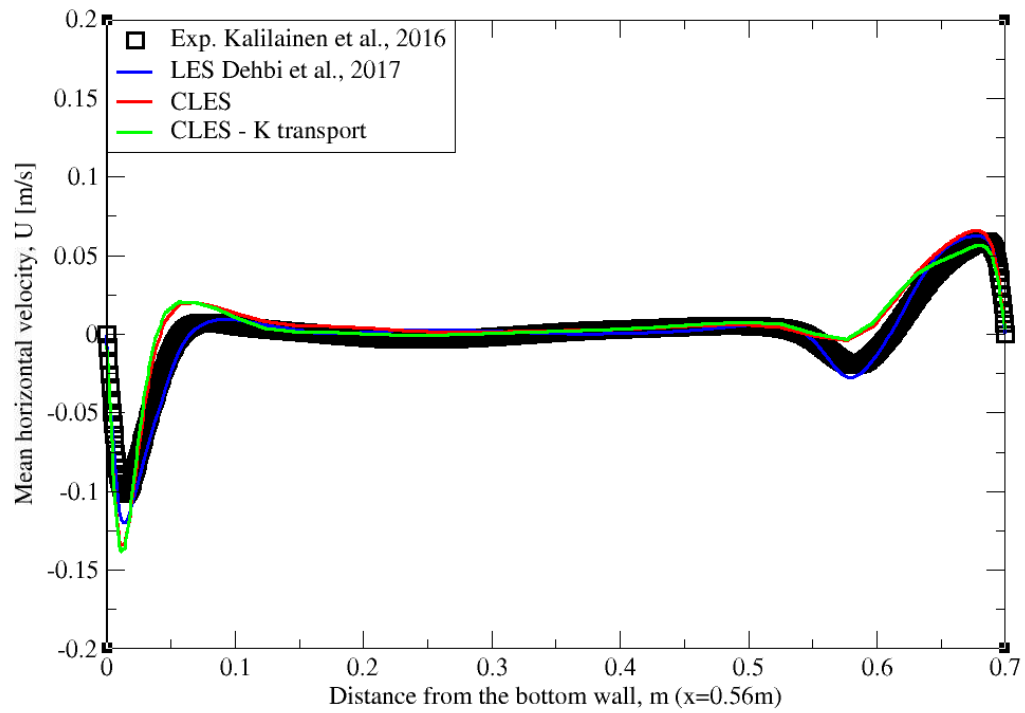
Figure A.17 – Comparison for mean horizontal profiles between bottom and top walls from both Smagorinsky models against reference LES and experimental databases. Profiles are obtained at (x = 0.56 m) using same mesh after 2400 time units.
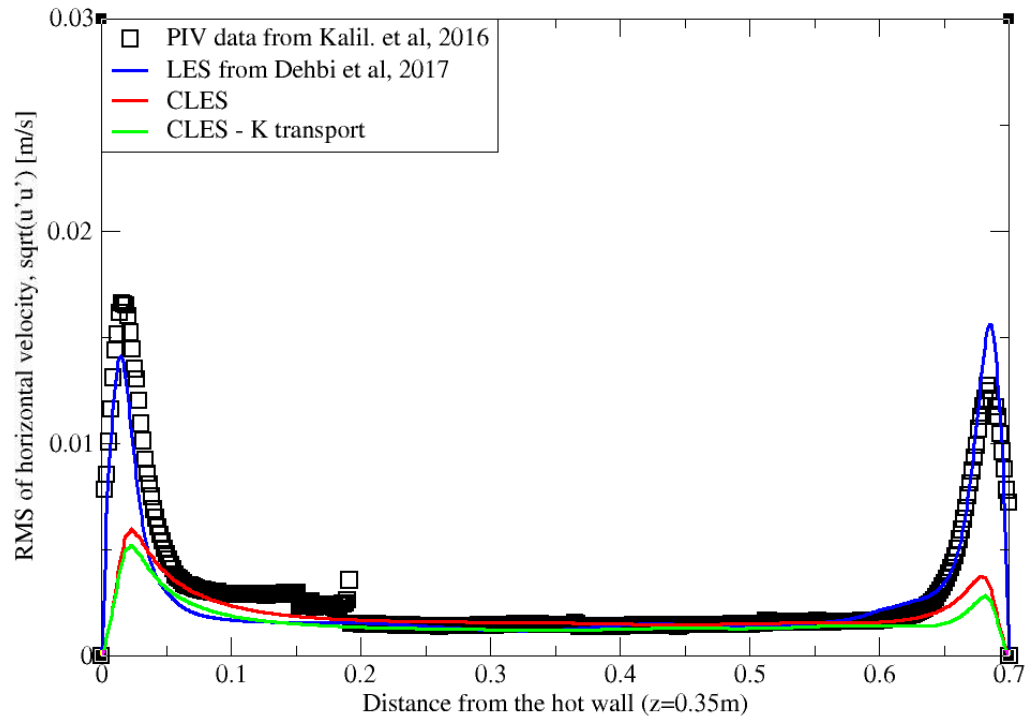
Figure A.18 – Comparison for RMS horizontal velocity between hot and cold walls from both Smagorinsky models against reference LES and experimental databases. Profiles are obtained at (z = 0.35 m) using same mesh after 2400 time units.
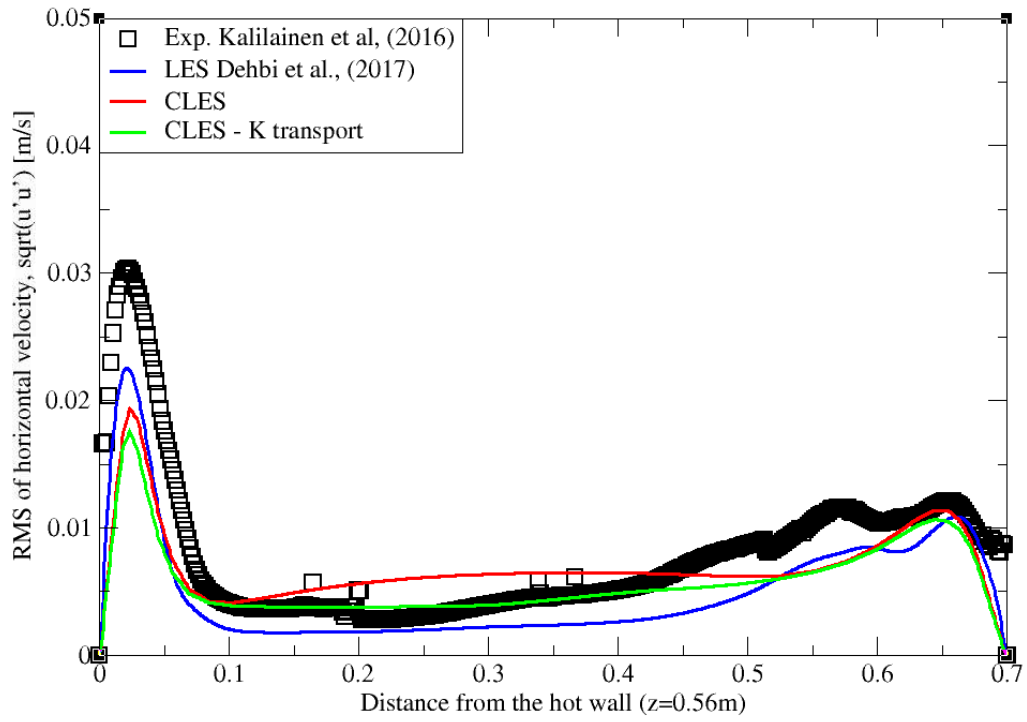
Figure A.19 – Comparison for RMS horizontal velocity between hot and cold walls from both Smagorinsky models against reference LES and experimental databases. Profiles are obtained at (z = 0.56 m) using same mesh after 2400 time units.
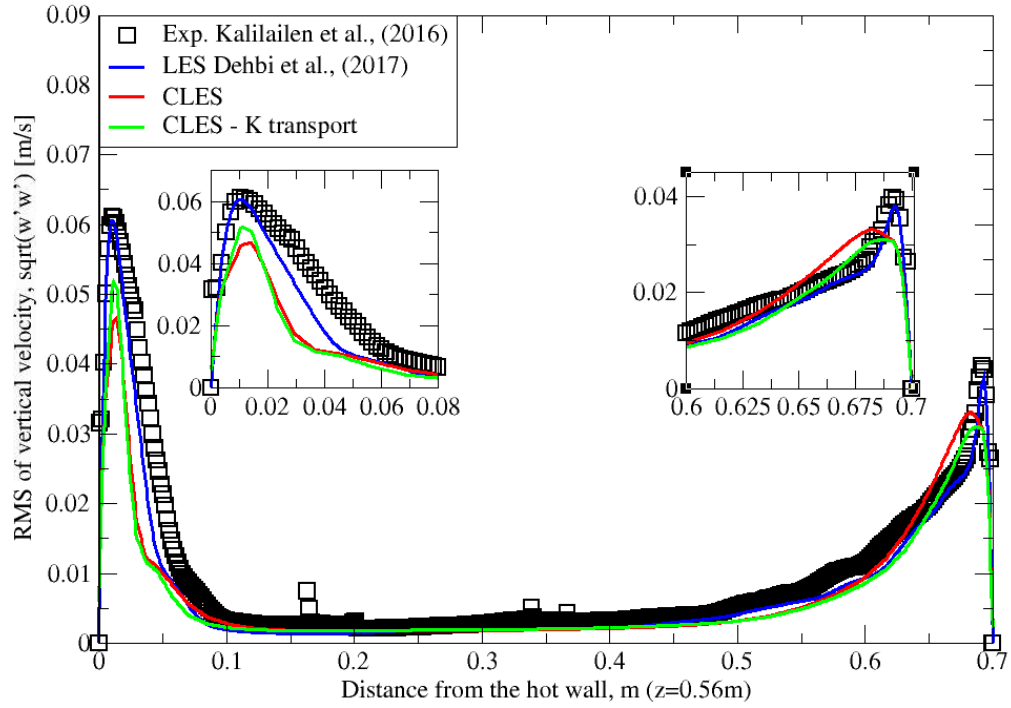
Figure A.20 – Comparison for RMS vertical velocity between hot and cold walls from both Smagorinsky models against reference LES and experimental databases. Profiles are obtained at (z = 0.35 m) using same mesh after 2400 time units.
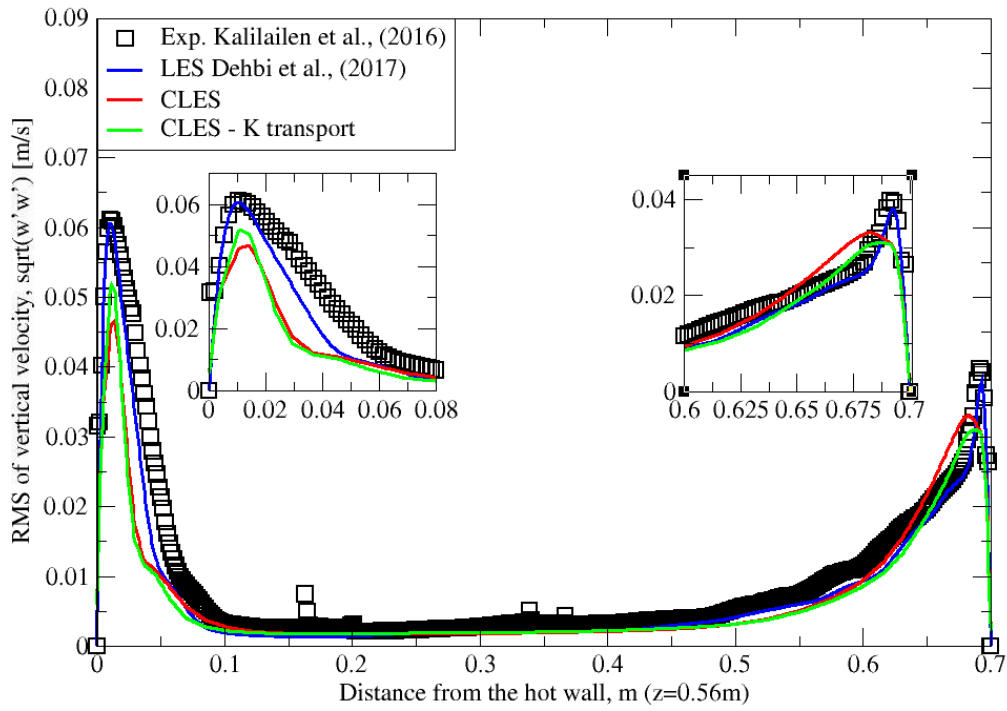
Figure A.21 – Comparison for RMS vertical velocity between hot and cold walls from both Smagorinsky models against reference LES and experimental databases. Profiles are obtained at (z = 0.56 m) using same mesh after 2400 time units.

Bibliography

Abe, K., Kondoh, T., & Nagano, Y. (1994). A new turbulence model for predicting fluid flow and heat transfer in separating and reattaching flows - i. flow field calculations. *Int. Journal of Heat and Mass Transfer, 37*, 139–151.

Abramov, A., & Smirnov, E. (2006). Numerical simulation of turbulent convection of air in a square cavity heated on the side. *High Temperature, 44*, 91–98.

Akbar, M. K., Rahman, M., & Ghiaasiaan, S. M. (2009). Particle transport in a small square enclosure in laminar natural convection. *Journal of Aerosol Science, 40*, 747–761.

Ali, A., Afgan, I., Laurence, D., & Revell, A. (2021). A dual-mesh hybrid rans-les simulation of the buoyant flow in a differentially heated square cavity with an improved resolution criterion. *Journal of Computers and Fluids, 104949.*

Ampofo, F., & Karayiannis, T. (2003). Experimental benchmark data for turbulent natural convection in an air filled square cavity. *Int. J. Heat Mass Transfer, 46*, 3551–3572.

Armenio, V., Piomelli, U., & Fiorotto, V. (1999). Effect of the subgrid scales on particle motion. *Physics of Fluids, 11*. https://doi.org/10.1063/1.870162

Azadi, M., Azadi, M., & Mohebbi, A. (2010). A cfd study of the effect of cyclone size on its performance parameters. *Journal of Hazardous Materials, 182*, 835–841.

Bagheri, G. H., Salmanzadeh, M., Golkarfard, V., & Ahmadi, G. (2012). Simulation of solid particles behavior in a heated cavity at high rayleigh numbers. *Aerosol Science Technology, 46*, 1382–1391.

Baïri, A., Laraqi, N., & Garcia de Maria, J. (2007). Numerical and experimental study of natural convection in tilted parallelepipedic cavities for large rayleigh numbers. *Experimental Thermal and Fluid Science, 31*, 309–324.

Balashazy, I. (1994). Simulation of particle trajectories in bifurcating tubes. *J. Comp. Phys.*, 11–22.

Bejan, A. (1995). *Convection heat transfer, second edition.*

Beniston, M. (2012). *From turbulence to climate: numerical investigations of the atmosphere with a hierarchy of models.*

Benjamin, D., & François, B. (2017). Natural convection above circular disks of evaporating liquids. *Physical review fluids, 2.*

Bernard, P., & Wallace, J. (2002). *Turbulent flow; analysis, measurement, and prediction.*

Bernardo, S., Mori, M., Peres, A., & Dionísio, R. (2006). 3-d computational fluid dynamics for gas and gas–particle flows in a cyclone with different inlet section angles. *Powder Technology, 162,* 190–200.

Betts, P., & Bokhari, I. (2000). Experiments on turbulent natural convection in an enclosed tall cavity. *International Journal of Heat and Fluid Flow, 21 (6),* 675–683.

Bhaskar, K., Murthy, Y., Raju, M., Tiwari, S., & Srivastava, J. (2007). Cfd simulation and experimental validation studies on hydrocyclone. *Minerals Engineering, 20,* 60–71.

Bini, M., & Jonesa, W. P. (2007). Particle acceleration in turbulent flows: a class of nonlinear stochastic models for intermittency. *Physics of Fluids, 19.* https://doi.org/10.1063/1.2709706

Bocksell, T. L., & Loth, E. (2001). Random walk models for particle diffusion in free-shear flows. *AIAA Journal, 39.* https://doi.org/10.2514/2.1421

Bocksell, T. L., & Loth, E. (2006). Stochastic modeling of particle diffusion in a turbulent boundary layer. *International Journal of Multiphase Flow, 32.* https://doi.org/10.1016/j.ijmultiphaseflow.2006.05.013

Bose, S. T., & Park, G. I. (2018). Wall-modeled large-eddy simulation for complex turbulent flows. *Annual Review of Fluid Mechanics, 50.* https://doi.org/10.1146/annurev-fluid-122316-045241

Bosshard, C., Dehbi, A., Deville, M., Leriche, E., & Soldati, A. (2013). Large eddy simulation of the differentially heated cubic cavity flow by the spectral element method. *Journal of Computers and Fluids, 86,* 210–227.

Bosshard, C., Dehbi, A., Deville, M., Leriche, E., & Soldati, A. (2014). Large eddy simulation of particulate flow inside a differentially heated cavity. *Nuclear Engineering and Design, 267,* 154–163.

Boussinesq, J. (1868). Mémoire sur l'influence des frottements dans les mouvements réguliers des fluides. *J. Math. Pures Appl. sér. II, 13,* 377–423.

Boussinesq, J. (1877). Essai sur la théorie des eaux courantes. *Mémoires présentés par divers savants à l'Académie des sciences, XXIII, 1,* 1–680.

Boussinesq, J. (1897). Théorie de l'écoulement tourbillonnant et tumultueux des liquides. *Gauthier-Villars et Fils, Paris.*

Box, G. E. P., & Muller, M. E. (1958). A note on the generation of random normal deviates. *The Annals of Mathematical Statistics, 29.* https://doi.org/10.1214/aoms/1177706645

Boysan, F., Ayers, W. H., & Swithenbank, J. (1982). A fundamental mathematical modelling approach to cyclone design. *Trans. Inst. Chem. Engrs., 60,* 222–230.

Brar, L., Sharma, R., & Elsayed, K. (2015). The effect of the cyclone length on the performance of stairmand high-efficiency cyclone. *Powder Technology, 286,* 668–677.

Briggs, D., & Jones, D. (1985). Two dimensional periodic natural convection in a rectangular enclosure of aspect ratio one. *Journal of Heat Transfer, 107,* 850–854.

Bush, R. H., Chyczewski, T., Duraisamy, K., Eisfeld, B., Rumsey, C. L., & Smith, B. (2019). Recommendations for future efforts in rans modeling and simulation. *AIAA Scitech 2019 Forum.* https://doi.org/10.2514/6.2019-0317

Caporaloni, M., Tampieri, F., Trombetti, F., & Vittori, O. (1975). Transfer of particles in non-isotropic air turbulence, 32, 565–568. *Journal of Atmospheric Sciences.*

Cernick, M. J., Tullis, S. W., & Lightstone, M. F. (2015). Particle subgrid scale modelling in large-eddy simulations of particle-laden turbulence. *Journal of Turbulence, 16.* https://doi.org/10.1080/14685248.2014.969888

Chapman, D. (1979). Computational aerodynamics, development and outlook. *AIAA, 17,* 1293–1313.

Chen, X.-Q., & Pereira, J. (1997). Efficient computation of particle dispersion in turbulent flows with a stochastic probabilistic model. *Int. J. Heat Mass Transfer, 40,* 1727–1741.

Cheng, Y. (2003). Aerosol deposition in the extrathoracic region. aerosol. sci. tech- nol. 37 (8), 659–671.

Chorda, R., Blasco, J., & Fueyo, N. (2002). An efficient particle-locating algorithm for application in arbitrary 2d and 3d grids. *Int. J. Multiphase Flow, 28,* 1565–1580.

Chuah, T., Gimbun, J., & Choong, T. (2006). A cfd study of the effect of cone dimensions on sampling aerocyclones performance and hydrodynamics. *Powder Technology, 162,* 126–132.

Colagrossi, A., Marrone, S., P.Colagrossi, & Touz, D. L. (2021). Davinci's observation of turbulence: a frenchitalian study aiming at numerically reproducing the physics behind one of his drawings, 500years later. *Physics of Fluids, 33-115122,* 1–16. https://doi.org/10.1063/5.0070984

Coles, D. E., & Hirst, E. A. (1969). Compiled data. *In Proceedings of Computation of Turbulent Boundary Layers, AFOSR-IFP Stanford Conference, 2.*

Colomer, G., Costa, M., Cònsul, R., & Oliva, A. (2004). Three-dimensional numerical simulation of convection and radiation in a differentially heated cavity using the discrete ordinates method. *International Journal of Heat and Mass Transfer, 47 (2),* 257–269.

Darmofal, D., & Haimes, H. (1996). An analysis of 3d particle path integration algorithms. *J. Comp. Phys., 123,* 182–195.

Dasgupta, S., Jackson, R., & Sundaresan, S. (1997). Developing flow of gas-particle mixtures in vertical ducts. *Ind. Eng. Chem. Res., 36,* 3375–3390.

De Vahl Davis, G. (1968). Laminar natural convection in an enclosed rectangular cavity. *International Journal of Heat and Mass Transfer, 11,* 1675–1693.

Dehbi, A. (2008a). A cfd model for particle dispersion in turbulent boundary layer flows. *Nuclear Engineering and Design, 238.* https://doi.org/10.1016/j.nucengdes.2007.02.055

Dehbi, A. (2008b). Turbulent particle dispersion in arbitrary wall-bounded geometries: a coupled cfd-langevin-equation based approach. *International Journal of Multiphase Flow, 34.* https://doi.org/10.1016/j.ijmultiphaseflow.2008.03.001

Dehbi, A. (2010). Validation against dns statistics of the normalized langevin model for particle transport in turbulent channel flows. *Powder Technology, 200.* https://doi.org/10.1016/j.powtec.2010.02.009

Dehbi, A. (2011). Prediction of extrathoracic aerosol deposition using rans-random walk and les approaches. *Aerosol Science and Technology, 45.* https://doi.org/10.1080/02786826. 2010.550962

Dehbi, A., & De Crécy, F. (2011). Validation of the langevin particle dispersion model against experiments on turbulent mixing in a t-junction. *Powder Technology, 206.* https://doi.org/10.1016/j.powtec.2010.09.036

Dehbi, A., Kalilainen, J., Lind, T., & Auvinen, A. (2017). A large eddy simulation of turbulent particle-laden flow inside a cubical differentially heated cavity. *Journal of Aerosol Science, 103,* 67–82.

Dehbi, A., Knasiak, K., Güntay, S., & Suckow, D. (2001). Drop size measurements using two different optical devices. *J. Aerosol. Sci., 32,* S33–S34.

Dehbi, A., Suckow, D., & Güntay, S. (2001). Aerosol retention in low-subcooling pools under realistic accident conditions. *Nucl. Eng. Des., 203,* 229–241.

Dehbi, A., Suckow, D., Lind, T., Guentay, S., Danner, S., & Mukin, R. (2016). Key findings from the artist project on aerosol retention in a dry steam generator, nuclear engineering and technology, volume 48, issue 4, pages 870-880.

Derksen, J. (2003). Separation performance predictions of a stairmand high-efficiency cyclone. *AIChE Journal, 49,* 1359–1371.

Derksen, J., Sundaresan, S., & van den Akker, H. (2006). Simulation of mass- loading effects in gas–solid cyclone separators. *Powder Technology, 163,* 59–68.

Derksen, J., & Van den Akker, H. (2000). Simulation of vortex core precession in a reverse-flow cyclone. *AIChE Journal, 46,* 1317–1331.

Derksen, J., van den Akker, H., & Sundaresan, S. (2008). Two-way coupled large-eddy simulations of the gas–solid flow in cyclone separators. *American Institute of Chemical Engineers, 54,* 872–884.

Devenish, B., Bartello, P., Brenguier, J.-L., Collins, L., Grabowski, W., IJermans, R., Malinowski, S., Reeks, M., Vassilicos, J., Wang, L.-P., & Warhaft, Z. (2012). Droplet growth in warm turbulent clouds, quarterly journal of the royal meteorological society 138 (667), 1401–1429.

Dollet, B., & Boulogne, F. (2017). Natural convection above circular disks of evaporating liquids. *Physical Review Fluids, 2.* https://doi.org/10.1103/PhysRevFluids.2.053501

Drew, D. A. (1983). Mathematical modeling of two-phase flow. *Annual Review of Fluid Mechanics, 15.* https://doi.org/10.1146/annurev.fl.15.010183.001401

Dritselis, C., & Vlachos, N. (2008). Numerical study of educed coherent structures in the near-wall region of a particle-laden channel flow. *Physics of Fluids, 20.* https://doi.org/10.1063/1.2919108

Dueñas-Pamplona, J., García, J., Sierra-Pallares, J., Ferrera, C., Agujetas, R., & López-Mínguez, J. (2021). A comprehensive comparison of various patient-specific cfd models of the left atrium for atrial fibrillation patients, computers in biology and medicine, volume 133, 104423.

Durbin, P. (1991). Near-wall turbulence closure modelling without 'damping functions'. *Theoret. Comput. Fluid Dynamics, 3,* 1–13.

Durbin, P. A., & Pettersson Reif, B. A. (2010). *Statistical theory and modeling for turbulent flows: second edition.* https://doi.org/10.1002/9780470972076

Egorov, Y., Menter, F. R., Lechner, R., & Cokljat, D. (2010). The scale-adaptive simulation method for unsteady turbulent flow predictions. part 2: application to complex flows. *Flow, Turbulence and Combustion, 85.* https://doi.org/10.1007/s10494-010-9265-4

Elghobashi, S. (1994). On predicting particle-laden turbulent flows. *Applied Scientific Research, 52.* https://doi.org/10.1007/BF00936835

Elsayed, K., & Lacor, C. (2012). Modeling and pareto optimization of gas cyclone separator performance using rbf type artificial neural networks and genetic algorithms. *Powder Technology, 217,* 84–99.

Elsayed, K., & Lacor, C. (2014). Analysis and optimisation of cyclone separators geometry using rans and les methodologies. *Turbulence and Interactions,* 65–74.

Elsayed, K., & Lacor, C. (2011-b). Analysis and optimization of aircyclones using artificial neural network, response surface methodology and cfd simulation approaches. *Powder Technology, 212,* 115–133.

Elsayed, K., & Lacor, C. (2011-a). The effect of cyclone inlet dimensions on the flow pattern and performance. *Applied Mathematical Modelling, 35,* 1952–1968.

Erol, H., Turgut, O., & Unal, R. (2019). Experimental and numerical study of stairmand cyclone separators: a comparison of the results of small-scale and large-scale cyclones. *Heat and Mass Transfer, 55,* 2341–2354.

Fluent, A. (2015). Fluent 15 users guide usa: lebanon.

Frederick, R., & Valencia, A. (1989). Heat transfer in a square cavity with a conducting partition on its hot wall. *Int. Commun. Heat Mass Transfer, 16,* 347–354.

Frisch, U. (1995). *Turbulence; the legacy of a.n. kolmogorov.*

Fukagata, K., Zahrai, S., & Bark, F. H. (2004). Dynamics of brownian particles in a turbulent channel flow. *Journal of Heat and Mass Transfer, 40.* https://doi.org/10.1007/s00231-003-0462-8

Gao, Z. W., Liu, Z. X., Wei, W. D., Li, C. X., Wang, S. H., Qi, X. Y., & Huang, W. (2022). Numerical analysis on the influence of vortex motion in a reverse stairmand cyclone separator by using les model. *Petroleum Science, 19*(2), 848–860. https://doi.org/https://doi.org/10.1016/j.petsci.2021.11.009

Germano, M., Piomelli, U., Moin, P., & Cabot, W. H. (1991). A dynamic subgrid-scale eddy viscosity model. *Phys. Fluids, A3,* 1760–1765.

Geurts, B. J. (2004). *Elements of direct and large-eddy simulation.*

Geurts, B. J., & Kuerten, J. G. (2012). Ideal stochastic forcing for the motion of particles in large-eddy simulation extracted from direct numerical simulation of turbulent channel flow. *Physics of Fluids, 24.* https://doi.org/10.1063/1.4745857

Gharaibah, E., Read, A., & Scheuerer, G. (2015). Overview of cfd multiphase flow simulation tools for subsea oil and gas system design, optimization and operation. *OTC Brasil 2015: The Atlantic: From East to West - An Ocean of Innovation.* https://doi.org/10.4043/26326-ms

Gicquel, L. Y. M., Givi, P., Jaberi, F. A., & Pope, S. B. (2002). Velocity filtered density function for large eddy simulation of turbulent flows. *Physics of Fluids, 14*. https://doi.org/10.1063/1.1436496

Gimbun, J., Chuah, T. G., Choong, T. S. Y., & Fakhru'l-Razi, A. (2005). Prediction of the effects of cone tip diameter on the cyclone performance. *Journal of Aerosol Science, 36*, 1056–1065.

Girimaji, S. S., & Abdol-Hamid, K. S. (2005). Partially-averaged navier stokes model for turbulence: implementation and validation. *43rd AIAA Aerospace Sciences Meeting and Exhibit - Meeting Papers*. https://doi.org/10.2514/6.2005-502

Gong, Y., Luo, K., Ma, X., Shuai, A., & Xu, H. (2021). Atomic-level insights into transition mechanism of dominant mixing modes of multi-component fuel droplets: from evaporation to diffusion, fuel, volume 304, 15, 121464.

Gosman, A. D., & Ioannides, E. (1981). Aspects of computer simulation of liquid-fuelled combustors. *AIAA Paper*. https://doi.org/10.2514/6.1981-323

Griffiths, W. D., & Boysan, F. (1996). Computational fluid dynamics (cfd) and empirical modelling of the performance of a number of cyclone samplers. *Journal of Aerosol Science, 24*, 281–304.

Gritskevich, M. S., Garbaruk, A. V., Schütze, J., & Menter, F. R. (2012). Development of ddes and iddes formulations for the k- shear stress transport model. *Flow, Turbulence and Combustion, 88*. https://doi.org/10.1007/s10494-011-9378-4

Gronald, G., & Derksen, J. (2011). Simulating turbulent swirling flow in a gas cyclone: a comparison of various modelling approaches. *Powder Technology, 205*, 160–171.

Güntay, S., Suckow, D., Dehbi, A., & Kapulla, R. (2008). Artist: introduction and first results. *Nuclear Engineering and Design, 231*, 109–120.

Hadziabdic, M., Borrelli, M., & Niceno, B. (2021). Simulation of rayleigh-benard convection at up to ra = 10e16 by generalized elliptic-relaxation hybrid rans-les model. *International Journal of Heat and Fluid Flow, 3*. https://doi.org/org/10.1016/j.ijheatfluidflow.2021.108819

Hadziabdic, M., & Hanjalic, K. (2020). Elliptic-relaxation hybrid rans-les (er-hrl) for complex wall-bounded fluid and heat flows, in book: progress in rans-based scale-resolving flow simulation methods ii. *bulletin 121- ERCOFTAC, 121*.

Hadžiabdić, H., Hafizović, M., Ničeno, B., & Hanjalić, K. (2022). A rational hybrid rans-les model for cfd predictions of microclimate and environmental quality in real urban structures. *Building and Environment, 217*, 109042. https://doi.org/10.1016/J.BUILDENV.2022.109042

Hadžiabdić, M. (2006). *Les, rans and combined simulation of impinging flows and heat transfer, phd thesis - tudelft institutional repository, isbn: 90-901-5233-4*. https://doi.org/http://resolver.tudelft.nl/uuid:47cb00a2-d935-4a0a-b68b-a0440cfb9d26

Hadžiabdić, M., & Hanjalić, K. (2008). Vortical structures and heat transfer in a round impinging jet, volume 596, pp. 221-260. *Journal of Fluid Mechanics*. https://doi.org/10.1017/S002211200700955X

Hanjalic, K., & Launder, B. (2011). *Modelling turbulence in engineering and the environment.* https://doi.org/10.1017/cbo9781139013314

Hanjalić, K., Popovac, M., & Hadžiabdić, M. (2004). A robust near-wall elliptic relaxation eddy-viscosity turbulence model for cfd. *International Journal of Heat and Fluid Flow, 25,* 1047–1051.

Heinz, S. (2003). On fokker-planck equations for turbulent reacting flows. part 2. filter density function for large eddy simulation. *Flow, Turbulence and Combustion, 70.* https://doi.org/10.1023/B:APPL.0000004934.22265.74

Hinds, W. C. (1999). *Aerosol technology (2nd edition).*

Hoekstra, A. (2000). Gas flow field and collection efficiency of cyclone separators. *PhD thesis, Technische Universiteit Delft.*

Hoekstra, A., Derksen, J., & van den Akker, H. (1999). An experimental and numerical study of turbulent swirling flow in gas cyclones. *Chemical Engineering Science, 54,* 2055–2065.

Hoffmann, A. C., & Stein, L. E. (2008). *Gas cyclones and swirl tubes: principles, design and operation.* https://doi.org/10.1007/978-3-540-74696-6

Horn, M., & Schmid, H. J. (2008). A comprehensive approach in modeling lagrangian particle deposition in turbulent boundary layers. *Powder Technology, 186.* https://doi.org/10.1016/j.powtec.2007.11.048

Horne, W., & Mahesh, K. (2019). A particle-resolved direct-numerical simulation study of particle-laden turbulent channel flow using a massively parallel, unstructured, overset method. *11th International Symposium on Turbulence and Shear Flow Phenomena, TSFP 2019.*

Ibrahim, A., Saury, D., & Lemonnier, D. (2013). Coupling of turbulent natural convection with radiation in an air-filled differentially-heated cavity at ra = 1.5×10^9. *Journal of Computers and Fluids, 88,* 115–125.

Iliopoulos, I., & Hanratty, T. (1999). Turbulent dispersion in a non-homogeneous field. *Journal of Fluid Mechanics, 392.* https://doi.org/10.1017/S0022112099005431

Iliopoulos, I., Mito, Y., & Hanratty, T. J. (2003). A stochastic model for solid particle dispersion in a nonhomogeneous turbulent field. *International Journal of Multiphase Flow, 29.* https://doi.org/10.1016/S0301-9322(02)00165-9

Jang, K., Lee, G. G., & Huh, K. Y. (2018). Evaluation of the turbulence models for gas flow and particle transport in urans and les of a cyclone separator. *Computers Fluids, 172,* 274–283. https://doi.org/https://doi.org/10.1016/j.compfluid.2018.04.032

Jiao, J., Zheng, Y., Sun, G., & Wang, J. (2006). Study of the separation efficiency and the flow field of a dynamic cyclone. *Separation and Purification Technology, 49,* 157–166.

Jones, A. V., & Kissane, M. (2000). State of understanding of fission product transport in the circuit and of aerosol behaviour in the containment of phebus. *Journal of Aerosol Science, 31,* S37–S38.

José de Souza, F., Salvo, R., & Martins, D. (2012). Large eddy simulation of the gas–particle flow in cyclone separators. *Separation and Purification Technology, 94,* 61–70.

Kalilainen, J., Rantanen, P., Lind, T., Auvinen, A., & A., D. (2016). Experimental investigation of a turbulent particle-laden flow inside a differentially heated cavity. *Journal of Aerosol Science, 100*, 73–87.

Kallio, G. A., & Reeks, M. W. (1989). A numerical simulation of particle deposition in turbulent boundary layers. *International Journal of Multiphase Flow, 15*. https://doi.org/10.1016/0301-9322(89)90012-8

Kam, T., Hsia, L. C., & Chang, T. (1998). Clean room particle monitor, airflow simulation and measurement for aerosol reduction. *Journal of Aerosol Science, 29*, 254.

Kapulla, R. (2008). Artist phase vi: droplet retention tests data report. *Paul Scherrer Institute Archive, Informationsliste, D 1 2 3 4 5 8 9 A.*

Kaya, F., & Karagoz, I. (2008). Performance analysis of numerical schemes in highly swirling flows in cyclones. *Current Science, 94*, 1273–1278.

Kelvin), W. T. ((1887). Stability of motion (continued from the may, june and august numbers). broad rivers flowing down an inclined plane bed. *Philos. Mag., 24 (148), 24*, 272–278.

Kennard, E. H. (1938). Kinetic theory of gases. *McGraw-Hill.*

Kepa, A. (2010). Divison of outlet flow in a cyclone vortex finder-the cfd calculations. *Separation and Purification Technology, 75*, 127–131.

Kim, H., Dehbi, A., & Kalilainen, J. (2018). A large eddy simulation of turbulent particle-laden flow inside a cubical differentially heated cavity. *Journal of Aerosol Science, 186*, 216–228.

Kipfer, P., Reck, F., & Greiner, G. (2003). Local exact particle tracking on unstructured grids. *Computer Graphics Forum, 22*, 1–9.

Kolmogorov, A. N. (1991). The local structure of turbulence in incompressible viscous fluid for very large reynolds numbers. *Proceedings of the Royal Society of London. Series A: Mathematical and Physical Sciences, 434*. https://doi.org/10.1098/rspa.1991.0075

Lee, M., & Moser, R. D. (2015). Direct numerical simulation of turbulent channel flow up to re 5200. *Journal of Fluid Mechanics, 774*. https://doi.org/10.1017/jfm.2015.268

Legg, B., & Raupach, M. (1982). Markov-chain simulation of particle dispersion in inhomogeneous flows: the mean drift velocity induced by a gradient in eulerian velocity variance," boundary-layer meteorol. 24(1), 3–13 (1982). *Boundary-Layer Meteorol.*

Leonard, A. (1974). Energy cascade in large-eddy simulation of turbulent fluid flows. *Adv. Geophys, 18A*, 237–262.

Li, G., & Modest, F. (2001). An effective particle tracing scheme on structured/unstructured grids in hybrid finite volume/pdf monte carlo methods. *J. Comp. Phys., 173*, 187–207.

Lilly, D. K. (1992). A proposed modication of the germano subgrid-scale closure method. *Phys. Fluids, A4*, 633–635.

Lohner, R., & Ambrosiano, J. (1990). A vectorized particle tracer for unstructured grids. *J. Comp. Phys., 91*, 22–31.

Longest, P., Hindle, M., Choudhuri, S., & Xi, J. (2008). Comparison of ambient and spray aerosol deposition in a standard induction port and more realistic mouth–throat geometry. *Journal of Aerosol Science, 39 (7)*, 572–591.

Luo, K., Yu, H., Dai, Z., Fang, M., & Fan, J. (2016). Cfd simulations of flow and dust dispersion in a realistic urban area. eng. appl. comput. fluid mech. 10 (1), 228–242.

Ma, L., Ingham, D., & Wen, X. (2000). Numerical modelling of the fluid and particle penetration through small sampling cyclones. *Journal of Aerosol Science, 31*, 1097–1119.

MacInnes, J. M., & Bracco, F. V. (1992). Stochastic particle dispersion modeling and the tracer-particle limit. *Physics of Fluids A, 4*. https://doi.org/10.1063/1.858337

Mallinson, G., & De Wahl Davis, G. (1977). Three-dimensional natural convection in box: a numerical study. *Journal of Fluid Mechanics, 33, part 1*, 1–33.

Mallouppas, G., & Wachem, B. (2013). Large eddy simulations of turbulent particle-laden channel flow. *International Journal of Multiphase Flow, 54*. https://doi.org/10.1016/j.ijmultiphaseflow.2013.02.007

Marchioli, C., Picciotto, M., & Soldati, A. (2007). Influence of gravity and lift on particle velocity statistics and transfer rates in turbulent vertical channel flow. *International Journal of Multiphase Flow, 33*. https://doi.org/10.1016/j.ijmultiphaseflow.2006.09.005

Marchioli, C., Salvetti, M. V., & Soldati, v. (2008). Some issues concerning large-eddy simulation of inertial particle dispersion in turbulent bounded flows. *Physics of Fluids, 20*. https://doi.org/10.1063/1.2911018

Marchioli, C., & Soldati, A. (2002). Mechanisms for particle transfer and segregation in a turbulent boundary layer. *Journal of Fluid Mechanics, 468*. https://doi.org/10.1017/S0022112002001738

Marchioli, C., Soldati, A., Kuerten, J. G. M., Arcen, B., Tanière, A., Goldensoph, G., Squires, K. D., Cargnelutti, M. F., & Portela, L. M. (2008). Statistics of particle dispersion in direct numerical simulations of wall-bounded turbulence: results of an international collaborative benchmark test. *International Journal of Multiphase Flow, 34*. https://doi.org/10.1016/j.ijmultiphaseflow.2008.01.009

Marks, R. J. (1991). *Introduction to shannon sampling and interpolation theory.*

Martignoni, W., Bernardo, S., & Quintani, L. (2007). Evaluation of cyclone geometry and its influence on performance parameters by computational fluid dynamics (cfd). *Brazilian Journal of Chemical Engineering, 24*, 83–94.

Masoud, D., & Shahidzadeh, M. (2011). A cfd study of the effect of vortex finder thickness on gas cyclone separator performance. *Journal of Applied Sciences, 11*, 2570–2577.

Mathieu, J., & Scott, J. (2000). *An introduction to turbulent flow.*

Matida, E., Finlay, W., Lange, C., & Grgic, B. (2004). Improved numerical simulation of aerosol deposition in an idealized mouth–throat. *Journal of Aerosol Science, 35 (1), 1–19.*

Maxey, M. R. (1987). The motion of small spherical particles in a cellular flow field. *Physics of Fluids, 30*. https://doi.org/10.1063/1.866206

Menter, F. R. (2013). *Best practice: scale-resolving simulations in ansys cfd, ver. 2.00.*

Menter, F. R. (2015). *Best practice: scale-resolving simulations in ansys cfd, ver. 2.00.*

Menter, F. R. (2018). Stress-blended eddy simulation (sbes)—a new paradigm in hybrid rans-les modeling. *Notes on Numerical Fluid Mechanics and Multidisciplinary Design, 137*. https://doi.org/10.1007/978-3-319-70031-1_3

Menter, F. R., & Egorov, Y. (2010). The scale-adaptive simulation method for unsteady turbulent flow predictions. part 1: theory and model description. *Flow, Turbulence and Combustion, 85*. https://doi.org/10.1007/s10494-010-9264-5

Mergui, S., & Penot, F. (1996). Convection naturelle en cavité carrée différentiellement chauffée investigation expérimentale à ra=1.69×109. *Int. J. Heat Mass Transfer, 39 (3)*, 563–574.

Minier, J. P., Simonin, O., & Gabillard, M. (1991). Numerical modelling of cyclone separators. *Proceedings of the 11th International Conference on Fluidized Bed Combustion,ASME, New York, 1251-1259.*

Mito, M., & Hanratty, T. J. (2002). Use of a modified langevin equation to describe turbulent dispersion of fluid particles in a channel flow. *Flow, Turbulence and Combustion, 68*. https://doi.org/10.1023/A:1015614823809

Mito, Y., & Hanratty, T. J. (2004). A stochastic description of wall sources in a turbulent field: part 2. calculation for a simplified model of horizontal annular flows. *International Journal of Multiphase Flow, 30*. https://doi.org/10.1016/j.ijmultiphaseflow.2004.02.003

Mofakham, A., & Ahmadi, G. (2019). Particles dispersion and deposition in inhomo- geneous turbulent flows using continuous random walk models. phys. fluids 31 (8), 13. *Phys. Fluids.*

Mofakham, A., & Ahmadi, G. (2020). On random walk models for simulation of particle-laden turbulent flows, international journal of multiphase flow, 122-103157.

Moin, P., & Kim, J. (1982). Numerical investigation of turbulent channel flow. *Journal of Fluid Mechanics, 118*. https://doi.org/10.1017/S0022112082001116

Moin, P., Squires, K., Cabot, W., & Lee, S. (1991). A dynamic subgrid-scale model for compressible turbulence and scalar transport. *Physics of Fluids A, 3*. https://doi.org/10.1063/1.858164

Morency, F., Beaugendre, H., & Habashi, W. (2003). Fensap-ice: a study of effects of ice shapes on droplet impingement. *AIAA, 1223.*

Morrison, G. C., Zhao, P., & Kasthuri, L. (2006). The spatial distribution of pollutant transport to and from indoor surfaces. *Atmospheric Environment, 40*, 3677–3685.

Moser, Kim, & Mansour. (1999). Dns of turbulent channel flow up to $re\tau$=590. *Physics of Fluids.*

Mukin, R., & Dehbi, A. (2016). Simulation of flow on the secondary side of a steam generator bundle. *Computational fluid dynamics for nuclear reactor safety-5. (CFD4NRS-5). Workshop proceedings.*

Nansteel, M., & Grief, R. (1984). Natural convection in enclosures with two- and three dimensional partitions. *Int. J. Heat Mass Transfer, 27*, 561–571.

Narasimha, M., Brennan, M., Holtham, P., & Napier-Munn, T. (2007). A comprehensive cfd model of dense medium cyclone performance. *Minerals Engineering, 20*, 414–426.

Naterer, G. F. (2002). Multiphase flow with impinging droplets and airstream interaction at a moving gas/solid interface. *J. Multiphase Flow, 28*, 451–477.

Ničeno, B. (2001). *An unstructured parallel algorithm for large-eddy and conjugate heat transfer simulations, phd thesis - tudelft institutional repository, isbn:90-9015233-4.*

Norment, H. (1985). Three-dimensional airflow and hydrometeor trajectory calculation with applications. *AIAA 23rd Aerospace Sciences and Meeting, Reno, NV.*

Nowbahar, A., Sardina, G., Picano, F., & Brandt, L. (2013). Turbophoresis attenuation in a turbulent channel flow with polymer additives, vol 732 , 706 - 719. *Journal of Fluid Mechanics*.

Oliviera, P., Gosman, A., & Issa, R. (1997). A method for particle location and field interpolation on complex, threedimensional computational meshes. *Adv. in Engineering Software*, *28*, 607–614.

Ontko, J. S. (1996). Cyclone separator scaling revisited. *Powder Technology, 87*. https://doi.org/10.1016/0032-5910(95)03085-9

Patankar, N., & Joseph, D. (2001). Lagrangian numerical simulation of particulate flows. *J. Multiphase Flow, 27*, 1685–1706.

Picciotto, M., Marchioli, C., & Soldati, A. (2005). Characterization of near-wall accumulation regions for inertial particles in turbulent boundary layers. *Physics of Fluids, 17*. https://doi.org/10.1063/1.2033573

Piomelli, U., Moin, P., & Ferziger, J. H. (1988). Model consistency in large-eddy simulation of turbulent channel flows. *Physics of Fluids, 31*, 1884–1894.

Pisarev, G., Hoffmann, A., Peng, W., & Dijkstra, H. (2011). Large eddy simulation of the vortex end in reverse flow centrifugal separators. *Applied Mathematics and Computation, 217*, 5016–5022.

Pointwise. (2021). *Fort Worth, Texas 76104-1107, USA*.

Pokrajac, D., & Lazic, P. (2002). An efficient algorithm for high accuracy particle tracking in finite elements. *Advances in Water Resources, 25*, 353–369.

Pope, S. (2000). *Turbulent flows*.

Pouraria, H., Seo, J. K., & Paik, J. K. (2016). Numerical modelling of two-phase oil-water flow patterns in a subsea pipeline. *Ocean Engineering, 115*. https://doi.org/10.1016/j.oceaneng.2016.02.007

Poussou, S. B., Mazumdar, S., Plesniak, M. W., Sojka, P. E., & Chen, Q. (2010). Flow and contaminant transport in an airliner cabin induced by a moving body: model experiments and cfd predictions. *Atmospheric Environment, 44*, 2830–2839.

Pozorski, J., & Apte, S. (2009). Filtered particle tracking in isotropic turbulence and stochastic modeling of subgrid-scale dispersion. *International Journal of Multiphase Flow, 35*. https://doi.org/10.1016/j.ijmultiphaseflow.2008.10.005

Pui, D., Romay-Novas, F., & Liu, B. (1987). Experimental study of particle deposition in bends of circular cross section. *Aerosol Sci. Technol., 7*, 301–315.

Puragliesi, R. (2010). *Numerical investigation of particle-laden thermally driven turbulent flows in enclosure, eo: 4600. ecole polytechnique federale de lausanne, lausanne*.

Puragliesi, R., Dehbi, A., Leriche, E., Soldati, A., & Deville, M. O. (2011). Dns of buoyancy driven flows and lagrangian particle tracking in a square cavity at high rayleigh number. *Journal of Heat and Fluid Flow, 32*, 915–931.

Qiu, Y., Deng, B., & Kim, C. (2012). Numerical study of the flow field and separation efficiency of a divergent cyclone. *Powder Technology, 217*, 231–237.

Ra, Y., & Reitz, R. (2009). A vaporization model for discrete multi-component fuel sprays, international journal of multiphase flow, volume 35, issue 2, pages 101-117.

Rahman, M., Cheng, W., Samtaney, R., & Urzay, J. (2016). Large-eddy simulations of sandstorms as charged-particle suspensions in turbulent boundary layers. in: proceedings of the summer program, pages 45-51.

Raoufi, A., Shams, M., Farzaneh, M., & Ebrahimi, R. (2008). Numerical simulation and optimization of fluid flow in a cyclone vortex finder. *Chemical Engineering and Processing, 47,* 128–137.

R.B. Xiang, R., & Lee, K. (2005). Numerical simulation of flow patterns in cyclones of different cone dimensions. *Particle Particle System Characterization, 22,* 212–218.

Reeks, M. W. (1991). On a kinetic equation for the transport of particles in turbulent flows. *Physics of Fluids A, 3.* https://doi.org/10.1063/1.858101

Reeks, M. (1983). The transport of discrete particles in inhomogeneous turbulence, journal of aerosol science, issue 14 (6), 729–739.

Reynolds, O. (1883). An experimental investigation of the circumstances which determine whether the motion of water shall be direct or sinuous, and of the law of resistance in parallel channels. *Philos. Trans. R. Soc. Lond. A, 174,* 935–982.

Reynolds, O. (1894). On the dynamical theory of incompressible viscous flows and the determination of the criterion. *Philos. Trans. R. Soc. London Ser. A, 186,* 123–161.

Reynolds, O. (1895). On the dynamical theory of incompressible viscous fluids and the determination of the criterion. *Philos. Trans. R. Soc. Lond. A, 186,* 123–164.

Rouson, D. W., & Eaton, J. K. (2001). On the preferential concentration of solid particles in turbulent channel flow. *Journal of Fluid Mechanics, 428.* https://doi.org/10.1017/S0022112000002627

Safikhani, H., Shams, M., & Dashti, S. (2011). Numerical simulation of square cyclones in small sizes. *Advanced Powder Technology, 22,* 359–365.

Sagaut, P. (2006). *Large eddy simulation for incompressible flows.* https://doi.org/10.1007/b137536

Sajjadi, H., Tavakoli, B., Ahmadi, G., Dhaniyala, S., Harner, T., & Holsen, T. (2016). Computational fluid dynamics (cfd) simulation of a newly designed passive particle sampler. environ. pollut. 214, 410–418.

Salat, J., Xin, S., Joubert, P., Sergent, A., Penot, F., & Le Quéré, P. (2004). Cexperimental and numerical investigation of turbulent natural convection in a large air-filled cavity. *Int. J. Heat Fluid Flow,* 824–832.

Saufi, A., Frassoldati, A., Faravelli, T., & Couci, A. (2019). Dropletsmoke++: a comprehensive multiphase cfd framework for the evaporation of multidimensional fuel droplets, international journal of heat and mass transfer, volume 131, pages 836-853.

Sayed, M. A., Dehbi, A., Hadžiabić, M., Niceno, B., & Mikityuk, M. (2022). Cfd simulation of particle-laden flow in a 3d differentially heated cavity using coarse large eddy simulation. *Flow, Turbulence and Combustion.* https://doi.org/doi.org/10.1007/s10494-022-00356-4

Sayed, M. A., Dehbi, A., Hadžiabić, M., Niceno, B., & Mikityuk, M. (2021-c). On sub-grid scale modeling in a differentially heated cavity using coarse large eddy simulation.

Engineering, Turbulence, Modelling and Measurements (ETMM13). https://doi.org/doi.org/10.48550/arXiv.2110.00389

Sayed, M. A., Dehbi, A., Niceno, B., & Mikityuk, K. On the prediction of turbulent kinetic energy in channel flow using wall-modeled large eddy simulations. In: *AIAA 2020-1329.* 2020. https://doi.org/https://doi.org/10.2514/6.2020-1329.

Sayed, M. A., Dehbi, A., Niceno, B., & Mikityuk, K. (2021-b). Particle subgrid scale modeling in hubrid rans/les of turbulent channel flow at low-to-moderate reynolds number. *Powder Technology.* https://doi.org/https://doi.org/10.1016/j.powtec.2021.11.057

Sayed, M. A., Dehbi, A., Ničeno, B., Mikityuk, K., & Krinner, M. (2021-a). Flow simulation of gas cyclone separator at high reynolds number using the elliptic-relaxation hybrid les/rans (er-hrl) model, proceedings of the 6th world congress on momentum, heat and mass transfer (mhmt'21). https://doi.org/10.11159/icmfht21.lx.110

Schiller, L., & Naumann, Z. (1935). *A drag coefficient correlation* (Vol. 77). https://doi.org/10.1016/j.ijheatmasstransfer.2009.02.006

Schmitt, F. G. (2017). Turbulence from 1870 to 1920: the birth of a noun and of a concept. *Comptes Rendus Mecanique, 345,* 620–626.

Schmitt, F. G., & Huang, Y. (2016). *Stochastic analysis of scaling time series: from turbulence theory to applications.*

Schuetz, S., Mayer, G., Bierdel, M., & Piesche, M. (2004). Investigations on the flow and separation behavior of hydrocyclones using computational fluid dynamics. *International Journal of Mineral Processing, 73,* 229–237.

Sebilleau, F., Issaa, R., Lardeau, S., & Walker, S. (2018). Direct numerical simulation of an air-filled differentially heated square cavity with rayleigh numbers up to 1e11. *International journal of Heat and Mass Transfer, 123,* 297–319.

Seldner, D., & Westermann, T. (1988). Algorithms for interpolation and localization. *J. Comp. Phys., 79,* 1–11.

Sergent, A., Joubert, P., Xin, S., & Le Quéré, P. (2013). Resolving the stratification discrepancy of turbulent natural convection in differentially heated air filled cavities – part ii: end walls effects using large eddy simulation. *International Journal of Heat Fluid Flow, 39,* 15–27.

Sergent, A., Xin, S., Joubert, P., Le Quéré, P., Salat, J., & Penot, F. (2013). Resolving the stratification discrepancy of turbulent natural convection in differentially heated air filled cavities – part i: reference solution using chebyshev spectral methods. *International Journal of Heat Fluid Flow, 39,* 1–14.

Shampine, L. (1975). Computer solution of ordinary differential equations. the initial value problem. *W.H. Freeman, San Francisco.*

Shi, L., & Bayless, D. (2007). Comparison of boundary conditions for predicting the collection efficiency of cyclones. *Powder Technology, 173,* 29–37.

Shukla, S., Shukla, P., & Ghosh, P. (2011a). Evaluation of numerical schemes for dispersed phase modeling of cyclone separators. *Engineering Applications of Computational Fluid Mechanics, 5,* 235–246.

Shukla, S., Shukla, P., & Ghosh, P. (2011b). Evaluation of numerical schemes using different simulation methods for the continuous phase modeling of cyclone separators. *Advanced Powder Technology, 22*, 209–219.

Shur, M. L., Spalart, P. R., Strelets, M. K., & Travin, A. K. (2008). A hybrid rans-les approach with delayed-des and wall-modelled les capabilities, volume 29, issue 6. *International Journal of Heat and Fluid Flow*. https://doi.org/10.1016/j.ijheatfluidflow.2008.07.001

Shur, M. L., Spalart, P. R., Strelets, M. K., & Travin, A. K. (2015). An enhanced version of des with rapid transition from rans to les in separated flows. *Flow, Turbulence and Combustion, 95*. https://doi.org/10.1007/s10494-015-9618-0

Sikovsky, D. P. (2014). Singularity of inertial particle concentration in the viscous sublayer of wall-bounded turbulent flows, issue 92, 41–64. *Flow, Turbulence and Combustion.*

Slack, M., Prasad, R., & Boysan, F. (2000). Advances in cyclone modeling using unstructured grids. *Institution of Chemical Engineers, 78*, 1098–1104.

Smagorinsky, J. (1963). General circulation experiments with the primitive equations. i. the basic experiment. *Mon. Weather Rev., 91*, 99–164.

Soldati, A., & Marchioli, C. (2009). Physics and modelling of turbulent particle deposition and entrainment: review of a systematic study. *International Journal of Multiphase Flow, Volume 35, Issue 9, September 2009, Pages 827-839.*

Spalart, P. R. (2000). Strategies for turbulence modelling and simulations. *International Journal of Heat and Fluid Flow, 21*. https://doi.org/10.1016/S0142-727X(00)00007-2

Spalart, P. R., & Allmaras, S. (1992). A one-equation turbulence model for aerodynamic flows. *AIAA*, 5–21.

Spalart, P. R., Deck, S., Shur, M. L., Squires, K. D., Strelets, M. K., & Travin, A. (2006). A new version of detached-eddy simulation, resistant to ambiguous grid densities. *Theoretical and Computational Fluid Dynamics, 20*. https://doi.org/10.1007/s00162-006-0015-0

Spalart, P. R., Jou, W. H., Strelets, M., & Allmaras, S. R. (1997). Comments on the feasibility of les for wings, and on a hybrid rans/les approach. *C. Liu and Z. Liu (Eds.), Advances in LES/DNS, Proc. of the rst AFOSR int. conf. on DNS/LES, Rouston Lousiana, U.S.A. Greyden Press, Columbus*, 1–11.

Speziale, C. G., Sarkar, S., & Gatski, T. B. (1991). Modeling pressure-strain correlation in turbulence: a dynamic invariant approach. *J. Fluid Mech., 227*, 245–272.

Strelets, M. (2001). Detached eddy simulation of massively separated flows. *39th Aerospace Sciences Meeting and Exhibit*. https://doi.org/10.2514/6.2001-879

Su, Y., Zheng, A., & Zhao, B. (2011). Numerical simulation of the effect of the inlet configuration on square cyclone separator performance. *Powder Technology, 210*, 293–303.

Talbot, L., Cheng, R., Schefer, R., & Willis, D. (1980). Thermophoresis of particles in a heated boundary layer. *Journal of Fluid Mechanics, 101*, 737–758.

Tavakol, M., Ghahramani, E., Abouali, O., Yaghoubi, M., & Ahmadi, G. (2017). Deposition fraction of ellipsoidal fibers in a model of human nasal cavity for laminar and turbulent flows. j aerosol sci 113, 52–70.

Tennekes, H., & Lumley, J. (1972). *A first course in turbulence.*

Thornton, C., & Ning, Z. (1998). A theoretical model for the stick/bounce behaviour of adhesive, elastic-plastic spheres. *Powder Technology, 99*(2), 154–162. https://doi.org/https://doi.org/10.1016/S0032-5910(98)00099-0

Thorpe, S. (2005). *The turbulent ocean.*

Tian, L., & Ahmadi, G. (2013). Fiber transport and deposition in human upper tracheo-bronchial airways. *Journal of Aerosol Science, 60, 1–20.*

Tian, Y., & Karayiannis, T. (2000a). Low turbulence natural convection in an air filled square cavity. part i. thermal and fluid flow fields. *Int. J. Heat Mass Transfer, 43*, 849–866.

Tian, Y., & Karayiannis, T. (2000b). Low turbulence natural convection in an air filled square cavity. part ii. the turbulence quantities. *Int. J. Heat Mass Transfer, 43*, 867–884.

Travin, A., Shur, M., Strelets, M., & Spalart, P. R. (2004). Physical and numerical upgrades in the detached-eddy simulation of complex turbulent flows. *Fluid Mechanics and its Applications, 65.* https://doi.org/10.1007/0-306-48383-1_16

Trias, F., Gorobets, A., Soria, M., & Oliva, A. (2010a). Direct numerical simulation of a differentially heated cavity of aspect ratio 4 with rayleigh numbers up to 1011 — part i: numerical methods and time-averaged flow. *International Journal of Heat and Mass Transfer, 53 (4)*, 665–673.

Trias, F., Gorobets, A., Soria, M., & Oliva, A. (2010b). Direct numerical simulation of a differentially heated cavity of aspect ratio 4 with rayleigh numbers up to 1011 — part ii: heat transfer and flow dynamics. *International Journal of Heat and Mass Transfer, 53 (4)*, 674–683.

Trias, F., Soria, M., Oliva, A., & Pérez-Segarra, C. (2007). Direct numerical simulations of two- and three-dimensional turbulent natural convection flows in a differentially heated cavity of aspect ratio 4. *Journal of Fluid Mechanics, 586*, 259–293.

Valverde, R., Coury, J., & Gonçalves, J. (2011). Numerical modeling of particle dynamics in a cyclone separator. *21 st Brazilian Congress of Mechanical Engineering, Natal, RN, Brazil*, 24–28.

Vinkovic, I., Doppler, D., Lelouvetel, J., & Buffat, M. (2011). Direct numerical simulation of particle interaction with ejections in turbulent channel flows. *International Journal of Multiphase Flow, 37.* https://doi.org/10.1016/j.ijmultiphaseflow.2010.09.008

Wan, G., Sun, G., Xue, X., & Shi, M. (2008). Solids concentration simulation of different size particles in a cyclone separator. *Powder Technology, 183*, 940–194.

Wana, M. P., Chaoa, C. Y. H., Nga, Y. D., Sze Toa, G. N., & Yub, W. C. (2007). Dispersion of expiratory droplets in a general hospital ward with ceiling mixing type mechanical ventilation system. *Aerosol Science and Technology, 41*, 244–258.

Wang, B., Xu, D., Chu, K., & Yu, A. (2006). Numerical study of gas–solid flow in a cyclone separator. *Applied Mathematical Modelling, 30*, 1326–1342.

Wang, Q., & Squires, K. (1998). Large eddy simulation of particle-laden turbulent channel flow. *Physics of Fluids, vol 8, issue 5.* https://doi.org/https://doi.org/10.1063/1.868911

Warhaft, Z. (2008). Laboratory studies of droplets in turbulence: towards understanding the formation of clouds, fluid dynamics research, issue 41 (1), 011201.

Wasilewski, M., Anweiler, S., & Masiukiewicz, M. (2019). Characterization of multiphase gas–solid flow and accuracy of turbulence models for lower stage cyclones used in suspension preheaters. *Chinese Journal of Chemical Engineering, 27*, 1618–1629. https://doi.org/https://doi.org/10.1016/j.cjche.2018.11.019

Wilcox, D. (1993). *Turbulence modeling for cfd*.

Wyngaard, J. (2010). *Turbulence in the atmosphere*.

Xiang, R., Park, S., & Lee, K. (2001). Effects of cone dimension on cyclone performance. *Journal of Aerosol Science, 32*, 549–561.

Xin, S., & Le Quéré, P. (1995). Direct numerical simulation of two dimensional chaotic natural convection in a differentially heated cavity of aspect ratio 4. *Journal of Fluid Mechanics, 304*, 87–118.

Xin, S., Salat, J., Joubert, P., Sergent, A., Penot, F., & Le Quéré, P. (2013). Resolving the stratification discrepancy of turbulent natural convection in differentially heated air-filled cavities. part iii: a full convection-conduction-surface radiation coupling. *International Journal of Heat Fluid Flow, 42*, 33–48.

Yang, S., Sun, Y., Wang, J., Cahyadi, A., & Chew, J. (2016). Influence of operating parameters and flow regime on solid dispersion behavior in a gas–solid spout-fluid bed, chemical engineering science, volume 142, 13 pages 112-125.

Zamankhan, P., Ahmadi, G., Wang, Z., Hopke, P., Cheng, Y.-S., Su, W., & Leonard, D. (2006). Airflow and deposition of nano-particles in a human nasal cavity. *Journal of Aerosol Science and Technology. 40 (6), 463–476.*

Zamansky, R., Vinkovic, I., & Gorokhovski, M. (2010). Les approach coupled with stochastic forcing of subgrid acceleration in a high reynolds number channel flow, issue 11 (30), 1–18. *Journal of Turbulence*. https://doi.org/https://doi.org/10.1080/14685248.2010.496787

Zamansky, R., Vinkovic, I., & Gorokhovski, M. (2011). Solid particle acceleration in a high reynolds number channel flow: dns and les with stochastic modelling of subgrid acceleration. *Journal of Physics: Conference Series, 333*. https://doi.org/10.1088/1742-6596/333/1/012019

Zhang, T., Wei, C., Feng, C., Ren, Y., Wu, H., & Prei, S. (2019). Advances in characteristics analysis, measurement methods and modelling of flow dynamics in airlift reactors. *Chemical Engineering and Processing - Process Intensification, 144*. https://doi.org/10.1016/j.cep.2019.107633

Zhao, B., Su, Y., & Zhang, J. (2006). Simulation of gas flow pattern and separation efficiency in cyclone with conventional single and spiral double inlet configuration. *Chemical Engineering Research and Design, 84*, 1158–1165.

Zhou, Q., & Leschziner, M. A. (1999). An improved particle-locating algorithm for eulerian-lagrangian computations of two-phase flows in general coordinates. *Int. J. Multiphase Flow, 25*, 813–825.

Mohamed Aly SAYED

Date of birth: 05.11.1994

Mobile : +447542334834
Address: 50 Brashland Dr - NN4 0SS Northampton - UK

LinkedIn: Mohamed Sayed
E-mail: muhammmedaly@gmail.com

PROFILE

I'm a very hard working and enthusiastic individual. I enjoy working with open-minded teams where I can integrate new ideas in a collective effort. Working on my PhD program and supervising other academics has promoted my **project management** and communication skills. I'm also known to be very **autonomous** and task-oriented. I perceive myself to be curious to explore new things and always willing to push boundaries.

EDUCATION

- **École polytechnique fédérale de Lausanne (EPFL)** — Lausanne, Switzerland
  Ph.D. in Complex Particulate Turbulent Flows — *Nov 2018 – October 2022*

- **Grenoble INP University** — Grenoble, France
  M.Sc. in Fluid Mechanics & Energetics — *Sep 2017 – August 2018*

- **Cairo University** — Cairo, Egypt
  B.Sc. in Aerospace Engineering — *Sep 2012 – July 2017*

EXPERIENCE

- **Aston Martin Formula One Team** — Silverstone, UK
  CFD Engineer — *Oct 2022 - present*
  - Develop the CFD methodology used for predicting the flowfield.
  - Write Python scripts to automate the CFD baseline for an optimized framework
  - Investigate and assess correlation data for the best fit with the wind tunnel
  - Provide support for the Aerdynamics department.

- **Paul Scherrer Institut (PSI)** — Villigen, Switzerland
  PhD Researcher — *Nov 2018 - Oct 2022*
  - Implementation of Lagrangian Particle Tracking (LPT) algorithm in T-Flows.
  - Validation and testing of hybrid RANS/LES models for complex industrial flows.
  - Implementing wall-modeled Large Eddy Simulation (WMLES) and particle Sub-grid scale models.
  - Performing numerical simulations of complex industrial flows using in-house and commercial CFD codes.
  - Assessing the performance of hybrid RANS/LES models in predicting mono-dispersed particulate flows.

- **ETH Zürich — CMTFD 151-0170-00L** — Zürich, Switzerland
  Teaching Assistant — *Feb 2020 - Feb 2022*
  - Solving Benchmark problems using ANSYS Fluent.
  - Giving Exercises on single-phase and multi-phase flow modeling.
  - Exercises on Eulerian/Lagrangian two-phase flow modeling.

- **Swissloop** — Zurich, Switzerland
  CFD Advisor — *July 2019 - present*
    - Mentoring CFD simulations of Swissloop pod, and giving seminars.
    - Supervising M.Sc. and B.Sc. theses under Swissloop project.
- **ArcelorMittal Maizières Research SA** — Metz, France
  Engineering Intern — *Feb 2018 - August 2018*
    - Optimization of Heating Strategies inside Steel Reheating Furnaces.
    - Front-end developer: created software to analyze products inside reheating furnaces.

Workshops

- **ETH Zurich** — Zurich, Switzerland
  Parallel Programming workshop — *August 2020*
    - Distributed memory parallelization with the Message Passing Interface.
    - MPI intermediate: Derived datatyoes and shared Memory One-sided Communication.
    - Shared Memory Parallelization with OpenMP.
    - Advanced MPI: Memory models and shared memory synchronization rules.
- **AMIT Learning** — Cairo, Egypt
  Embedded Systems Software Diploma — *Jul 2017 - Jan 2018*
    - C Programming & Data Structure, Software Engineering, Embedded system Tools, microcontroller and microprocessor AVR &ARM, Interfacing, RTOS, Testing and validating, and Automotive Bus technology.
- **American University in Cairo (AUC)** — Cairo , Egypt
  Renewable Energy Workshop — *June - Jul 2017*
    - On & Off-grid PV Solar Applications.
- **California Polytechnic State University** — California , USA
  Robotics workshop — *Jul - Aug 2016*
    - Design and assemble an autonomous mobile robot with GPS and IMU.
    - PLC programming language on Allen Bradly (RS Logix 5000 software).
- **EgyptAir** — Cairo, Egypt
  Engineering Intern [hands-off] — *2014*
    - Aircraft Maintenance and Overhauling.

Fellowships

- The Zentith Award for Academic Excellence (Valar MBA) - Zenith   (2022 - 2023)
- SNSF PhD Fellowship - SNSF [200021-175532]   (2018 - 2022)
- STEM Master's Fellowship - Al Alfi Foundation   (2017 - 2018)

Supervisions

- Imperial College London — M.Sc. thesis "Study of Hyperloop pod acceleration and deceleration on tube walls" conducted by Tomas Mrazek, (Feb. 2022 - June 2022).
- ETH Zurich — M.Sc. thesis "Study of Hyperloop pod equipped with compressor to overcome the Kantrowitz limit" conducted by Maurice Bizzozero, (Aug. 2020 - March 2021).
- ETH Zurich — B.Sc. thesis "On the Aerodynamic Performance of Successive Travelling Hyperloop Pods", conducted by Maria Krinner, (Feb. 2020 - June 2020).

Conferences

- Paper presenter at EUROMECH-625 on the Advances in LES of Turbulent Multiphase Flows (June 2022)
- Paper presenter at ERCOFTAC on engineering, turbulence, modelling and measurements (Aug. 2021)
- Paper presenter at the 6th International Conference on Multiphase Flow and Heat Transfer (Apr. 2021).
- Paper presenter at CFD for Nuclear Reactor Safety (CFD4NRS) (Nov. 2020).
- Paper presenter at AIAA SciTech convention in Florida, USA (Jan. 2020).
- Paper presenter at HZDR short course and conference in Germany (Sep. 2019).
- Exhibitor at SpaceX Hyperloop Public Conference (Jan. 2017).

Activities

- Member of the green team at the PPA-PSI (2021 - present).
- Volunteer at Resala charitable organization (2015 - 2017).
- IRC member at US Embassy in Cairo (2014).
- IEEE member - Cairo University Branch (2013).
- WAN Student Activity head at Cairo University (2012).

Publications

- Journal publications
  - T. Mrazek, S. Yohei, M. A. Sayed, N. Nick, 2022, Investigation of shock wave reflected at tube end, and its impact on pod and tube structure after reflection, Journal of Aerospace Science and Technology. (under review)
  - M. A. Sayed, M. Hadziabic, A. Dehbi, B. Niceno, K. Mikityuk, 2022, Simulation of Flow and Heat Transfer in a Differentially Heated Cubical Cavity Using Coarse Large Eddy Simulation, International Journal of Thermal Sciences.
  - M. A. Sayed, A. Dehbi, M. Hadziabic, B. Niceno, K. Mikityuk, 2022, CFD Simulation of Particle-Laden Flow in a 3D Differentially Heated Cavity Using Coarse Large Eddy Simulation,Journal of Flow, Turbulence and Combustion.
  - M. A. Sayed, A. Dehbi, B. Niceno, K. Mikityuk, 2021, Particle Subgrid Scale Modeling in Hybrid RANS/LES of Turbulent Channel Flow at Low to Moderate Reynolds Number Journal of Powder Technology.
  - M. Bozzizero, S. Yohei, M. A. Sayed, 2021, Aerodynamic study of a Hyperloop pod equipped with compressor to overcome the Kantrowitz limit, Journal of Wind Engineering and Industrial Aerodynamics.

- Conference proceedings
  - M. A. Sayed, A. Dehbi, M. Hadziabic, B. Niceno, K. Mikityuk, 2021, On sub-grid scale modeling in a differentially heated cubical cavity using coarse large eddy simulation. 13th International ERCOFTAC symposium on engineering, turbulence, modelling and measurements (ETMM).
  - M. A. Sayed, A. Dehbi, B. Niceno, K. Mikityuk, M. Krinner, Flow Simulation of Gas Cyclone Separator at High Reynolds Number Using the Elliptic-Relaxation Hybrid LES/RANS (ER-HRL) Model, 6th International Conference on Multiphase Flow and Heat Transfer (ICMFHT 2021), April 2021.
  - M. A. Sayed, A. Dehbi, B. Niceno, K. Mikityuk, Validation of Wall Modeled Large Eddy Simulation Against Direct Numerical Simulation In Particulate Channel Flow, the 8th Computational Fluid Dynamics for Nuclear-Reactor Safety (CFD4NRS-8th), 2020.
  - M. A. Sayed, A. Dehbi, B. Niceno, K. Mikityuk, On the Prediction of Turbulent Kinetic Energy in Channel Flow Using Wall-Modeled Large Eddy Simulation, AIAA 2020-1329.

Research Interests

- Computational Fluid Dynamics (CFD)
- Lagrangian Particle Tracking (LPT)
- Turbulence Modeling: Hybrid LES/RANS methods
- Machine Learning (ML) and Deep Neural Networks (DNN)
- Blockchain Technology

Language Skills

- **Arabic** (Native), **English** (Proficient), **German** (B1), **French** (A2)

Technical Skills

- MATLAB, C, C++, C#, Python, Fortran 90/95, LabVIEW, Paraview, Github, COMSOL, SpaceClaim, NX, CATIA, ANSOFT Maxwell, Solidworks, TensorFlow, SnappyHexMesh, Shell scripting, Simulink, Pointwise, ANSYS Fluent, Design of experiments (DOE), OpenFOAM, StarCCM+, Microsoft Office, LaTeX, OSs (Windows 10 - MacOS X - Ubuntu)

Soft Skills

- Resilience, self-motivation, leadership, public speaking, troubleshooting and design sense, perseverance, business development, self-reflection, project management, autonomy.

Mohamed Aly Sayed has been appointed as a PhD candidate at Paul Scherrer Institut from 2018 - 2022. He studied his B.Sc. of Aerospace Engineering at Cairo University in Egypt (2012 - 2017), and M.Sc. of Fluid Mechanics and Energetics at Grenoble university Alpes in France (2017 - 2018). During his Ph.D., Mohamed has been investigating the dispersion of Lagrangian particles in complex wall-bounded turbulent flows where he published several papers in respected journals and conferences. He also participated as a teaching assistant at ETH university in Zurich (ETHZ) giving Computational Fluid Dynamics (CFD) exercises in multiphase flow modeling. In addition, he has been supervising MSc and BSc theses from Swissloop team at ETHZ and in collaboration with other prestigious universities. Mohamed has recently commenced working for Aston Martin Formula One team (AMR GP Ltd) as a CFD engineer as of October 2022.